



Achieving 0.1 K absolute calibration accuracy for high spectral resolution infrared and far infrared climate benchmark measurements

Thèse

Joseph Taylor

Doctorat en génie électrique

Philosophiae Doctor (Ph.D.)

Québec, Canada
© Joseph Taylor, 2014

Résumé

Mesurer le rayonnement infrarouge de manière résolue spectralement à partir de satellites avec une très haute précision radiométrique constitue un besoin critique pour les futures missions de référence climatique. Pour les spectres de rayonnement infrarouge, il a été déterminé qu'une précision de mesure exprimée comme une erreur de température de brillance inférieure à 0,1 K est nécessaire pour la détection de tendances au-delà de la variabilité naturelle des signatures climatiques sur une décennie.

Le "Space Science and Engineering Center" de l'Université du Wisconsin (UW-SSEC), avec le soutien financier du programme d'incubateur d'instrument de la NASA, a développé "l'Absolute Radiance Interferometer" (ARI). L'ARI est conçu pour répondre aux exigences nécessaires afin de réaliser des mesures de radiance absolue résolues spectralement à partir de l'espace, dans le cadre d'une mission de référence pour suivre les tendances du climat.

Le défi dans le développement de capteurs infrarouges pour une telle mission est d'atteindre cette haute précision avec un design qui peut être qualifié pour le vol spatial, qui a une longue durée de vie et qui est relativement petit, simple et abordable. L'approche pour la conception de l'ARI fait usage de composants ayant un historique de vol spatial qui sont combinés en un ensemble fonctionnel pour tester les performances détaillées. La simplicité requise est réalisable en raison des grandes différences dans les exigences d'échantillonnage et de bruit par rapport à celles des sondeurs infrarouges de télédétection typiques pour la recherche ou les déploiements opérationnels pour la météo.

L'aspect original de cet instrument et de cette thèse est donc la démonstration de l'atteinte de la haute précision radiométrique. Le but de cet effort est de démontrer avec succès la possibilité de telles mesures dans des conditions de laboratoire et de vide, sur un sous-ensemble de la gamme des températures de brillance attendues en orbite. Des progrès dans la compréhension de aspects instrumentaux des spectromètres ont été accomplis en lien avec la poursuite de cet objectif et sont également rapportés dans cette thèse.

Abstract

Spectrally resolved infrared radiances measured from orbit with extremely high absolute accuracy constitute a critical observation for future climate benchmark missions. For the infrared radiance spectra, it has been determined that a measurement accuracy, expressed as an equivalent brightness temperature error, of 0.1 K confirmed on orbit is required for signal detection above natural variability for decadal climate signatures.

The University of Wisconsin Space Science and Engineering Center (UW-SSEC), with funding support from the NASA Instrument Incubator Program (IIP), developed the Absolute Radiance Interferometer (ARI). The ARI is designed to meet the uncertainty requirements needed to establish a spectrally resolved thermal infrared climate benchmark measurements from space.

The challenge in the infrared sensor development for a climate benchmark measurement mission is to achieve this ultra-high accuracy with a design that can be flight qualified, has long design life, and is reasonably small, simple, and affordable. In this area, our design approach for the Absolute Radiance Interferometer (ARI) made use of components with strong spaceflight heritage (direct analogs with high TRL) combined into a functional package for detailed performance testing. The required simplicity is achievable due to the large differences in the sampling and noise requirements for the benchmark climate measurement from those of the typical remote sensing infrared sounders for weather research or operations.

The new aspect of the interferometer development is the ultra high absolute accuracy sought, and is the subject of this thesis. The goal of this effort is to successfully demonstrate this measurement capability under laboratory and vacuum conditions, over a subset of the range of equivalent earth scene brightness temperatures expected on-orbit. Advances in instrumental aspects have been achieved in the pursuit of this goal.

Table of Contents

Résumé	iii
Abstract	v
Table of Contents	vii
List of Tables	xi
List of Figures	xiii
Dedication.....	xxvii
Acknowledgements	xxix
Introduction.....	1
Climate benchmark measurements from space.....	1
Fourier Transform Infrared Spectrometers.....	3
Key advances in FTS.....	3
Motivations and thesis outline	4
1 Research project description and methodology	5
1.1 Calibration accuracy of existing remote sensing IR FTS sensors	5
1.2 The Absolute Radiance Interferometer.....	7
1.2.1 Top-level trade studies and final specification	10
1.3 Experimental set-up.....	17
1.4 Calibration	19
1.4.1 Calibration approach	20
1.4.2 Calibration uncertainty	21
1.5 Radiometric uncertainty estimate	24
1.5.1 Calibration verification methodology	26
1.5.2 Predicted calibration and calibration validation uncertainty	27
1.6 Challenges.....	38

2	Nonlinearity and nonlinearity correction.....	41
2.1	Impact of nonlinearity in Fourier Transform Spectrometers.....	41
2.1.1	Mathematical representation	43
2.2	Nonlinearity correction algorithm	46
2.3	Determining the required linearity.....	51
2.4	Nonlinear response and correction in the ARI prototype	53
2.4.1	Nonlinearity characterization via out-of-band response	54
2.4.2	Nonlinearity correction for the ARI long-wave detector	60
2.4.3	Nonlinearity correction verification.....	66
2.5	Impact on radiometric uncertainty.....	68
2.6	Recommendations for future designs	69
3	Optical design, stray light and vignetting	71
3.1	Optical design	71
3.1.1	Fore-optics.....	72
3.1.2	Aft-optics design – FIR output port (DTGS detector).....	74
3.1.3	Aft-optics Design – IR output port (HgCdTe, InSb detectors).....	75
3.2	Stray light and vignetting	77
3.2.1	Calibration verification testing under vacuum.....	77
3.2.2	Post-vacuum stray light diagnostic testing	84
3.3	Shear, field angle, and non-uniform scene	98
3.4	Recommendations for future designs	101
4	Polarization induced calibration biases.....	103
4.1	Theoretical model	107
4.2	Refined polarization model following Stokes formalism.....	115
4.3	Polarization sensitivity characterization and verification	119

4.3.1	Four-source polarization test.....	120
4.3.2	Two source polarization test with linear polarizer	130
4.3.3	Polarization characterization and verification summary	145
4.4	Recommendations for future designs.....	147
5	Low signal to noise ratio and calibration	149
6	Conclusion: demonstration of 0.1 K calibration accuracy.....	159
6.1	Radiometric uncertainty.....	159
6.2	Calibration verification results.....	161
6.3	Conclusion.....	173
7	References.....	177
A.	Polarization induced calibration bias model	185

List of Tables

Table 1: Infrared measurement requirements for climate benchmark measurements from space.	14
Table 2: ARI key design parameters.	15
Table 3: ARI calibration source and OARS temperature uncertainty budget. Note that a temperature uncertainty of 0.045 K for the calibration reference blackbodies and the OARS is used in the ARI radiometric uncertainty analysis for all environments.	24
Table 4: Uncertainty estimates used in the radiometric uncertainty analysis for the on-orbit configuration. For the flight sensor, it has been assumed that the OARS emissivity and associated uncertainty is determined from laboratory testing with a very high emissivity source. (* $e_{\text{OARS}}=0.999\pm 0.0006$ (200 cm^{-1}), ± 0.0004 (800 cm^{-1}), ± 0.0002 (1400 cm^{-1}), ± 0.0001 (2000 cm^{-1}), ± 0.000075 (2600 cm^{-1}))	28
Table 5: Uncertainty estimates used in the radiometric uncertainty analysis for laboratory configuration.	30
Table 6: Uncertainty estimates used in the radiometric uncertainty analysis for vacuum configuration.	33
Table 7: Quadratic nonlinearity coefficient characterization via low wavenumber out-of-band analysis for the LW MCT.	56
Table 8: Relative orientation of scene select mirror and sensor polarizations, and resulting transmission for unpolarized light.	106
Table 9: Polarization model parameters.	111
Table 10: Possible target and calibration reference combinations for the four-source polarization test. The results presented herein are for an OARS target with HBB and CBB calibration references.	122
Table 11: A summary of the polarization characterization measurement results for the two-source and four-source polarization tests is presented here. Brackets are used to indicate results that were not explicitly measured, but have been extrapolated assuming a 90° spacing of the zero-crossing polarization sensitivity points.	146
Table 12: ARI DTGS data collections used for instrument calibration verification results presented herein. Average OARS, blackbody reference, and instrument temperatures are provided.	163
Table 13: ARI LW MCT data collections used for instrument calibration verification results presented herein. Average OARS, blackbody reference, and instrument temperatures are provided.	163

List of Figures

Figure 1: A notional illustration indicating the primary Absolute Radiance Interferometer subsystems and optical path.....	8
Figure 2: Front view of the completed ARI sensor prototype, showing the Ambient Blackbody (ABB) calibration reference, the Hot Blackbody (HBB) calibration reference, and the On-orbit Absolute Radiance Standard (OARS) calibration verification blackbody; any of these sources can be selected using the scene selection mirror (SSM). The OARS includes the Heated Halo On-orbit Cavity Emissivity Monitor (OCEM), which is located inside the OARS case and not visible here.	9
Figure 3: Internal view of the completed ARI sensor prototype. Primary components are labelled, and include the ABB Generic Interferometer for Climate Studies (GICS), the Stirling cooler, the fore-optics, far-infrared (FIR) aft-optics and deuterated triglycine sulfate (DTGS) detector, the infrared (IR) aft-optics and detector dewar module, and the second input port reference source.	10
Figure 4: Interferometer configurations [78]: (a) substrate plus compensator, 2 port; (b) substrate plus compensator, 4 port; (c) single substrate, self-compensated, 4-port; (d) uncompensated, uncoated single substrate, 4-port.	12
Figure 5: Solid model of the ABB Generic Flight Interferometer (GFI) (provided by ABB [79]).	16
Figure 6: Preliminary solid model of the ABB Generic Interferometer for Climate Studies (GICS) (provided by ABB [80]).	16
Figure 7: Typical on-orbit calibration, calibration verification, and scene view configuration.	18
Figure 8: Typical laboratory calibration, calibration verification, and scene view configuration.	18
Figure 9: The ARI uses a 45° scene selection mirror rotated about the local optical axis (often referred to as a “barrel-roll” scene mirror configuration) to select the viewport that the instrument views. The angle of reflection at the scene mirror is the same for all calibration and scene views: (a) the instrument views the radiance from HBB blackbody at the zenith position; (b) the radiance from the ABB blackbody at the 90° position is selected; (c) the radiance from the CBB blackbody at the 0° position is selected; and (d) the OARS radiance at the 270° position is directed into the instrument.	19
Figure 10: Predicted on-orbit radiometric calibration uncertainty (dashed) and calibration verification source uncertainty (solid) (k = 3).	28
Figure 11: Predicted on-orbit combined radiometric calibration and verification uncertainty (k = 3).	29
Figure 12: Predicted laboratory radiometric calibration uncertainty (dashed) and calibration verification source uncertainty (solid) (k = 3).	31
Figure 13: Predicted laboratory combined radiometric calibration and verification uncertainty (k = 3).	31

Figure 14: Predicted vacuum radiometric calibration uncertainty (dashed) and calibration verification source uncertainty (solid) ($k = 3$).....33

Figure 15: Predicted vacuum combined radiometric calibration and verification uncertainty ($k = 3$).34

Figure 16: ARI calibration uncertainty ($k = 3$) (a) predicted on-orbit, (b) in the laboratory test configuration, and (c) during vacuum testing.....36

Figure 17: ARI calibration verification uncertainty ($k = 3$) (a) predicted on-orbit, (b) in the laboratory test configuration, and (c) during vacuum testing.37

Figure 18: Analysis conducted by Tobin et al [96], indicate that this should not be an issue for the large dataset means associated with the infrared climate benchmark measurement. The nominal self-apodization correction corresponds to a uniformly illuminated field of view. Typically, the field of view is not uniformly illuminated and the spatial and radiometric distribution of the non-uniformity is random for large datasets. The histogram of the spectral shifts, with respect to the to on-axis field of view (FOV) after self-apodization correction, observed for CrIS is shown.39

Figure 19: Example of a simulated measurement of an atmospheric spectra (U.S. standard atmosphere, top of atmosphere (TOA)) with detection bandwidth of less than one octave affected by quadratic nonlinearity (quadratic artifacts indicated by arrows) [25, 105].....42

Figure 20: Example of a simulated measurement of an atmospheric spectra (U.S. standard atmosphere, top of atmosphere (TOA)) with detection bandwidth of greater than one octave affected by quadratic nonlinearity (quadratic artifacts indicated by arrow) [25, 105].42

Figure 21: A stylized representation of a hypothetical detector-response curve exhibiting nonlinearity [97]. The abscissa represents the absolute magnitude of the incident photon flux on the detector and the measured signal is on the ordinate axis. The figure assumes a modulation efficiency of 70%, and does not include the DC signal due to the electronics biasing or detector dark current.43

Figure 22: The quadratic and cubic nonlinearity spectral artifacts corresponding to a single octave ($\Delta_1 = 2\Delta_0$) uniform spectral band distribution with sufficient sampling such that out-of-band artifacts are not aliased in-band. Artifacts are not to scale.....45

Figure 23: The quadratic and cubic nonlinearity spectral artifacts corresponding to a two-octave ($\Delta_1 = 3\Delta_0$) uniform spectral band distribution with sufficient sampling such that out-of-band artifacts are not aliased in-band. When the spectral bandpass is greater than one octave, the quadratic artifact also overlaps the in-band measurement. Artifacts are not to scale.....46

Figure 24: The 0.1 K requirement and the predicted radiometric uncertainty (Total RU, blue) derived in Chapter 1 can be used to determine the allowable radiometric uncertainty (Max NL RU, red) due to nonlinearity.....51

Figure 25: For the model, the effect of nonlinearity was applied directly to the calibrated radiance, rather than the individual scene and calibration reference measurements. The model employs a quadratic nonlinear

behaviour for the calibrated radiance bias, with zero bias when the scene radiance is equal to either reference radiance [122]...... 52

Figure 26: The model results indicated that the residual nonlinearity, expressed as a percentage error in the calibrated radiance, should be limited to less than 0.03% when considering a range of scene temperatures from 230 – 320 K, and wavenumber range of 200 – 2600 cm^{-1} 53

Figure 27: DTGS measured signal, normalized to the in-band peak for a 216.07 K target. The top panel shows the real spectrum (red), the imaginary component of the spectrum (light blue), and the shape of the quadratic nonlinearity (grey). The bottom panel illustrates the low wavenumber out-of-band signal from 0 – 200 cm^{-1} , and the fit for the quadratic nonlinearity. The wavenumber range for the fit region is 40 – 160 cm^{-1} . The dashed lines in the bottom panel indicate $\pm 0.03\%$ 56

Figure 28: LW MCT measured signal, normalized to the in-band peak for a 216.07 K target. The top panel shows the real spectrum (green), the imaginary component of the spectrum (light blue), and the shape of the quadratic nonlinearity (grey). The bottom panel illustrates the low wavenumber out-of-band signal from 0 – 300 cm^{-1} , and the fit for the quadratic nonlinearity. The wavenumber range for the fit region is 25 – 300 cm^{-1} , and the 60 Hz spikes have been excluded from the fit data. The dashed lines in the bottom panel indicate $\pm 0.03\%$ 57

Figure 29: DTGS low wavenumber out-of-band signal for a range of blackbody temperatures. The real spectrum is indicated in red, and the fit for the quadratic nonlinearity is shown in grey. The wavenumber range for the fit is 40 – 160 cm^{-1} 58

Figure 30: LW MCT low wavenumber out-of-band signal for a range of blackbody temperatures. The real spectrum is indicated in green, and the fit for the quadratic nonlinearity is indicated in grey. The wavenumber range for the fit is 25 – 300 cm^{-1} , and the 60 Hz spikes have been excluded from the fit data. 59

Figure 31: ARI LW MCT results for in-band optimization of the quadratic nonlinearity coefficient. The OARS temperature and fit weight are indicated for each dataset, and the weighted RMS residual used in the optimization is provided in the bottom panel. The cold calibration reference was operated at a temperature 243.2 K, and the hot calibration reference at 333.9 K for all datasets. 63

Figure 32: The relative contributions of the linear and quadratic terms of the nonlinearity correction (Eq. (2.18)) to a 333.93 K hot reference blackbody (top panel), a 243.18 K cold reference blackbody (middle panel), and a 293.16 K OARS blackbody (bottom panel) for the LW MCT are shown. For this particular data collection, the instrument temperature is approximately 296 K. The contributions are expressed as a percentage of the raw measurement. The black dashed lines indicate the 3dB points of the responsivity. 64

Figure 33: Nonlinearity corrected spectra are indicated in dark green and uncorrected spectra are shown in light green. The low wavenumber out-of-band artifact associated with the quadratic nonlinearity is reduced to near zero for the nonlinearity corrected spectra. The quadratic nonlinearity coefficient determined from the in-band optimization has been used in the nonlinearity correction ($a_2 = 0.018$). The

values determined via out-of-band approximation (a_2') for each OARS temperature are also included for reference (see Table 7).....	65
Figure 34: Nonlinearity corrected and uncorrected spectra. Nonlinearity corrected spectra corresponding to quadratic nonlinearity correction coefficients of 0.014 (light orange), 0.020 (dark orange), and the value determined from the out-of-band characterization (dark grey) for each data collection are shown.	66
Figure 35: ARI LW MCT measured and predicted brightness temperature for a 272.9 K OARS target, during vacuum testing. For this case, the cold calibration reference was operated at a temperature 217.6 K, the hot calibration reference at 300.2 K. The nonlinearity corrected result is shown in blue, while the uncorrected result is in red. The black dashed lines indicate the 3dB points of the responsivity.....	68
Figure 36: The radiometric uncertainty contribution from the nonlinearity correction for the data used for the in-band optimization of the quadratic nonlinearity coefficient. The uncertainty contribution for a 20% uncertainty in the nonlinearity coefficient (blue), a 50% uncertainty of \tilde{k} in the DC level model, and the combined RSS uncertainty (grey) are provided. All uncertainties correspond to a $k = 3$ coverage factor.	70
Figure 37: Notional illustration of the primary ARI optical subsystems.	71
Figure 38: Top view of the ARI optical ray trace, overlaid on solid model; fore-optics (red), FIR aft-optics (blue), IR aft optics (green).....	72
Figure 39: ARI fore-optics ray trace, side view (coloured by field angle).	73
Figure 40: ARI fore-optics ray trace, top view (coloured by field angle).....	73
Figure 41: ARI FIR aft-optics assembly (modified ABB E-AERI aft optics assembly) installed in ARI Prototype.	74
Figure 42: Zemax ray trace of ARI FIR aft-optics assembly (modified ABB E-AERI aft optics assembly).....	75
Figure 43: ARI IR aft-optics, S-HIS spare detector dewar, and Stirling cooler installed in ARI Prototype	76
Figure 44: Zemax ray trace of ARI IR aft-optics with S-HIS spare detector dewar installed.....	76
Figure 45: ARI blackbody configuration during the first cycle of vacuum testing.	78
Figure 46: Cross-section of OARS with 3rd generation Heated Halo installed.	79
Figure 47: In the first vacuum cycle configuration, end-to-end calibration verification for a 217 K OARS target with 217 K CBB and 305 K HBB calibration reference sources, indicated a brightness temperature residual of roughly 0.5 K at 700 cm^{-1} for the long-wave MCT detector. Observed and predicted OARS brightness temperatures are shown in the top panel, and the difference is presented in the bottom panel. A 30-point moving average filter has been used to smooth the observed brightness temperature.	79
Figure 48: In the first vacuum cycle configuration, end-to-end calibration verification for a 217 K OARS target with 217 K CBB and 305 K HBB calibration reference sources, the DTGS detector result was within the	

predicted uncertainty. Observed and predicted OARS brightness temperatures are shown in the top panel, and the difference is presented in the bottom panel. A 30-point moving average filter has been used to smooth the observed brightness temperature..... 80

Figure 49: End-to-end calibration verification for a 217 K OARS target, with the Heated Halo assembly removed, at the 3:00 position with a 217 K CBB calibration reference source at the 6:00 position and a 305 K HBB calibration reference source at the 12:00 position. Results indicated a brightness temperature residual of roughly 0.2 K at 700 cm^{-1} for the long-wave MCT detector. Observed and predicted OARS brightness temperatures are shown in the top panel, and the difference is presented in the bottom panel. A 30-point moving average filter has been used to smooth the observed brightness temperature..... 82

Figure 50: End-to-end calibration verification for a 217 K OARS target at the 3:00 position with a 217 K CBB calibration reference source at the 9:00 position (180 degrees separation from the OARS in scene mirror rotation angle) and a 305 K HBB calibration reference source at the 12:00 position. Results indicated a brightness temperature residual of roughly 0.2 K at 700 cm^{-1} for the long-wave MCT detector. Observed and predicted OARS brightness temperatures are shown in the top panel, and the difference is presented in the bottom panel. A 30-point moving average filter has been used to smooth the observed brightness temperature..... 82

Figure 51: End-to-end calibration verification for a 217 K OARS target, with the Heated Halo assembly removed, at the 3:00 position with a 217 K CBB calibration reference source at the 9:00 position (180 degrees separation from the OARS in scene mirror rotation angle) and a 305 K HBB calibration reference source at the 12:00 position. Observed and predicted OARS brightness temperatures are shown in the top panel, and the difference is presented in the bottom panel. A 30-point moving average filter has been used to smooth the observed brightness temperature..... 83

Figure 52: End-to-end calibration verification for a 333 K OARS target, with the Heated Halo assembly removed, at the 3:00 position with a 217 K CBB calibration reference source at the 9:00 position (180 degrees separation from the OARS in scene mirror rotation angle) and a 305 K HBB calibration reference source at the 12:00 position. Results show a small brightness temperature residual for wavenumbers below 700 cm^{-1} for the long-wave MCT detector. Observed and predicted OARS brightness temperatures are shown in the top panel, and the difference is presented in the bottom panel. A 30-point moving average filter has been used to smooth the observed brightness temperature. 83

Figure 53: Solid model (left) and photo (right) of ARI aperture stop (mirror M3). Non-mirror surfaces are black anodized, which is significantly reflective in the infrared..... 84

Figure 54: A stray-light baffle was added to the ARI aperture stop at mirror M3; (a) baffle after application of Z306, and (b) installed at mirror M3..... 85

Figure 55: (a) Cutaway view of heated entrance aperture ring assembly with key components labelled, and (b) a cross-sectional view of the heated entrance aperture ring assembly installed on the OARS..... 85

Figure 56: The Zemax footprint diagram for the optical surface located at the entrance to the blackbody. The sizing of the aperture and field stops, afocal ratio of the fore-optics telescope, and blackbody entrance

diameter were specified to provide significant margin. The thin black line indicates the 30 mm entrance aperture diameter at the blackbody and the coloured rings represent the footprint for the nine fields used in the Zemax prescription. The pupil of the beam is located closer to the halo entrance aperture, rather than the blackbody entrance aperture.....86

Figure 57: The positions of the nine field footprints at the field stop.....86

Figure 58: Plan view of the optical ray trace between the scene mirror and the blackbody entrance aperture. Beam footprints at the halo and blackbody optical planes are also provided. The coloured rings represent the footprint for the 9 fields used in the Zemax prescription. Zemax field positions at the field stop are shown in Figure 57.....87

Figure 59: Profile view of the optical ray trace between the scene mirror and the blackbody entrance aperture. Beam footprints at the halo and blackbody optical planes are also provided. The coloured rings represent the footprint for the 9 fields used in the Zemax prescription. Zemax field positions at the field stop are shown in Figure 57.....87

Figure 60: ARI front-end configuration and coordinate system definition used for stray light testing.88

Figure 61: Stray light diagnostic tests. A recirculating chiller is used to cool the OARS and CBB to 243 K. The instrument, including the calibration and verification sources, is purged with dry air and a dew point of less than 233 K was maintained.....88

Figure 62: Long-wave detector brightness temperature results for the baseline end-to-end calibration verification dataset with CBB and OARS aperture rings unpowered. The OARS and the CBB cavity temperatures are approximately 243 K. The top panel shows the mean observed OARS brightness temperature, and the predicted OARS brightness temperature, with the difference provide in the bottom panel. A 30-point moving average filter has been used to smooth the observed brightness temperature.89

Figure 63: Long-wave detector brightness temperature results for the baseline end-to-end calibration verification dataset with CBB aperture ring unpowered, and the OARS aperture ring heated to 333 K. The OARS and the CBB cavity temperatures are approximately 243 K. The top panel shows the mean observed OARS brightness temperature, and the predicted OARS brightness temperature, with the difference provide in the bottom panel. A 30-point moving average filter has been used to smooth the observed brightness temperature.....90

Figure 64: Long-wave detector brightness temperature residuals (observed – predicted) for end-to-end calibration verification datasets with the CBB and OARS aperture rings unpowered, baseline (red, dataset 140127), and after installation of the Z306 baffle at the aperture stop (blue, dataset 140205A). The OARS and the CBB cavity temperatures are approximately 243 K. The results have been spectrally averaged in 25 cm⁻¹ wide bins for noise reduction. Error bars represent statistical error only.....90

Figure 65: Long-wave detector brightness temperature residuals (observed – predicted) for end-to-end calibration verification datasets with the CBB aperture ring unpowered and the OARS aperture ring heated to 333 K, baseline (red, 140130), and after installation of the Z306 baffle at the aperture stop (blue, 140205B). The OARS and the CBB cavity temperatures are approximately 243 K. The results

have been spectrally averaged in 25 cm⁻¹ wide bins for noise reduction. Error bars represent statistical error only..... 91

Figure 66: Long-wave detector brightness temperature residuals (observed – predicted) for end-to-end calibration verification datasets with the CBB and OARS aperture rings unpowered, baseline (red, dataset 140130), and after installation of the Z306 baffle at the aperture stop (blue, dataset 140205B). The result with the CBB and OARS entrance aperture rings removed is shown in green (dataset 14021). The OARS and the CBB cavity temperatures are approximately 243 K. The results have been spectrally averaged in 25 cm⁻¹ wide bins for noise reduction. Error bars represent statistical error only..... 92

Figure 67: 3-d model of ARI field stop. In the diagram on the left, note the limited extent of the stopping surface, creating a potential susceptibility to stray light. The suggested modification is illustrated on the right..... 93

Figure 68: (a) Field stop (FS) modification that both reduces diameter of field stop by 16%, and extends the stopping surface using Z306 painted aluminum tape. (b) Modified field stop with no reduction to field stop diameter, but with further extension of the stopping surface..... 93

Figure 69: An aperture stop mask for testing the effect of reducing the aperture size was fabricated and installed in the ARI at the aperture stop at the M3 mirror. The aperture stop mask reduces the AS diameter by 25%..... 94

Figure 70: Impact of reduction of aperture and field stop sizes on long-wave residual brightness temperature error. The baseline result, with nominal aperture stop and field stop sizes, is shown in red (dataset 140205B). Reducing the aperture stop size (diameter reduced by 25%) provides a small improvement in the 500 – 650 cm⁻¹ region (blue, dataset 140206). Reduction of the field stop size, without extension of the field stop surface resulted in a significant increase the residual error (green, dataset 140228A). The results have been spectrally averaged in 25 cm⁻¹ wide bins for noise reduction. Error bars represent statistical error only..... 95

Figure 71: Increasing the extent of the stop surface at the field stop resulted in a significant reduction in the long-wave bias. The baseline result, with nominal aperture stop and field stop sizes, is shown in red (dataset 140205B). There is negligible dependence on the field or aperture stop size with the improved field stop surface installed; dataset 140227 (blue), reduced field stop diameter by 16%, reduced AS diameter by 25%; dataset 140228B (green), reduced AS diameter by 25%; dataset 140302 (pink), standard AS and FS sizes; dataset 140303 (purple), standard AS and FS sizes and extended baffling at field stop. The results have been spectrally averaged in 25 cm⁻¹ wide bins for noise reduction. Error bars represent statistical error only..... 95

Figure 72: Long-wave detector brightness temperature result with OARS and CBB cavities at 243 K, OARS entrance aperture ring at 333 K, and CBB entrance aperture ring unheated (dataset 140302). The mean measured brightness temperature is shown in light blue, with the modelled measurement in red, and predicted OARS brightness temperature in black. The modelled measurement includes a 0.110% view (with respect to total beam area) outside of the blackbody for the CBB and HBB, and 0.121% for the OARS. A 30-point moving average filter has been used to smooth the observed brightness temperature.

Note that the spectrally resolved brightness temperatures are not flat because the emissivity is not equal to one.96

Figure 73: Long-wave brightness temperature residual with both entrance aperture rings at ambient. This configuration represents the nominal operational configuration for the instrument. The baseline result, with nominal aperture stop and field stop sizes, and no additional baffling at the aperture or field stop is shown in red (dataset 140127). With the improved aperture and field stops, only a small residual remains (blue, dataset 140305B). The remaining residual behaves like that due to a small obstruction, monotonically increasing in brightness temperature with wavenumber. The results have been spectrally averaged in 25 cm⁻¹ wide bins for noise reduction. Error bars represent statistical error only.....97

Figure 74: Long-wave detector brightness temperature result with OARS and CBB cavities at 243 K, OARS and CBB entrance aperture rings unheated (dataset 140305B). The mean measured brightness temperature is shown in light blue, with the modelled measurement in red, and predicted OARS brightness temperature in black. The modelled measurement includes a 0.110% view (with respect to total beam area) outside of the blackbody for the CBB and HBB, and 0.121% for the OARS. A 30-point moving average filter has been used to smooth the observed brightness temperature.....97

Figure 75: DTGS brightness temperature residual with both entrance aperture rings at ambient. This configuration represents the nominal operational configuration for the instrument. The baseline result, with nominal aperture stop and field stop sizes, and no additional baffling at the aperture or field stop is shown in red (dataset 140127). The result with improved aperture and field stops is shown in blue (dataset 140305B). Due to the higher noise in the DTGS measurement, the average size has been increased to 50 cm⁻¹, and the low SNR spectral regions at the edge of the bands have been omitted from the plot. The results have been spectrally averaged in 50 cm⁻¹ wide bins for noise reduction. Error bars represent statistical error only.98

Figure 76: (a) Cube corner shear produces only a pure offset of the wavefront for rays propagating parallel to the optical axis. (b) Cube corner shear for off-axis rays results in a wavefront shear that is no longer perpendicular to the optical axis, and results in an additional optical path difference [25]. 100

Figure 77: A simple representation of instrument field of view at the entrance to the blackbody that is comprised of the prescribed footprint and an off-axis footprint associated with stray light passing the field stop. 100

Figure 78: A small shift in the blackbody position (- θ_0) changes the uniformity and the effective angle for the stray light footprint. 101

Figure 79: A small shift in the blackbody position (+ θ_0) changes the uniformity and the effective angle for the stray light footprint. 101

Figure 80: Propagation of the transverse optical field [129]. 103

Figure 81: The rotated polarization ellipse [129]. 104

Figure 82: Representing the scene select mirror and sensor as a series pair of partial polarizers is useful when considering the calibration bias due to polarization. The first polarizer represents the scene select

mirror, and the second polarizer represents the combined instrument polarization sensitivity due to the rest of the optical components within the sensor. 105

Figure 83: The coordinate system used for the sensor polarization angle (α) and the scene selection mirror angle (δ) is illustrated, with an example scene selection mirror angle corresponding to $\delta = 90^\circ$ indicated. A clock face position reference is also provided. 108

Figure 84: Scene select mirror reflectance and polarization (top and middle panel, respectively), and instrument polarization (bottom panel) parameters used in the model. Measurements of the ARI scene select mirror reflectance were not available, so existing data for reflectance from gold on diamond point turned aluminum mirror was used. The long-wave limit of the measurement data was 500 cm^{-1} . Consequently, the 500 cm^{-1} values were assumed for the $200 - 500\text{ cm}^{-1}$ region in the model. 112

Figure 85: Modelled spectrally resolved brightness temperature error due to polarization as a function of ARI front-end rotation angle. 113

Figure 86: Modelled brightness temperature error due to polarization as a function of front-end rotation angle with respect to the nominal orientation for a series of wavenumber values. The amplitude of the variation is indicated to the right of each plot. It is clear that the scene, calibration, and calibration views must be optimally placed with respect to the polarization axis of the instrument in order to achieve the accuracy requirement of the climate benchmark measurement. 114

Figure 87: The coordinate system used for Stokes formalization polarization model is illustrated. The sensor polarization sensitivity axis is at angle α . A right-handed notation is used, with positive counter clockwise rotation with the zero degree reference on the x-axis. 115

Figure 88: The positions of the polarization sensitivity zero crossings were predicted via a polarization model for the instrument during the design phase [138]. The results for output port 1 are shown, with the Stokes parameters plotted as a function of scene selection mirror angle (δ). The key quantity is the phase, indicated under each plot. The phase of the intensity ($I = S_0$) is 2 degrees, and the four zero-crossings of the sinusoidal polarization intensity occur at $2^\circ, 92^\circ, 182^\circ, \text{ and } 272^\circ$ 116

Figure 89: The positions of the polarization sensitivity zero crossings were predicted via the Mueller calculus based polarization model for the instrument. The results for the LW MCT channel (fore-optics, interferometer, IR aft optics at output port 1) are shown, with the Stokes parameters plotted as a function of scene selection mirror angle. The key quantity of interest is the intensity (S_0). The model predicts the phase of the intensity to be 86° and the four zero-crossings of the sinusoidal polarization intensity occur at $-4^\circ, 86^\circ, 176^\circ, \text{ and } 266^\circ$ 118

Figure 90: The positions of the polarization sensitivity zero crossings were predicted via the Mueller calculus based polarization model for the instrument. The results for the DTGS channel (fore-optics, interferometer, FIR aft optics at output port 2) are shown, with the Stokes parameters plotted as a function of scene selection mirror angle. The key quantity of interest is the intensity (S_0). The model predicts the phase of the intensity to be 86° and the four zero-crossings of the sinusoidal polarization intensity occur at $-4^\circ, 86^\circ, 176^\circ, \text{ and } 266^\circ$ 119

Figure 91: With optimal positioning of the calibration and verification module for elimination of polarization induced calibration biases, the calibration bias due to polarization should be largest at the polarization characterization view and zero at the calibration, calibration verification, and scene viewports. 120

Figure 92: ARI front-end configuration for the four-source polarization tests..... 121

Figure 93: Measured spectrally resolved brightness temperature error (LW MCT, green) as a function of ARI front-end rotation angle. Spectral averages (50 cm⁻¹ width) are shown as black markers with error bars. Error bars represent the statistical variation in the average (3σ/N). 124

Figure 94: Measured spectrally resolved brightness temperature error (DTGS, red) as a function of ARI front-end rotation angle. Spectral averages (100 cm⁻¹ width) are shown as black markers with error bars. Error bars represent the statistical variation in the average (3σ/N). 125

Figure 95: Spectrally averaged, measured brightness temperature error (LW MCT, green) as a function of ARI front-end rotation angle. Spectral averages (50 cm⁻¹ width) are shown with error bars. Error bars represent the statistical variation in the spectral average (3σ/N). 126

Figure 96: Spectrally averaged, measured brightness temperature error (DTGS, red) as a function of ARI front-end rotation angle. Spectral averages (100 cm⁻¹ width) are shown with error bars. Error bars represent the statistical variation in the spectral average (3σ/N). 127

Figure 97: Spectrally averaged, measured brightness temperature error (LW MCT, green) as a function of ARI front-end rotation angle. Spectral averages (50 cm⁻¹ width) are shown with error bars. Error bars represent the statistical variation in the spectral average (3σ/N). The dark blue dashed line indicates the resulting curve fit. 129

Figure 98: Spectrally averaged, measured brightness temperature error (DTGS, red) as a function of ARI front-end rotation angle. Spectral averages (100 cm⁻¹ width) are shown with error bars. Error bars represent the statistical variation in the spectral average (3σ/N). The dark blue dashed line indicates the resulting curve fit. 130

Figure 99: Front-end configuration for the 2-source polarization test with linear polarizer (top view). The linear polarizer position is indicated in green. 131

Figure 100: Front-end configuration for 2-source polarization test with linear polarizer (front view)..... 131

Figure 101: The scene mirror cylindrical baffle is replaced with a modified baffle, highlighted in green, that accommodates the mounting of a 50 mm rotating polarizer mount. The heated halo is not installed for the tests (but is included in this solid model assembly)..... 132

Figure 102: Modified scene mirror baffle and linear polarizer assembly..... 132

Figure 103: LW MCT channel spectrally resolved magnitude instrument responsivity, for linear polarization orientations from 0° to 180° degrees in 15° increments. 134

Figure 104: DTGS channel spectrally resolved magnitude instrument responsivity, for linear polarization orientations from 0° to 180° degrees in 15° increments. 135

Figure 105: LW MCT channel magnitude instrument responsivity with spectral averaging. To further improve signal to noise, the 0.5 cm^{-1} resolution data is averaged to a lower spectral resolution. The spectral bin size is selected to optimize signal to noise while maintaining sufficient spectral resolution to resolve low frequency features. 135

Figure 106: DTGS channel magnitude instrument responsivity with spectral averaging. To further improve signal to noise, the 0.5 cm^{-1} resolution data is averaged to a lower spectral resolution. The spectral bin size is selected to optimize signal to noise while maintaining sufficient spectral resolution to resolve low frequency features. 136

Figure 107: LW MCT channel spectrally averaged magnitude responsivity versus linear polarizer angle. 136

Figure 108: DTGS channel spectrally averaged magnitude responsivity versus linear polarizer angle. 137

Figure 109: LW MCT magnitude responsivities plotted as a relative difference with respect to the magnitude response for the linear polarizer at 45° . Note that the sign of the relative difference changes in the $750 - 950 \text{ cm}^{-1}$ region for all linear polarizer angles. 137

Figure 110: DTGS magnitude responsivities plotted as a relative difference with respect to the magnitude response for the linear polarizer at 45° . Note that the sign of the relative difference changes in the $850 - 950 \text{ cm}^{-1}$ region for all linear polarizer angles. 138

Figure 111: LW MCT channel spectrally averaged magnitude responsivity plotted as a function of linear polarizer angle for a series of spectral bins. The blue dashed line indicates the sinusoidal fit, and the fit parameters are provided on the right. 140

Figure 112: DTGS channel spectrally averaged magnitude responsivity plotted as a function of linear polarizer angle for a series of spectral bins. The blue dashed line indicates the sinusoidal fit, and the fit parameters are provided on the right. 141

Figure 113: LW MCT 90° responsivity pair plot, as defined by Eq. (4.36). The legend specifies the polarizer angles used for the magnitude responsivity pair ($\gamma, \gamma_2 = \gamma + 90^\circ$). 143

Figure 114: DTGS 90° responsivity pair plot, as defined by Eq. (4.36). The legend specifies the polarizer angles used for the magnitude responsivity pair ($\gamma, \gamma_2 = \gamma + 90^\circ$). 143

Figure 115: LW MCT 90° responsivity pair, as defined by Eq. (4.36), plotted as a function of γ . Spectral range and fit parameters are specified to the right of each panel. 144

Figure 116: DTGS 90° responsivity pair, as defined by Eq. (4.36), plotted as a function of γ . Spectral range and fit parameters are specified to the right of each panel. 145

Figure 117: Ideal blackbody radiances were used for the simulation of the low signal to noise effect. Results are presented for 900 cm^{-1} 151

Figure 118: Simulated low SNR effect. The distributions (normalized to peak value) are provided for a range of signal to noise values. The results for the measurement ratio in the calibration equation are shown in

the top panel (grey). The individual scene and cold reference measurement ratios are shown in the middle (red) and bottom (blue) panels, respectively. The zero noise and zero signal limits are also indicated. 151

Figure 119: Simulated low SNR effect. The dependence of the mean value on the SNR for the calibration equation measurement ratio is shown in the top panel (green). The individual scene and cold reference measurement ratios are shown in the middle (red) and bottom (blue) panels, respectively. The zero noise and zero signal limits are also indicated. 152

Figure 120: Simulated low SNR effect. The mean value of the radiance is plotted versus SNR. 152

Figure 121: Predicted and measured brightness temperature for the ARI DTGS detector channel for a 252.8 K OARS target, calibrated using a cold reference blackbody at 215.6 K, and a hot reference blackbody at 301.7 K. The calibration results the full dataset average (grey) and a standard rolling window method (blue) are provided. The predicted brightness temperature is indicated in black, and the dashed red line represents the brightness temperature associated with 50% of the combined hot and cold reference blackbody radiance. The rolling window calibration result is impacted by the low SNR effect near the edges of the detector response, and the resulting calibrated brightness temperature approaches the brightness temperature associated with 50% of the combined hot and cold reference blackbody radiance in that spectral region. 154

Figure 122: Predicted and ARI DTGS measured brightness temperature for a 252.8 K OARS target, calibrated using a cold reference blackbody at 215.6 K, and a hot reference blackbody at 301.7 K. The calibration results for the full dataset average (grey) are shown in the top panel, a standard rolling window method (blue) in the second panel, and the low SNR optimized rolling window calibration (red) in the bottom two panels. The results in the third panel correspond to a responsivity interpolation window size of 100 samples, and 250 samples for the bottom panel. 156

Figure 123: To further reduce noise, and provide a better visualization of the results provided in Figure 122, spectral averaging of the results has been applied (bin width of 25 cm^{-1}). 156

Figure 124: A closer view of the results presented in Figure 122 in the long wavelength region of the measurement. The long-wave spectral cut-off is dominated by the transmission properties of the Caesium Iodide beam splitter. 157

Figure 125: A closer view of the results presented in Figure 122 in the short wavelength limit of the DTGS measurement. The impact of the low signal to noise optimized calibration method is most evident in this spectral region. 157

Figure 126: Predicted on-orbit radiometric calibration uncertainty (dashed) and calibration verification source uncertainty (solid) ($k = 3$). 160

Figure 127: Predicted laboratory radiometric calibration uncertainty (dashed) and calibration verification source uncertainty (solid) ($k = 3$). 160

Figure 128: Predicted vacuum radiometric calibration uncertainty (dashed) and calibration verification source uncertainty (solid) ($k = 3$). 161

Figure 129: Radiance summary for the ARI LW MCT channel calibration verification conducted under vacuum. The OARS was operated over a range of temperatures from approximately 218 K to 334 K.	164
Figure 130: Radiance summary for the ARI DTGS channel calibration verification conducted under vacuum. The OARS was operated over a range of temperatures from approximately 216 K to 334 K.	165
Figure 131: ARI calibration verification results for tests conducted under vacuum. Observed brightness temperature for the DTGS detector is shown in red and the black dashed line indicates predicted brightness OARS brightness temperature. The noise is roughly a factor of 4 larger than the on-orbit noise specification due to shorter dwell times.....	166
Figure 132: DTGS detector brightness temperature residuals (observed – predicted) for end-to-end calibration verification datasets conducted under vacuum. The results have been spectrally averaged in 50 cm ⁻¹ wide bins for noise reduction. Error bars represent statistical error only. Total (calibration and calibration verification) radiometric uncertainty is shown in blue, and the grey dashed lines indicate ± 0.1 K. The effect of low SNR is evident at the edges of the spectral band (refer to Chapter 5 for details).	167
Figure 133: ARI calibration verification results for tests conducted under vacuum. Observed brightness temperature for the long-wave MCT detector is shown in green and the black dashed line indicates predicted brightness OARS brightness temperature.	168
Figure 134: Long-wave MCT detector brightness temperature residuals (observed – predicted) for end-to-end calibration verification datasets conducted under vacuum. The results have been spectrally averaged in 25 cm ⁻¹ wide bins for noise reduction. Error bars represent statistical error only. Total (calibration and calibration verification) radiometric uncertainty is shown in blue, and the grey dashed lines indicate ± 0.1 K. The artifact associated with the original field stop is evident. The solution to this issue was implemented post-vacuum testing (see Chapter 4).	169
Figure 135: ARI vacuum calibration verification results for the long-wave detector with nonlinearity correction, 800 cm ⁻¹ . Meeting these uncertainty bounds in the vacuum environment demonstrates the capability to meet the 0.1 K (k = 3) uncertainty requirement on-orbit.	170
Figure 136: ARI vacuum calibration verification results for the long-wave detector without nonlinearity correction, 800 cm ⁻¹	170
Figure 137: ARI vacuum calibration verification results for the long-wave detector with nonlinearity correction, 1000 cm ⁻¹ . Meeting these uncertainty bounds in the vacuum environment demonstrates the capability to meet the 0.1 K (k = 3) uncertainty requirement on-orbit.	171
Figure 138: ARI vacuum calibration verification results for the long-wave detector without nonlinearity correction, 1000 cm ⁻¹	171
Figure 139: ARI vacuum calibration verification results for the far infrared (DTGS) detector, 450 cm ⁻¹ . Meeting these uncertainty bounds in the vacuum environment demonstrates the capability to meet the 0.1 K (k = 3) uncertainty requirement on-orbit.	172

Figure 140: ARI vacuum calibration verification results for the far infrared (DTGS) detector, 800 cm^{-1} . Meeting these uncertainty bounds in the vacuum environment demonstrates the capability to meet the 0.1 K ($k = 3$) uncertainty requirement on-orbit. 172

Dedication

This thesis is dedicated to my family, especially my incredible wife Angie.

Acknowledgements

First and foremost, I would like to express my sincere appreciation and thanks to my advisor, Dr. Jerome Genest, for providing this unique opportunity and for his patience, support and incredible wealth of knowledge and expertise. I have learned a great deal during the course of this thesis and class work, and perhaps more importantly, have come to understand how much more I have yet to learn.

I also offer my sincere thanks to Dr. Henry Revercomb for his continued enthusiasm, amazing insight and intuition, and wisdom. Thank you for your support of this opportunity.

I would like to recognize the other members of my thesis committee: Dr. Simon Thibault, Dr. Frederic Grandmont, and Dr. David Tobin. Thank you for your comments, feedback, and questions.

Much recognition and appreciation is owed to the UW-SSEC ARI instrument team. The incredible expertise and dedication of this group of individuals was critical to the success of the instrument development and demonstration. Many thanks to Hank Revercomb, Fred Best, Doug Adler, Jon Gero, Jeff Wong, Mark Schwarz, Claire Pettersen, Nick Ciganovich, Mark Mulligan, Paul Schnettler, and the other members of the team for your work on this project. In particular, I would like to especially thank Doug Adler for his tireless dedication and continued help with instrument configuration changes and data collection. Additionally, I thank Frederic Grandmont and Henry Buijs at ABB for their support during interferometer troubleshooting and analysis.

Finally, I would like to thank my family for their love and support: my wife Angie, and sons Ronan and Connor, as well as my parents Bob and Winnie, and mom-in-law Maxine. To Ronan and Angie, completing this thesis took much more of my family time than I anticipated. Words cannot express my thanks for your support, patience, and understanding throughout this process.

This project was supported by (1) NASA Grant Number IIP-07-0006 “A New Class of Advanced Accuracy Satellite Instrumentation (AASI) for the CLARREO Mission” carried out at the University of Wisconsin, Space Science and Engineering Center under the direction of Principal Investigator Henry Revercomb, and teamed with Harvard University; (2) NASA Contract Number NNL10AA12B, Task Order-1, Number NNL10AC86TD, Amendment/Modification Number 000001; (3) NASA Contract Number NNL10AA12B, Task Order-2, Number NNL12AQO8T, Item Number 001; and UW-SSEC internal research funding.

Introduction

Spectrally resolved infrared radiances measured from orbit with extremely high absolute accuracy constitute a critical observation for future climate benchmark missions. For the infrared radiance spectra, it has been determined that a measurement accuracy, expressed as an equivalent brightness temperature error, of 0.1 K confirmed on orbit is required for temperature trend detection above natural variability for decadal climate signatures [1-3].

The primary goal of this thesis project is the successful demonstration of the absolute radiometric calibration accuracy required for climate benchmark measurements in the infrared and far infrared.

The University of Wisconsin Space Science and Engineering Center (UW-SSEC), with funding support from the NASA Instrument Incubator Program (IIP), developed the Absolute Radiance Interferometer (ARI). The ARI is designed to meet the uncertainty requirements needed to establish spectrally resolved thermal infrared climate benchmark measurements from space.

Climate benchmark measurements from space

The absolute accuracy and sampling of current space-based Earth observations is insufficient to confidently detect climate change signals on a decadal time scale. The need for improved accuracy for decadal detection of climate change has been recognized and specified in United States interagency reports [2-5] and international observing system and intercalibration plans [6-8].

The climate benchmark measurement concept and accuracy requirement for the infrared and far infrared is defined in the NIST, NOAA, and NASA study and report *Achieving Satellite Instrument Calibration For Climate Change* (ASIC3) [2, 4], and the US National Research Council (NRC) Decadal Survey (DS) *Earth science and applications from space: National imperatives for the next decade and beyond* [1].

There are three fundamental characteristics for the climate benchmark measurement:

- The measurement is traceable to fundamental SI (Système international d'unités) standards on-orbit and robust to gaps in the measurement record. The Bureau International des Poids et Mesures defines SI traceability as the property of a measurement result related to stated references in SI units through an unbroken chain of comparisons all having stated uncertainties and “it is essential that they (the measuring instruments) should be periodically calibrated against more accurate standards” [9];
- The measurement provides sufficient information content and accuracy to determine change in essential climate variables on a decadal time scale;
- The measurement has sufficient temporal and spatial sampling such that the sampling bias in the observations is well below the predicted decadal climate change and natural climate variability.

The NRC Decadal Survey states the principles on which new climate missions should be based:

Design of climate observing and monitoring systems from space must ensure the establishment of global, long-term climate records, which are of high accuracy, tested for systematic errors on-orbit, and tied to irrefutable standards. [...] For societal objectives that require long-term climate records, the accuracy of core benchmark observations must be verified against absolute

standards on-orbit by fundamentally independent methods, such that the accuracy of the record archived today can be verified by future generations. Societal objectives also require a long-term record not susceptible to compromise by interruptions.

Furthermore, the Decadal Survey defines the Climate Absolute Radiance and Refractivity Observatory (CLARREO) mission and recommends it as a highest priority. The NRC Decadal Survey defines three types of measurements for CLARREO:

- Spectrally resolved infrared and far infrared radiances with spectral coverage from 200 – 2000 cm^{-1} at 0.5 cm^{-1} spectral resolution (unapodized), with 0.1 K accuracy (99% confidence) and on-orbit traceability to the SI standard for the Kelvin;
- The phase delay rate of the signal from the low Earth orbit (LEO) Global Navigation Satellite System radio occultation (GNSS-RO) occulted by the atmosphere with an accuracy of 0.06% (95% confidence) for a range of altitudes from 5 to 20 km in the atmosphere. The measurement is traceable on-orbit to the SI standard for the second;
- Spectrally resolved nadir reflectance of solar radiation from Earth to space determined with an accuracy of 0.3% (95% confidence) with respect to the mean spectral reflectance of the Earth. Note that this reflected solar (RS) measurement is relative to the solar spectral irradiance, and traceability of the SI standard for the Watt is provided via the use of comparisons with solar spectral observations made by the Total Solar Irradiance Spectrometer (TSIS).

The CLARREO mission and payload described in the NRC Decadal Survey called for three small satellites, each of which requires a specific orbit. Each satellite was to be equipped with a GNSS-RO receiver and infrared interferometers for the spectrally resolved infrared and far infrared radiance measurement. Additionally, the third satellite also included the instrumentation required for the reflected solar measurement.

The infrared climate benchmark measurement enables two new approaches to climate analysis. The first approach makes direct use of the climate benchmark measurement to determine climate forcings and feedbacks via “spectral fingerprinting” [10-13]. This method enables attribution of spectral changes in the absolute spectrally resolved radiances to individual factors including greenhouse gases, atmospheric temperature, water vapour, and clouds; thus providing a quantification of longwave feedback and forcing strength. The second approach uses the infrared climate benchmark measurements as an absolute calibration verification reference measurement for satellite instruments that do not meet decadal accuracy or sampling requirements. These include polar orbiting instruments such as the Cross-track Infrared Sounder (CrIS) and the Infrared Atmospheric Sounding Interferometer (IASI), as well as geostationary radiometers. In this approach the climate benchmark measurement provides an on-orbit SI traceable reference measurement and detailed radiometric performance estimates for other sensors can be completed using simultaneous nadir overpasses (SNOs) to perform inter-comparisons between the climate benchmark measurement and the measurement of the sensor to be characterized [14, 15]. This helps to address the needs of the operational weather community for improved absolute accuracy while opening the possibility of using the operational sounder observations to contribute to the long-term climate record.

A simple instrument design is key to achieving the ultra-high absolute accuracy requirements associated with infrared spectral radiances for climate benchmark measurements from space. The required simplicity is achievable due to the large differences in the sampling and noise requirements for the climate measurement

from those of the typical remote sensing infrared sounders for weather research or operational weather prediction. Studies show that for the climate benchmark measurement paradigm, which emphasizes information content rather than calorimetry, the key climate information can be obtained with nadir only viewing, relatively large ground footprints (<100 km), and modest requirements on noise performance [16, 17]. The key is to demonstrate extremely low combined measurement and sampling biases for the climate products, which consist of annual averages of nadir radiance spectra averaged over large latitude-longitude regions (of the order of 15° x 30°) and seasonal averages on even larger spatial scales (of the order of 50° x 50° latitude-longitude regions). These striking differences from weather-driven requirements lead to very important reductions in sensor size, mass, and power that enable the novel climate accuracy requirements to be achieved with a relatively low demand on spacecraft resources and cost.

Fourier Transform Infrared Spectrometers

The Fourier Transform Spectrometer (FTS) approach is well suited for the combined requirement of ultra high accuracy and broad spectral coverage at high spectral resolution in the IR. FTS technology inherently provides broad spectral coverage with a small number of detectors, a very well defined instrument line shape (ILS) that can be easily monitored and measured, the spectral resolution required for accurate line shape and position determination, and to accurately calibrate the entire spectral scale using well-known atmospheric absorption lines due to the Connes advantage [18, 19]. With appropriate selection of metrology laser wavelength, measured spectra are Nyquist sampled, allowing rigorous spectral matching to other coincident instruments and to future climate benchmark observations. These properties eliminate some of the largest calibration errors traditionally associated with IR instruments based on filters or gratings for spectral separation [20-22].

The design of most Fourier Transform infrared (FTIR) spectrometers can be traced back to Michelson's original two-beam interferometer [23, 24]. For a historical review and perspective of FTS the reader is referred to Genest and Tremblay [25], and Davis, Abrams and Brault [26].

Key advances in FTS

Michelson used the Fourier theorem to devise a relationship between the observed visibility of interference fringes and the spectra of the sources. To transform the interferogram to the corresponding spectrum Michelson and Stratton developed a mechanical computer that could calculate an interferogram given a spectrum [27, 28]. These calculated interferograms were compared to the measured interferograms. The process was limited by the capability of the machine and the lack of detector technology available at the time.

In the 1950's there was a resurgence of interest in interference spectroscopy. This was in large part due to the discovery of the Fellgett (multiplex) [29, 30] and Jacquinot (throughput) [31] advantages for FTS instruments. These two advantages, along with the development of the rapid scan FTS concept by Mertz [27, 32] drove a renewed interest in Fourier Transform Spectroscopy.

The numerical expense of the calculation of the Fourier Transform coupled with the lack of efficient computing capability limited the application of FTS. In the 1960's the development of the Cooley-Tukey algorithm [33, 34], which facilitated the calculation of the Fast Fourier Transform (FFT) and significant advancements in computing power and availability made FTS a more feasible tool for routine spectroscopy.

Most recently, high spatial resolution imaging FTS (IFTS) has become a reality. Since more information can be extracted from data when both spatial and spectral information is available, the benefit of IFTS is clear. Advancements in computer processing power and IR focal plane arrays in the last decade have made imaging FTS possible.

Ongoing technological developments have since fostered improved FTS performance and radiometric accuracy. These developments include advancements in mirror drive technology and velocity control, reference laser stability and fringe referencing, optical material and coatings, sampling algorithms, calibration reference sources, and tighter manufacturing tolerance capability.

Motivations and thesis outline

The goal of this thesis is to successfully demonstrate the infrared and far-infrared climate benchmark measurement capability under vacuum conditions, over a subset of the range of equivalent earth scene brightness temperatures expected on-orbit. Advances in instrumental aspects have been achieved in the pursuit of this goal.

This document is divided into seven chapters, including the introduction and conclusion.

In this chapter, the introduction to the topic, a summary of the objective, rationale and application was presented.

Chapter 1 discusses the measurement, calibration, and calibration verification methodology. The instrument description, experimental configuration, and radiometric uncertainty analysis are presented. The primary challenges, solutions, and analysis methodology are presented in Chapters 2 through 6.

Chapter 2 reviews nonlinearity and nonlinearity correction theory and impact on calibration accuracy.

Chapter 3 reviews the instrument optical design and discusses observed vignetting and stray light issues, diagnostic tests and analysis, and solutions to observed problems.

Chapter 3 presents polarization induced calibration error, including the modeled and measured polarization sensitivity of the instrument and associated calibration bias.

Chapter 5 discusses the impact of low signal to noise ratio (SNR) on calibration accuracy and a method for mitigating the effect.

Chapter 6 presents the experimental results demonstrating the 0.1 K accuracy and concluding remarks. Additionally, results are compared to related research efforts, and further work is identified.

The work in this thesis has led to publications in various journals, conferences, and workshops [35-49].

This project was supported by (1) NASA Grant Number IIP-07-0006 "A New Class of Advanced Accuracy Satellite Instrumentation (AASI) for the CLARREO Mission" carried out at the University of Wisconsin, Space Science and Engineering Center under the direction of Principal Investigator Henry Revercomb, and teamed with Harvard University; (2) NASA Contract Number NNL10AA12B, Task Order-1, Number NNL10AC86TD, Amendment/Modification Number 000001; (3) NASA Contract Number NNL10AA12B, Task Order-2, Number NNL12AQO8T, Item Number 001; and UW-SSEC internal research funding.

1 Research project description and methodology

We begin with an overview of the measurement, calibration, and calibration verification methodology. The instrument description, experimental configuration, and radiometric uncertainty analysis are presented.

1.1 Calibration accuracy of existing remote sensing IR FTS sensors

In this section, we review current state of the art in remote sensing IR FTS sensors, and demonstrated calibration accuracy of these instruments. The instruments presented herein have their own unique scientific requirements and applications and were not designed with climate benchmark measurements as a primary objective. Key differences in top-level requirements include:

- Radiometric Accuracy: A measurement accuracy, expressed as an equivalent brightness temperature error, of 0.1 K ($\geq 99\%$ confidence) is required for signal detection above natural variability for decadal climate signatures. The radiometric accuracy requirements for climatological benchmark measurements and fingerprinting exceed those for existing high spectral resolution infrared remote sensing ground-based and airborne instruments by a factor of 3 – 10, and current spaceflight instruments by a factor of 3 – 5.
- Calibration traceability: On-orbit calibration traceability to absolute standards is an important component for climate benchmark measurements, and provides an independence from unproven assumptions on stability. The primary method currently used to provide SI traceability for IR radiances measured from on-orbit instruments is based on pre-flight instrument characterizations and calibrations that cannot account for drift over very long periods on orbit, coupled with validation activities that help constrain the on-orbit performance.
- Spectral Coverage: The spectral coverage is extended from the normal sounding region (typically some part or all of the 3-15 μm region) to continuous coverage from 3 to 50 μm , yielding a new, enhanced sensitivity to upper level water vapour and cloud properties.

Spaceflight FTS sensors designed with climatological fingerprinting as the primary scientific objective can be designed to have significantly lower mass and power requirements than current spaceflight spectrally resolved IR sensors, due to the reduced requirements on sample rate, cross-track coverage (none), along track coverage (non-contiguous, limited by atmospheric correlation length), and noise performance. This helps make it practical to fly these sensors on multiple small satellites for achieving the spatial and temporal coverage needed to achieve acceptable sampling biases.

The following paragraphs provide a summary of the performance and calibration accuracy of the Atmospheric Emitted Radiance Interferometer (AERI), the Scanning High-resolution Interferometer Sounder (S-HIS), and the Cross-track Infrared Sounder (CrIS). These instruments represent the current state of the art calibration accuracy for ground-based, airborne, and space-borne IR FTS sensors, respectively.

The AERI is a ground-based Fourier-transform spectrometer developed for the measurement of the atmospheric downwelling infrared radiance spectrum at the Earth's surface with high absolute accuracy. The Atmospheric Emitted Radiance Interferometer instrument was designed and fabricated by the University of Wisconsin – Space Science and Engineering Center (UW-SSEC) and ABB-Bomem for the Department of

Energy (DOE) Atmospheric Radiation Measurement (ARM) program. The interferometer utilizes a 4-port configuration with cube corner mirrors. The AERI measures downwelling atmospheric emitted radiance from 3.3 μm (3020 cm^{-1}) to 19 μm (520 cm^{-1}) for the standard range AERI, or 3.3 μm (3020 cm^{-1}) to 25 μm (400 cm^{-1}) for the extended range AERI (ER-AERI), with a narrow zenith field of view. The AERI systems achieve an absolute radiometric calibration of better than 1% (99% confidence) of ambient radiance, with a reproducibility of better than 0.2%. The knowledge of the AERI spectral calibration is better than 1.5 parts per million (1- σ) in the wavenumber range of 400 cm^{-1} to 3000 cm^{-1} [50]. The AERI calibration blackbody performance and calibration methodology have been verified with direct traceability to NIST [51, 52].

In 1979 the UW-SSEC led a Phase A study of the High-resolution Interferometer Sounder (HIS) for geosynchronous orbit and the design of a proof-of-concept HIS instrument for the NASA high altitude ER2 aircraft. This study was conducted with the Santa Barbara Research Center (SBRC) teamed with Bomem and both instruments were based on the Bomem dynamically aligned plane-mirror interferometer design. Although the GEO HIS was never built, the HIS aircraft instrument was successfully flown on over 30 missions on the NASA ER2 from 1985 through 1998. The HIS replacement, the Scanning-HIS (S-HIS, named for its cross-track scanning capability), was also designed around a Bomem dynamically aligned plane mirror interferometer with UW-SSEC designed and fabricated on-board blackbody references. S-HIS has continued the successful HIS record from 1998 to the present with many successful missions conducted on the NASA DC-8, ER-2, WB-57, Global Hawk and Proteus aircraft. S-HIS, like the HIS on the ER2, is flown without active thermal control and operates in an environment open to the atmosphere on the ER-2, Proteus, WB-57, and Global Hawk. The S-HIS provides spectral coverage from 580 – 3000 cm^{-1} at 0.5 cm^{-1} spectral resolution (unapodized). For a wide range of scene temperatures (230 – 340 K typical), the calibration uncertainty (99% confidence) estimate for the S-HIS is less than 0.2 K [53-55]. UW-SSEC experience with the S-HIS has led to a more complete understanding of issues with absolute calibration and tests with the NIST Transfer Radiometer (TXR) solidly confirm the calibration uncertainty estimates. To verify the S-HIS calibration accuracy and provide direct NIST traceability of the S-HIS radiance observations, laboratory tests of the S-HIS and the NIST Transfer Radiometer (TXR) were conducted using a thermal chamber to simulate flight temperatures for the S-HIS instrument. Two basic tests were conducted: (1) comparison of radiances measured by the Scanning HIS to those from the TXR, and (2) measurement of the reflectivity of a UW-SSEC blackbody by using the TXR as a stable detector [56-60].

The Cross-track Infrared Sounder (CrIS) on the Suomi NPP (NPOESS Preparatory Project) satellite was launched 28 October 2011. CrIS is an infrared Fourier transform spectrometer with 1305 spectral channels, and produces high-resolution, three-dimensional temperature, pressure, and moisture profiles. The interferometer core was developed by ABB Bomem, and uses a flat-mirror Michelson configuration. It is equipped with a dynamic alignment system to minimize misalignments within the interferometer and has a maximum optical path difference of $\pm 0.8\text{ cm}$. Spectral coverage is 3.92 μm - 15.38 μm (650 cm^{-1} – 2550 cm^{-1}), with a spectral resolution of 0.625 cm^{-1} in the LWIR band, 1.25 cm^{-1} in the MWIR band, and 2.5 cm^{-1} in the SWIR band. Each spectral band uses 3 x 3 photovoltaic Mercury-Cadmium-Telluride (PV MCT) detector arrays to provide a 14 km instantaneous field of view (IFOV) from 833 km altitude. The CrIS radiometric accuracy specification is expressed as a 1- σ percent radiance uncertainty with respect to a 287 K Planck radiance for scenes with an equivalent brightness temperature range of 233 K – 287 K. Specified requirements are $\leq 0.45\%$ for the longwave, $\leq 0.58\%$ for the midwave, and $\leq 0.77\%$ for the shortwave. The pre-launch and on-orbit radiometric uncertainty analysis conducted by Tobin et al [61, 62] indicate that the

radiometric uncertainty for CrIS is less than 0.2 K in the midwave and shortwave bands, and less than 0.3 K in the longwave band (99% confidence).

For a detailed survey of current state of performance in remote sensing IR FTS sensors, refer to Taylor [63]. The review article by Persky also provides an excellent summary of space-borne FTS [28]. Written in 1995, the Persky document includes planned launches through 2002.

1.2 The Absolute Radiance Interferometer

The thesis objective is a component of a larger project being undertaken at the University of Wisconsin Space Science and Engineering Center (UW-SSEC), in partnership with Harvard University (HU). The project was funded by a NASA Instrument Incubator Program (IIP) grant “A New Class of Advanced Accuracy Satellite Instrumentation (AASI) for the CLARREO Mission”, with further support from the NASA Earth Sciences Technology Office (ESTO) and the UW-SSEC. The University of Wisconsin and Harvard University team has a long history with the scientific and measurement concepts that have formed the foundation for climate benchmark measurements from space [2, 3, 16, 17, 21, 64-67].

The objective of the project is to advance the technological development of a new class of Advanced Accuracy Satellite Instrumentation (AASI) for the measurement of absolute spectrally resolved infrared radiance emitted from Earth to space from a small satellite in low Earth orbit. The AASI employs four primary technologies:

1. The On-orbit Absolute Radiance Standard (OARS), a high emissivity blackbody source that uses multiple miniature phase-change cells to provide a revolutionary in situ standard with absolute temperature accuracy proven over a wide range of temperatures. The OARS is a source that will be used to maintain SI traceability of the radiance spectra measured by the calibrated interferometer sensor [68, 69].
2. The On-orbit Cavity Emissivity Module (OCEM) that directly determines the on-axis emissivity of the OARS throughout the instrument lifetime on-orbit. Two versions will be developed, one using a monochromatic laser source [70, 71] and one based on a broadband heated halo source [72-74].
3. The On-orbit Spectral Response Module (OSRM) that uniquely determines the spectral instrument line shape of the interferometers over the lifetime of the instrument on-orbit.
4. The Absolute Radiance Interferometer (ARI) for measuring spectrally resolved radiances with a spectral coverage of $200 - 2500 \text{ cm}^{-1}$ at 0.5 cm^{-1} spectral resolution and a radiometric accuracy of better than 0.1 K ($\geq 99\%$ confidence) brightness temperature at scene temperature [37, 39, 43, 46, 47, 49].

The first three technologies are either fundamentally new or have never been designed for on-orbit application. The new aspect of the interferometer work is the ultra high absolute accuracy sought, and is the subject of this thesis.

A notional diagram of the Absolute Radiance Interferometer is shown in Figure 1. Photos of the completed ARI sensor prototype are provided in Figure 2 and Figure 3. The Absolute Radiance Interferometer is comprised of:

- Ultra-high accuracy blackbody calibration reference sources;
- A scene selection mirror assembly;
- A fore-optics telescope designed specifically for high radiometric accuracy;
- A 4-port cube-corner, rocking arm interferometer with a diode laser based metrology system (the ABB Generic Interferometer for Climate Studies (GICS));
- Two aft optics assemblies, 1 at each output port of the interferometer;
- A 77 K multiple semi-conductor detector (450 – 3000 cm^{-1}) and dewar assembly;
- A very small mechanical cooler for the semi-conductor detector and dewar subassembly;
- A DTGS pyroelectric detector (200 – 1400 cm^{-1}) assembly.

The ARI calibration reference blackbodies are based on the UW SSEC Geostationary Imaging FTS (GIFTS) blackbody design [75, 76]. The instrument was designed such that detailed performance testing can be conducted on a system with a clear path to space. For compatibility with an instrument incubator program (IIP) budget and schedule, the electronics are not flight designs.

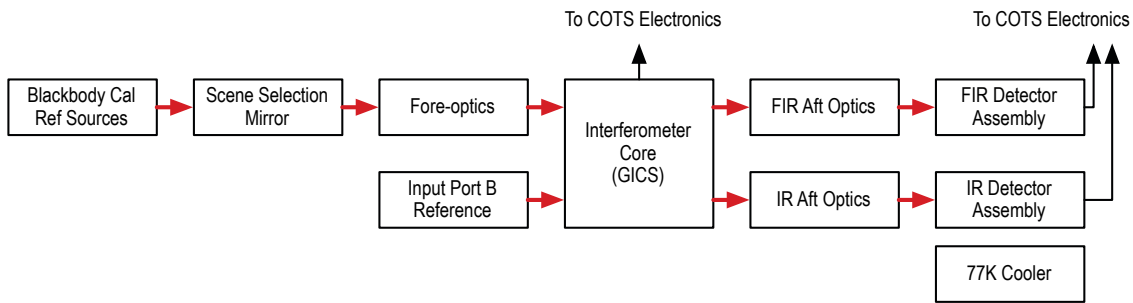


Figure 1: A notional illustration indicating the primary Absolute Radiance Interferometer subsystems and optical path.

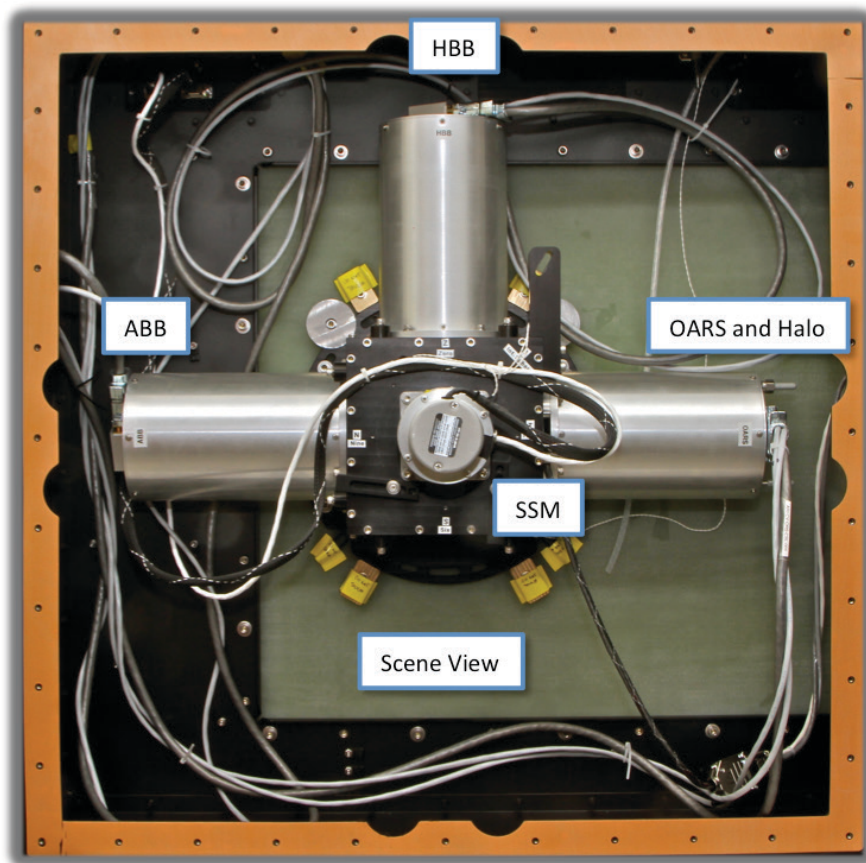
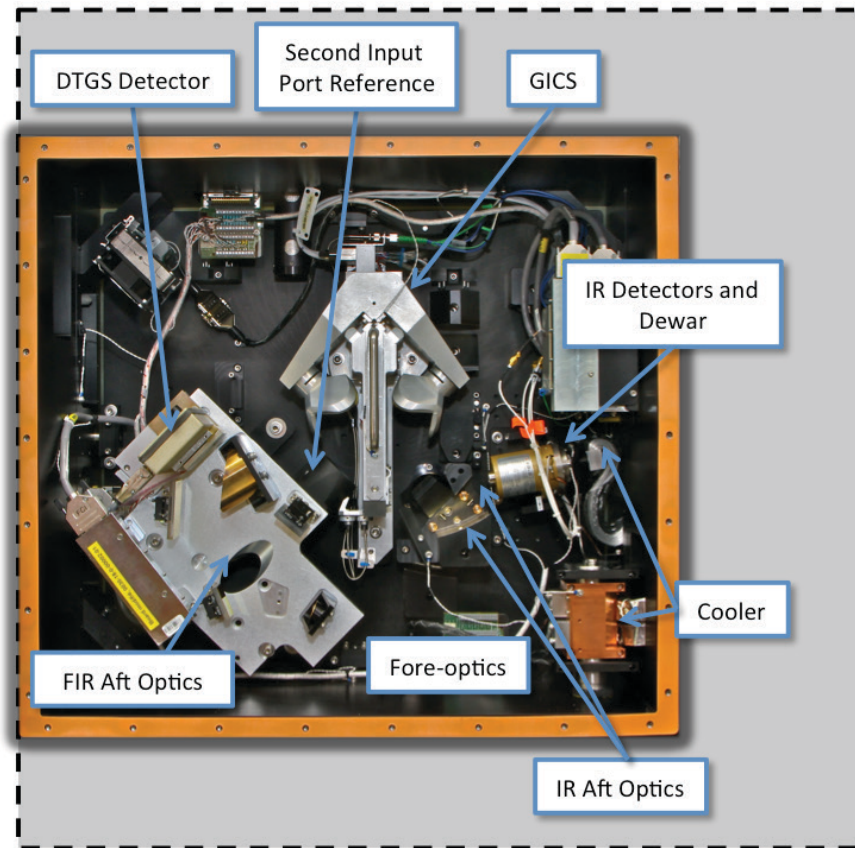


Figure 2: Front view of the completed ARI sensor prototype, showing the Ambient Blackbody (ABB) calibration reference, the Hot Blackbody (HBB) calibration reference, and the On-orbit Absolute Radiance Standard (OARS) calibration verification blackbody; any of these sources can be selected using the scene selection mirror (SSM). The OARS includes the Heated Halo On-orbit Cavity Emissivity Monitor (OCEM), which is located inside the OARS case and not visible here.



Dashed line indicates OTV enclosure envelope.

Figure 3: Internal view of the completed ARI sensor prototype. Primary components are labelled, and include the ABB Generic Interferometer for Climate Studies (GICS), the Stirling cooler, the fore-optics, far-infrared (FIR) aft-optics and deuterated triglycine sulfate (DTGS) detector, the infrared (IR) aft-optics and detector dewar module, and the second input port reference source.

1.2.1 Top-level trade studies and final specification

Several trade-studies were conducted during the design phase, prior to this thesis. Key studies and considerations included, but were not limited to, interferometer configuration, Technological Readiness Level (TRL) and flight heritage, beam splitter material and configuration, beam divergence and throughput, optical stop locations, spectral ranges for detector bands, and signal chain nonlinearity and sensitivity. A brief summary of some of the key trade studies and design considerations are provided in the following subsections. A summary of the optical design is provided in Section 3.1.

1.2.1.1 Interferometer Configuration

The design criteria included spectral resolution and range; sensitivity and throughput requirements; size, weight, and power considerations; as well as vibration and temperature concerns.

Flat mirrors compensate for two degrees of freedom in shear but are susceptible to tilt misalignment unless dynamic alignment is provided. Cat's eye and cube-corner mirrors protect against two degrees of freedom in

tilts but not shear. Cube corners can be compensated for shear if an additional flat return mirror is added at the exit of the cube-corner such that the beam retraces its steps back through the cube-corner. Given the 0.1 K calibration accuracy requirement, current cube-corner manufacturing and assembly techniques, the reduced sensitivity to shear compared to tilt for the range of divergence angle and aperture size under consideration for the ARI system, and the required maximum optical path difference (MOPD) for the ARI system, cube-corners were selected. The classical arrangement, with no additional flat return mirror in one arm, is appropriate for the required spectral resolution and coverage requirements. Furthermore, two port and four port configurations were considered. Since the four-port configuration is immune to the double pass problem associated with degenerate ports in the two-port configuration [25], a primary concern for the broadband coverage requirements, a four-port design was chosen.

1.2.1.2 Beam splitter

ABB's generic flight interferometer (GFI) utilizes a Zinc Selenide (ZnSe) beam splitter, which is the best candidate material for coverage of the 700 – 3000 cm^{-1} spectral range, but does not provide coverage in the FIR region required for the climate benchmark measurement. Several beam splitter materials and configurations were considered. Materials included Cesium Iodide, Silicon, and CVD diamond.

Pellicle and wire grids were also considered as beam splitter candidates. However, they are extremely delicate, vibration sensitive, and provide limited shortwave IR coverage. Due to these concerns it was decided that pellicle and wire grids were not a feasible option.

Silicon and CVD diamond provide spectral coverage well beyond the long-wave requirement (200 cm^{-1}) for the climate benchmark measurement. Silicon has outstanding efficiency well below 100 cm^{-1} , but exhibits strong phonon absorption at 618 cm^{-1} [77]. Phonon absorption is dependent on material thickness and can be minimized by making the silicon wafer very thin. In CVD diamond, intrinsic absorption limits its efficiency at shorter wavelengths. Considerations for phonon absorption in Silicon and material cost and machining capabilities for CVD diamond lead to evaluation of the use of thin substrates with no wedging. Secondly, the optimization of an antireflection coating over the entire spectral range of climate benchmarking measurement (200 – 2000 cm^{-1}) is not feasible within the scope of the demonstration effort. Accordingly, a single plate uncoated and uncompensated beam splitter configuration is the best option for both materials. The primary concern with this configuration is the associated extensive optical channeling. Channeling amplitude may be controlled through increasing beam divergence and optical element thickness, while the channeling frequency is a function of element thickness. However, beam divergence and beam splitter thickness are also subject to other design constraints. The stability of the fringing depends on temperature stability and the material's refractive index temperature dependence and thermal expansion coefficient. Accordingly, additional constraints are placed on thermal stability of the beam splitter temperature during the calibration cycle if the effect is to be made negligible after calibration. Finally, Silicon and CVD diamond beam splitters do not have significant flight heritage and would require additional testing and technology development that is not compatible with the IIP schedule and budget.

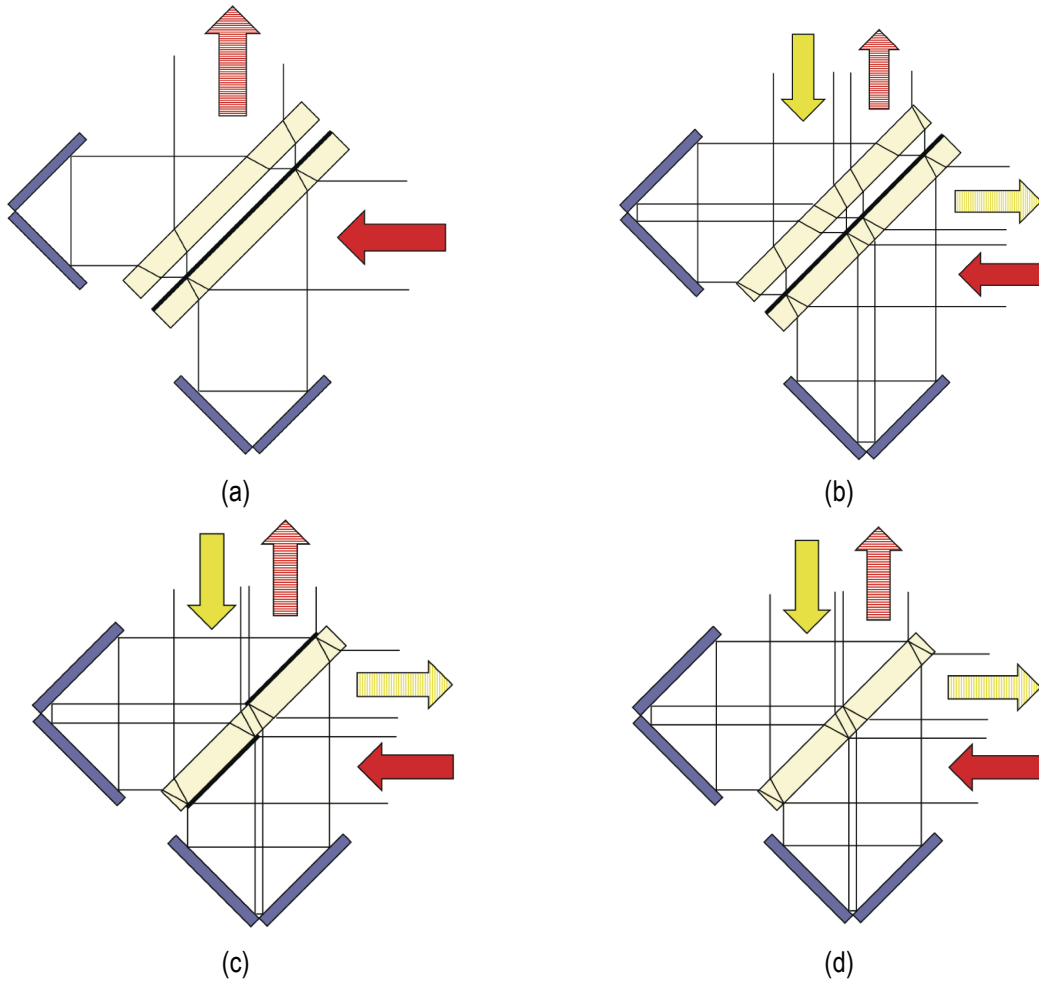


Figure 4: Interferometer configurations [78]: (a) substrate plus compensator, 2 port; (b) substrate plus compensator, 4 port; (c) single substrate, self-compensated, 4-port; (d) uncompensated, uncoated single substrate, 4-port.

Multiple Cesium Iodide beam splitter configurations were considered:

1. The traditional beam splitter with compensator arrangement is a common well-tested approach (Figure 4(a) and Figure 4(b)). The addition of a compensator reduces transmission and long-wave coverage due to the additional optical surfaces and material, but provides a highly symmetrical interferogram due to minimization of OPD dispersion. To avoid channeling, both substrates can be wedged. To maximize efficiency an AR coating can be applied to the compensator. Unfortunately, development of an AR coating compatible with the extremely broad spectral coverage requirement is not feasible for the demonstration effort.
2. The single substrate uncoated and uncompensated beam splitter configuration (Figure 4(d)) was also considered for Csl. This approach provides efficient amplitude splitting but channeling is still a primary concern. Channeling amplitude can be controlled through beam divergence and beam splitter thickness, while channeling period is dependent mainly on beam splitter thickness, and channeling stability depends on temperature stability and material properties.

3. A single substrate, self-compensated configuration was also studied (Figure 4(c)). This ABB-Bomem proprietary design requires retro-reflection and translation of the optical beam at the interferometer mirrors, and is thus only possible in a cube-corner (or equivalent) interferometer configuration. Parallelism of the substrate faces is crucial to this design and wedging of the beam splitter substrate causes misalignment and cannot be used to eliminate channeling. This configuration provides precise compensation of OPD dispersion and a highly symmetric interferogram.

Based on the above trades, a single substrate, self compensated Cesium Iodide beam splitter was chosen as the baseline for the ARI demonstration.

1.2.1.3 Technology Readiness Level (TRL) and Flight Heritage

The history of FTS in space has been remarkably successful, and has demonstrated that FTS instruments can be designed sufficiently rugged to survive launch. FTS have been packaged in small payloads for Small-Sat and rover applications, and several systems have survived and operated in space for significant periods of time.

ABB currently has 3 spaceborne FTS (ACE, GOSAT, CrIS) successfully launched and operating in space. These flight designs leverage over 35 years of research and commercial FTS design and manufacturing experience. ABB's newest flight design, the Generic Flight Interferometer, incorporates their FTS flight heritage from recent flight programs. Risk mitigation demonstration prototypes have been manufactured and tested (and continue to be tested) to establish Technology Readiness Level (TRL) and performance capability.

Given TRL and flight heritage requirements, cost considerations, and the significant UW SSEC experience with implementation, test and analysis, and high accuracy calibration of ABB-Bomem interferometers (S-HIS, AERI, NAST-I, CrIS), it was decided that the ARI interferometer core would be based on an existing ABB flight design. For compatibility with IIP project funding and schedule, commercial electronics are used.

The GFI and TANSO-FTS engineering demonstration units were compared in the context of the requirements for the ARI interferometer. Both interferometer cores meet or exceed defined requirements, minimize non-recurring engineering costs by leveraging existing ABB designs, can utilize ABB COTS electronics and software, and are designs with extensive space flight heritage and flight qualification.

Etendue, metrology, testing and qualification, maximum optical path difference (MOPD), mass, power, volume, scan speed stability, shear, modulation efficiency, transmittance, procurement costs and schedule were considered and the GFI based design was chosen as a baseline (with ABB commercial off-the-shelf (COTS) electronics for the IIP demonstration).

To meet the climate benchmark measurement requirements, minor modifications to the GFI were necessary. The resulting interferometer core is the ABB Generic Interferometer for Climate Studies (GICS).

1.2.1.4 Beam Divergence and Etendue

Beam splitter channeling, étendue, interferometer self-apodization, and non-uniform scene effect on instrument line shape (ILS) all depend on the beam divergence in the interferometer. Increased beam divergence minimizes channeling effects, but increases self-apodization, and results in larger corrections for ILS normalization and larger effects for non-uniform scenes. Étendue is a function of aperture size and

location, and beam divergence. Based on these considerations, a beam divergence (in the interferometer) of 25.8 mrad (half angle) was chosen. To maximize étendue the pupil is placed at the cube-corner. To maximize throughput and signal to noise for this beam divergence, it is desirable to maximize the pupil size. In light of cube-corner and beam splitter manufacturing limitations, a maximum achievable pupil size of 1" diameter was used.

1.2.1.5 Specifications

The primary drivers of the ARI specifications are based on the requirements for infrared climate benchmark measurements from space, for a mission such as CLARREO, and include:

- Information Content: To unequivocally detect change and refine climate models, it is necessary to capture the spectral signatures of regional and seasonal climate change that can be associated with physical climate forcing and response mechanisms.
- Absolute Accuracy: To achieve the goal of resolving a climate change signal in the decadal time frame, the absolute accuracy for the infrared measurements must be less than 0.1 K (\geq 95% confidence) brightness temperature for combined measurement and sampling uncertainty as applied to annual averages of 15°x30° latitude/longitude regions. Note that the 95% confidence applies to the combined accuracy for both measurement and sampling uncertainties. The required measurement accuracy is 0.1 K with greater than 99% confidence.
- Calibration transfer to other spaceborne IR sensors: To enhance the value of IR Earth observing sensors for climate process studies, a CLARREO IR measurement accuracy approaching 0.1 K (\geq 99% confidence) is required (for Simultaneous Nadir Overpass (SNO) comparisons).

The above drivers, along with independent studies, were used to derive the infrared measurement requirements for climate benchmark measurements from space (Table 1).

Table 1: Infrared measurement requirements for climate benchmark measurements from space.

Specification	Value
Spectral Coverage	200 – 2000 cm^{-1}
Spectral Resolution	0.5 cm^{-1} unapodized (\pm 1 cm maximum optical path difference)
Noise (NE Δ T) (10 second measurement)	< 5 K for climate record < 0.5 K for calibration transfer
Spatial Footprint and Angular Sampling	100 km or less Nadir only
Pre-launch Calibration Validation	Characterization against NIST primary infrared standards and evaluation of flight blackbodies with NIST facilities
On-orbit Calibration	Onboard warm blackbody reference (~300K) and space view, supplemented with characterization testing

These requirements, and the results of the key trade studies have been used as a basis for the UW-SSEC Absolute Radiance Interferometer design (Table 2).

Table 2: ARI key design parameters.

Parameter	Description
Spectral Coverage	Goal: 200 – 3000 cm ⁻¹
Spectral Resolution	0.5 cm ⁻¹ unapodized (±1 cm maximum optical path difference)
Interferometer Scan Speed	0.5 – 2 cm/sec
Interferometer Configuration	4 port Cube Corner Self-compensated beam splitter
Metrology Type	Diode laser (1550 nm), fiber coupled
Heritage	Significant space flight and/or flight qualification design heritage
Detectors	Output port 1: DTGS pyroelectric uncooled Output port 2: Multiband cooled (HgCdTe, InSb)
Fore-optics	Provide compatibility with a 1" aperture Blackbody Maximize interferometer throughput Minimize instrument mass and volume All reflective (uncoated gold)
Aft-optics	Output port 1: FIR coverage. All reflective (uncoated gold) Output port 2: IR coverage. Combination of reflective and refractive optics acceptable.

1.2.1.6 Interferometer Core

At the heart of the UW-SSEC ARI sensor is the ABB Generic Interferometer for Climate Studies, which is based directly on the ABB Generic Flight Interferometer. The challenge in the infrared FTS sensor development for a climate benchmark mission such as CLARREO is to achieve ultra-high accuracy (0.1 K, ≥ 99% confidence) with a design that can be flight qualified, has long design life, and is reasonably small and affordable.

ABB has participated in many recent mission definitions involving FTS. Strong similarities in the requirements at the level of the interferometer module caused ABB to pursue developing a generic flight architecture, the Generic Flight Interferometer (GFI). The GFI includes an Opto-Mechanical Assembly (OMA) that consists of an interferometer module equipped with a metrology assembly. The OMA is entirely free of electronic components apart from the interferometer scanning actuator. A 6U control card that conveys the functionality of metrology detection, laser source, actuator drive, servo control, housekeeping, telemetry and command/data handling complements this Opto-Mechanical Assembly (OMA). The OMA architecture draws its heritage from a commercial instrument (Bomem MB Series) that dates back to the mid 1980's. This instrument is known for its exquisite response stability and is used in production plants around the world to provide critical concentration measurement as control feedback for industrial fabrication processes. The ACE-SCISAT FTS was the first to implement a space design based on this architecture. Launched in 2003, ACE continues to operate today (2014), well beyond its design lifetime requirement of 2 years. More recently the TANSO-FTS onboard IBUKI (GOSAT) launched in 2009 by JAXA was also based on an evolution of the ACE-FTS and MB

Series. The GFI thus represents a third generation of flight interferometers and includes some of the latest technology developed for commercial applications.

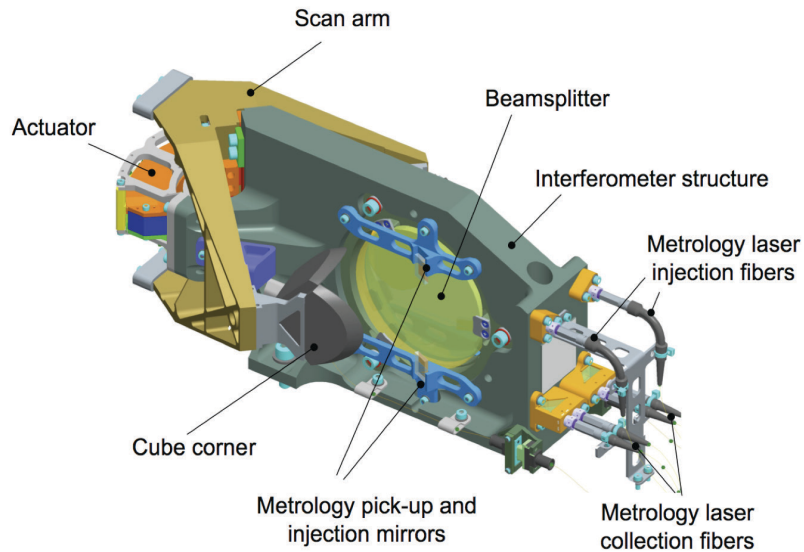


Figure 5: Solid model of the ABB Generic Flight Interferometer (GFI) (provided by ABB [79]).

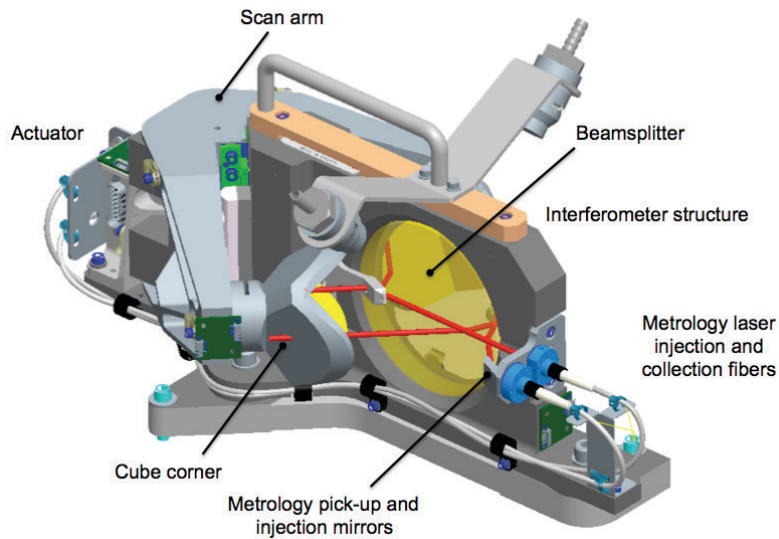


Figure 6: Preliminary solid model of the ABB Generic Interferometer for Climate Studies (GICS) (provided by ABB [80]).

To meet the UW-SSEC ARI requirements, only small adaptations of the GFI architecture were required. The resulting interferometer core is the ABB Generic Interferometer for Climate Studies. The key differences from the GFI are:

- The beam splitter substrate and coatings have been replaced with materials that maximize efficiency over the 3 – 50 μm range (CsI beam splitter, modified production coating);
- Mounting of the beam splitter has been optimized for CsI material properties;

- A self-compensated beam splitter design is used instead of a substrate and compensator design;
- GICS utilizes a 4-port configuration while GFI uses a 2-port configuration;
- Laser metrology components have been relocated for compatibility with 4-port operation;
- Replicated monolithic cube-corners are used in the GICS;
- Due to cost considerations, the GFI flight electronics have been replaced with modified commercial electronics and software for the IIP demonstration.

The GICS is a vacuum compatible interferometer. The IIP demonstration unit has a mass of < 7 kg (Opto-Mechanical Assembly), and the power requirements for the flight design are 18W average, 23W peak. Again, for cost considerations modified COTS electronics are used for the IIP demonstration. While new coating recipes with optimized FIR performance are in development as part of a joint ABB and Université Laval R&D project, to minimize schedule risk for IIP the GICS uses a modified ABB production unit coating.

1.3 Experimental set-up

The normal operational concept for an IR climate benchmark measurement from space is very simple. To collect the primary climate record, sequential nadir views of the earth are separated by several samples of the onboard calibration blackbody and the primary space view and calibration is performed frequently (on the order of once per minute). Much less frequently, views of the OARS are collected over the full range of earth scene brightness temperatures. The other scenes that are also viewed infrequently include (1) the secondary space view, (2) the OARS with emissivity monitoring sources of the On-orbit Cavity Emissivity Monitor (OCEM) activated, and (3) the On-orbit Spectral Response Monitor (OSRM). A similar operational concept is used for laboratory testing, with calibration and verification target arrangement and view sequence optimized for each test. Calibration is completed separately for each interferometer mirror sweep direction. For efficient data collection, interferograms are recorded for both directions. Accordingly, at least two interferograms, one for each sweep direction, must be collected at each successive scene mirror position.

Determination of the number of interferograms collected at each scene mirror position is based on instrument thermal stability, with a goal of minimizing calibration errors associated with nonlinear changes in instrument emission between calibration reference views while maximizing time spent viewing the target scene and calibration bodies.

On-orbit, the sensor will be radiometrically calibrated using views of a dedicated onboard full-aperture blackbody reference and space (Figure 7). For laboratory testing the space reference is replaced by a second dedicated blackbody reference (Figure 8). Rotation of a scene select mirror is used to direct calibration, calibration verification, or scene radiance into the instrument. By design, the ARI uses a 45° scene mirror rotated about the local optical axis (often referred to as a “barrel-roll” scene mirror configuration), such that the angle of reflection at the scene mirror is the same for all calibration and scene views. The calibration and scene selection via the 45° scene mirror is illustrated in Figure 9. The figure shows the scene selection mirror (SSM) at four different rotation angles corresponding to the four primary viewports in the instrument. For clarity, an isometric cross-sectional view of the calibration and verification assembly is used, looking away from the instrument. The ARI is designed such that the entire calibration validation assembly can be rotated to place the viewports, which are spaced at 90° in SSM rotation angle, at the zeros of the instrument polarization sensitivity (see Chapter 4 for details).

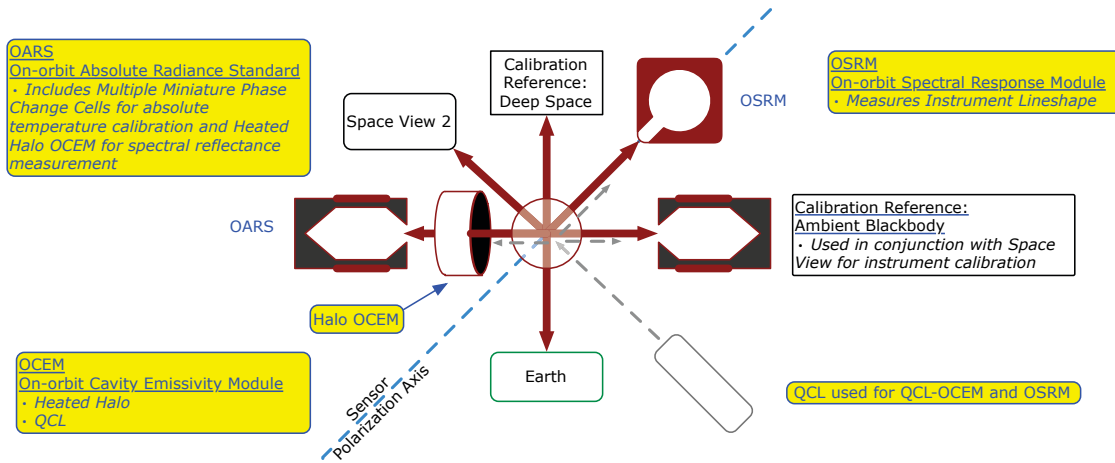


Figure 7: Typical on-orbit calibration, calibration verification, and scene view configuration.

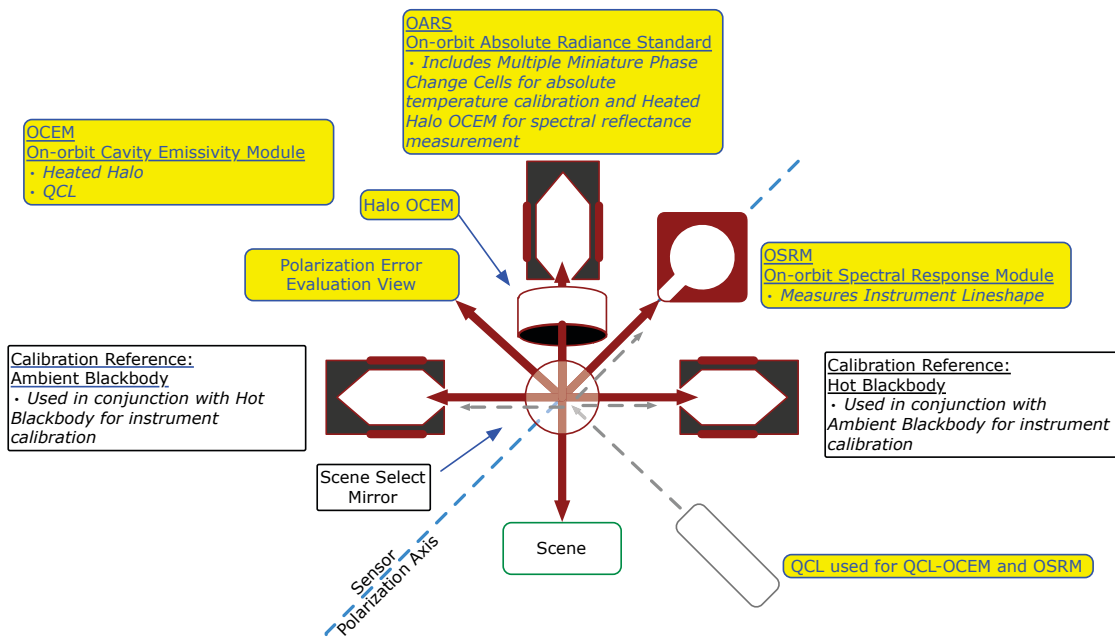


Figure 8: Typical laboratory calibration, calibration verification, and scene view configuration.

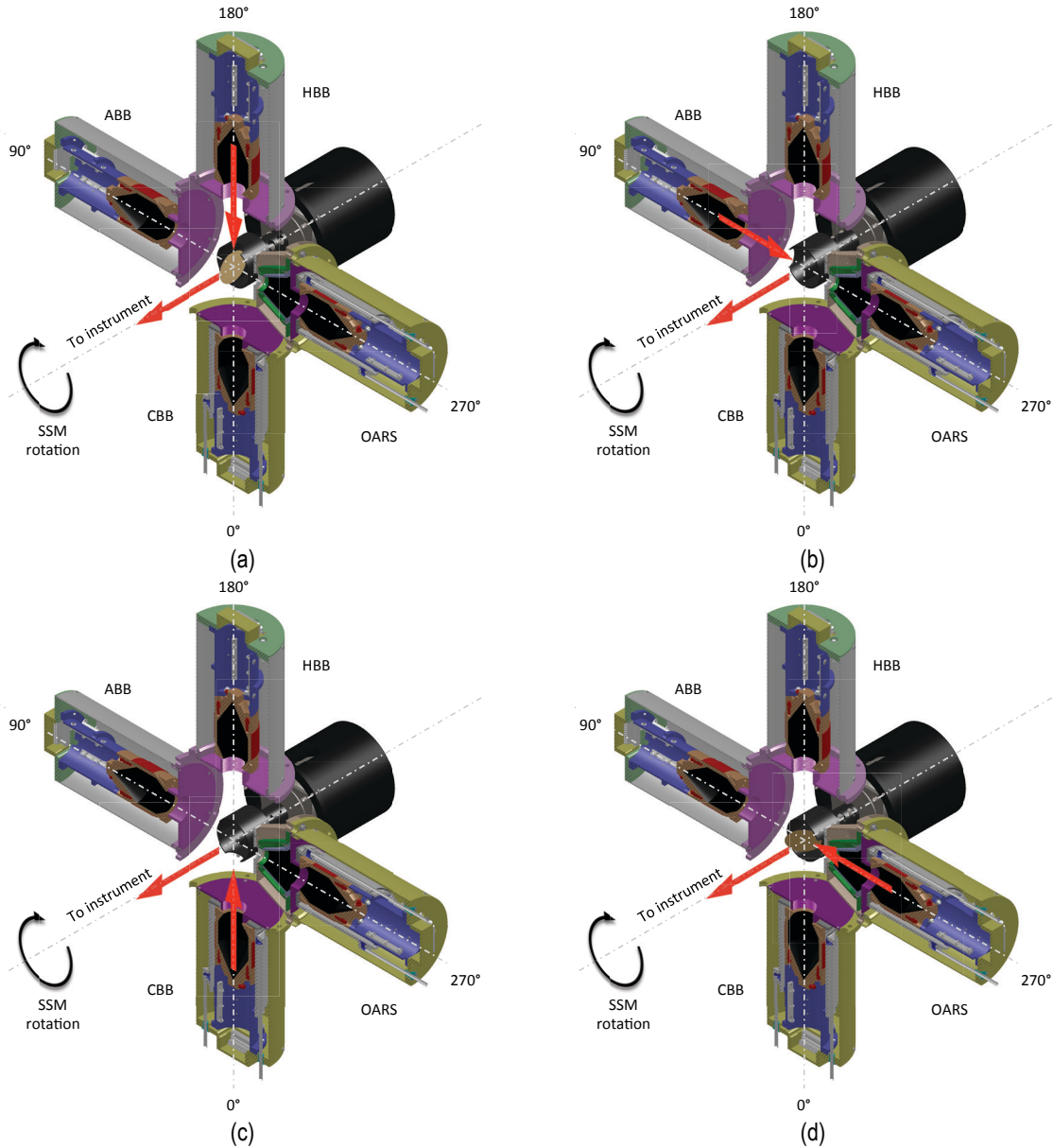


Figure 9: The ARI uses a 45° scene selection mirror rotated about the local optical axis (often referred to as a “barrel-roll” scene mirror configuration) to select the viewport that the instrument views. The angle of reflection at the scene mirror is the same for all calibration and scene views: (a) the instrument views the radiance from HBB blackbody at the zenith position; (b) the radiance from the ABB blackbody at the 90° position is selected; (c) the radiance from the CBB blackbody at the 0° position is selected; and (d) the OARS radiance at the 270° position is directed into the instrument.

1.4 Calibration

The general objective of the calibration of an electro-optical instrument, for the measurement of radiant sources, is to obtain a functional relationship between incident radiance and instrument output. Calibration establishes the relationship between instrument output and the corresponding values realized by standards, producing results compatible with accepted units [81].

Ideally, the Fourier transform of the interferogram is proportional to the incident spectral radiance over the desired wavenumber range. Radiometric and spectral calibration define the relationship of the instrument

output to the measured radiance, and fix the ordinate scale of the measurement to the radiance scale and the abscissa to the optical frequency scale.

1.4.1 Calibration approach

The complex calibration method is used for this thesis. Complex calibration is an efficient method developed to correct the amplitude and phase of the measured spectrum [82]. This approach requires two distinct calibration references, or a single reference operated and observed at two distinct temperatures. The basic calibration expression for the complex calibration method is:

$$L_S(\sigma_k) = (L_H(\sigma_k) - L_C(\sigma_k)) \operatorname{Re} \left\{ \frac{S_S(\sigma_k) - S_C(\sigma_k)}{S_H(\sigma_k) - S_C(\sigma_k)} \right\} + L_C(\sigma_k). \quad (1.1)$$

In Eq. (1.1), $L_S(\sigma_k)$ is the calibrated radiance at wavenumber sampling interval σ_k ; $S_S(\sigma_k)$, $S_C(\sigma_k)$ and $S_H(\sigma_k)$ are the complex measured spectra for the scene, cold reference, and hot reference views respectively; and $L_C(\sigma_k)$ and $L_H(\sigma_k)$ are the calculated radiances for the respective cold and hot reference views. Radiances are expressed in units of $\text{mW}/(\text{m}^2 \cdot \text{sr} \cdot \text{cm}^{-1})$, and the wavenumber scale is specified in units of cm^{-1} . The calculated radiance from a non-ideal blackbody cavity is the sum of the emitted and reflected radiance from the cavity:

$$L(\sigma_k) = e(\sigma_k) B(\sigma_k, T) + (1 - e(\sigma_k)) B(\sigma_k, T_R), \quad (1.2)$$

where $e(\sigma_k)$ is the effective emissivity of the blackbody, $B(\sigma_k, T)$ is the Planck radiance for an ideal blackbody of temperature T , and $B(\sigma_k, T_R)$ is the Planck radiance of the background, of mean temperature T_R , that is reflected from the cavity, assuming that the background contribution can be approximated by a Lambertian emitter at temperature T_R .

The radiances can be converted to equivalent brightness temperatures via inversion of Planck's Law:

$$BT(\sigma_k) = \frac{hc(1 \times 10^2)\sigma_k}{k \cdot \ln \left(1 + \frac{2hc^2(1 \times 10^8)\sigma_k^3}{L(\sigma_k)/(1 \times 10^3)} \right)}. \quad (1.3)$$

$BT(\sigma_k)$ is the equivalent brightness temperature, expressed in Kelvin (K), associated with the radiance $L(\sigma_k)$ (units of $\text{mW}/(\text{m}^2 \cdot \text{sr} \cdot \text{cm}^{-1})$), h is Planck's constant (units of J·s), c is the speed of light in a vacuum (units of m/s), and k is the Boltzmann constant (units of J/K). The equivalent brightness temperature is the temperature at which an ideal blackbody would have to be in order to produce the measured radiance at the given wavelength. An unattenuated radiance from an ideal blackbody corresponds to an equivalent brightness temperature that is constant for all wavelengths. For all other cases the effective brightness temperature will have wavelength dependence.

Equation (1.1) can be re-written more conventionally in terms of the spectrally resolved gain $G(\sigma_k)$ and offset $L^0(\sigma_k)$ of the instrument:

$$G(\sigma_k) = \frac{S_H(\sigma_k) - S_C(\sigma_k)}{L_H(\sigma_k) - L_C(\sigma_k)}, \quad (1.4)$$

$$L^0(\sigma_k) = \frac{S_C(\sigma_k)}{G(\sigma_k)} - L_C(\sigma_k), \quad (1.5)$$

$$L(\sigma_k) = \text{Re} \left\{ \frac{S_S(\sigma_k)}{G(\sigma_k)} - L^0(\sigma_k) \right\}. \quad (1.6)$$

Interferograms are recorded for both mirror sweep directions (sweep direction 0 and sweep direction 1). The spectra for each sweep direction are calibrated separately, since the phase behaviour of the measured spectra can be dependent on mirror sweep direction. The resulting calibrated radiances are averaged together to create the mean calibrated radiance corresponding to a given scene dwell.

If the reference spectra are collected with sufficient frequency such that the change in instrument emission between reference views is small and the measured spectra and calculated radiances for the reference views may be accurately interpolated to the time of the scene measurement, then any complex offset or phase associated with the warm instrument emission is cancelled in the ratio of complex difference spectra contained in Eq. (1.1).

1.4.2 Calibration uncertainty

Calibration accuracy and direct traceability to absolute standards are equally important to climate benchmark measurements. Accordingly, it is prudent to adopt the terminology and evaluation of measurement uncertainty recommended by the national and international institutions that govern traceability to the *Système international d'unités* (SI). The Bureau International des Poids et Mesures (BIPM) ensures worldwide uniformity of measurements and their traceability to the *Système international d'unités*. The BIPM Joint Committee for Guides in Metrology (JCGM) has responsibility for the following two documents: the *Guide to the Expression of Uncertainty in Measurement* (known as the GUM) [83]; and the *International Vocabulary of Metrology – Basic and General Concepts and Associated Terms* (known as the VIM) [81]. The vocabulary and uncertainty analysis methods described in this section, and adopted for this effort will follow the recommendations presented in the JCGM GUM and VIM, and the US National Institute of Standards and Technology (NIST) guidelines.

It is preferable to carry out an uncertainty analysis before the measurement is assembled such that the significant sources of uncertainty are identified early, and the measurement is planned to ensure that the uncertainties are under control. The difference between error and uncertainty should always be borne in mind. As an example, the result of a measurement after correction can unknowably be very close to the unknown value of the measurand, and thus have negligible error, even though it may have a large uncertainty [83, 84].

The uncertainty of the result of a measurement generally consists of several components, which may be grouped into two categories according to the *method* used to estimate their numerical values:

- Type A: those that arise from a random effect and are evaluated by statistical methods;
- Type B: those that arise from a systematic effect and must be evaluated by other means.

Examples of Type A evaluation of uncertainty include calculating the standard deviation of the mean of a series of independent observations, using the method of least squares to fit a curve to data in order to parameterize the curve and their standard deviations, or carrying out an analysis of variance in order to identify and quantify random effects in certain kinds of measurements.

A Type B evaluation of standard uncertainty is usually based on scientific judgment using all the relevant information available, and may include:

- Prior measurement data;
- Experience with or knowledge of the behaviour and property of relevant materials and instruments;
- Manufacturer’s specifications;
- Data provided in calibration and other reports; and
- Uncertainties assigned to reference data taken from handbooks.

The designations *Type A* and *Type B* apply to the two distinct methods by which uncertainty components may be evaluated [83, 84]. However, it is typically acceptable that a standard uncertainty obtained from a Type A evaluation may be called a *Type A standard uncertainty*; and a standard uncertainty obtained from a Type B evaluation may be called a *Type B standard uncertainty*. The NIST Guidelines for Evaluating and Expressing the Uncertainty of NIST Measurement Results [84] recommend that the terms “random uncertainty” and “systematic uncertainty” be avoided because while the adjectives “random” and “systematic” are appropriate modifiers for the word “error”, they are not appropriate descriptors for “uncertainty”. The guideline goes on to specifically state:

- The designations Type A and Type B have nothing to do with the traditional terms “random” and “systematic”;
- There are no “Type A errors” or “Type B errors”; and
- “Random uncertainty” (i.e., an uncertainty component that arises from a random effect) is not a synonym for Type A standard uncertainty; and “systematic uncertainty” (i.e., an uncertainty component that arises from a correction for a systematic error) is not a synonym for Type B standard uncertainty

In most cases the measurand Y is not measured directly, but is determined from N other quantities X_1, X_2, \dots, X_N through a functional relationship f :

$$Y = f(X_1, X_2, \dots, X_N). \quad (1.7)$$

An estimate of the measurand Y , denoted by y , is obtained from Equation (1.7) using input estimates x_1, x_2, \dots, x_N for the values of the N input quantities X_1, X_2, \dots, X_N . Therefore the output estimate y , which is the result of the measurement, is given by:

$$y = f(x_1, x_2, \dots, x_N). \quad (1.8)$$

The result of a measurement is not ideal, and only an approximation or estimate of the value of the measurand. Thus, the result is complete only when accompanied by a quantitative statement of its uncertainty [84].

The combined standard uncertainty of a measurement result, $u_c(y)$, is taken to represent the estimated standard deviation of the result, and is the positive square root of the estimated variance. The variance is obtained by combining the individual uncertainties and covariances as appropriate:

$$u_c^2(y) = \sum_{i=1}^N \left(\frac{\partial f}{\partial x_i} \right)^2 u^2(x_i) + \sum_{i=1}^N \sum_{\substack{j=1 \\ j \neq i}}^N \frac{\partial f}{\partial x_i} \frac{\partial f}{\partial x_j} u(x_i, x_j), \quad (1.9)$$

where $u(x_i)$ is the standard uncertainty associated with the input estimate x_i , $u(x_i, x_j)$ is the estimated covariance associated with x_i and x_j , and the partial derivatives $\partial f / \partial x_i$ are often referred to as the sensitivity coefficients. If the individual uncertainties are independent, then $u(x_i, x_j) = 0$ and Eq. (1.9) reduces to:

$$u_c^2(y) = \sum_{i=1}^N \left(\frac{\partial f}{\partial x_i} \right)^2 u^2(x_i). \quad (1.10)$$

This method is often called the law of propagation of uncertainty and commonly referred to as the “root-sum-of-squares” (square root of the sum of the squares) or “RSS” method of combining uncertainty components estimated as standard deviations.

Equation (1.10) is only valid if the input quantities X_i are not significantly correlated. If some of the X_i are significantly correlated, the correlations must be taken into account. The degree of correlation between x_i and x_j is characterized by the estimated correlation coefficient, $r(x_i, x_j)$:

$$r(x_i, x_j) = \frac{u(x_i, x_j)}{u(x_i)u(x_j)}, \quad (1.11)$$

where $-1 \leq r(x_i, x_j) \leq 1$. For the very special case where *all* of the input estimates are correlated with correlation coefficients $r(x_i, x_j) = +1$, Equation (1.9) reduces to:

$$u_c^2(y) = \sum_{i=1}^N \left(\frac{\partial f}{\partial x_i} u(x_i) \right)^2. \quad (1.12)$$

The estimated standard uncertainty $u_c(y)$ becomes a simple linear sum of the terms representing the variation of the output estimate y generated by the standard uncertainty of each input estimate x_i . This linear sum should not be confused with the RSS law of error propagation despite the apparently similar form [83].

The combined standard uncertainty u_c is a widely employed measure of uncertainty. However, a measure of uncertainty that defines an interval about the measurement result within which the value of the measurand is confidently believed to lie is often of more practical use. The measure of uncertainty intended to meet this requirement is termed expanded uncertainty, U , and is obtained by multiplying u_c by a coverage factor, k :

$$U = k \cdot u_c . \quad (1.13)$$

When the normal distribution applies, $k = 2$ defines an interval having a level of confidence of approximately 95 percent, and $k = 3$ defines an interval having a level of confidence greater than 99 percent. Traditionally, outside the field of metrology, the confidence level has been specified by describing expanded uncertainties as 2- σ or 3- σ uncertainties ($k = 2$ or $k = 3$ respectively).

1.5 Radiometric uncertainty estimate

A differential error analysis of the calibration equation was used to guide the instrument development of the ARI, and to determine a radiometric uncertainty estimate for the instrument. The accuracy of the reference blackbodies was then chosen to ensure that the instrument measurements that enter into the calibration equation are adequate to meet the overall calibration requirements. The ARI reference blackbodies are based on the UW-SSEC Geostationary Imaging FTS (GIFTS) blackbody design [75, 76]. Minor design modifications were made for the OARS, along with the addition of multiple miniature phase-change cells. The OARS uses transient temperature melt signatures from three different phase change materials to provide absolute calibration for the blackbody thermistor sensors covering a wide, continuous range of temperatures [68, 69, 85]. The system uses very small masses of phase change material (<1 g), making it well suited for spaceflight application.

The effective temperature uncertainty for the ARI reference blackbodies and OARS, are summarized in Table 3.

Table 3: ARI calibration source and OARS temperature uncertainty budget. Note that a temperature uncertainty of 0.045 K for the calibration reference blackbodies and the OARS is used in the ARI radiometric uncertainty analysis for all environments.

Temperature Uncertainty (3 sigma)	Laboratory OARS & ARI Cal Sources	On-Orbit ARI Cal Source	On-Orbit OARS	Comments for On-Orbit OARS
Temperature Calibration Standard				
(Thermometrics SP60 Probe with Hart Scientific 2560 Thermistor Module)	0.005	0.005	0.010	Phase Change Calibration Uncertainty
Blackbody Readout Electronics Uncertainty				
Readout Electronics Uncertainty (at delivery)	0.001	0.005	0.000	Combined with above for On-orbit
Blackbody Thermistor Temperature Transfer Uncertainty				
Gradient Between Temperature Standard and Cavity Thermistors	0.010	0.010	0.008	
Calibration Fitting Equation Residual Error	0.002	0.002	0.015	
Cavity Temperature Uniformity Uncertainty				
Cavity to Thermistor Gradient Uncertainty <small>(1/2 of total max expected gradient)</small>	0.015	0.015	0.015	
Thermistor Wire Heat Leak Temperature Bias Uncertainty*	0.020	0.008	0.020	
Paint Gradient <small>(due to radiative coupling to surrounding temperatures)</small>	0.018	0.015	0.018	
<small>*due to conductive coupling of leads to a temperature different than the cavity</small>				
Long-term Stability				
Blackbody Thermistor <small>(value for 8 years of drift assuming 100 C is 5mK)</small>	0.005	0.010	0.005	Short Term Stability
Blackbody Controller Readout Electronics	0.000	0.015	0.005	Short Term Stability
Effective Radiometric Temperature Weighting Factor Uncertainty				
Monte Carlo Ray Trace Model Uncertainty in Determining Teff <small>(radiometric error that accounts for non-isothermal cavity temperature)</small>	0.030	0.025	0.025	Improved with better modeling
RSS combination of all contributors:	0.045	0.040	0.045*	

*Value used in ARI Radiometric Uncertainty Analysis

Recall the complex calibration equation, Eq. (1.14), and the expression for the radiance from a non-ideal blackbody, Eq. (1.15):

$$L_S(\sigma_k) = (L_H(\sigma_k) - L_C(\sigma_k)) \operatorname{Re} \left\{ \frac{\mathcal{S}_S(\sigma_k) - \mathcal{S}_C(\sigma_k)}{\mathcal{S}_H(\sigma_k) - \mathcal{S}_C(\sigma_k)} \right\} + L_C(\sigma_k), \quad (1.14)$$

$$L(\sigma_k) = e(\sigma_k) B(\sigma_k, T) + (1 - e(\sigma_k)) B(\sigma_k, T_R). \quad (1.15)$$

The uncertainty associated with the calibrated radiance may be estimated by calculating the combined uncertainty for $L_S(\sigma_k)$. There is no expected first order correlation for the input quantities in Eq. (1.14), and it is valid to use Eq. (1.10) (RSS method) for estimation of the combined uncertainty:

$$\begin{aligned} u_{L_S}^2 = & \left(\frac{\partial L_S}{\partial T_H} \right)^2 u^2(T_H) + \left(\frac{\partial L_S}{\partial e_H} \right)^2 u^2(e_H) + \left(\frac{\partial L_S}{\partial T_{R,H}} \right)^2 u^2(T_{R,H}) \\ & + \left(\frac{\partial L_S}{\partial T_C} \right)^2 u^2(T_C) + \left(\frac{\partial L_S}{\partial e_C} \right)^2 u^2(e_C) + \left(\frac{\partial L_S}{\partial T_{R,C}} \right)^2 u^2(T_{R,C}) \\ & + \left(\frac{\partial L_S}{\partial X} \right)^2 u^2(X), \end{aligned} \quad (1.16)$$

where T_H and T_C are the temperature of the hot and cold calibration reference targets, with respective uncertainties $u(T_H)$ and $u(T_C)$; $T_{R,H}$, $T_{R,C}$ are the mean temperature of the background radiance that is reflected from the hot and cold reference targets, with respective uncertainties $u(T_{R,H})$ and $u(T_{R,C})$; e_H and e_C are the effective emissivities of the hot and cold blackbodies, with uncertainties $u(e_H)$ and $u(e_C)$; and X represents the measured spectra term:

$$X = \operatorname{Re} \left\{ \frac{\mathcal{S}_S(\sigma_k) - \mathcal{S}_C(\sigma_k)}{\mathcal{S}_H(\sigma_k) - \mathcal{S}_C(\sigma_k)} \right\}. \quad (1.17)$$

Assessment of the combined uncertainty $u^2(X)$ of the measured spectra is completed via models and perturbation analysis.

It has been assumed that the potentially dominant source of uncertainty associated with the measured spectra will be signal chain nonlinearity. This assumption is based on past experience with design, analysis, and testing of the AERI [50, 51, 86-88], S-HIS [54, 89-91], and GIFTS [75, 92] instruments, and testing and analysis of the CrIS [61, 93-95] instrument. The impact of signal chain nonlinearity and residual error after nonlinearity correction is discussed in Chapter 2.

Polarization sensitivity induced error can also be a significant contributor to measurement uncertainty for infrared instruments, but the instrument design is expected to mitigate first and second order polarization

induced calibration errors. The challenge presented by polarization sensitivity induced error, and the instrument design solution used to mitigate the effect's associated uncertainty contribution are presented in further detail in Chapter 4.

1.5.1 Calibration verification methodology

The primary calibration verification process is radiometric calibration verification conducted using external reference sources. The external reference sources are high-accuracy, SI traceable blackbodies operated over a range of temperatures. The resultant measured brightness temperatures are compared to predicted brightness temperatures.

The radiance bias $\Delta L(\sigma)$ may be expressed as the difference between the true radiance $L(\sigma)$ and the observed calibrated radiance $L_s(\sigma_k)$:

$$\Delta L(\sigma) = L(\sigma) - L_s(\sigma_k). \quad (1.18)$$

Since we cannot exactly know the true radiance, the uncertainty in the verification of the calibrated radiance includes a contribution from the uncertainty in the determination of the true radiance in addition to the uncertainty in the measured radiance:

$$\begin{aligned} u^2(\Delta L) &= \left(\frac{\partial(\Delta L)}{\partial L} \right)^2 u^2(L) + \left(\frac{\partial(\Delta L)}{\partial L_s} \right)^2 u^2(L_s) \\ &= \left(\frac{\partial(L(\sigma))}{\partial L} + \frac{\partial(L_s(\sigma))}{\partial L} \right)^2 u^2(L) + \left(\frac{\partial(L(\sigma))}{\partial L_s} + \frac{\partial(L_s(\sigma))}{\partial L_s} \right)^2 u^2(L_s) \\ &= \left(\frac{\partial(L(\sigma))}{\partial L} \right)^2 u^2(L) + \left(\frac{\partial(L_s(\sigma))}{\partial L_s} \right)^2 u^2(L_s) \\ &= u^2(L) + u^2(L_s). \end{aligned} \quad (1.19)$$

Note that the true (predicted) radiance and the observed calibrated radiance are independent. Consequently:

$$\frac{\partial(L_s(\sigma))}{\partial L} = 0, \quad (1.20)$$

and,

$$\frac{\partial(L(\sigma))}{\partial L_s} = 0. \quad (1.21)$$

The uncertainty associated with the On-orbit Absolute Radiance Standard (OARS) is given by:

$$u_{L_{OARS}}^2 = \left(\frac{\partial L_{OARS}}{\partial T_{OARS}} \right)^2 u^2(T_{OARS}) + \left(\frac{\partial L_{OARS}}{\partial e_{OARS}} \right)^2 u^2(e_{OARS}) + \left(\frac{\partial L_{OARS}}{\partial T_{R,OARS}} \right)^2 u^2(T_{R,OARS}). \quad (1.22)$$

In Eq. (1.22), T_{OARS} is the temperature of the OARS with uncertainty $u(T_{OARS})$, e_{OARS} is the OARS effective emissivity with uncertainty $u(e_{OARS})$, and $T_{R,OARS}$ is the mean temperature of the background radiance that is reflected from the radiance standard, with uncertainty $u(T_{R,OARS})$.

Measurements that are traceable to international standards on-orbit are required to achieve climate monitoring and prediction goals. The miniature phase change cells (MPCCs) incorporated into the OARS provide temperature traceability to physical standards, while the On-orbit Cavity Emissivity Monitor provides in-situ monitoring of any changes in the OARS emissivity.

1.5.2 Predicted calibration and calibration validation uncertainty

The predicted calibration and calibration validation uncertainty for the laboratory, vacuum, and on-orbit calibration configurations and thermal environments are provided in the following sections (§1.5.2.1, §1.5.2.2, and §1.5.2.3 respectively). The temperatures, emissivities, and associated uncertainties for each environment are tabulated, and figures illustrating the calibration, calibration validation, and combined uncertainty are provided. The radiometric uncertainty is expressed as equivalent brightness temperature and presented versus scene temperature at optical frequencies of 200, 600, 1000, 1400, 1800, 2200, and 2600 cm^{-1} . Perturbation analysis of the equations for describing the complex calibration method, Eq. (1.14), and the predicted radiance from a non-ideal blackbody, (1.15), is used to determine the individual uncertainty contributions. The individual radiometric uncertainties are converted to equivalent blackbody brightness temperature, via inversion of Planck's law. Since there is no expected first order correlation for the input quantities, the individual uncertainty contributions are combined via the RSS method.

The radiometric uncertainty contributions due to other factors such as signal chain nonlinearity are not included in the predicted calibration and calibration validation uncertainty analysis. It is expected that the instrument can be designed such that the uncertainty contributions due to these other factors is not significant. Furthermore, based on the radiometric uncertainty analysis completed via the perturbation of the complex calibration equation, a limit can be established for the radiometric uncertainty contribution associated with these other potential contributors, such that the 0.1 K on-orbit requirement can still be met with sufficient margin. Pre-launch characterization and testing of the instrument must verify that the instrument is performing within expected radiometric uncertainty.

Signal chain linearity, stray light, polarization, and the low signal to noise ratio for the far infrared measurements, have been identified as potential sources of radiometric uncertainty. These challenges are addressed in detail in Chapters 2 through 5, respectively.

While the results of the vacuum environment testing are the subject of this thesis, and the results of the testing in the laboratory environment are not presented herein, it is useful to include the uncertainty estimates for both the laboratory and vacuum environment to more clearly illustrate the dependence on calibration configuration and thermal environment for instrument testing and calibration assessment.

1.5.2.1 On-orbit calibration configuration and thermal environment

Figure 10 shows the radiometric calibration uncertainty estimate, on-orbit, and converted to equivalent brightness temperature. The calibration reference sources on-orbit are a space view target (ST) and the

internal calibration target (ICT), which is near instrument (ambient) temperature. Uncertainty estimates are tabulated in Table 4. On-orbit validation uncertainty is also shown in Figure 10 with contributors included in Table 4. Combined calibration and calibration verification uncertainty is shown in Figure 11. The on-orbit temperatures and uncertainty estimates are based on past experience with the testing and analysis of flight sensors and thermal modeling of the flight environment.

Table 4: Uncertainty estimates used in the radiometric uncertainty analysis for the on-orbit configuration. For the flight sensor, it has been assumed that the OARS emissivity and associated uncertainty is determined from laboratory testing with a very high emissivity source. (* $e_{OARS}=0.999\pm 0.0006$ (200 cm^{-1}), ± 0.0004 (800 cm^{-1}), ± 0.0002 (1400 cm^{-1}), ± 0.0001 (2000 cm^{-1}), ± 0.000075 (2600 cm^{-1}))

Temperatures			Associated Uncertainty	
Cold Cal Ref (Space Target)	T_C	4 K	$u(T_C)$	0 K
Hot Cal Ref (Internal Cal Target)	T_H	295 K	$u(T_H)$	0.045 K
Verification Target (OARS)	T_{OARS}	230 – 320 K	$u(T_{OARS})$	0.045 K
Reflected Radiance, Cold Cal Ref	$T_{R,C}$	290 K	$u(T_{R,C})$	0 K
Reflected Radiance, Hot Cal Ref	$T_{R,H}$	290 K	$u(T_{R,H})$	4 K
Reflected Radiance, Verification Target	$T_{R,OARS}$	290 K	$u(T_{R,OARS})$	4 K
Emissivities				
Cold Cal Ref (Space Target)	e_C	1	$u(e_C)$	0
Hot Cal Ref (Internal Cal Target)	e_H	0.999	$u(e_H)$	0.0006
Verification Target (OARS)	e_{OARS}	0.999	$u(e_{OARS})$	0.0006*

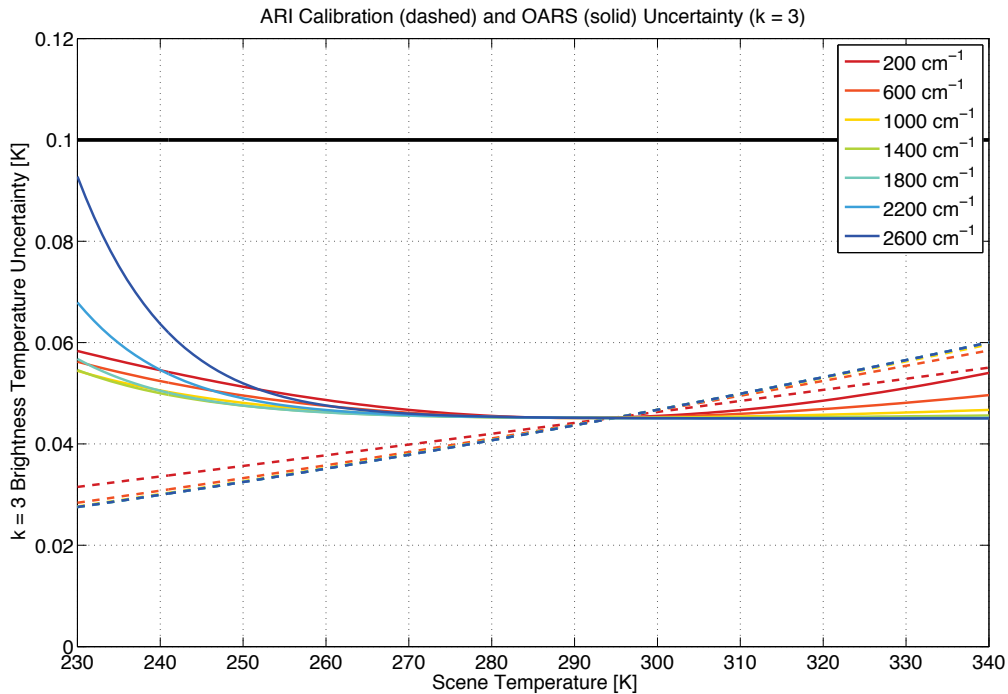


Figure 10: Predicted on-orbit radiometric calibration uncertainty (dashed) and calibration verification source uncertainty (solid) (k = 3).

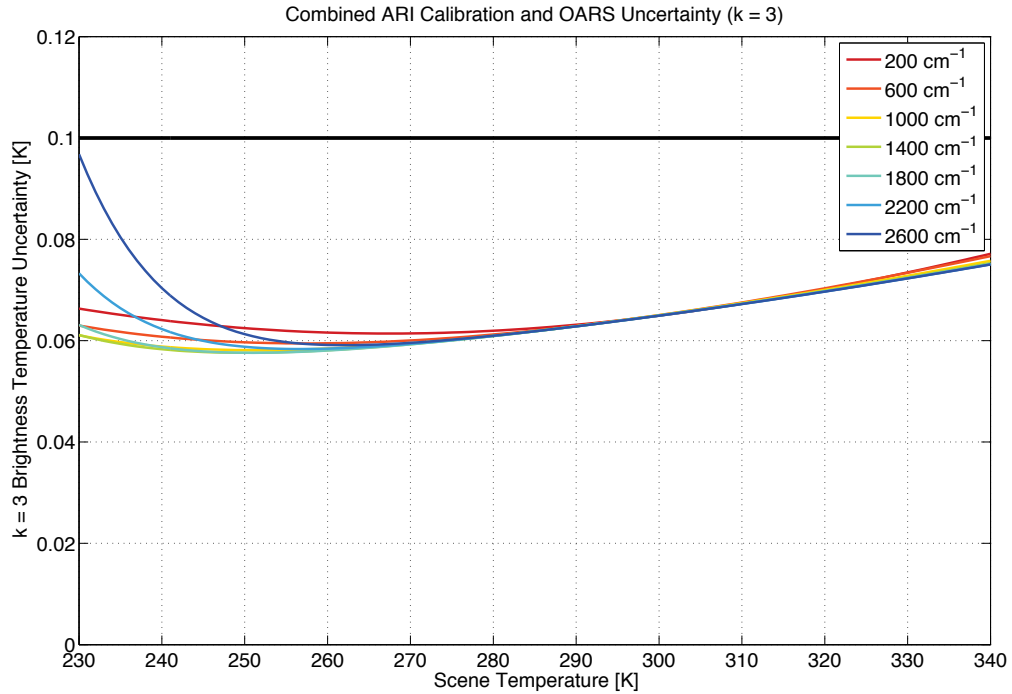


Figure 11: Predicted on-orbit combined radiometric calibration and verification uncertainty (k = 3).

1.5.2.2 Laboratory calibration configuration and thermal environment

For cost compatibility with the scope of the NASA Instrument Incubator Program funded project, initial testing was conducted in a laboratory environment, with ambient temperatures and pressure for all tests. Following the IIP testing, the NASA Earth Science Technology Office provided additional funding for testing under vacuum. The vacuum test results are the primary subject of this thesis, but the radiometric uncertainty analysis for the laboratory environment is included for completeness, and to provide further perspective on the challenges associated with laboratory-based radiometric calibration testing and assessment of a flight instrument.

For laboratory testing, an ambient calibration blackbody and hot calibration blackbody are used as calibration reference sources. The challenges associated with the laboratory calibration reference configuration and IIP demonstration include:

- Increased uncertainty associated with a blackbody compared to that of a space view. A true space view has no reflected radiance or emissivity uncertainty contributions;
- Increased uncertainty associated with the emissivity of OARS verification blackbody. For the on-orbit analysis, it was assumed that the OARS emissivity and associated uncertainty is determined from laboratory testing with a very high emissivity source, resulting in reduced emissivity uncertainty for the OARS with increasing wavenumber (* $e_{\text{OARS}}=0.999\pm 0.0006$ (200 cm^{-1}), ± 0.0004 (800 cm^{-1}), ± 0.0002

(1400 cm⁻¹), ±0.0001 (2000 cm⁻¹), ±0.000075 (2600 cm⁻¹)). This characterization is outside the scope of the IIP demonstration.

- Increased uncertainty due to nonlinearity. The effective brightness temperature of the calibration references for the on-orbit configuration bracket much of the expected range of the scene equivalent brightness temperature. For laboratory testing the separation of the calibration reference brightness temperatures is much less and the calibration equation becomes much more sensitive to extrapolation error which compounds errors due to uncorrected nonlinearity in the detector signal chain.

Uncertainty estimates for the laboratory configuration and environment are provided in Table 5. Figure 12 shows the radiometric uncertainties for the ARI calibration and OARS predicted radiance for the laboratory configuration, converted to equivalent brightness temperature. Figure 13 shows the combined radiometric calibration and calibration verification uncertainty estimate for the expected laboratory configuration and conditions.

Table 5: Uncertainty estimates used in the radiometric uncertainty analysis for laboratory configuration.

Temperatures			Associated Uncertainty	
Cold Cal Ref (Ambient Cal Blackbody)	T_C	293 K	$u(T_C)$	0.045 K
Hot Cal Ref (Hot Cal Blackbody)	T_H	333 K	$u(T_H)$	0.045 K
Verification Target (OARS)	T_{OARS}	213 – 333 K	$u(T_{OARS})$	0.045 K
Reflected Radiance, Cold Cal Ref	$T_{R,C}$	290 K	$u(T_{R,C})$	4 K
Reflected Radiance, Hot Cal Ref	$T_{R,H}$	290 K	$u(T_{R,H})$	4 K
Reflected Radiance, Verification Target	$T_{R,OARS}$	290 K	$u(T_{R,OARS})$	4 K
Emissivities				
Cold Cal Ref (Space Target)	e_C	0.999	$u(e_C)$	0.0006
Hot Cal Ref (Internal Cal Target)	e_H	0.999	$u(e_H)$	0.0006
Verification Target (OARS)	e_{OARS}	0.999	$u(e_{OARS})$	0.0006

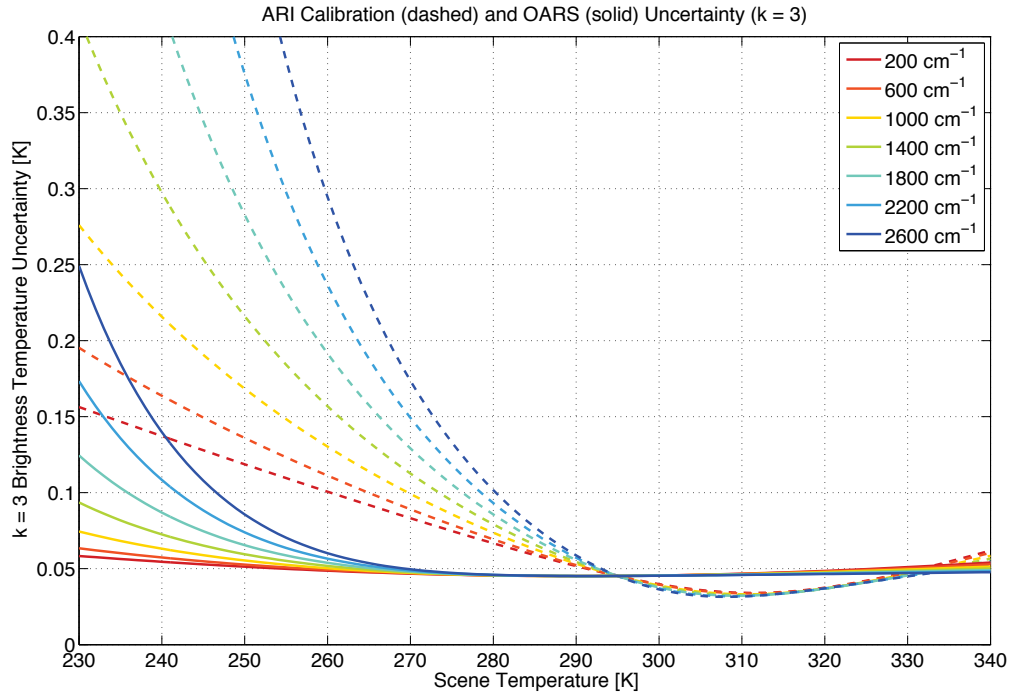


Figure 12: Predicted laboratory radiometric calibration uncertainty (dashed) and calibration verification source uncertainty (solid) ($k = 3$).

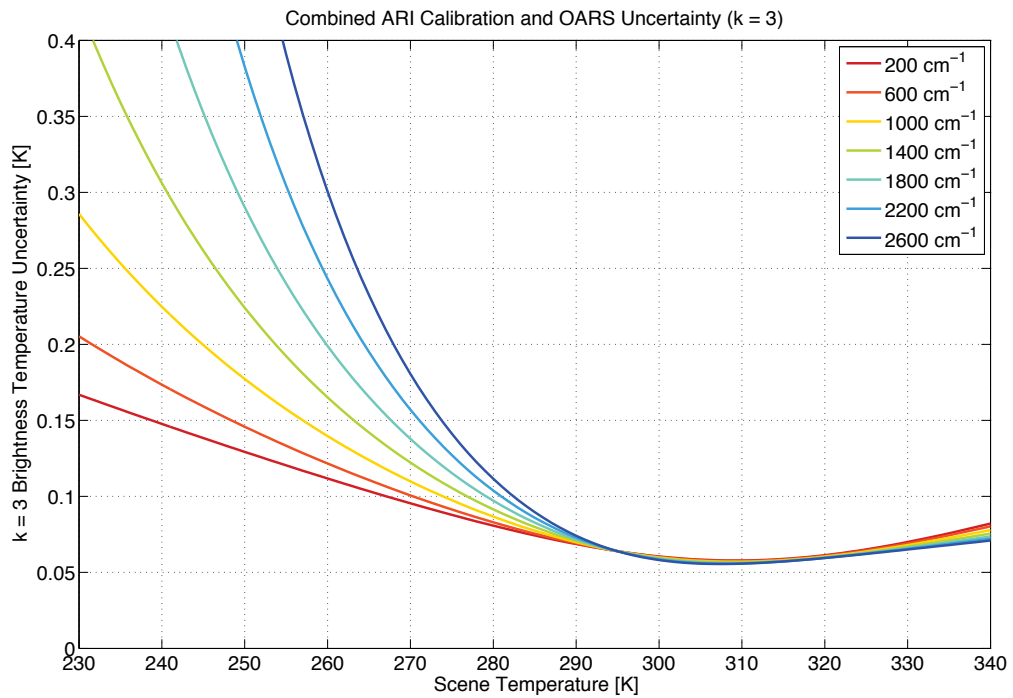


Figure 13: Predicted laboratory combined radiometric calibration and verification uncertainty ($k = 3$).

1.5.2.3 Vacuum calibration configuration and thermal environment

An ambient (or slightly warm biased) onboard blackbody and space view are used for calibration references on-orbit. For vacuum testing, a cold calibration blackbody and a warm-biased calibration blackbody are used as calibration reference sources. The primary challenges identified for the laboratory demonstration also apply to the vacuum calibration reference configuration and demonstration. Specifically,

- Increased uncertainty associated with a blackbody compared to that of a space view. A true space view has no reflected radiance or emissivity uncertainty contributions;
- Increased uncertainty associated with emissivity of OARS verification blackbody. For the on-orbit analysis, it was assumed that the OARS emissivity and associated uncertainty is determined from laboratory testing with a very high emissivity source, resulting in reduced emissivity uncertainty for the OARS with increasing wavenumber ($\epsilon_{\text{OARS}}=0.999\pm 0.0006$ (200 cm^{-1}), ± 0.0004 (800 cm^{-1}), ± 0.0002 (1400 cm^{-1}), ± 0.0001 (2000 cm^{-1}), ± 0.000075 (2600 cm^{-1})). This characterization is outside the scope of the demonstration.

However, the vacuum configuration allows for closer emulation of the on-orbit environment and calibration configuration. Key advantages of the vacuum testing, compared to testing in the laboratory environment include:

- Heat transfer conditions for the vacuum configuration are more representative of those associated with the on-orbit environment. Convection effects are significant in the laboratory environment and not present under vacuum. Increased convection results in slightly higher cavity temperature uniformity uncertainty for the calibration references in the laboratory environment, as indicated in Table 3. The impact is small (5 mK) and a temperature uncertainty of 0.045 K for the ARI calibration sources and the OARS was used for the radiometric uncertainty analysis for all environments;
- Operation under vacuum provides complete mitigation of atmospheric absorption providing a clear assessment of the radiometric performance uncontaminated by atmospheric absorption and emission features;
- Additional resources provided by the NASA ESTO for vacuum testing allowed for the fabrication of a second OARS, which was used as a cold reference blackbody. Since there are no dew point concerns for vacuum testing, the OARS and cold reference blackbody could be operated at the cold set point limit of the blackbody controllers and the recirculating chillers. This provided not only an extended range of calibration verification temperatures, but more importantly, a reference blackbody temperature configuration is closer to the on-orbit configuration.

The impact of the calibration reference configuration can be estimated by calculating the combined uncertainty for the calibrated radiance L_s for the vacuum configuration and expected conditions. Uncertainty estimates for the vacuum configuration and environment are provided in Table 6. Figure 14 shows the radiometric uncertainties for the ARI calibration and OARS predicted radiance for the vacuum configuration, converted to equivalent brightness temperature. Figure 15 shows the combined radiometric calibration and calibration verification uncertainty estimate for the expected vacuum configuration and conditions. Meeting the combined

calibration and calibration verification uncertainty in the vacuum calibration reference configuration and vacuum environment demonstrates the capability to meet the 0.1 K ($k = 3$) uncertainty requirement on-orbit.

Table 6: Uncertainty estimates used in the radiometric uncertainty analysis for vacuum configuration.

Temperatures			Associated Uncertainty	
Cold Cal Ref (Cold Cal Blackbody)	T_C	215 K	$u(T_C)$	0.045 K
Hot Cal Ref (Warm Cal Blackbody)	T_H	300 K	$u(T_H)$	0.045 K
Verification Target (OARS)	T_{OARS}	213 – 333 K	$u(T_{OARS})$	0.045 K
Reflected Radiance, Cold Cal Ref	$T_{R,C}$	295 K	$u(T_{R,C})$	4 K
Reflected Radiance, Hot Cal Ref	$T_{R,H}$	295 K	$u(T_{R,H})$	4 K
Reflected Radiance, Verification Target	$T_{R,OARS}$	295 K	$u(T_{R,OARS})$	4 K
Emissivities				
Cold Cal Ref (Space Target)	e_C	0.999	$u(e_C)$	0.0006
Hot Cal Ref (Internal Cal Target)	e_H	0.999	$u(e_H)$	0.0006
Verification Target (OARS)	e_{OARS}	0.999	$u(e_{OARS})$	0.0006

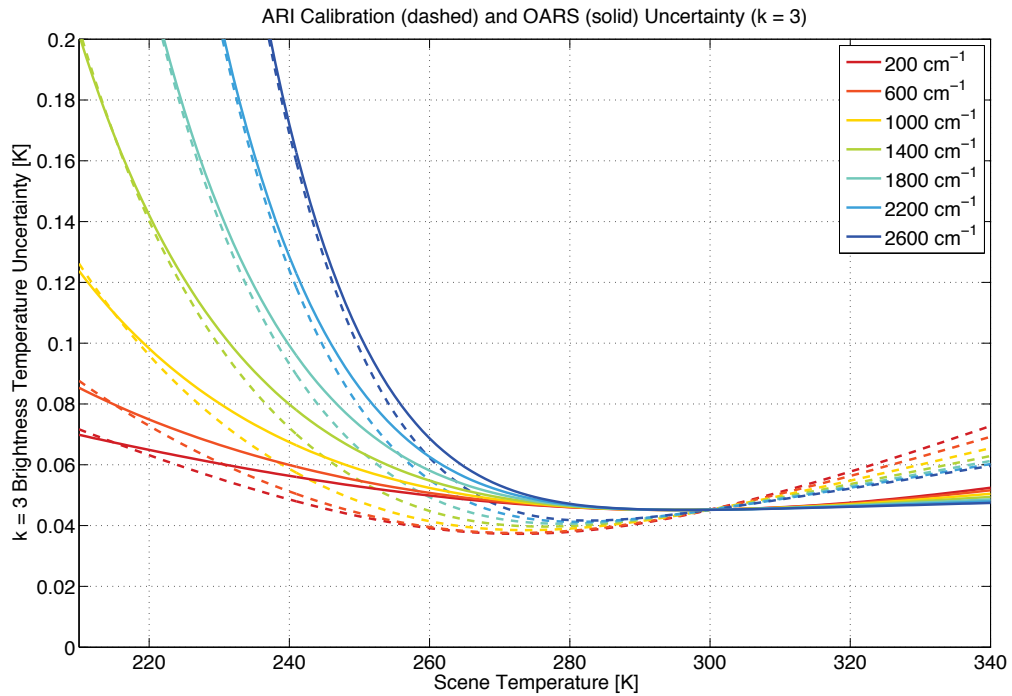


Figure 14: Predicted vacuum radiometric calibration uncertainty (dashed) and calibration verification source uncertainty (solid) ($k = 3$).

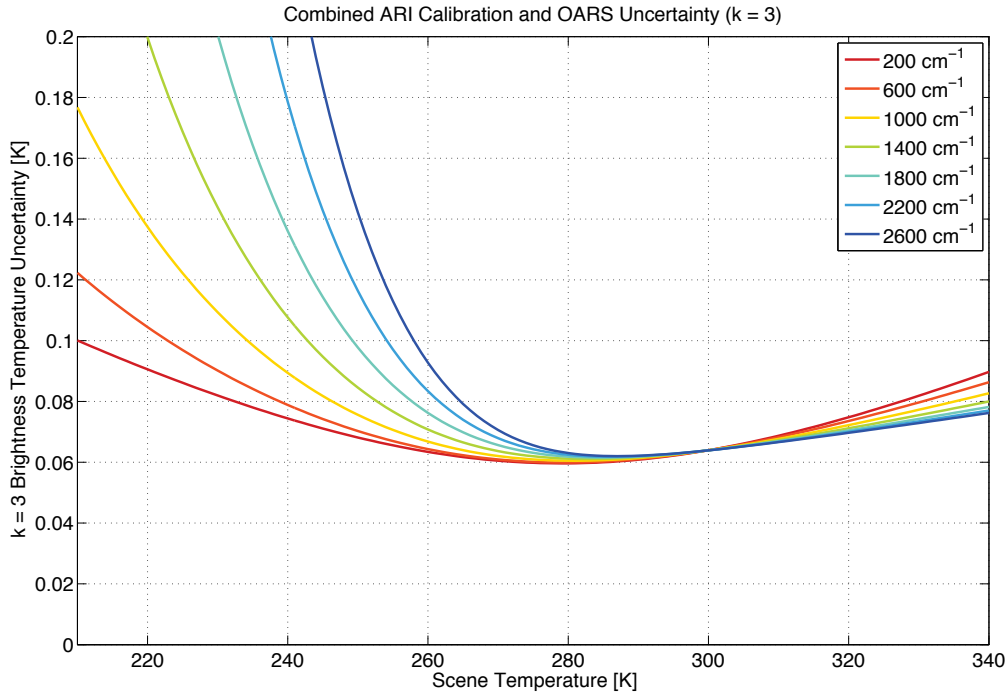


Figure 15: Predicted vacuum combined radiometric calibration and verification uncertainty ($k = 3$).

Figure 16 provides a comparison of ARI predicted on-orbit calibration uncertainty with those for the laboratory and vacuum test configurations and thermal environments. The contributions from each uncertainty source are provided, along with the RSS contribution.

For the on-orbit configuration, the dominant contributor to the calibration uncertainty is the temperature uncertainty for the onboard reference, for all scene temperatures and observation wavelengths. The onboard calibration reference is controlled to a temperature very close to, but slightly warmer than, the instrument temperature ($\Delta T = +5$ K), and as a result the radiometric uncertainty contributions due to the onboard blackbody emissivity and the reflected radiance from the onboard blackbody have a negligible contribution.

For the laboratory configuration and environment, the calibration uncertainty is dominated by the contribution from the hot calibration reference temperature uncertainty for scene temperatures above approximately 315 K for all wavelengths. Note that 315 K is roughly the midpoint between the ambient and hot calibration references for the laboratory configuration. For scene temperatures below 315 K the primary contributor to the calibration uncertainty is the uncertainty in the cold reference blackbody temperature, which is operated slightly above the ambient temperature for the laboratory testing. The uncertainties associated with the hot blackbody reference temperature and emissivity, and the cold blackbody reference emissivity and reflected radiance become significant contributors to the calibration accuracy for cold scene temperatures. The smallest contributor at all wavelengths and scene temperatures is the reflected radiance from the hot blackbody calibration reference.

The radiometric uncertainty associated with the hot blackbody calibration reference temperature, emissivity, and reflected radiance for the vacuum configuration is very similar to that for the on-orbit configuration and conditions. The key difference between the vacuum and on-orbit configurations is substitution of a cold

blackbody calibration reference in the vacuum configuration for the space view that is available on-orbit. A true space view has negligible reflected radiance, temperature, or emissivity uncertainty contributions. For the vacuum configuration, the calibration uncertainty due to the uncertainty in the cold blackbody calibration reference emissivity and reflected radiance increase with decreasing scene temperature and increasing observation wavelength. Short wavelengths and cold verification target temperatures are particularly susceptible to the radiometric uncertainty contributions from cold reference blackbody emissivity and reflected radiance. The cold blackbody calibration reference temperature uncertainty contribution to the calibration uncertainty is not insignificant, but is not the dominant contributor over the range of scene temperatures considered.

In Figure 17, a comparison of ARI predicted on-orbit calibration validation uncertainty with those for the laboratory test and vacuum-based test configurations is shown. Again, the contributions from each uncertainty source are provided, along with the RSS contribution. It is clear in Figure 17, that similar trends are observed for each environment, but the uncertainty contributions associated with the OARS emissivity and reflected temperature increase much more quickly with decreasing OARS temperature and decreasing observation wavelength. As was noted earlier, it was assumed that for the flight instrument, and thus the on-orbit configuration, the OARS emissivity and associated uncertainty would be determined from laboratory testing with a very high emissivity source, resulting in reduced emissivity uncertainty for the OARS with increasing wavenumber. This is out of scope for the demonstration unit, and results in the increased uncertainty that is evident in Figure 17.

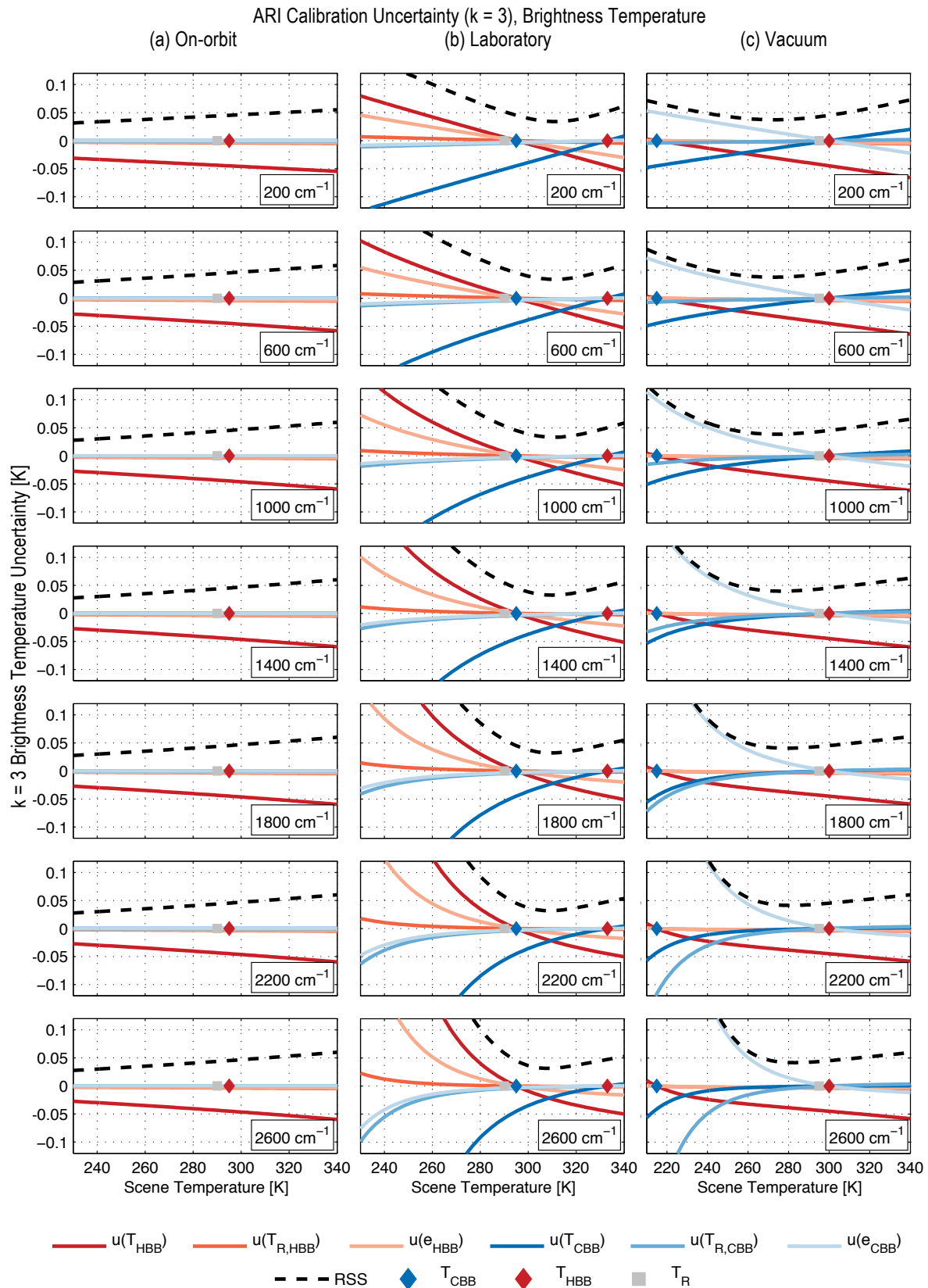


Figure 16: ARI calibration uncertainty ($k = 3$) (a) predicted on-orbit, (b) in the laboratory test configuration, and (c) during vacuum testing.

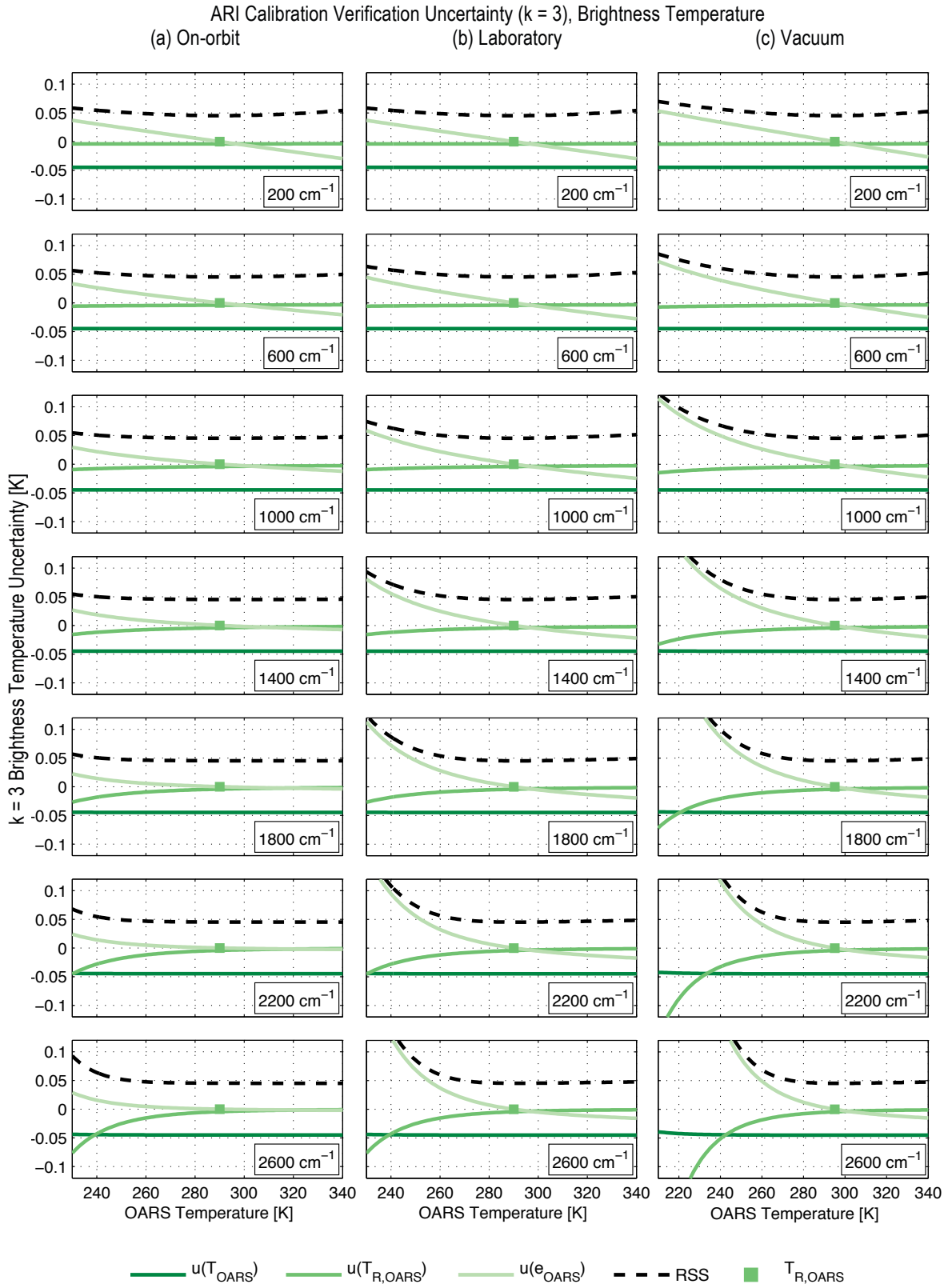


Figure 17: ARI calibration verification uncertainty ($k = 3$) (a) predicted on-orbit, (b) in the laboratory test configuration, and (c) during vacuum testing.

1.6 Challenges

The primary challenges of demonstrating the high absolute accuracy required for decadal climate trending in the infrared and far infrared are signal chain linearity (Chapter 2); optical design, stray light and vignetting (Chapter 3); calibration biases due to sensor polarization sensitivity (Chapter 4); and the low signal to noise ratio for the FIR measurements (Chapter 5). Additionally, as noted in the previous section, there are challenges associated with demonstrating the required measurement accuracy in a laboratory environment, and inferring on-orbit performance based on tests in a laboratory or vacuum environment. This challenge is addressed via rigorous uncertainty analysis, using accurate parameters representative of each environment.

Foreseen technological issues, which were addressed by the instrument design and calibration methodology, included the effects of vibrations (cooler and external sources), immunity to mean operating temperature differences and short-term variations, and optical channelling. The effect of non-uniform scenes on instrument line-shape was identified as a concern at the beginning of the project, but studies conducted by Tobin et al [96] indicate that this should not be an issue for the large dataset means associated with the infrared climate benchmark measurement. Tobin examined the effect of non-uniform scenes on instrument line-shape with respect to the spectra corrected via the nominal self-apodization correction. The nominal self-apodization correction corresponds to a uniformly illuminated field of view. Typically, the field of view is not uniformly illuminated due to clouds, surface, or other atmospheric features, and the nature of the non-uniformity is random for statistically large datasets. There is an equal chance of the self-apodization correction under or over correcting a given non-uniform scene. While the distribution of spectral shifts with respect to the on-axis field of view over a large dataset is highly non-Gaussian, it is symmetric about zero and should not be an issue for the large dataset means associated with the climate benchmark measurement (Figure 18).

Distribution of spectral shifts with respect to FOV5

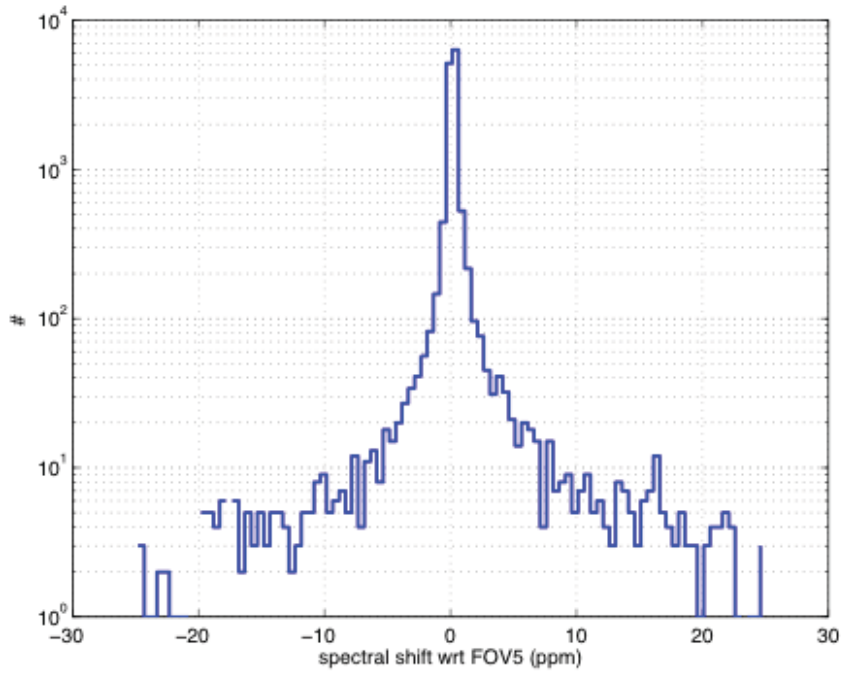


Figure 18: Analysis conducted by Tobin et al [96], indicate that this should not be an issue for the large dataset means associated with the infrared climate benchmark measurement. The nominal self-apodization correction corresponds to a uniformly illuminated field of view. Typically, the field of view is not uniformly illuminated and the spatial and radiometric distribution of the non-uniformity is random for large datasets. The histogram of the spectral shifts, with respect to the to on-axis field of view (FOV5) after self-apodization correction, observed for CrIS is shown.

2 Nonlinearity and nonlinearity correction

2.1 Impact of nonlinearity in Fourier Transform Spectrometers

In an ideal photometric detector the photocurrent is linearly proportional to the incident flux on the detector surface. In practice, the detector signal chain can display a nonlinear response, either due to the detector itself or the associated signal chain electronics.

In interferometric systems response linearity is extremely important due to the large dynamic range of the incident flux on the detector [25, 97-100]. The measured amplitude of the interferogram must be linearly proportional to the incident flux on the detector for the transformed spectrum to have an accurate spectral shape.

In most FTIR applications, thermal detectors such as thermopiles and bolometers have been replaced by quantum photodetectors, such as Indium Antimonide (InSb) and Mercury-Cadmium-Telluride (HgCdTe or MCT) detectors, because of their high sensitivity and fast response time.

The nonlinear response of photoconductive (PC) MCT detectors is well established, with a typical nonlinear behaviour ranging from a few percent to more than 20% deviation from linearity at maximum flux intensities. The doping associated with extremely sensitive detectors can lead to even higher nonlinearity levels. Conversely, photovoltaic (PV) InSb detectors are usually operated in a range, even in interferometry applications, where they exhibit an extremely linear response. Unfortunately, the long-wave responsivity limit for InSb is typically no better than 5.5 μm . Photovoltaic MCT detectors are expected to provide much better linearity than photoconductive MCT detectors [101], and tests by Theocharus et al [102, 103] have confirmed that expectation [102, 103]. However, high sensitivity PV MCT detectors in interferometric systems have also been shown to exhibit non-negligible nonlinear behaviour [61, 93-95, 104].

In a Fourier Transform Spectrometer nonlinearity manifests itself by distortion of the resultant spectrum in the spectral region where the detector is sensitive (in-band), and by the creation of spectral artifacts indicating the presence of a detected signal in the spectral region where the detector is not sensitive (out-of-band). An important diagnostic of quadratic nonlinear response in FTS, first noted by Chase [99], is the analysis of the spectral range between zero and the lowest detectable wavenumber for the presence of spurious spectral response. This effect is illustrated in Figure 19 and Figure 20.

Figure 19 represents a typical example of a measurement with a detection bandwidth of less than one octave and a quadratic nonlinear response. The large spectral artifact between zero and the long-wave cut-off, and the secondary spectral artifact located beyond the shortwave cut-off of the detection band may be described in terms of the autocorrelation of the true spectrum.

The impact due to quadratic nonlinearity becomes more complex for measurements in which the detection band is larger than one octave. An example of such a scenario is shown in Figure 20. In this case the quadratic nonlinear response of the detector overlaps into the optical bandpass and introduces additional offsets in spectral intensity [25, 97, 105].

In addition to spectral artifacts, an important consequence of nonlinear signal chain response in FTS systems is the first order scaling effect. The centerburst of the interferogram represents the lowest spectral resolution

information, and the largest dynamic range of the interference signal. The effect of nonlinearity in this region of the interferogram will result in distortion of the broad spectral continuum [25, 97, 105] which, at first order manifests itself as an otherwise unexpected gain on the spectrum.

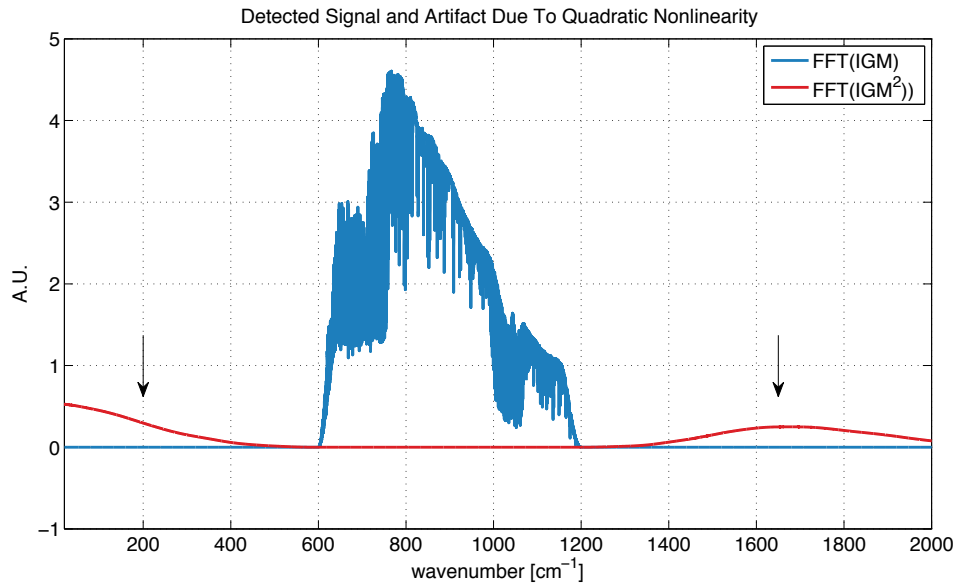


Figure 19: Example of a simulated measurement of an atmospheric spectra (U.S. standard atmosphere, top of atmosphere (TOA)) with detection bandwidth of less than one octave affected by quadratic nonlinearity (quadratic artifacts indicated by arrows) [25, 105].

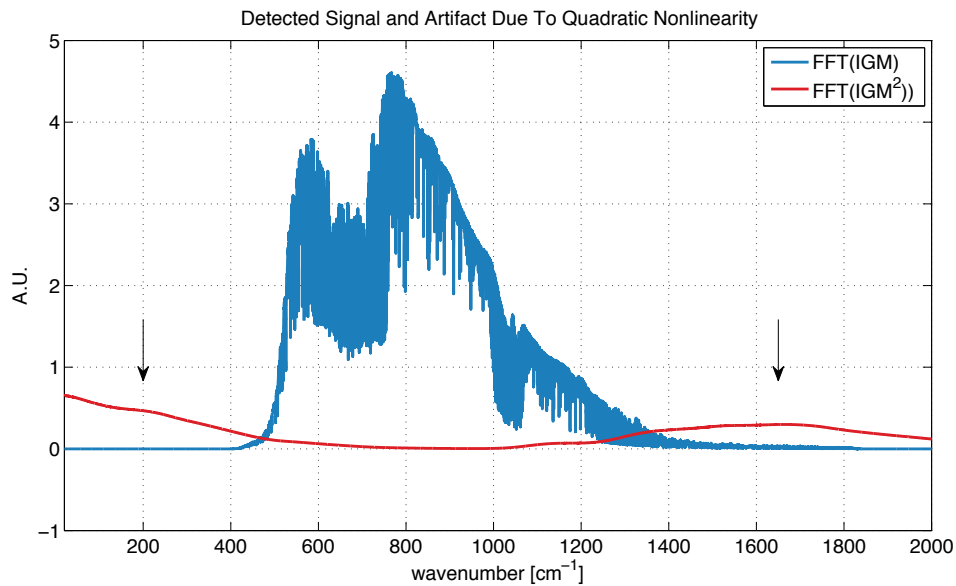


Figure 20: Example of a simulated measurement of an atmospheric spectra (U.S. standard atmosphere, top of atmosphere (TOA)) with detection bandwidth of greater than one octave affected by quadratic nonlinearity (quadratic artifacts indicated by arrow) [25, 105].

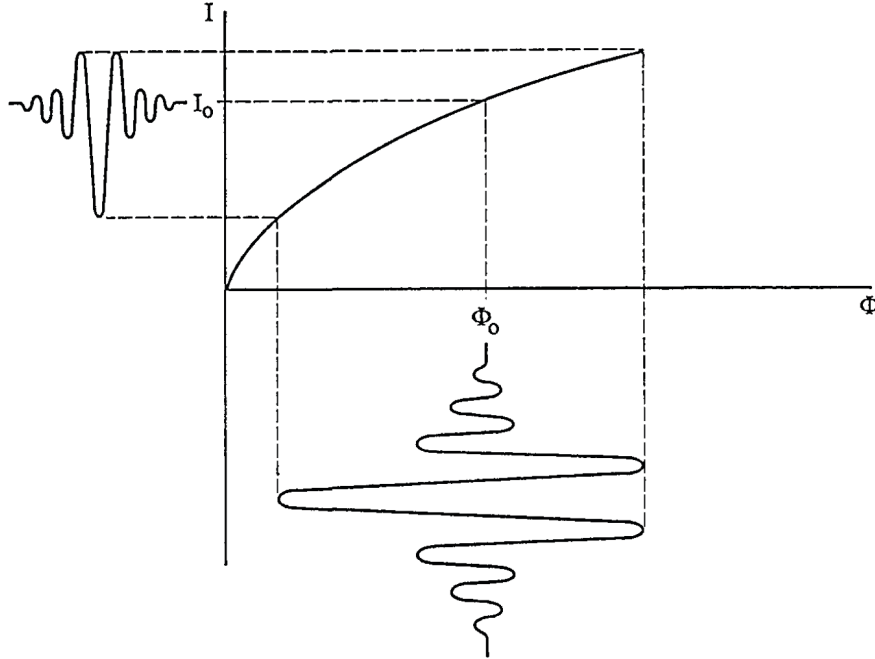


Figure 21: A stylized representation of a hypothetical detector-response curve exhibiting nonlinearity [97]. The abscissa represents the absolute magnitude of the incident photon flux on the detector and the measured signal is on the ordinate axis. The figure assumes a modulation efficiency of 70%, and does not include the DC signal due to the electronics biasing or detector dark current.

Figure 21, taken from Abrams et al [97], provides a stylized representation of a hypothetical detector-response curve exhibiting nonlinearity. The abscissa represents the absolute magnitude of the incident photon flux on the detector and the measured signal is on the ordinate axis. The real, linear interferogram is provided below the x-axis and the measured interferogram, distorted by the nonlinear response of the detector signal chain is indicated to the left of the y-axis. The figure assumes a modulation efficiency of 70%, and does not include the DC signal due to the electronics biasing or detector dark current. It is clear from the figure that successful correction of the nonlinear response requires accurate knowledge of both the response curve parameterization and the total signal. The total measured signal, including DC and AC components, defines the position of the measured signal on the nonlinear response curve.

2.1.1 Mathematical representation

A brief mathematical framework is useful for illustrating the nature of the spectral artifacts associated with a measured nonlinear interferogram [25, 105].

The measured nonlinear interferogram $I_m(x_k)$ can be represented as the result of a nonlinear operator applied $\mathcal{R}\{\cdot\}$ to the ideal interferogram $I(x_k)$:

$$I_m(x_k) = \mathcal{R}\{I(x_k)\}. \quad (2.1)$$

The nonlinear and linear interferograms are sampled at discrete optical path differences, x_k . Assuming a memory-less nonlinear response, the measured nonlinear interferogram can be represented by a Taylor series expansion of the ideal interferogram:

$$I_m(x_k) = \sum_{n=0}^{\infty} b_n I^n(x_k). \quad (2.2)$$

An interferogram consists of an unmodulated DC component and a modulated AC component varying about the average value:

$$I(x_k) = I_{DC} + I_{AC}(x_k). \quad (2.3)$$

Equations (2.2) and (2.3) can be combined to express the measured nonlinear interferogram explicitly in terms of the modulated and unmodulated components of the ideal interferogram:

$$\begin{aligned} I_m(x_k) &= \sum_{n=0}^{\infty} b_n [I_{DC} + I_{AC}(x_k)]^n \\ &= \sum_{n=0}^{\infty} b_n \sum_{q=0}^n \binom{n}{q} I_{DC}^{n-q} I_{AC}^q(x_k), \end{aligned} \quad (2.4)$$

where,

$$[I_{DC} + I_{AC}(x_k)]^n = \sum_{k=0}^n \binom{n}{k} I_{DC}^{n-k} I_{AC}^k(x_k), \quad (2.5)$$

and,

$$\binom{n}{k} = \frac{n!}{k!(n-k)!}. \quad (2.6)$$

Grouping the terms by powers of $I_{AC}^q(x_k)$ leads to:

$$\begin{aligned} I_m(x_k) &= \sum_{q=0}^{\infty} I_{AC}^q(x_k) \overbrace{\sum_{n=q}^{\infty} b_n \binom{n}{q} I_{DC}^{n-q}}^{A_q} \\ &= \sum_{q=0}^{\infty} A_q I_{AC}^q(x_k). \end{aligned} \quad (2.7)$$

An expression up to the third order in the interferogram domain is given by:

$$I_m(x_k) = A_0 + A_1 I_{AC}(x_k) + A_2 I_{AC}^2(x_k) + A_3 I_{AC}^3(x_k) + O(I_{AC}^4), \quad (2.8)$$

where $O(I_{AC}^4)$ represents the error in I_{AC}^4 in the neglected terms.

Since the Fourier transform is a linear operation, the spectrum affected by nonlinearity is the sum of the Fourier transform of each term in the measured nonlinear interferogram.

$$\begin{aligned} S_m(\sigma_k) &= \mathcal{F}\{I_m(x_k)\} \\ &= A_1 S(\sigma_k) + A_2 S(\sigma_k) \otimes S(\sigma_k) + A_3 S(\sigma_k) \otimes S(\sigma_k) \otimes S(\sigma_k), \end{aligned} \quad (2.9)$$

where $S_m(\sigma_k)$ is the measured spectrum corresponding to the nonlinear interferogram, and \otimes represents the linear convolution operator. Figure 22 and Figure 23 show the quadratic and cubic spectral artifacts corresponding to a uniform spectral band distribution one octave and two octaves wide, respectively. When the bandwidth is less than or equal to one octave, the quadratic artifact is completely out-of-band. When the bandwidth is greater than one octave, the quadratic artifact overlaps with the in-band signal. Genest et al [25] present the bandwidth considerations for spectral artifacts associated with higher order nonlinearity.

To summarize, nonlinearity in FTS produces two primary sources of systematic error:

- Distortion of the broad spectral continuum associated with a change in effective responsivity. This is a multiplicative effect.
- Out-of-band spectral artifacts that may be described in terms of the autocorrelation of the linear spectrum. This is an additive effect and leads to radiometric errors for a quadratic nonlinearity when the detection bandwidth is greater than one octave.
- The third order nonlinearity, if present, produces an additional additive in-band component.

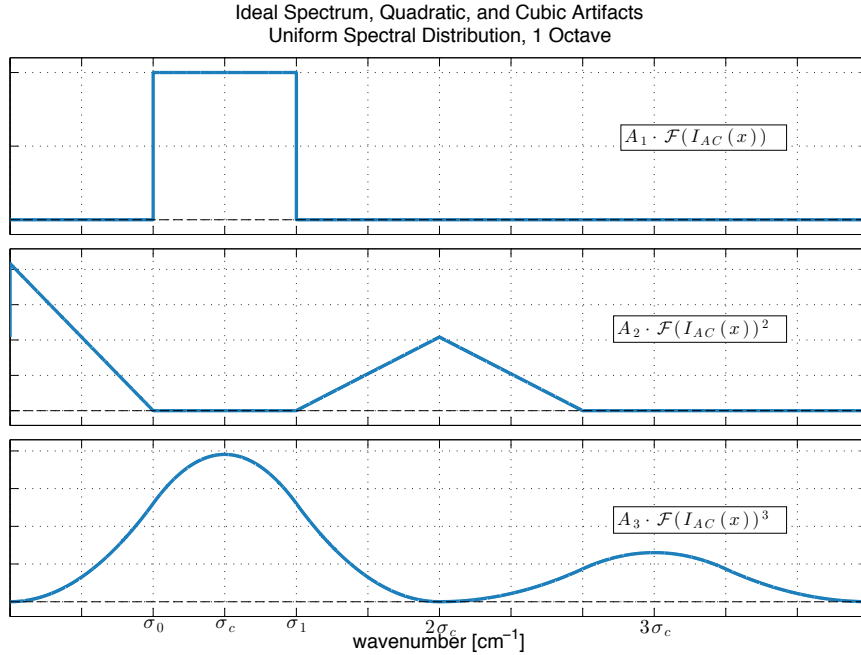


Figure 22: The quadratic and cubic nonlinearity spectral artifacts corresponding to a single octave ($\sigma_1 = 2\sigma_0$) uniform spectral band distribution with sufficient sampling such that out-of-band artifacts are not aliased in-band. Artifacts are not to scale.

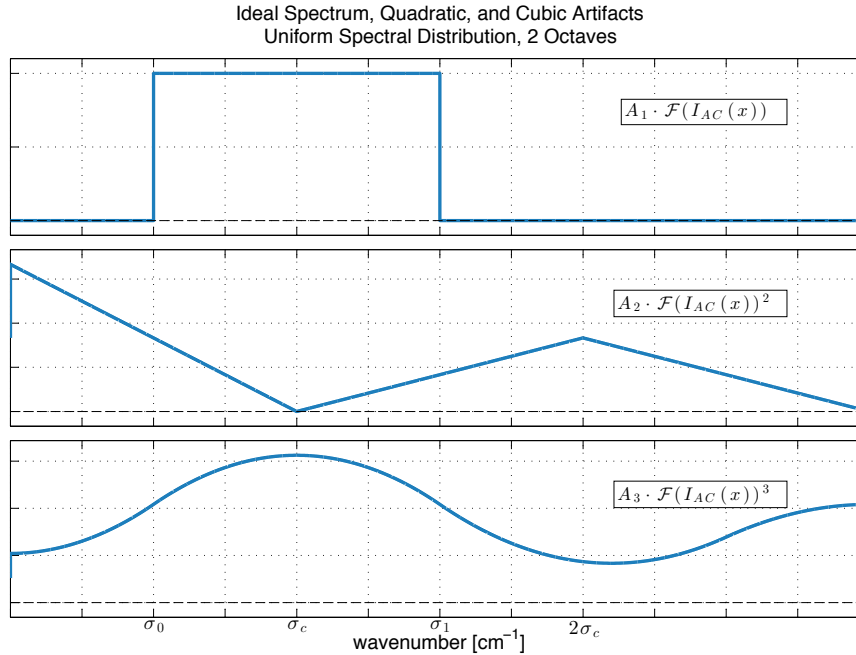


Figure 23: The quadratic and cubic nonlinearity spectral artifacts corresponding to a two-octave ($\sigma_1 = 3\sigma_0$) uniform spectral band distribution with sufficient sampling such that out-of-band artifacts are not aliased in-band. When the spectral bandpass is greater than one octave, the quadratic artifact also overlaps the in-band measurement. Artifacts are not to scale.

2.2 Nonlinearity correction algorithm

Several approaches have been developed for nonlinearity correction in Fourier Transform Spectrometers, including photometric correction [100, 106], electronic correction [107, 108], and algorithmic correction in post processing software [50, 61, 93, 94, 97, 99, 104, 106, 109-111].

The nonlinearity correction used for the ARI is an algorithmic approach, built on the nonlinearity correction method developed at the UW-SSEC. The UW-SSEC nonlinearity correction algorithm is based directly on photoconductive (PC) HgCdTe detector theory [112] and has been successfully applied to the AERI (Atmospheric Emitted Radiance Interferometer), S-HIS (Scanning High-resolution Interferometer Sounder), NAST-I (NPOESS Airborne Sounder Testbed – Interferometer), and CrIS (Cross-track Infrared Sounder) sensors [50, 61, 87, 93-95, 104, 110, 113, 114]. While the CrIS detectors are photovoltaic (PV) HgCdTe, the CrIS instrument demonstrated a second order nonlinear detector response. The nonlinearity correction is applicable to any nonlinear response that can be expressed as a polynomial expansion, regardless of the physical principles that result in the nonlinear response.

The UW-SSEC nonlinearity correction algorithm is based on the research completed by Reine [112] describing the nonlinear response of PC HgCdTe photoconductors to large signal photon levels. The principle application of Reine's work at the time was ATMOS, the Atmospheric Trace Molecule Spectroscopy Experiment. ATMOS was designed to study the Earth's atmospheric composition via solar occultation measurements. The primary instrument was an FTS [115, 116] that was used to obtain high resolution infrared spectra of the atmosphere with the Sun as the source.

Reine defined a relationship between the photon flux density Q and the photo-generated conduction band electron concentration Δn ,

$$Q \equiv c_1 \Delta n + c_2 (\Delta n)^2 + c_3 (\Delta n)^3, \quad (2.10)$$

where c_i are constants that are a function of the physical properties of the detector, and defined in detail in the Reine document [112].

The UW-SSEC nonlinearity correction model assumes that the corrected linear interferogram signal I_L is proportional to the photon flux density and the measured nonlinear interferogram I_{NL} is proportional to the photo-generated conduction band electrons,

$$I_L(x_k) = \sum_{n=0}^{\infty} c_n I_{NL}^n(x_k). \quad (2.11)$$

As noted in Section 2.1.1, an interferogram consists of an unmodulated DC component and a modulated AC component varying about the DC level. Equation (2.11) can be rewritten accordingly, explicitly noting the AC and DC components of the interferogram

$$\begin{aligned} I_{L_{AC}}(x_k) + V_C &= \sum_{n=0}^{\infty} c_n [V_{NL} + I_{NL_{AC}}(x_k)]^n \\ &= \sum_{n=0}^{\infty} c_n \sum_{q=0}^n \binom{n}{q} V_{NL}^{n-q} I_{NL_{AC}}^q(x_k). \end{aligned} \quad (2.12)$$

In Eq. (2.12), the modulated AC component of the interferogram is denoted by the subscript AC and V is the DC level. While both Eq. (2.12) and Eq. (2.4) are Taylor expansions, equation (2.12) describes the linear signal as an expansion of the nonlinear signal, and equation (2.4) does the opposite. Once again, the terms are grouped by powers of the AC signal:

$$I_{L_{AC}}(x_k) + V_C = \sum_{q=0}^{\infty} I_{NL_{AC}}^q(x_k) \sum_{n=q}^{\infty} c_n \binom{n}{q} V_{NL}^{n-q} \quad (2.13)$$

Experience with nonlinearity characterization, and successful development and application of nonlinearity correction for the AERI, NAST-I, S-HIS, and CrIS instruments has shown that the 3rd order and higher nonlinearity terms are not significant for the HgCdTe detectors, throughput, and photon flux levels, and radiometric accuracy requirements associated with these atmospheric sounders. Consequently, the cubic term in Eq. (2.11) is typically omitted. While the radiometric accuracy requirements for the ARI are more demanding than those of the atmospheric sounders noted, it is reasonable to begin with the assumption that the cubic and higher order terms can be omitted. However, if this simplification results in a nonlinearity correction that does not provide the required radiometric accuracy, then the inclusion of higher order terms must be considered.

Omitting the cubic and higher order terms, Eq. (2.13) can be simplified as:

$$\begin{aligned}
I_{L_{AC}}(x_k) + V_C &= \sum_{q=0}^2 I_{NL_{AC}}^q(x_k) \sum_{n=q}^2 c_n \binom{n}{q} V_{NL}^{n-q} + O(I_{NL_{AC}}^3(x_k)) \\
&\cong \sum_{q=0}^2 I_{NL_{AC}}^q(x_k) \sum_{n=q}^2 c_n \binom{n}{q} V_{NL}^{n-q} \\
&= c_0 + c_1 (I_{NL_{AC}}(x_k) + V_{NL}) + c_2 (I_{NL_{AC}}(x_k) + V_{NL})^2 \\
&= (c_0 + c_1 + c_2 V_{NL}^2) + (c_1 + 2c_2 V_{NL}) I_{NL_{AC}}(x_k) + c_2 I_{NL_{AC}}^2(x_k).
\end{aligned} \tag{2.14}$$

Fourier transforming Eq. (2.14) into the spectral domain produces:

$$\mathcal{S}_L(\sigma_k) = (c_1 + 2c_2 V_{NL}) \mathcal{S}_{NL}(\sigma_k) + c_2 \mathcal{S}_{NL}(\sigma_k) \otimes \mathcal{S}_{NL}(\sigma_k), \tag{2.15}$$

where \otimes indicates linear convolution, and \mathcal{S} is the complex spectrum. The Fourier transform of the DC signal is a delta function at zero wavenumbers, and is not explicitly included in Eq. (2.15). In the UW-SSEC nonlinearity formulation, $c_1 = 1$, which is equivalent to dividing equation (2.15) by c_1 :

$$\begin{aligned}
\frac{\mathcal{S}_L(\sigma_k)}{c_1} &= \frac{(c_1 + 2c_2 V_{NL}) \mathcal{S}_{NL}(\sigma_k) + c_2 \mathcal{S}_{NL}(\sigma_k) \otimes \mathcal{S}_{NL}(\sigma_k)}{c_1} \\
\frac{\mathcal{S}_L(\sigma_k)}{c_1} &= \left(1 + 2 \frac{c_2}{c_1} V_{NL}\right) \mathcal{S}_{NL}(\sigma_k) + \frac{c_2}{c_1} \mathcal{S}_{NL}(\sigma_k) \otimes \mathcal{S}_{NL}(\sigma_k) \\
\tilde{\mathcal{S}}_L(\sigma_k) &= (1 + 2a_2 V_{NL}) \mathcal{S}_{NL}(\sigma_k) + a_2 \mathcal{S}_{NL}(\sigma_k) \otimes \mathcal{S}_{NL}(\sigma_k).
\end{aligned} \tag{2.16}$$

The division of equation (2.15) by a constant has no impact on the calibrated radiance calculation, as the constant is included in all numerator and denominator terms of the calibration equation, and reduces to one:

$$\begin{aligned}
L_S(\sigma_k) &= (L_H(\sigma_k) - L_C(\sigma_k)) \operatorname{Re} \left\{ \frac{\tilde{\mathcal{S}}_S(\sigma_k) - \tilde{\mathcal{S}}_C(\sigma_k)}{\tilde{\mathcal{S}}_H(\sigma_k) - \tilde{\mathcal{S}}_C(\sigma_k)} \right\} + L_C(\sigma_k) \\
&= (L_H(\sigma_k) - L_C(\sigma_k)) \operatorname{Re} \left\{ \frac{\frac{\mathcal{S}_S(\sigma_k)}{c_1} - \frac{\mathcal{S}_C(\sigma_k)}{c_1}}{\frac{\mathcal{S}_H(\sigma_k)}{c_1} - \frac{\mathcal{S}_C(\sigma_k)}{c_1}} \right\} + L_C(\sigma_k) \\
&= (L_H(\sigma_k) - L_C(\sigma_k)) \operatorname{Re} \left\{ \frac{\mathcal{S}_S(\sigma_k) - \mathcal{S}_C(\sigma_k)}{\mathcal{S}_H(\sigma_k) - \mathcal{S}_C(\sigma_k)} \right\} + L_C(\sigma_k).
\end{aligned} \tag{2.17}$$

Consequently, the explicit notation of $\tilde{\mathcal{S}} = \mathcal{S}/c_1$ is not necessary, and for simplicity the mathematical formulation for performing the nonlinearity correction is written as:

$$\mathcal{S}_L(\sigma_k) = (1 + 2a_2 V_{NL}) \mathcal{S}_{NL}(\sigma_k) + a_2 \mathcal{S}_{NL}(\sigma_k) \otimes \mathcal{S}_{NL}(\sigma_k). \tag{2.18}$$

The nonlinearity correction needs to be applied prior to radiometric calibration. Furthermore, Eq. (2.18) can be used to determine the nonlinearity coefficient a_2 from the out-of-band region of the spectrum. In the low frequency out-of-band region where the quadratic nonlinearity produces a spectral artifact, the linear interferogram and associated linear spectrum are zero, and Eq.(2.18) can be re-arranged to define a_2 :

$$\begin{aligned}
0 &= (1 + 2a_2V_{NL})S_{NL}(\sigma_k) + a_2S_{NL}(\sigma_k) \otimes S_{NL}(\sigma_k) \\
0 &= S_{NL}(\sigma_k) + a_2[2V_{NL}S_{NL}(\sigma_k) + S_{NL}(\sigma_k) \otimes S_{NL}(\sigma_k)] \\
a_2 &= \frac{-S_{NL}(\sigma_k)}{2V_{NL}S_{NL}(\sigma_k) + S_{NL}(\sigma_k) \otimes S_{NL}(\sigma_k)}.
\end{aligned} \tag{2.19}$$

As evident in Eq. (2.19), the DC level needs to be accounted for when characterizing a_2 from the out-of-band response. To simplify the out of band determination of a_2 , the nonlinearity coefficient can be approximated by the ratio of the measured nonlinear spectrum to the autocorrelation of the measured nonlinear spectrum,

$$a_2' = \frac{-S_{NL}(\sigma_k)}{S_{NL}(\sigma_k) \otimes S_{NL}(\sigma_k)}, \tag{2.20}$$

where a_2' is the first order approximation for the nonlinearity coefficient. This approximation is acceptable for small nonlinearities (<2%), but can affect the accuracy of the determination of the nonlinearity coefficient for detectors with a more significant nonlinear response. For highly nonlinear detectors Eq. (2.19) can be used to determine the nonlinearity coefficient a_2 , with DC level information provided by measurement or model. Alternatively, a correction for the approximation provided in Eq. (2.20) can be defined by combining Eq. (2.20) and Eq. (2.19) [117-119]:

$$\begin{aligned}
0 &= (1 + 2a_2V_{NL})S_{NL}(\sigma_k) + a_2S_{NL}(\sigma_k) \otimes S_{NL}(\sigma_k) \\
0 &= \frac{(1 + 2a_2V_{NL})S_{NL}(\sigma_k)}{S_{NL}(\sigma_k) \otimes S_{NL}(\sigma_k)} + a_2 \\
0 &= -a_2'(1 + 2a_2V_{NL}) + a_2 \\
0 &= -a_2' + (1 - 2a_2'V_{NL})a_2 \\
a_2 &= \frac{a_2'}{1 - 2a_2'V_{NL}}.
\end{aligned} \tag{2.21}$$

AC coupled preamplifiers are normally used with photoconductive and photovoltaic photodiode detectors. Additionally, consideration of quantization error associated with the finite resolution of analog to digital converters makes the use of DC coupled preamplifiers in interferometric applications prohibitive due to the relative size of the DC and AC signals. With the detector connected to a DC coupled preamplifier the signal for a typical interferogram consists of a DC component generally proportional to the average incident intensity; an AC component ranging from near zero away from the interferogram centerburst to a large fraction of the DC radiance component near the interferogram centerburst, assuming reasonable modulation efficiency; and the DC electrical bias level for zero incident intensity, which can be 5-10 times larger than the DC radiance

component [105]. When ADC digitization is applied to the DC coupled signal, the AC component of interest could span less than 10% of the ADC range, resulting in much larger quantization errors of the modulated signal than those associated with the digitization of an AC coupled signal for the same scene intensity. For an AC coupled preamplifier, the DC signal level is not available.

In addition to accurate parameterization of the nonlinearity coefficient, the unfiltered interferogram and DC level information are required for accurate application of the nonlinearity correction algorithm. The total measured signal, including DC and AC components, defines the position of the measured signal on the nonlinear response curve. If an AC coupled pre-amplifier is used and the DC level is not measured via additional electronics and output to the data stream, a DC level model is required.

The DC level can be estimated from the AC signal if the modulation efficiency and instrument self-emission are known. The UW-SSEC DC level model developed for the CrIS instrument is provided in Eq. (2.22) [120, 121]. The model includes a scene dependent contribution that depends on the incident integrated photon flux and an instrument offset term. For CrIS, the instrument offset term is estimated using the integrated photon flux for the deep space view.

$$V_{DC} = \underbrace{e_m^{-1} \frac{2}{N} \int_{\sigma_{\min}}^{\sigma_{\max}} |\mathcal{S}_{scene}(\sigma_k) - \mathcal{S}_{space}(\sigma_k)| d\sigma_k}_{V_{scene}} + \underbrace{e_m^{-1} \tilde{k} \cdot \frac{2}{N} \int_{\sigma_{\min}}^{\sigma_{\max}} |\mathcal{S}_{space}(\sigma_k)| d\sigma_k}_{V_{instrument}}. \quad (2.22)$$

In Eq. (2.22), \mathcal{S}_{scene} is the complex measured spectrum of the scene for which the DC level is to be estimated. The scene can be an Earth, Internal Calibration Target (ICT), or deep space (DS) view. \mathcal{S}_{space} is the complex measured spectrum of deep space view acquired nearest in time to \mathcal{S}_{scene} , \tilde{k} is an empirically determined constant, σ_{\min} and σ_{\max} are the optical bandpass limits of the instrument responsivity for the respective detector, e_m is a scalar estimate of the modulation efficiency, and N is the number of points in the undecimated interferogram. Data reduction for the CrIS instrument is accomplished via numerical filtering and decimation. The frequency response of the numerical filter has been removed from \mathcal{S}_{scene} and \mathcal{S}_{space} in Eq. (2.22).

The model assumes that the modulation efficiency can be estimated by:

$$e_m = \frac{\frac{2}{N} \int_{\sigma_{\min}}^{\sigma_{\max}} |\mathcal{S}_{scene}(\sigma_k) - \mathcal{S}_{space}(\sigma_k)| d\sigma_k}{V_{DC,scene} - V_{DC,space}}, \quad (2.23)$$

where $V_{DC,scene}$ is the DC level for the interferogram of the scene with complex spectrum \mathcal{S}_{scene} , and $V_{DC,space}$ is the DC level of the interferogram for the deep space view measurement (with measured spectrum \mathcal{S}_{space}). As in Eq. (2.22), the frequency response of the numerical filter has been removed from \mathcal{S}_{scene} and \mathcal{S}_{space} in Eq. (2.23).

2.3 Determining the required linearity

It is desirable to define an acceptable limit for nonlinear response. Given the results of the radiometric uncertainty analysis for the on-orbit calibration reference configuration and environment, the limit on the nonlinearity contribution to the radiometric uncertainty can be defined. The combined calibration and calibration verification uncertainty estimate was used for this analysis. Accordingly, the root sum of squares of the combined radiometric uncertainty determined in Chapter 1, and the modelled calibration bias due to nonlinearity should be less than 0.1 K. An example of the result at 600 cm^{-1} is shown in Figure 24. The total combined calibration and calibration validation uncertainty (as presented in Chapter 1) is shown in blue, and the maximum allowable radiometric uncertainty due to nonlinearity is indicated in red.

A simple model for a calibration bias due to nonlinearity was utilized [122]. The effect of nonlinearity was applied directly to the calibrated radiance, rather than the individual scene and calibration reference measurements. The model employs a quadratic nonlinear behaviour for the calibrated radiance bias, with zero bias when the scene radiance is equal to either reference radiance. The result for 0.03% nonlinearity at 600 cm^{-1} is shown in Figure 25. The model results indicated that the residual nonlinearity, expressed as a percentage error in the calibrated radiance, should be limited to less than 0.03% when considering a range of scene temperatures from 230 – 320 K, and wavenumber range of 200 – 2600 cm^{-1} . The results for a representative set of wavenumbers are provided in Figure 26. Due to the nature of the calibration equation, which employs a ratio of differences of raw measurements, a given percentage error in the calibrated radiance due to nonlinearity is associated with a significantly higher percentage error in the individual raw measurements. However, a conservative approach was applied, and when characterizing the nonlinearity via the low wavenumber region out-of-band analysis, the 0.03% requirement was applied directly for the raw measurements. A detector response displaying less than 0.03% nonlinearity will not require nonlinearity correction. Similarly, if nonlinearity correction is needed, the residual nonlinearity after correction should satisfy the 0.03% requirement.

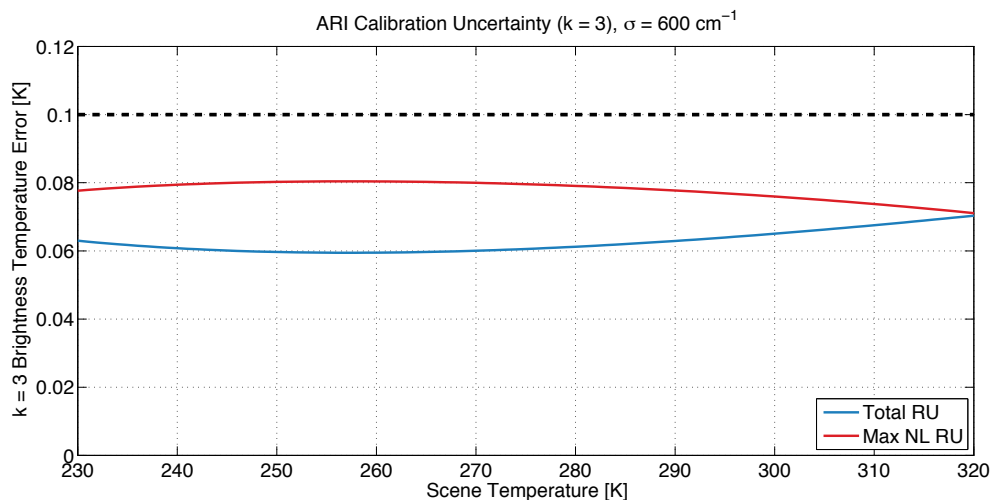


Figure 24: The 0.1 K requirement and the predicted radiometric uncertainty (Total RU, blue) derived in Chapter 1 can be used to determine the allowable radiometric uncertainty (Max NL RU, red) due to nonlinearity.

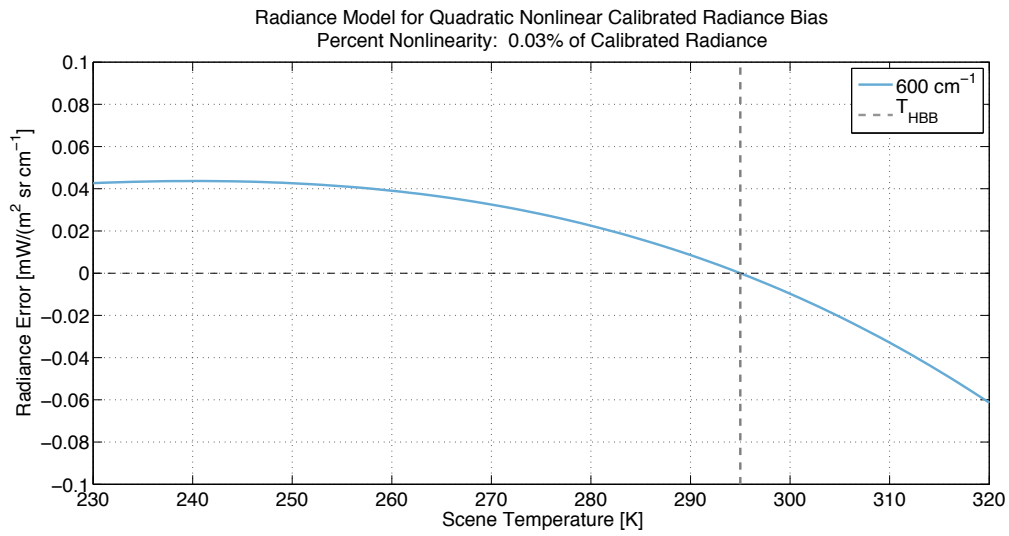


Figure 25: For the model, the effect of nonlinearity was applied directly to the calibrated radiance, rather than the individual scene and calibration reference measurements. The model employs a quadratic nonlinear behaviour for the calibrated radiance bias, with zero bias when the scene radiance is equal to either reference radiance [122].

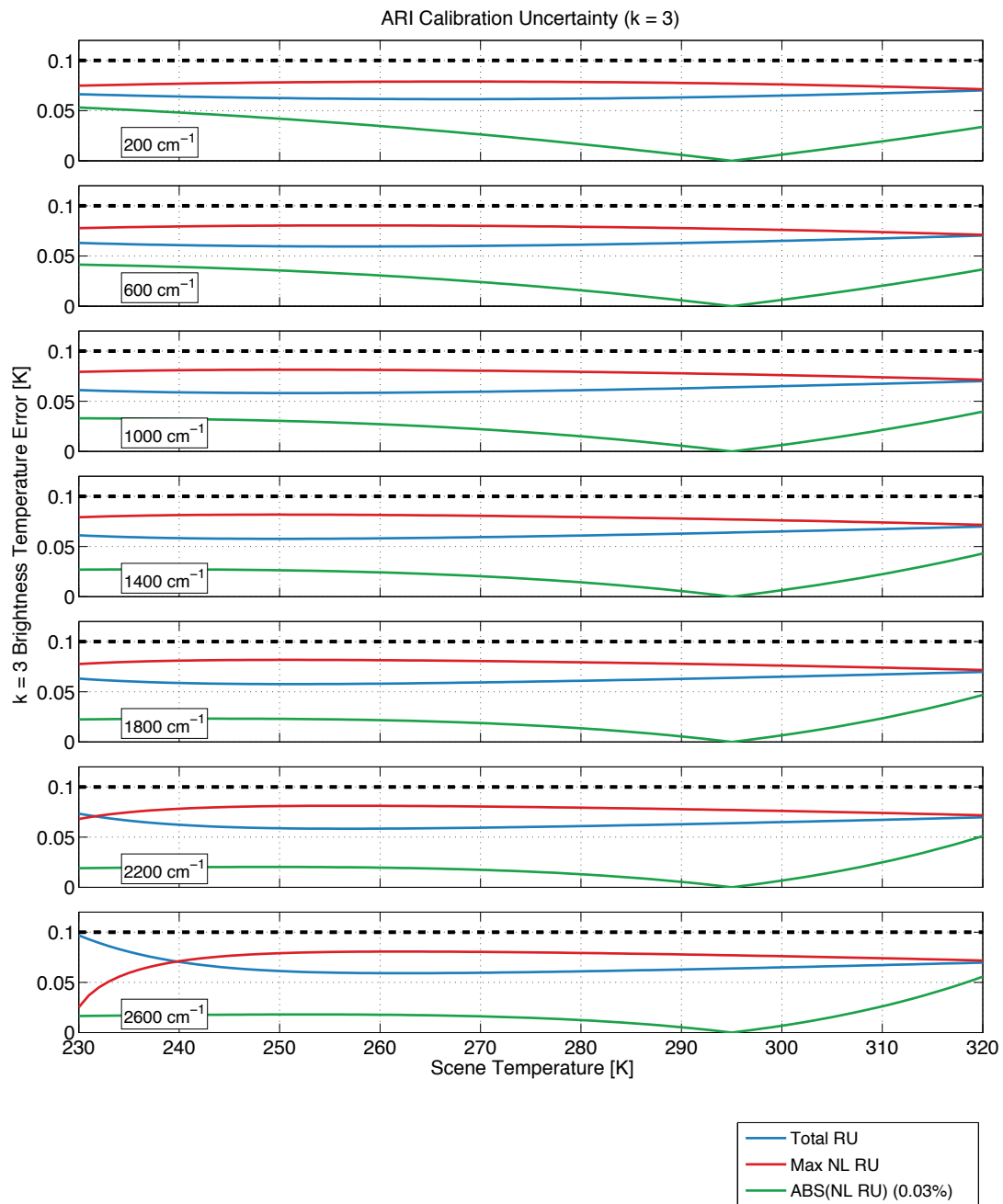


Figure 26: The model results indicated that the residual nonlinearity, expressed as a percentage error in the calibrated radiance, should be limited to less than 0.03% when considering a range of scene temperatures from 230 – 320 K, and wavenumber range of 200 – 2600 cm^{-1} .

2.4 Nonlinear response and correction in the ARI prototype

Due to the high radiometric accuracy requirements associated with climate trend detection in the infrared, it is desirable to emphasize linearity rather than sensitivity during detector selection for the flight instrument. It is equally important to ensure that the signal chain electronics are designed to provide a highly linear response.

For photoconductive detectors, the linearity advantages of current-mode preamplifiers that bias the detector with a constant voltage are well documented [25, 100, 123, 124]. A final consideration is the optical bandpass for any given detector. Referring to Figure 22, it is clear that given sufficient sampling (to avoid aliasing out-of-band artifacts in-band) and a primarily quadratic nonlinearity, restricting the detector bandpass to less than one octave avoids overlap of the quadratic nonlinearity spectral artifacts with the range of interest.

Due to cost and schedule considerations associated with the demonstration effort, readily available commercial options were selected for the signal chain electronics for both detector systems. A commercial off-the-shelf (COTS) deuterated triglycine sulfate (DTGS) pyroelectric detector module was procured for the far infrared (FIR) output, and an existing UW-SSEC detector and dewar assembly was used for the infrared output. The existing UW-SSEC detector dewar assembly houses a shortwave Indium Antimonide (InSb), and three photoconductive Mercury Cadmium Telluride detectors providing spectral coverage from 420 – 3300 cm^{-1} (extended long-wave (ELW) MCT: 400 – 1600 cm^{-1} , long-wave (LW) MCT: 550 – 1700 cm^{-1} , midwave (MW) MCT: 800 – 1820 cm^{-1} , (SW) shortwave InSb: 1820 – 3300 cm^{-1}). The commercial electronics are limited to two detector channels, and the long-wave (LW MCT) and FIR DTGS detectors were used for the ARI IIP demonstration.

2.4.1 Nonlinearity characterization via out-of-band response

The in-band and low wavenumber out-of-band signal, is shown in Figure 27 for the DTGS detector, and in Figure 28 for the LW MCT detector. The spectra correspond to the mean raw measurements of the OARS at approximately 217 K for data collected under vacuum. The mean spectra have been normalized to the maximum in-band signal in these figures. The plots show the real component of the spectra, and the corresponding mean interferograms have been circularly shifted such that the zero path difference maxima is centered within the interferogram vector prior to Fourier transformation to spectral space. The centered interferogram has been apodized to minimize ringing associated with potential DC discontinuities due to the circular shift. A Hamming apodization with a full-width equal to the length of the interferogram was used. Since a shift in the interferogram domain is the equivalent of a phase rotation in the spectral domain, centering the zero path difference maxima minimizes the phase, and imaginary component, in the spectral domain. Due to the finite optical path difference and asymmetry of the measured interferogram, the phase of the spectrum will not be identically zero even after centering of the ZPD sample within the interferogram. However, as evident in Figure 27 and Figure 28, the remaining imaginary component in the low wavenumber out-of-band region is negligible and using the real component of the spectra after ZPD centering is acceptable for the out-of-band determination of the nonlinearity coefficient. This method is preferable to using the magnitude of the spectrum due to the extremely low signal to noise in the out-of-band nonlinearity signature, and the rectification in the low signal to noise regions when taking the magnitude of the spectrum.

Referring to Figure 27, it is clear that the DTGS detector response, including signal chain electronics, is very linear. While the fit for the quadratic nonlinearity coefficient a_2' is non-zero, the low wavenumber out-of-band response shows no discernable nonlinearity artifact. Thus, the DTGS response is expected to be sufficiently linear, to less than 0.03%.

Conversely, it is clear from Figure 28 that the LW PC MCT detector used in the ARI prototype is significantly nonlinear, with a low wavenumber out-of-band quadratic nonlinearity of the order of 0.25% of the in-band peak signal. Consequently, a nonlinearity correction is required for the LW MCT.

As a sidebar, 200 Hz (100 cm^{-1} at 2 cm/sec interferometer sweep speed) noise is clearly evident in-band for the DTGS in Figure 27. In addition to the 200 Hz noise, 60 Hz harmonics (30 cm^{-1} at 2 cm/sec scan speed) are evident out-of-band for the LW MCT in Figure 28. These noise features are also evident in the in-band noise equivalent spectral radiance (NESR). The noise is removed by sufficiently long averages and calibration, and did not impact the prototype demonstration. The noise will be resolved for future versions of the instrument, and with sufficient resources, the instrument team is confident that the noise can be eliminated from the current ARI prototype as well. In fact, testing, implementation, and optimization of a new grounding and shielding scheme during pre-vacuum preparation had significantly improved the noise performance, eliminating the majority of the noise spikes present in the data collected during the IIP phase. The main issues were related to interconnecting subsystems for which the instrument team did not have full control of the design; including the interferometer, Stirling cooler, motor controller, and detector electronics. Unfortunately, despite the new grounding and shielding scheme and improved pre-vacuum performance, the noise features were present during vacuum testing.

Figure 29 (DTGS) and Figure 30 (LW MCT) show the out-of-band response for a range of blackbody source temperatures for data acquired under vacuum. The DTGS results do not show any clear out-of-band quadratic nonlinearity, and the signal in this spectral region is dominantly noise. The LW MCT results indicate a range of values for the first order approximation of the nonlinearity coefficient (a_2').

It is important to note that the output of a 4-port Fourier transform spectrometer is proportional to the difference of the fringe signals coming from the two input ports. An ambient, high emissivity cavity is used as the second input port reference for the ARI. Thus, the magnitude of the detected signal is proportional to the difference between the incident radiance at the first input port and the ambient radiance at the second port, and as the effective brightness temperature of the scene approaches the ambient temperature of the second port reference, the measured signal approaches zero. For low intensity signals, the out-of-band characterization of the nonlinearity becomes less certain. While the DTGS detector exhibits a very linear response, the impact of increased uncertainty for low level signals is still evident in the out of family results in the fit for the nonlinearity coefficient (a_2') for the DTGS detector with blackbody sources at 272 K and 293 K (Figure 29). The LW MCT detector has a significantly non-linear response and larger out-of-band artifact, but the behavior is also evident in the LW MCT results in Figure 30 for the 293 K blackbody and to a lesser extent, the 272 K blackbody. The out-of-band estimates and corrected values (per Eq. (2.21)) for the LW MCT are tabulated in Table 7. Omitting the 293 K case, the nonlinearity coefficient, as determined from the low wavenumber out-of-band artifact ranges from 0.0142 to 0.0189.

Table 7: Quadratic nonlinearity coefficient characterization via low wavenumber out-of-band analysis for the LW MCT.

OARS Temperature [K]	Quadratic Nonlinearity Coefficient	
	Out of Band Approximation	Corrected Value (Eq. (2.21))
217.58	0.0163	0.0162
232.66	0.0164	0.0163
252.79	0.0153	0.0152
272.92	0.0143	0.0142
292.58	0.0739	0.0762
313.16	0.0190	0.0189
333.16	0.0185	0.0184

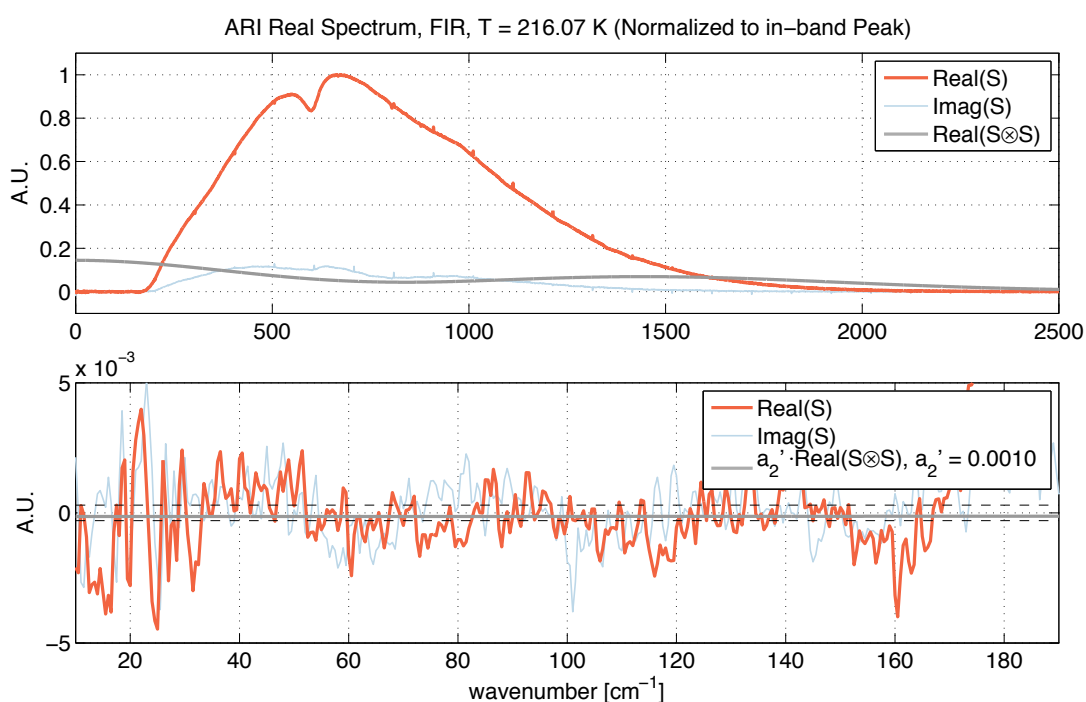


Figure 27: DTGS measured signal, normalized to the in-band peak for a 216.07 K target. The top panel shows the real spectrum (red), the imaginary component of the spectrum (light blue), and the shape of the quadratic nonlinearity (grey). The bottom panel illustrates the low wavenumber out-of-band signal from 0 – 200 cm⁻¹, and the fit for the quadratic nonlinearity. The wavenumber range for the fit region is 40 – 160 cm⁻¹. The dashed lines in the bottom panel indicate ±0.03%.

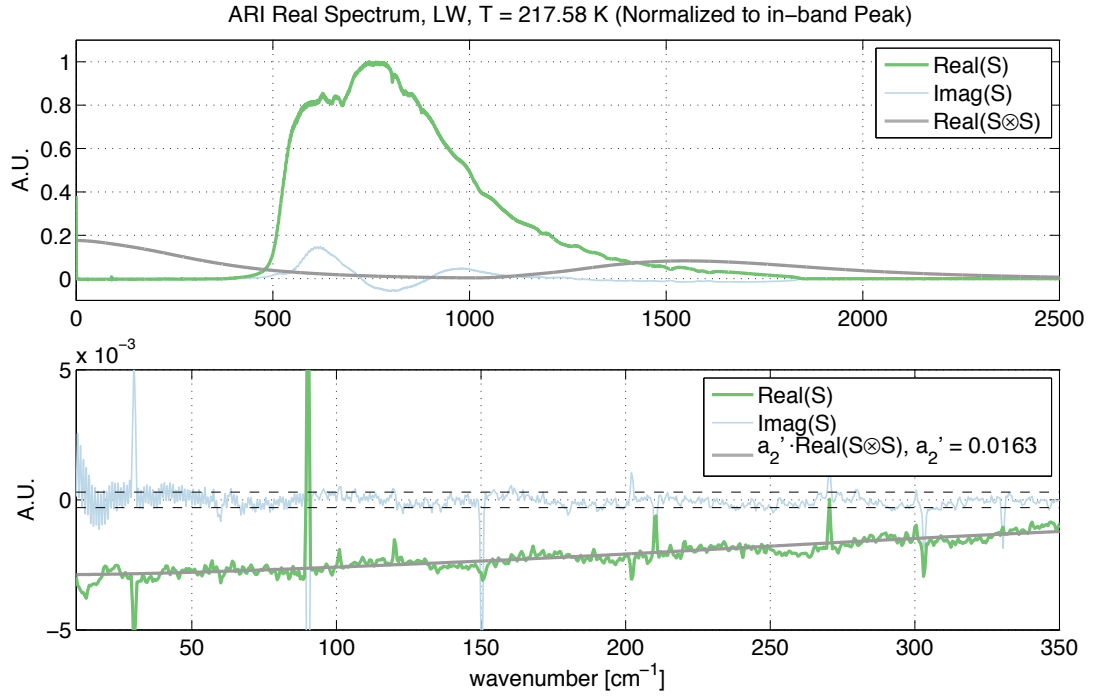


Figure 28: LW MCT measured signal, normalized to the in-band peak for a 216.07 K target. The top panel shows the real spectrum (green), the imaginary component of the spectrum (light blue), and the shape of the quadratic nonlinearity (grey). The bottom panel illustrates the low wavenumber out-of-band signal from 0 – 300 cm^{-1} , and the fit for the quadratic nonlinearity. The wavenumber range for the fit region is 25 – 300 cm^{-1} , and the 60 Hz spikes have been excluded from the fit data. The dashed lines in the bottom panel indicate $\pm 0.03\%$.

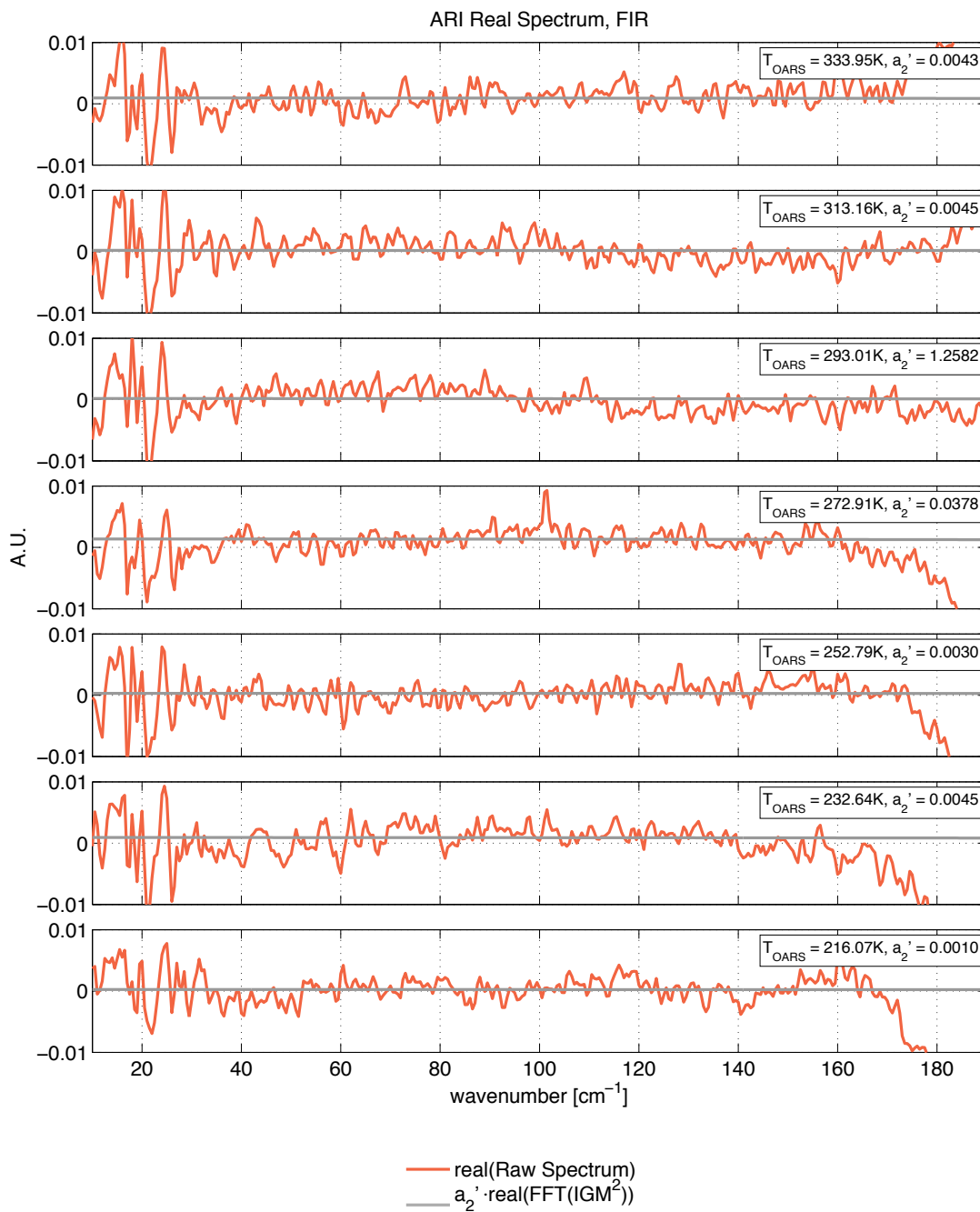


Figure 29: DTGS low wavenumber out-of-band signal for a range of blackbody temperatures. The real spectrum is indicated in red, and the fit for the quadratic nonlinearity is shown in grey. The wavenumber range for the fit is 40 – 160 cm^{-1} .

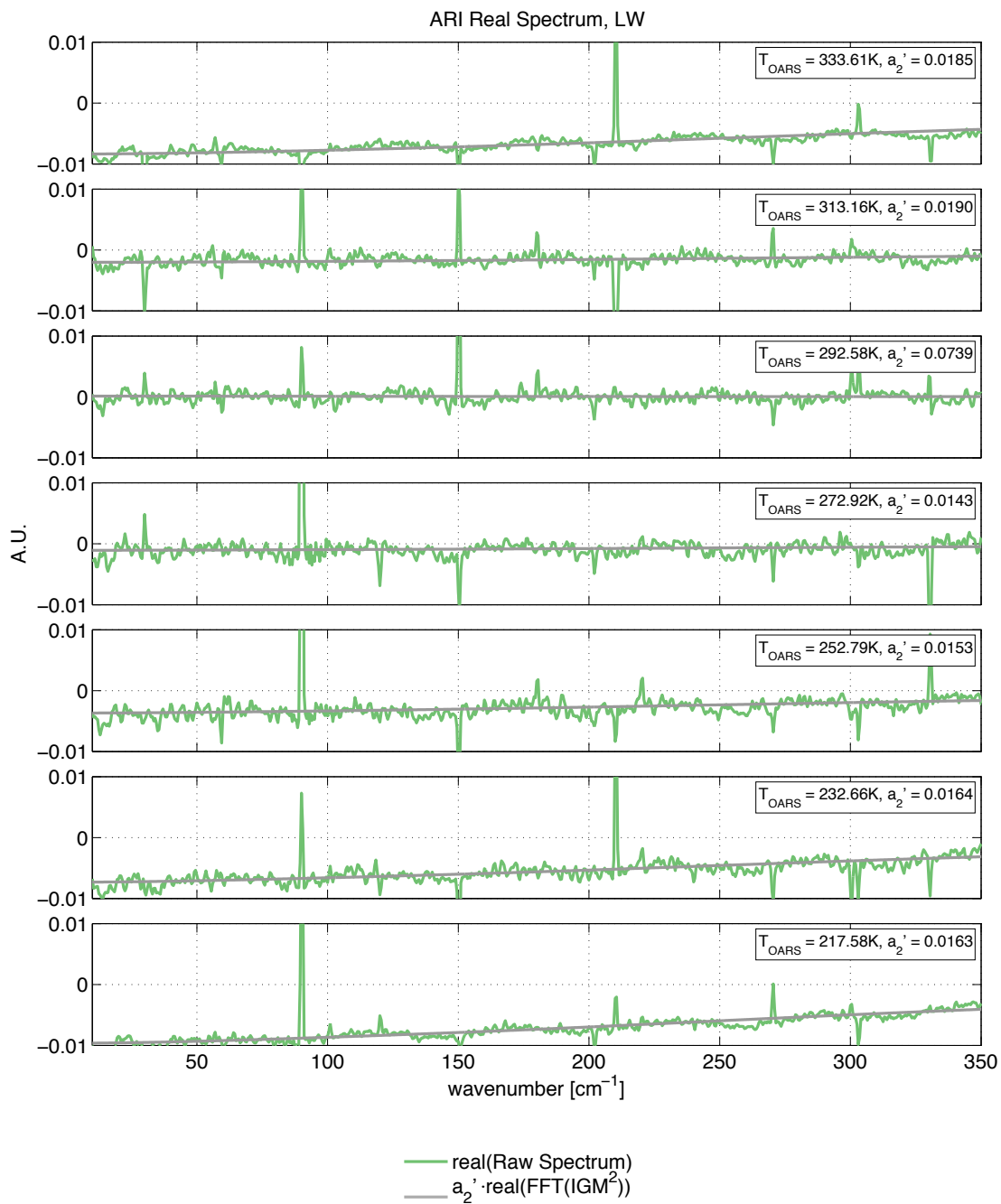


Figure 30: LW MCT low wavenumber out-of-band signal for a range of blackbody temperatures. The real spectrum is indicated in green, and the fit for the quadratic nonlinearity is indicated in grey. The wavenumber range for the fit is 25 – 300 cm^{-1} , and the 60 Hz spikes have been excluded from the fit data.

2.4.2 Nonlinearity correction for the ARI long-wave detector

As noted earlier in the chapter, the unfiltered interferogram and DC level data are required for accurate application of a nonlinearity correction algorithm. In the ARI, no decimation or filtering is applied to the measured interferograms and the raw interferogram is output in the standard data stream. This is critical for thorough assessment of the system linearity. Unfortunately, the commercial electronics used in the ARI prototype do not support the output of the DC level information and a DC level model is required.

The second order nonlinearity correction formulation described in Eq. (2.18) was used for nonlinearity correction of the ARI LW detector response, and the DC level model implemented for the ARI prototype is based on the UW-SSEC DC level model developed for the CrIS instrument, provided in Eq. (2.22). The equations are reproduced here:

$$S_L(\sigma_k) = (1 + 2a_2V_{NL})S_{NL}(\sigma_k) + a_2S_{NL}(\sigma_k) \otimes S_{NL}(\sigma_k). \quad (2.18)$$

$$V_{DC} = e_m^{-1}F \underbrace{\int_{\sigma_{\min}}^{\sigma_{\max}} |S_{scene}(\sigma_k) - S_{space}(\sigma_k)| d\sigma_k}_{V_{scene}} + e_m^{-1}\tilde{k} \cdot F \underbrace{\int_{\sigma_{\min}}^{\sigma_{\max}} |S_{space}(\sigma_k)| d\sigma_k}_{V_{instrument}}. \quad (2.22)$$

For the CrIS instrument, a deep space measurement for both interferometer sweep directions is collected each calibration cycle, and a calibration cycle is completed for each cross-track scan of the Earth. Thus, variations of the instrument emission associated with fluctuations in instrument temperature, and the corresponding contribution to the DC offset, are properly accounted for.

During laboratory and vacuum testing of the ARI prototype a deep space view is not available, and a measurement of a liquid nitrogen reference blackbody is used to emulate the space view. It is not practical to include a liquid nitrogen blackbody view for all ARI data collects. Furthermore, a liquid nitrogen blackbody reference was not available for vacuum testing. Thus, the measurements from a separate data collection of the liquid nitrogen blackbody and calibration references are used to form the emulated space view for all ARI datasets.

The ARI zero path difference (ZPD) position is determined during the initialization sequence that occurs when the instrument powered on. The ZPD position determination is approximate and based on a mechanical sequence. Accordingly, the ZPD position within the acquired interferogram will vary slightly between data collects that are separated by instrument power cycles. As a result, the liquid nitrogen blackbody measurement needs to be adjusted for differences in phase, in addition to differences in responsivity and offset between the liquid nitrogen blackbody data collection and the dataset for which the DC levels are being determined. To derive the required correction for differences in phase, responsivity, and offset between the liquid nitrogen data collection and the data collection for which the simulated space view is required, we consider two datasets of identical scenes, but different instrument responsivities, offsets, and ZPD position:

$$L = (L_{H_1} - L_{C_1}) \frac{S_1 - S_{C_1}}{S_{H_1} - S_{C_1}} - L_{C_1}, \quad (2.24)$$

$$L = (L_{H_2} - L_{C_2}) \frac{S_2 - S_{C_2}}{S_{H_2} - S_{C_2}} - L_{C_2} . \quad (2.25)$$

In equations (2.24) and (2.25) L is the predicted radiance for a Lambertian, non-ideal blackbody (defined in Eq. (1.2)); S is the complex measured spectra; the subscripts H and C refer to the hot and cold references, respectively; and the subscripts 1 and 2 identify the two data collections. Combining equations (2.24) and (2.25), a relationship between the two measurements, S_1 and S_2 , of the identical scene radiance L can be derived:

$$S_2 = \mathbb{R}_2 \left[\frac{S_1 - S_{C_1}}{\mathbb{R}_1} + L_{C_1} - L_{C_2} \right] + S_{C_2} . \quad (2.26)$$

Thus the simulated space view S'_{space} for a given dataset can be estimated from the liquid nitrogen blackbody data collection:

$$S'_{space} = \mathbb{R} \left[\frac{S_{LN} - S_{C_{LN}}}{\mathbb{R}_{LN}} + L_{C_{LN}} - L_C \right] + S_C , \quad (2.27)$$

where the subscript LN denotes the liquid nitrogen data collect, \mathbb{R} is the complex responsivity for the data collection for which the simulated space view is required, and \mathbb{R}_{LN} is the responsivity for the liquid nitrogen blackbody data collection,

$$\mathbb{R} = \frac{S_H - S_C}{L_H - L_C} , \quad (2.28)$$

$$\mathbb{R}_{LN} = \frac{S_{H_{LN}} - S_{C_{LN}}}{L_{H_{LN}} - L_{C_{LN}}} . \quad (2.29)$$

Replacing the space view term of the CrIS model with the simulated space view for ARI defined in Eq. (2.27), the ARI DC level model can be explicitly defined:

$$V_{DC} = \underbrace{e_m^{-1} \frac{2}{N} \int_{\sigma_{\min}}^{\sigma_{\max}} |S_{scene}(\sigma_k) - S'_{space}(\sigma_k)| d\sigma_k}_{V_{scene}} + \underbrace{e_m^{-1} \tilde{k} \cdot \frac{2}{N} \int_{\sigma_{\min}}^{\sigma_{\max}} |S'_{space}(\sigma_k)| d\sigma_k}_{V_{instrument}} . \quad (2.30)$$

Note that in (2.30), a scalar estimate is still used for the modulation efficiency and this value includes the factor of two required when considering the intensity from the two input ports is split between the two output ports (i.e. the maximum modulation efficiency is 0.5, and not 1 as often expressed). Based on modulation efficiency model data provided by the interferometer vendor [125], a value of 0.425 (0.85/2) has been used for the scalar estimate of the modulation efficiency For the ARI, which is a four port system with a infrared beam footprint that provides near full illumination of the LW MCT detector, $\tilde{k} = 1$ is appropriate.

2.4.2.1 In-band optimization of the quadratic nonlinearity coefficient

In addition to the out-of-band characterization, the quadratic nonlinearity coefficient for the ARI LW MCT detector was also determined via a nonlinear least squares optimization of the brightness temperature residuals for a range of OARS temperatures. This analysis was completed for data collected in the laboratory with a dry air purge. The cold temperature limit for the cold reference blackbody and the OARS was bounded by the dew point attainable in this configuration. The cold calibration reference was operated at a temperature 243.2 K, the hot calibration reference at 333.9 K, and data was collected for OARS temperatures of 243.2 K, 253.2 K, 273.1 K, 293.2 K, 313.2 K, and 333.9 K. The objective function for the optimization was formed from the weighted root mean square fit error for all brightness temperature residuals,

$$f(\sigma_k) = \sqrt{\frac{1}{n} \sum_{j=1}^n w_j [(BT_{obs}(\sigma_k) - BT_{pred}(\sigma_k))]^2}, \quad (2.31)$$

In Eq. (2.31), w_j is the weighting factor, $BT_{pred}(\sigma_k)$ is the predicted brightness temperature of the OARS, and $BT_{obs}(\sigma_k)$ is the nonlinearity corrected calibrated brightness temperature, with the minimization completed over a range of a_2 nonlinearity coefficients.

Each brightness temperature residual ($BT_{obs} - BT_{pred}$) is proportionally weighted by the minimum difference between the OARS temperature and the calibration reference temperatures, with a weight range from zero to one. The weighting factor w_j is defined as:

$$w_j = \frac{\tilde{w}_j}{\max(\tilde{w}_1, \dots, \tilde{w}_n)}, \quad (2.32)$$

where,

$$\tilde{w}_j = \min(|T_{OARS} - T_{HBB}|_j, |T_{OARS} - T_{CBB}|_j). \quad (2.33)$$

While the 3dB response frequencies for the LW MCT response are approximately 530 and 1080 cm^{-1} , a spectral range of 550 to 1500 cm^{-1} was used for the optimization such that the portion of the spectrum most strongly sensitive to the squared term of the correction was included. There is sufficient response within these spectral limits for the analysis. The results are shown in Figure 31 and the resulting value for the second order nonlinearity coefficient was 0.0181. This value is within the range of values determined from the out-of-band analysis of the data acquired under vacuum (refer to Table 7).

The relative contributions of the linear and quadratic terms of the nonlinearity correction (Eq. (2.18)) to the hot reference, cold reference, and OARS blackbody are shown in Figure 32. For this particular case, the hot blackbody temperature is 333.93 K, the cold blackbody temperature is 243.18 K, the OARS temperature is 293.16 K, and the instrument temperature is approximately 296 K. The contributions are expressed as a percentage of the raw measurement. The black dashed lines indicate the 3dB points of the responsivity.

It is useful to compare the nonlinearity corrected spectra to the uncorrected spectra in the low wavenumber out-of-band region where the artifact associated with the quadratic nonlinearity is most evident. Figure 33 shows the uncorrected and nonlinearity corrected spectra in this region. For this result, the nonlinearity coefficient determined from the in-band optimization ($a_2 = 0.018$) was used in the nonlinearity correction. While the quadratic nonlinearity coefficient derived from the out-of-band analysis in Section 2.4.1 spans a range of 0.0142 to 0.0189, it is clear in Figure 33 that the out-of-band artifact is near zero after nonlinearity correction using a constant quadratic nonlinearity coefficient of 0.018. Figure 34 shows the uncorrected spectra and the nonlinearity corrected spectra corresponding to quadratic nonlinearity correction coefficients of 0.014 (light orange), 0.020 (dark orange), and the value determined from the out-of-band characterization (dark grey) for each OARS temperature. For this range of quadratic nonlinearity correction coefficients, it is clear that there are only very small differences in the residual out-of-band artifact in the corrected spectra. However, the in-band correction is much more sensitive to small changes in a_2 , since even a small change in a_2 results in a large change in the $(1 + 2a_2V_{NL})S_{NL}(\sigma_k)$ term in the nonlinearity correction due to the typically large value of the DC level.

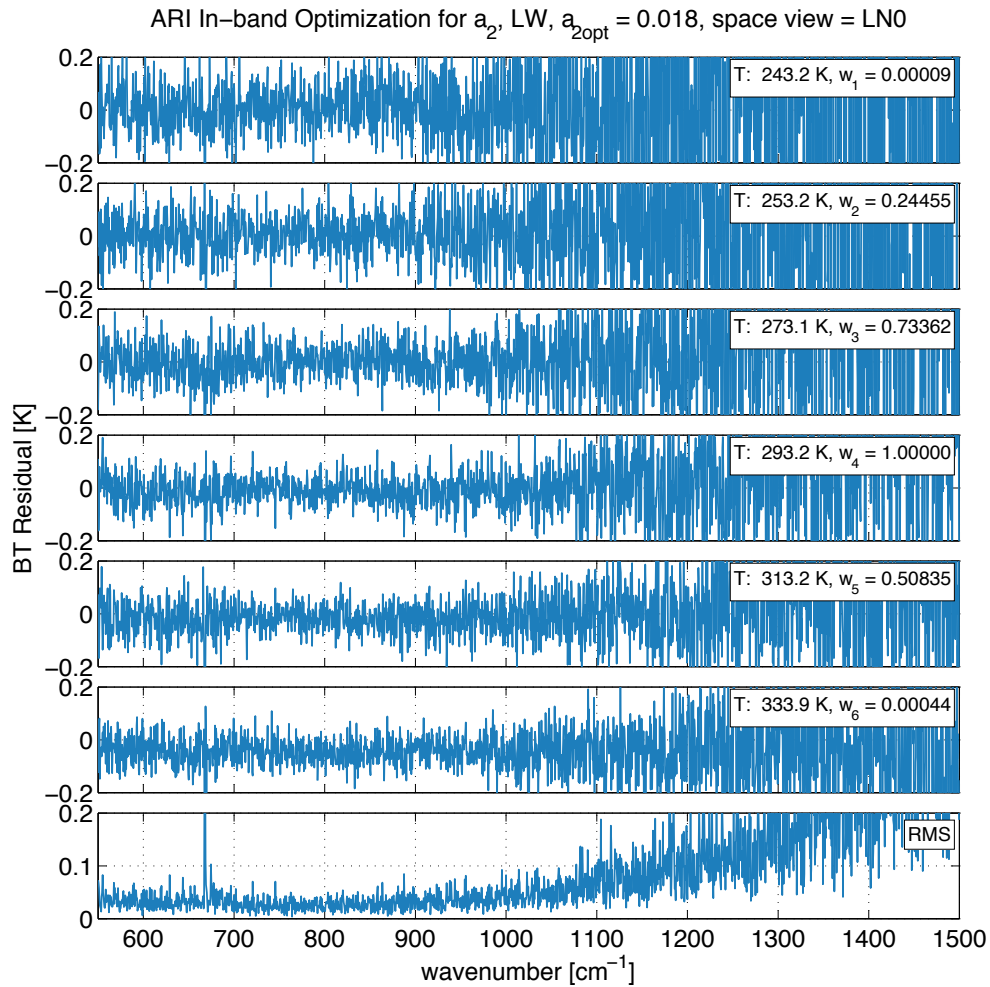


Figure 31: ARI LW MCT results for in-band optimization of the quadratic nonlinearity coefficient. The OARS temperature and fit weight are indicated for each dataset, and the weighted RMS residual used in the optimization is provided in the bottom panel. The cold calibration reference was operated at a temperature 243.2 K, and the hot calibration reference at 333.9 K for all datasets.

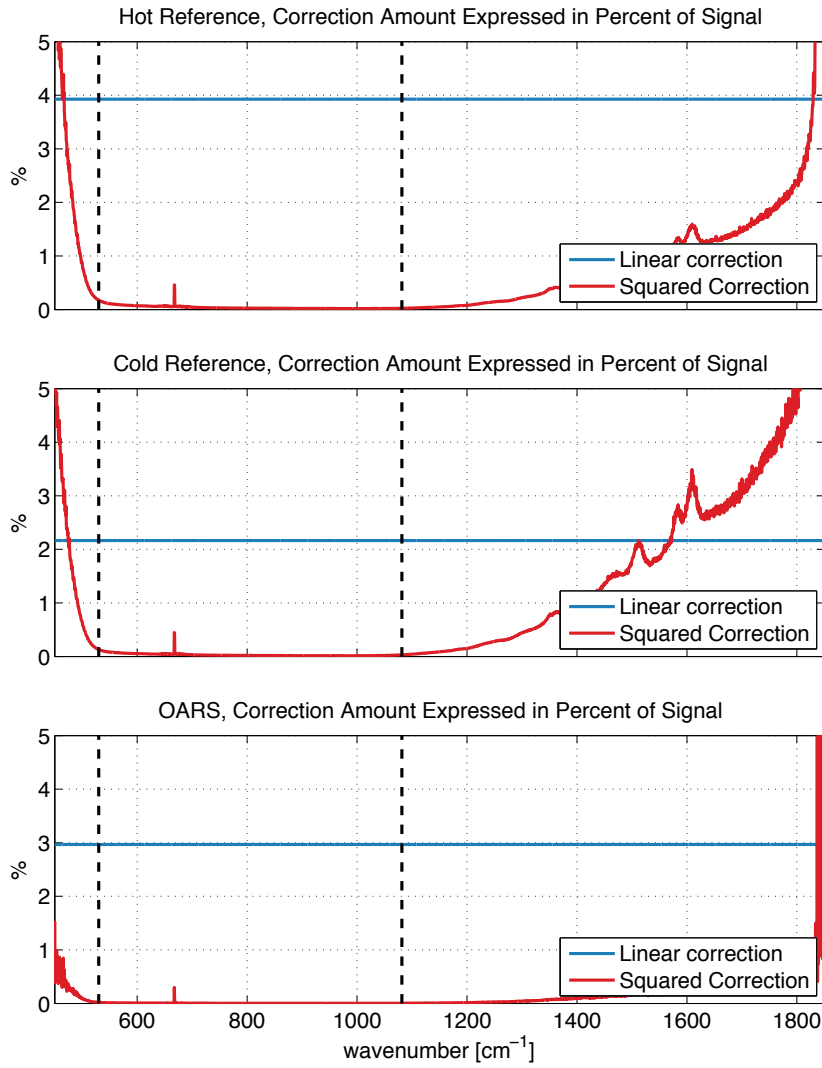


Figure 32: The relative contributions of the linear and quadratic terms of the nonlinearity correction (Eq. (2.18)) to a 333.93 K hot reference blackbody (top panel), a 243.18 K cold reference blackbody (middle panel), and a 293.16 K OARS blackbody (bottom panel) for the LW MCT are shown. For this particular data collection, the instrument temperature is approximately 296 K. The contributions are expressed as a percentage of the raw measurement. The black dashed lines indicate the 3dB points of the responsivity.

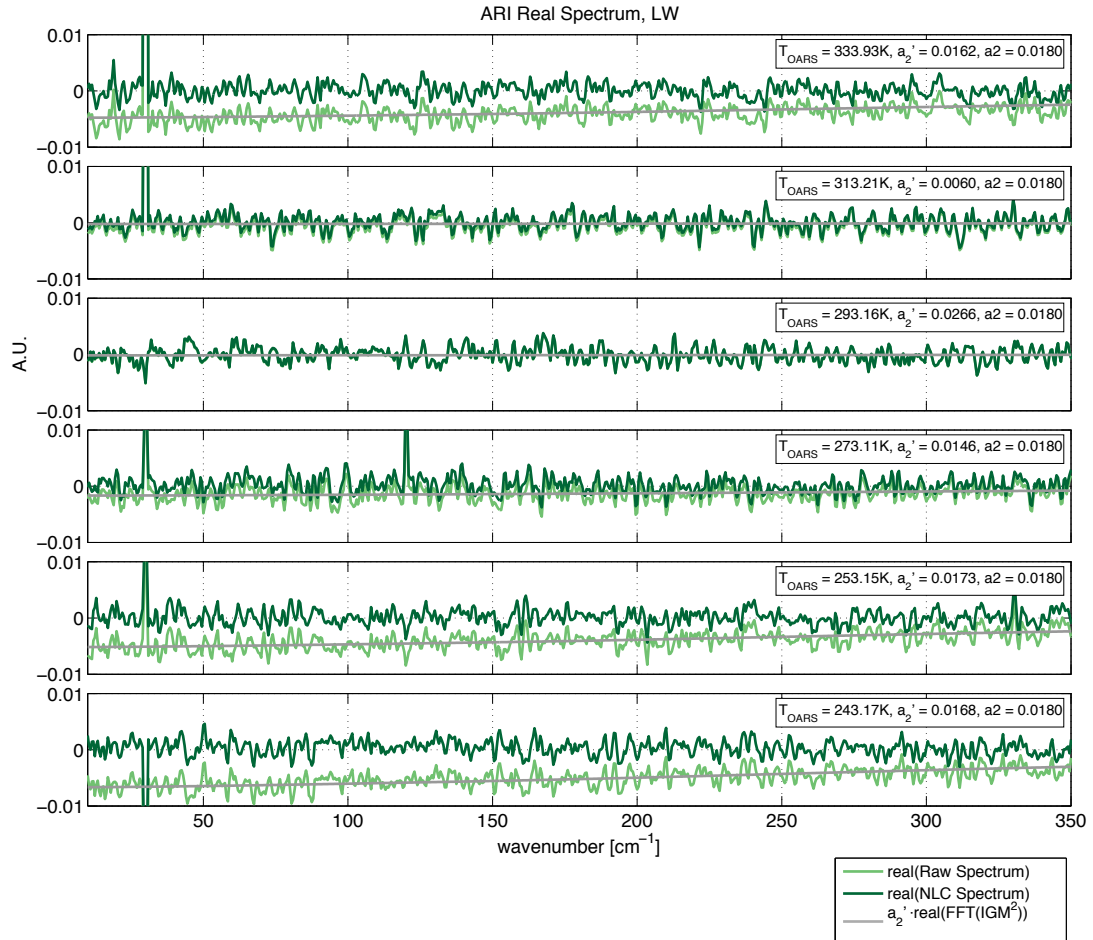


Figure 33: Nonlinearity corrected spectra are indicated in dark green and uncorrected spectra are shown in light green. The low wavenumber out-of-band artifact associated with the quadratic nonlinearity is reduced to near zero for the nonlinearity corrected spectra. The quadratic nonlinearity coefficient determined from the in-band optimization has been used in the nonlinearity correction ($a_2 = 0.018$). The values determined via out-of-band approximation (a_2') for each OARS temperature are also included for reference (see Table 7).

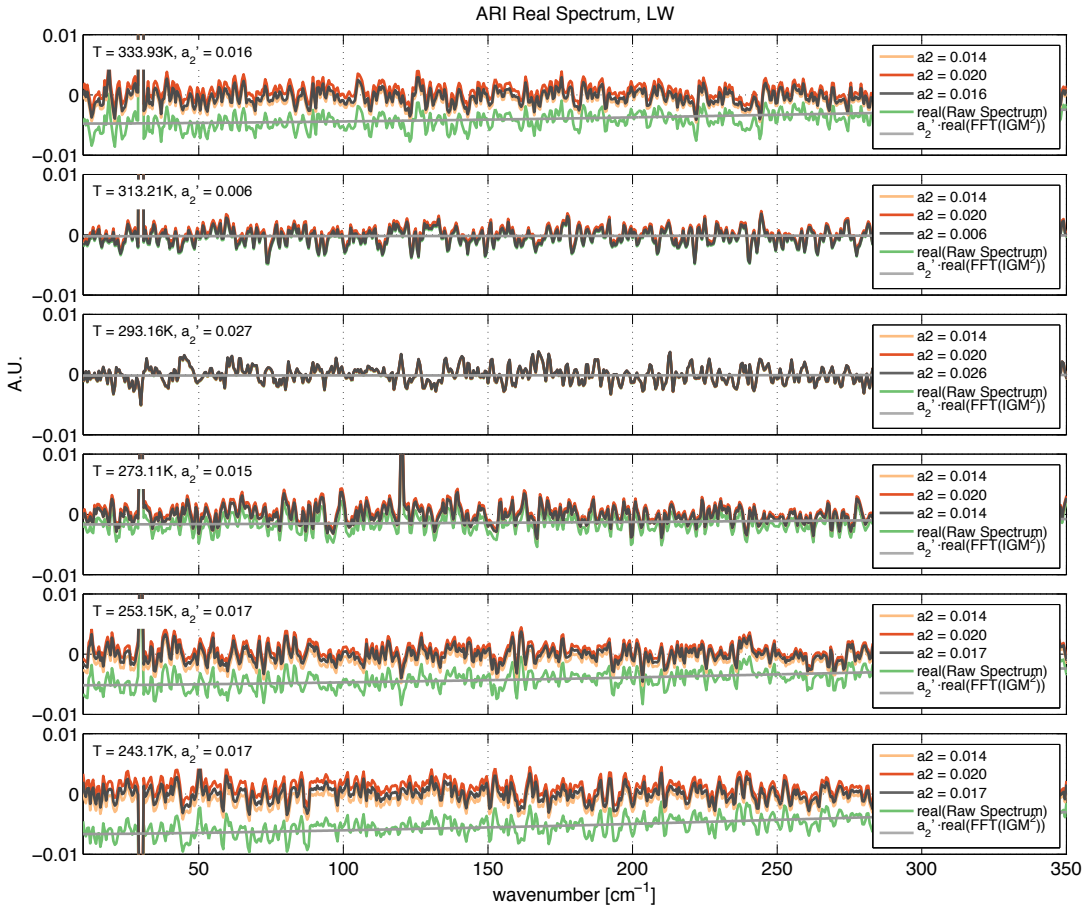


Figure 34: Nonlinearity corrected and uncorrected spectra. Nonlinearity corrected spectra corresponding to quadratic nonlinearity correction coefficients of 0.014 (light orange), 0.020 (dark orange), and the value determined from the out-of-band characterization (dark grey) for each data collection are shown.

2.4.3 Nonlinearity correction verification

One method of test and verification of the nonlinearity correction is to apply the correction to independent ARI data collections of blackbody reference data over a range of target and blackbody reference temperatures.

The full results for the LW MCT data acquired under vacuum, with and without nonlinearity correction, are provided in the final chapter. For the LW MCT data collected under vacuum, the cold calibration reference was operated at a temperature 217.6 K, the hot calibration reference at 300.2 K, and data collections were completed for OARS temperatures of 217.6 K, 232.7 K, 252.9 K, 272.9 K, 292.6, 313.2 K and 333.6 K. To illustrate an example of the nonlinearity correction verification, the result for the 272.9 K OARS dataset is included here in Figure 35. For this dataset, the OARS temperature is roughly midway between the cold and hot reference temperatures, and the error due to nonlinearity is large. The nonlinearity corrected residual is near zero with the spectral region defined by the 3dB responsivity limits, and the residual artifacts are primarily associated with stray-light and were resolved after vacuum testing (refer to Chapter 3 for further details). However, a small residual that increases with wavenumber is present in the spectral region above 1100 cm⁻¹. Using the long-wave 3dB limit of the response to define the long-wave limit of the spectral bandpass ($\lambda_0 = 530$

cm⁻¹), the shortwave limit corresponding to a single octave measurement is at twice the long-wave limit ($\sigma_1 = 2\sigma_0 = 1060 \text{ cm}^{-1}$). In Section 2.1, it was noted that the spectral artifact associated with the quadratic nonlinearity overlaps into the optical bandpass for measurements for which the detection bandpass is greater than one octave. From Figure 32 it is clear that the squared term of the nonlinearity correction begins to become significant for the spectral region outside of the single octave range, which suggests that the residual may be associated with a non-optimum nonlinearity correction. However, the spectral range (550 cm⁻¹ – 1500 cm⁻¹) used for the in-band optimization of the quadratic nonlinearity coefficient was selected to specifically include contributions from the detection bandpass outside of the single octave range. Furthermore, repeating the in-band optimization for a spectral range of 1100 – 1500 cm⁻¹ did not provide a significant reduction in the residual in this region. Simultaneous optimization of the quadratic nonlinearity coefficient and the DC level model was also tested, over the 550 – 1500 cm⁻¹ range, with the optimization of the DC level contribution completed via an additional multiplicative term k_{opt} in the model:

$$V_{DC} = k_{opt} \left[\underbrace{e_m^{-1} \frac{2}{N} \int_{\sigma_{min}}^{\sigma_{max}} |S_{scene}(\sigma_k) - S'_{space}(\sigma_k)| d\sigma_k}_{V_{scene}} + \underbrace{e_m^{-1} \tilde{k} \cdot \frac{2}{N} \int_{\sigma_{min}}^{\sigma_{max}} |S'_{space}(\sigma_k)| d\sigma_k}_{V_{instrument}} \right]. \quad (2.34)$$

For this optimization, the lower and upper bounds for the quadratic nonlinearity coefficient were set based on the out-of-band analysis. This process also did not provide a significant improvement in the residuals. Consequently, it seems likely that the small residual may be due to other contributors, such as a small residual stray-light effect, which is described in the following chapter.

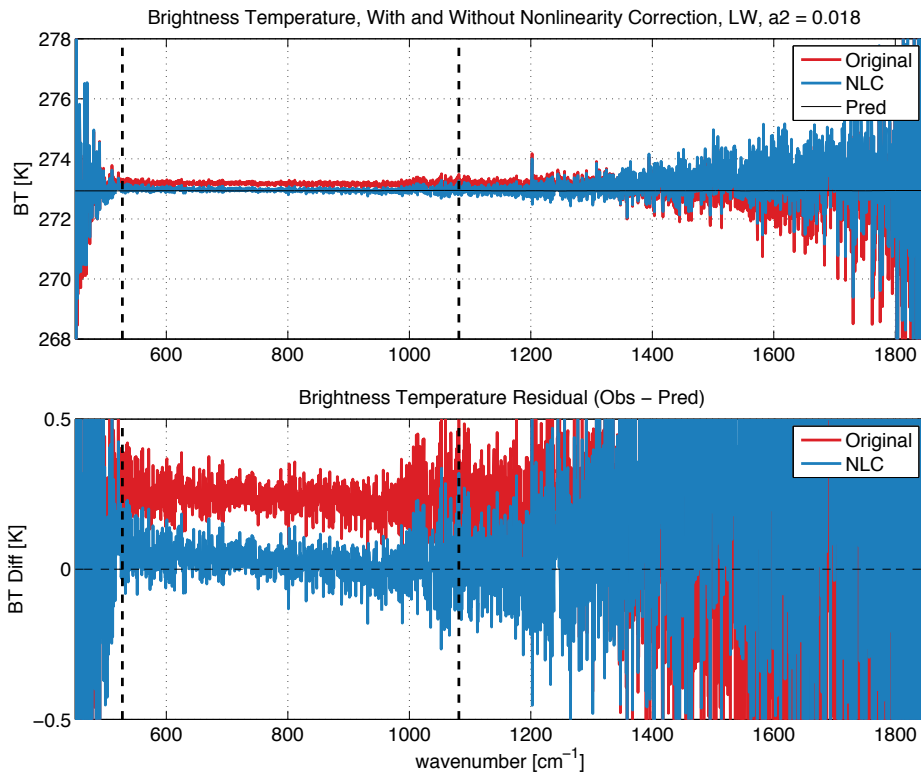


Figure 35: ARI LW MCT measured and predicted brightness temperature for a 272.9 K OARS target, during vacuum testing. For this case, the cold calibration reference was operated at a temperature 217.6 K, the hot calibration reference at 300.2 K. The nonlinearity corrected result is shown in blue, while the uncorrected result is in red. The black dashed lines indicate the 3dB points of the responsivity.

The 4-port configuration of the interferometer also allows direct comparison between the two output ports of detector response in overlapping spectral regions. The DTGS pyroelectric detector (50 – 1800 cm^{-1}) exhibits very linear response. The DTGS detector and MCT detectors, located at opposite output ports, have simultaneous and overlapping spectral coverage from approximately 550 cm^{-1} to 1400 cm^{-1} . The results for both detectors are presented and compared in the final chapter.

2.5 Impact on radiometric uncertainty

The need for a nonlinearity correction introduces an additional contributor to the radiometric uncertainty. The nonlinearity correction requires knowledge of the quadratic nonlinearity coefficient and the DC level, and both contribute to the radiometric uncertainty associated with the nonlinearity correction.

The quadratic nonlinearity coefficient derived from the out-of-band analysis in Section 2.4.1 spanned a range from 0.0142 to 0.0189, or 28.4% when expressed as a percent of the average value. However, it was clear from Section 2.4.2.1 that the in-band optimization for the quadratic nonlinearity coefficient provided a much more robust estimation of this parameter. Tobin uses a similar method for the assessment of the out-of-band estimate of nonlinearity for CrIS [61]. Additionally, Tobin explains that for the CrIS instrument the uncertainty in the determination of the a_2 values is further reduced via comparisons between individual fields of view for uniform scenes, with the knowledge that there are varying degrees of nonlinearity for the nine detectors in each of the LW and MW bands. This is particularly effective in the CrIS MW band, where there is at least one

detector with near-linear response. For the ARI, the DTGS detector exhibits very linear response, and the DTGS detector and LW MCT detectors have simultaneous and overlapping spectral coverage from approximately 550 cm^{-1} to 1400 cm^{-1} . Comparison of the two measurements may be used to reduce the uncertainty associated with nonlinearity correction for the LW detector. Accordingly, based on these considerations, 20% is a conservative $k = 3$ estimate for the uncertainty in the determination of a_2 .

The ARI DC level model, provided in Eq. (2.30), is composed of two terms. The first term is scene dependent, but is simply proportional to the integrated measurement of only the scene radiance. The uncertainty in this measurement is very small and can be expected to result in a negligible contribution to the uncertainty in the nonlinearity correction relative to the contribution from the uncertainty in a_2 . The second term in the DC level model represents the instrument contribution to the DC level and is constant for all sources (assuming the radiative loading of the instrument by the scene during time of observation is negligible). In this term, the parameter with the greatest uncertainty is $\tilde{\kappa}$. However, because the instrument term of the DC level model is scene independent, even large uncertainties in $\tilde{\kappa}$ result in very small contributions to the radiometric uncertainty. Even an extremely conservative estimate of 50% for the $k = 3$ uncertainty in $\tilde{\kappa}$ results in a negligible contribution to the radiometric uncertainty associated with the nonlinearity correction, as illustrated in Figure 36.

The radiometric uncertainty contribution from the nonlinearity correction, given these estimates of the uncertainty in the nonlinearity coefficient determination and the DC level model ($u(a_2) = 20\%$, $u(\tilde{\kappa}) = 50\%$) are provided in Figure 36 for the data used for the in-band optimization of the quadratic nonlinearity coefficient in Section 2.4.2.1. The radiometric uncertainty due to nonlinearity correction for this reference blackbody configuration and range of target temperatures approaches 0.1 K for the dataset requiring the largest nonlinearity correction. It is reasonable to argue that the uncertainty due to nonlinearity could be reduced further via on-orbit analysis using the OARS verification source over a range of OARS temperatures.

2.6 Recommendations for future designs

As noted earlier in the chapter, due to the high radiometric accuracy requirements associated with spectrally resolved infrared and far infrared measurements for decadal trending of climate change it is desirable to emphasize linearity rather than sensitivity during detector selection for the flight instrument. It is equally important to ensure that the signal chain electronics are designed to provide a highly linear response. The need for a nonlinearity correction introduces an additional contributor to the radiometric uncertainty, and should be avoided if possible. If detectors requiring a nonlinearity correction are necessary, it is important to limit the bandwidth to a single octave.

It is also desirable to add additional circuitry such that the DC level is measured directly prior to AC coupling and output to the data stream. With knowledge of the design of the preamplifier and sampling electronics, the measured DC level can be converted to the same units as that of the AC coupled signal output from the preamplifiers and digitized by the ADC.

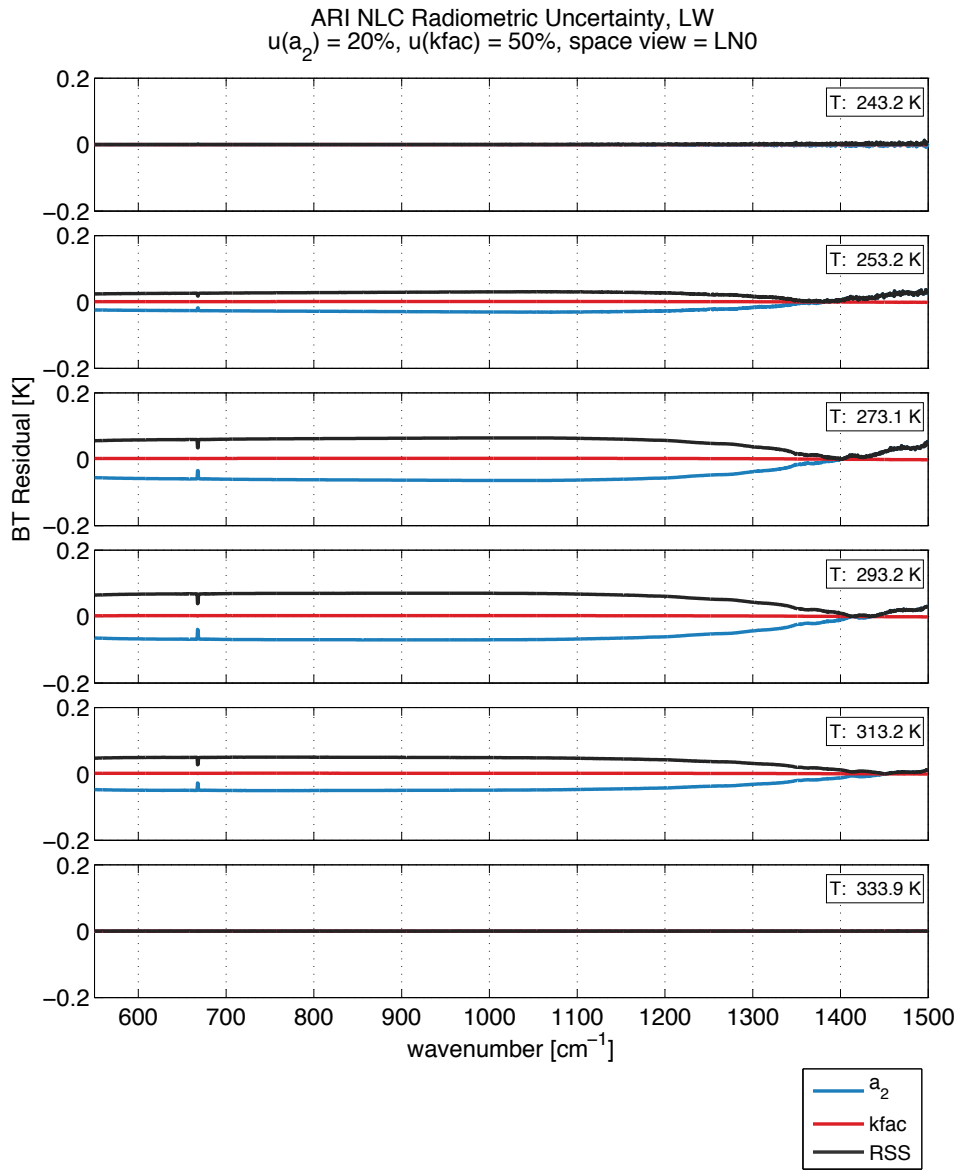


Figure 36: The radiometric uncertainty contribution from the nonlinearity correction for the data used for the in-band optimization of the quadratic nonlinearity coefficient. The uncertainty contribution for a 20% uncertainty in the nonlinearity coefficient (blue), a 50% uncertainty of \tilde{k} in the DC level model, and the combined RSS uncertainty (grey) are provided. All uncertainties correspond to a $k = 3$ coverage factor.

3 Optical design, stray light and vignetting

A radiometric bias for the long-wave detector was discovered during end-to-end ARI radiometric calibration verification under vacuum. No such error was observed for the DTGS detector. The LW bias was most evident when the OARS and CBB were both at 217 K, the coldest set point for the OARS and nominal set point for the CBB during vacuum testing. For this cold reference and verification target temperature, the calibration bias exceeded the predicted uncertainty. It was determined through a series of diagnostic tests during vacuum testing that the calibration error was potentially due to a combination of polarization and stray light contributors. Configuration adjustments were made such that the resulting residual bias was largely eliminated and within predicted calibration uncertainty for end-to-end ARI radiometric calibration verification under vacuum, and further diagnostic tests were completed post vacuum. These tests revealed that the bias was due solely to stray light, and a solution was identified, implemented, tested, and confirmed.

In this chapter, the stray light contribution to the LW bias error is discussed. A brief overview of the optical design of the ARI instrument, results of the diagnostic testing, and solutions for the demonstration effort and the proposed flight model are presented.

3.1 Optical design

We begin with a brief summary of the optical design of the ARI instrument. The optical system can be divided into distinct subsystems, illustrated in Figure 37.

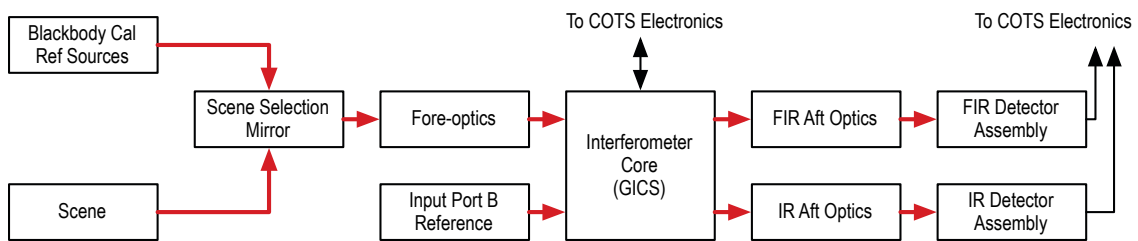


Figure 37: Notional illustration of the primary ARI optical subsystems.

Rotation of the scene select mirror is used to direct calibration reference or scene radiance into the ARI fore-optics. The fore-optics telescope consists of all reflective elements and defines the aperture stop, field stop, and afocal magnification. The output of the fore-optics is directed into one input of the interferometer, and a stable reference is located at the second input port. The second port reference is a modified laser beam dump that has an inverted cone blackbody geometry. The reference is thermally coupled to the instrument and operates at ambient instrument temperature. The output of the interferometer is input into two aft-optics assemblies, one at each of the interferometer output ports. The FIR aft-optics consist of all reflective elements, while the IR aft-optics assembly consists of two reflective elements, combined with in-dewar (77 K) refractive optics. Each reflective element is diamond point turned aluminum, plated with uncoated gold. The use of uncoated gold minimizes polarization issues while maintaining high transmission in the infrared and far infrared.

Key features of the fore and aft optic assemblies are presented in the following sections. A top view of the ARI fore and aft optics ray traces, overlaid on the solid model is shown in Figure 38.

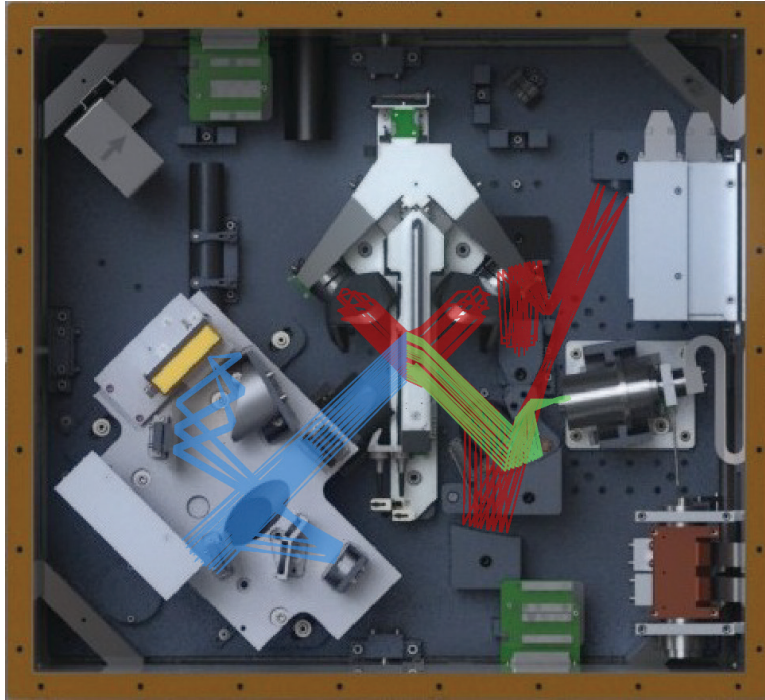


Figure 38: Top view of the ARI optical ray trace, overlaid on solid model; fore-optics (red), FIR aft-optics (blue), IR aft optics (green).

3.1.1 Fore-optics

The ARI optical design goals included:

- Spectral coverage of 200 – 3000 cm^{-1} ;
- Optimization of interferometer throughput;
- Maximal stray light control;
- Minimization of instrument mass and volume;
- Optimization of the heated halo geometrical fill factor;
- Compatibility with a 1" aperture Blackbody;
- Capability for tuning of polarization sensitivity "null" locations with respect to the position of the calibration reference bodies, OARS, and scene views.

These goals, combined with other instrument requirements, resulted in a fore-optics design that provides an afocal magnification of 2.3, accommodates well-defined field and aperture stops, and relays the aperture stop to pupils at the interferometer cube-corner and the halo entrance aperture [126]. The ARI fore-optics ray trace is shown in Figure 39 and Figure 40.

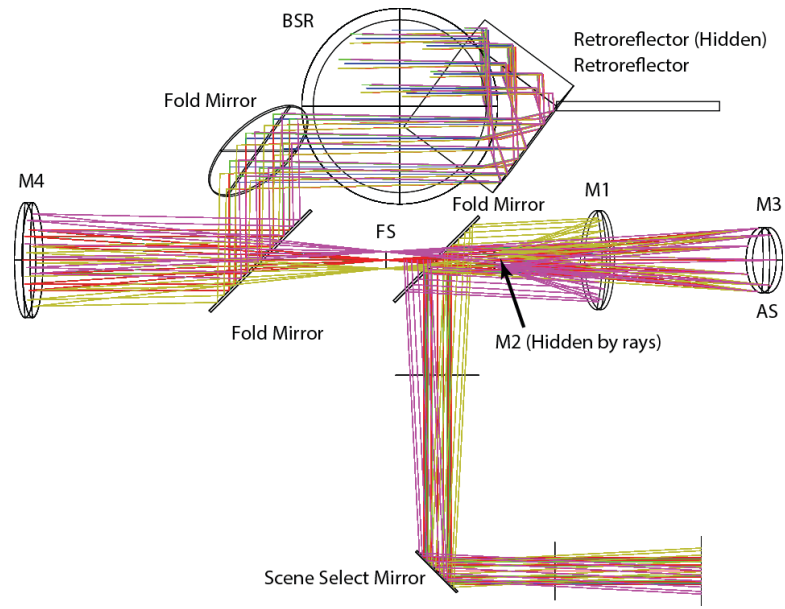


Figure 39: ARI fore-optics ray trace, side view (coloured by field angle).

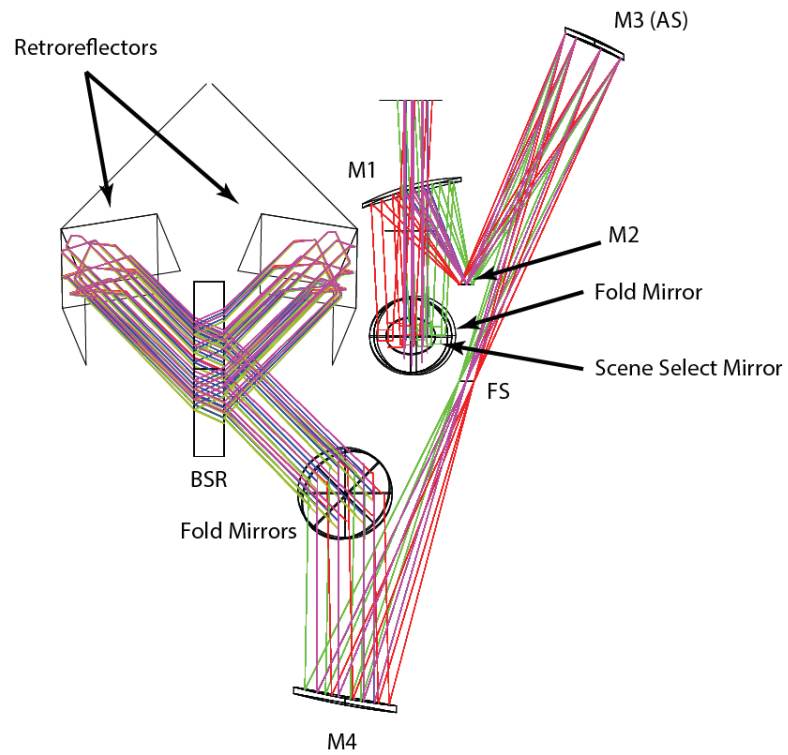


Figure 40: ARI fore-optics ray trace, top view (coloured by field angle).

3.1.2 Aft-optics design – FIR output port (DTGS detector)

The FIR aft-optic subsystem consists of all reflective elements. Originally, a custom design was baselined for the FIR aft-optic subsystem. However, due to schedule and budget considerations, the FIR aft-optics module for the IIP demonstration uses a current generation ABB E-AERI aft-optics system modified to include a field and aperture stop such that the sensor could be operated without the fore-optics in the system. The FIR aft-optics stops can be adjusted or removed so that they are not the limiting stops when the fore-optics are installed in the system, and to provide flexibility during testing. The modified ABB E-AERI aft-optics assembly is also compatible with a standard AERI 77 K detector and dewar module that houses an InSb and an MCT detector.

The optical design of ABB E-AERI aft-optics subsystem was analyzed for compatibility and performance with the GICS interferometer core and ARI Prototype fore-optics prior to final selection. The ABB E-AERI aft-optics subsystem is designed for a 45 mrad beam divergence, and ARI divergence was originally designed for a full-angle divergence of 51.6 mrad. For optimum compatibility with the ABB E-AERI aft-optics, the ARI fore-optics divergence was reduced to 45 mrad. The aperture stop size was increased from the original ARI value in order to minimize loss of throughput associated with the reduced divergence. As noted, the aperture stop size is limited by considerations of the pupil size at the cube-corner. While the increase in aperture size resulted in reduced margin for the pupil at the cube corner than that for the original design, optical analysis indicated that the margin remained sufficient. The DTGS detector module was simultaneously procured from ABB and the aft-optics, DTGS detector, and GICS were delivered as an aligned assembly. The ABB E-AERI aft-optics and DTGS detector module installed in the ARI prototype are shown in Figure 41. A top view of the ARI aft-optics ray trace is provided in Figure 42.

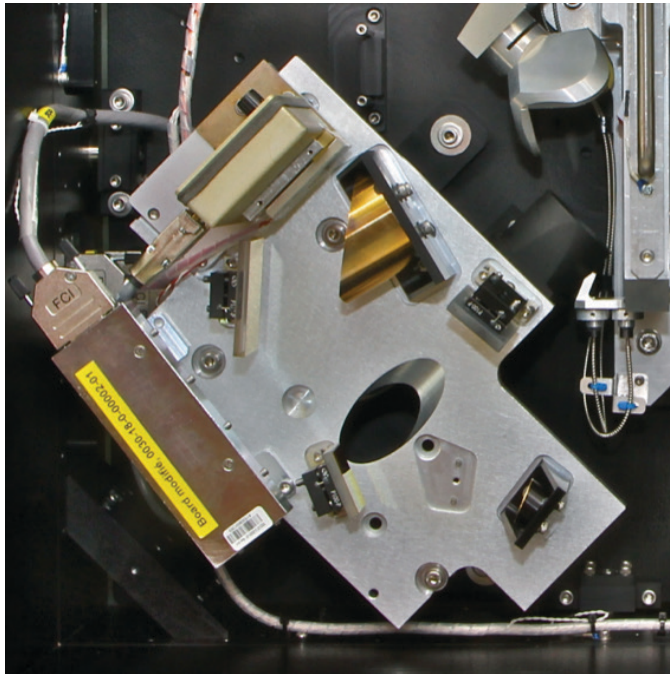


Figure 41: ARI FIR aft-optics assembly (modified ABB E-AERI aft optics assembly) installed in ARI Prototype.

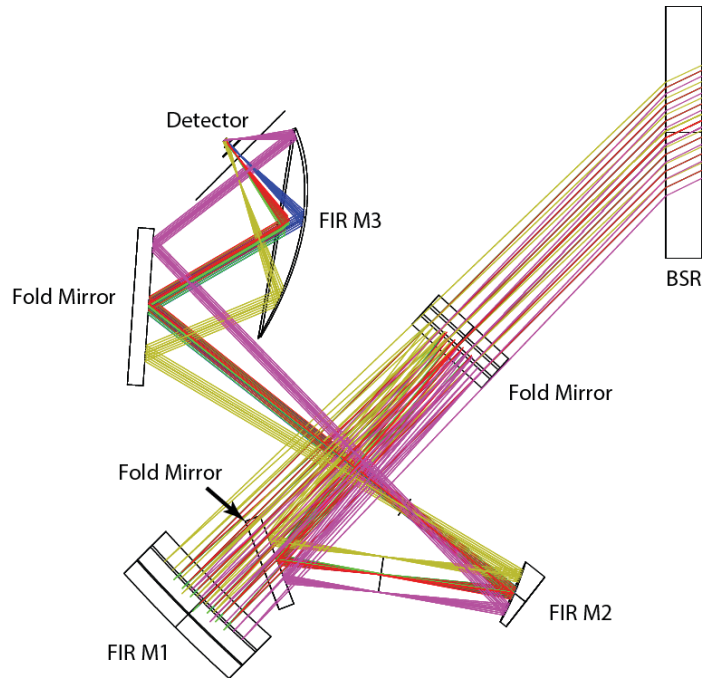


Figure 42: Zemax ray trace of ARI FIR aft-optics assembly (modified ABB E-AERI aft optics assembly). The rays are coloured by prescribed field angle.

3.1.3 Aft-optics Design – IR output port (HgCdTe, InSb detectors)

The IR aft-optics assembly consists of a two reflective elements (an off-axis parabolic and a flat fold mirror), combined with in-dewar (77 K) refractive optics. Originally, an ARI specific design was base-lined for the IR aft-optic subsystem. Two additional options were considered: (1) an existing S-HIS detector module, and (2) an existing UW-AERI detector module. Analysis of the optical prescriptions, electrical, and mechanical designs indicated that the S-HIS detector dewar configuration was optically, electrically, and mechanically compatible with the ARI Prototype. Given this analysis, and to maintain compatibility with the schedule and budget of the IIP demonstration, the spare S-HIS detector module option was selected and integrated into the ARI Prototype. The S-HIS detector dewar includes two refractive optical elements, and 3 side-by-side HgCdTe detectors (ELW, LW, MW) behind a shortwave InSb detector (combined spectral coverage of 450 – 3000 cm^{-1}). All detectors have a common field stop, but the side-by-side ELW, LW, and MW detectors share the pupil, which is located at the detector plane. The COTS interferometer electronics used for the ARI Prototype are limited to two detector channels, and only the LW HgCdTe detector (550 – 1500 cm^{-1}) and the DTGS detector assembly were used for the IIP demonstration.

The infrared aft-optics and S-HIS detector module, installed in the ARI prototype, are shown in Figure 43, and a top view of the infrared aft-optics ray trace is provided in Figure 44.

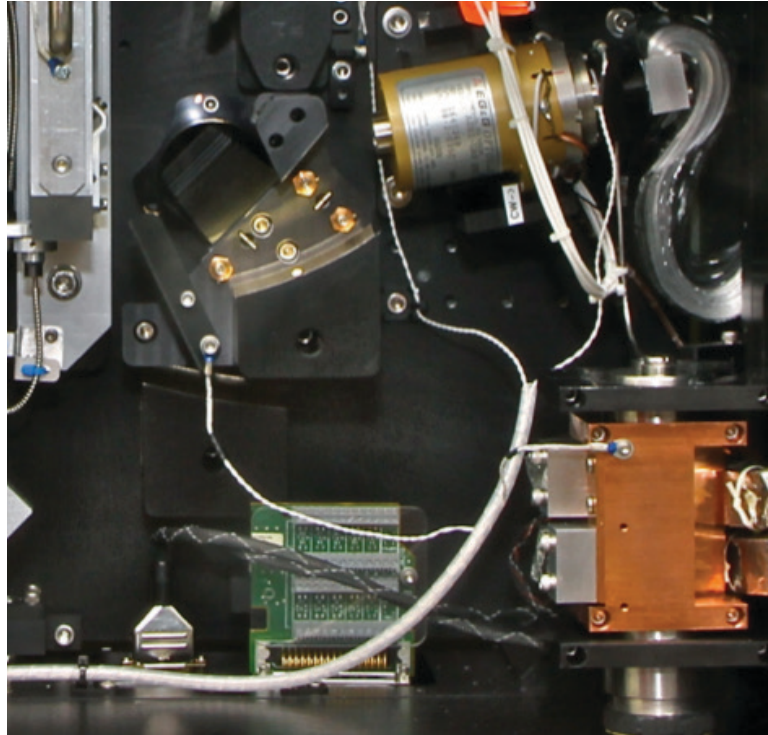


Figure 43: ARI IR aft-optics, S-HIS spare detector dewar, and Stirling cooler installed in ARI Prototype

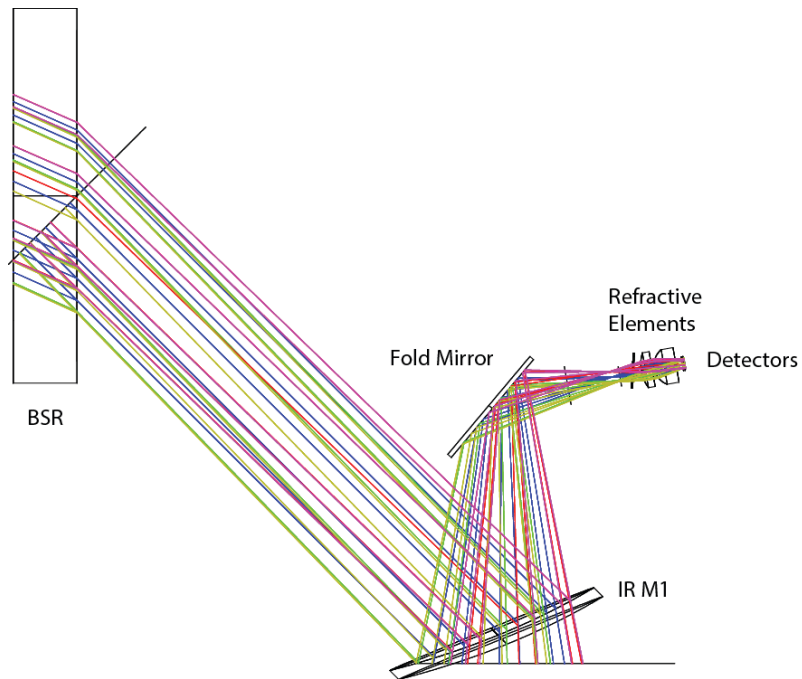


Figure 44: Zemax ray trace of ARI IR aft-optics with S-HIS spare detector dewar installed. The rays are coloured by prescribed field angle.

3.2 Stray light and vignetting

While ray trace analysis indicated the S-HIS detector dewar configuration was optically compatible with the ARI prototype, end-to-end calibration verification results revealed a small radiometric bias for the long-wave detector that was not present for the DTGS detector. Based on testing conducted during the vacuum test phase, it was hypothesized that this long-wave spectral band bias was the result of a combination of polarization and stray light. As noted in Chapter 1 (Section 1.3), the ARI is designed such that the entire calibration validation assembly can be rotated to place the viewports, which are spaced at 90° in SSM rotation angle, at the zeros of the instrument polarization sensitivity. If the orientation of the front end is not optimum with regards to the polarization sensitivity zeros, a calibration bias due to polarization will result. Views separated by 180° in scene mirror angle, regardless of the orientation of the polarization axis for the instrument, will have equal polarization bias. Thus, polarization was identified as a potential error contributor, since the error was significantly decreased with the CBB and OARS placed at 180° in scene mirror angle to one another. It was assumed that the tilted dewar window on the S-HIS detector dewar created an unaccounted for shift of the zero crossings of the polarization dependence on scene mirror angle for the LW detector. No such error was found for the DTGS detector, confirming proper optical clocking of the front-end assembly with respect to the instrument for suppressing errors related to polarization.

Extensive stray-light and polarization testing were planned, and conducted after the vacuum testing. Due to availability of the vacuum chamber, and the additional time associated with breaking vacuum for each configuration change, these tests were not conducted in the vacuum environment.

The results of the post-vacuum diagnostic tests and analysis revealed the dominant contributor to the observed bias was actually due to stray-light, which is presented in this chapter. Details of the polarization characterization are presented in Chapter 4.

3.2.1 Calibration verification testing under vacuum

The issue was first evident during end-to-end calibration verification testing in the first cycle of vacuum testing. For these tests, the cold blackbody reference (CBB) was located at the 6:00 position and operated at a temperature of approximately 217 K, the hot calibration reference (HBB) was at the 12:00 position and operated at a temperature of approximately 303 K, and the OARS was located at the 3:00 position and operated over a range of temperatures from 217 K to 333 K (Figure 45). The ambient blackbody was installed at the 9:00 position, and was not used for the end-to-end calibration verification testing.

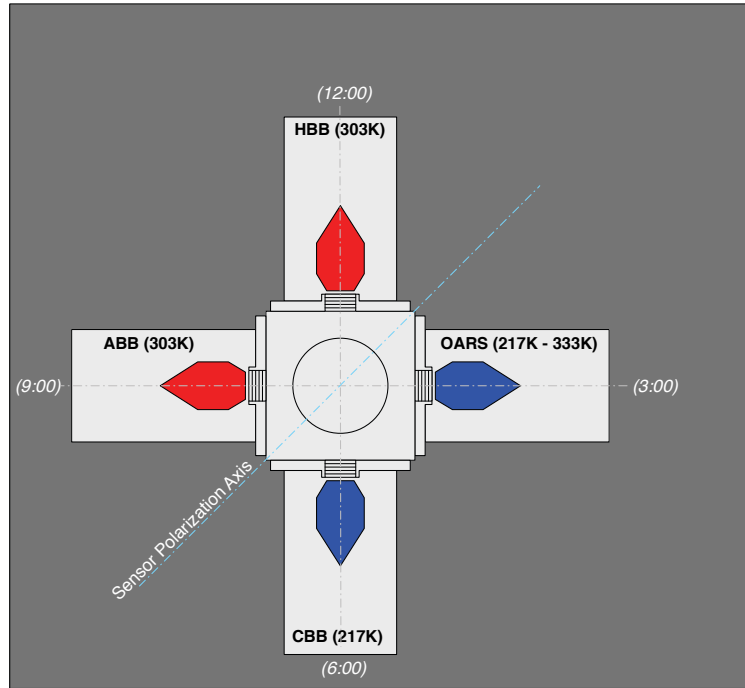


Figure 45: ARI blackbody configuration during the first cycle of vacuum testing.

For this phase of the vacuum tests, the 3rd generation Heated Halo was installed on the OARS. A cross-section of the OARS with the Heated Halo installed is shown on the left of Figure 46. The diameter of the halo neck is 21.25 mm, and a 21 mm knife-edge aperture plate is nominally used. Figure 46 illustrates a 17 mm knife-edge aperture plate. If the instrument field of view includes a direct view of the halo entrance aperture or neck, the measured brightness temperature will be warm biased for a cold OARS target and an ambient halo.

In this configuration, end-to-end calibration verification for a 217 K OARS target with 217 K CBB and 305 K HBB calibration reference sources, resulted in a measured brightness temperature of roughly 0.5 K warmer than predicted at 700 cm^{-1} for the MCT detector (Figure 47). The DTGS detector did not show a similar calibration bias (Figure 48).

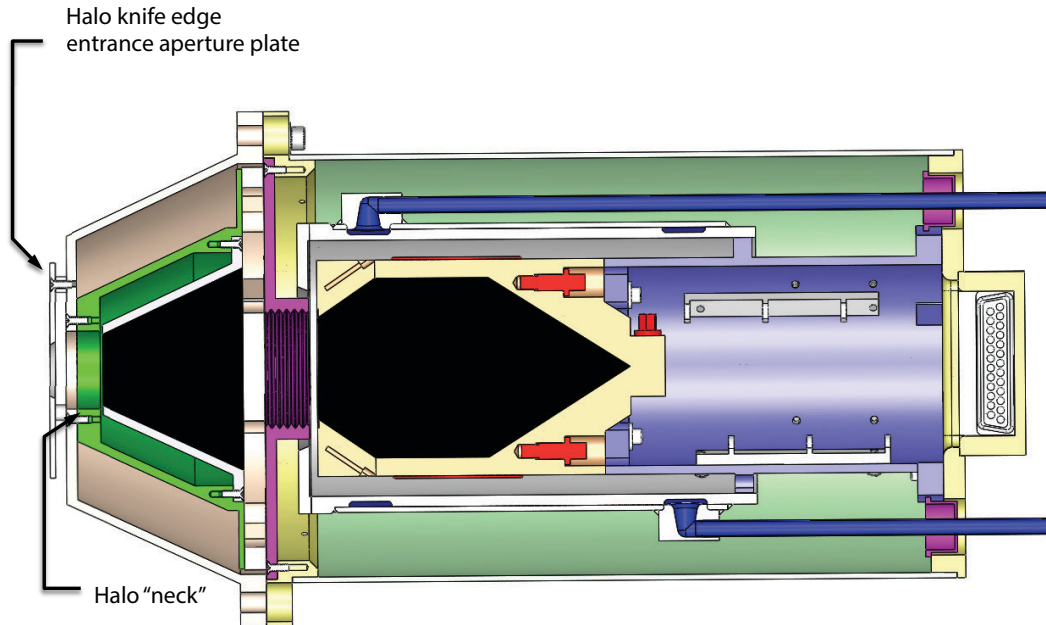


Figure 46: Cross-section of OARS with 3rd generation Heated Halo installed.

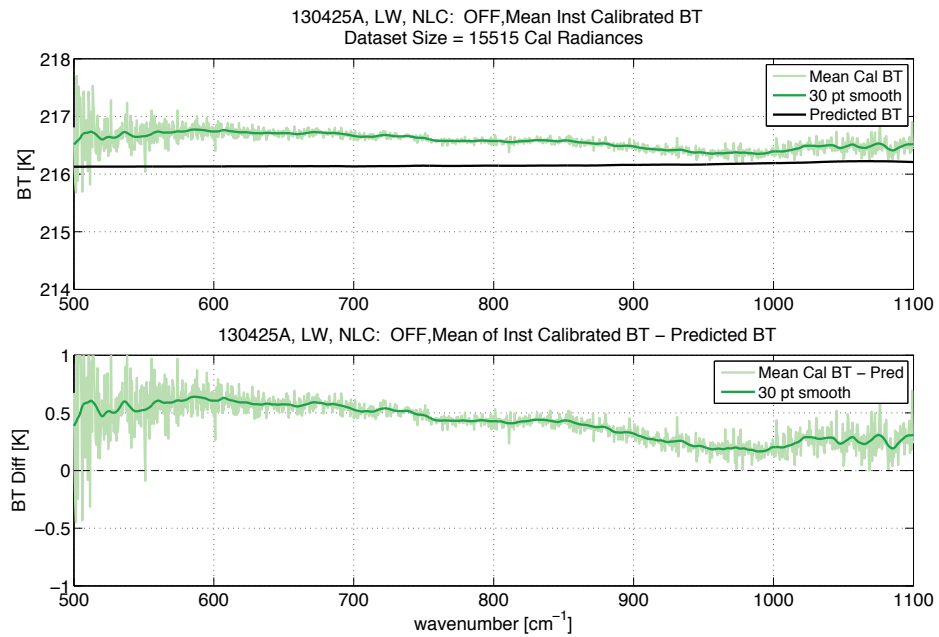


Figure 47: In the first vacuum cycle configuration, end-to-end calibration verification for a 217 K OARS target with 217 K CBB and 305 K HBB calibration reference sources, indicated a brightness temperature residual of roughly 0.5 K at 700 cm^{-1} for the long-wave MCT detector. Observed and predicted OARS brightness temperatures are shown in the top panel, and the difference is presented in the bottom panel. A 30-point moving average filter has been used to smooth the observed brightness temperature.

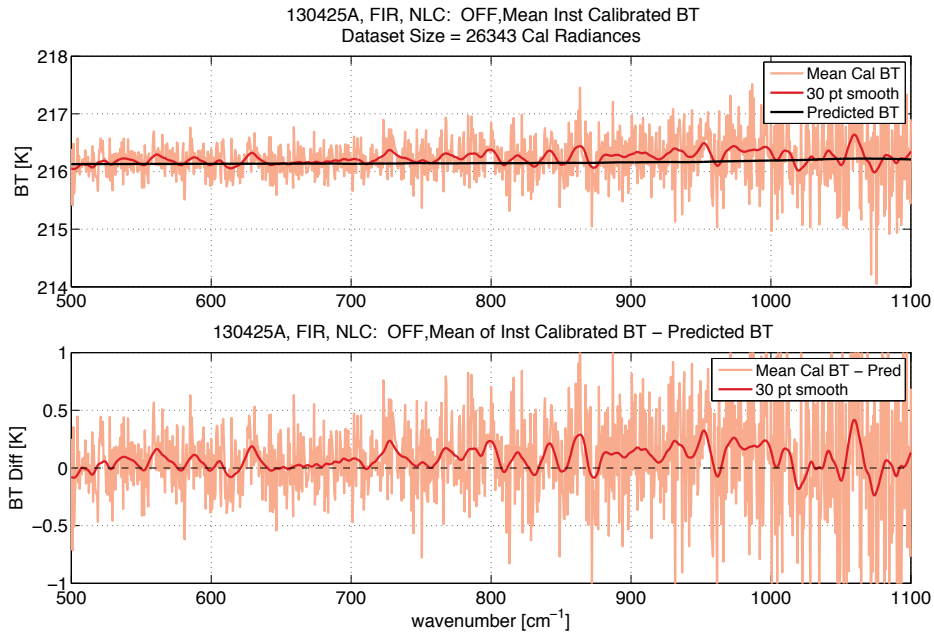


Figure 48: In the first vacuum cycle configuration, end-to-end calibration verification for a 217 K OARS target with 217 K CBB and 305 K HBB calibration reference sources, the DTGS detector result was within the predicted uncertainty. Observed and predicted OARS brightness temperatures are shown in the top panel, and the difference is presented in the bottom panel. A 30-point moving average filter has been used to smooth the observed brightness temperature.

To further diagnose the observed long-wave band calibration bias, data was collected in vacuum for a series of instrument configuration changes. The bias showed no dependence on displacement of the scene select mirror along its rotational axis, and was not affected by the removal of the shortwave filter from the front of the S-HIS detector dewar.

However, moving the CBB from the 6:00 position to the 9:00 position significantly reduced the long-wave detector bias, as did removing the Heated Halo from the OARS. These contributors were separated via sequential configurations and data collects. With the blackbodies at their original positions and temperatures as in Figure 45, but with the Heated Halo removed from the OARS, the long-wave residual was reduced to approximately 0.2 K at 700 cm^{-1} for the MCT detector (Figure 49, dataset 130705D).

Furthermore, with the Heated Halo installed on the OARS, calibration verification of a 217 K OARS at the 3:00 front-end position with the 217 K CBB moved directly opposite the OARS to the 9:00 front-end position also resulted in significant reduction in the original brightness temperature residual for the MCT detector (Figure 50, 130712). This magnitude of the remaining residual at 700 cm^{-1} is consistent with a small stray light contribution of roughly 0.2% from the ambient temperature Halo aperture plate, even with a well-centered beam. Since the OARS and CBB are located at 180° to one another for this measurement and operated at the same temperature, polarization affects will not be an issue in this configuration.

The combination of these two configuration changes, (1) removing the Heated Halo from the OARS, and (2) moving the CBB from the 6:00 to the 9:00 position such that it is 180° in scene mirror rotation angle from the OARS, resulted in a calibration verification result for the long-wave detector that showed no significant residual bias for an OARS and CBB temperature of 217 K (Figure 51, dataset 130710A). Further changes were made

to the Heated Halo in the following tests. It was found that an enlarging the Heated Halo neck (25.4mm) and entrance aperture (23mm) effectively mitigated the bias to the same degree as removing the Heated Halo. However, the heated halo emissivity measurements with these halo modifications in place produced emissivity values that were not realistic, and indicated a remaining unexpected contribution from out of the prescribed beam. These results implied that for the long-wave detector, some very low-level stray light from outside of the blackbody aperture was affecting the measurement.

In order to proceed with scheduled vacuum testing, the halo was removed, and the remaining in-vacuum radiometric calibration verification tests were completed with the CBB at the 9:00 position, opposite the OARS at the 3:00 position. In this configuration, a small residual long-wave detector bias was still evident for warm OARS temperatures. The size of this remaining bias, while within the radiometric uncertainty, increased with increasing OARS temperature. Polarization and stray-light were still suspected to be the primary contributors to this remaining bias. While positioning the CBB and OARS 180° to one another in scene mirror rotation angle matches any measurement bias associated with polarization for the two views, the HBB is still at 90° in scene mirror rotation angle to the both the OARS and CBB. As a result, the polarization induced measurement bias for the HBB view is opposite sign to that for the CBB and OARS if the viewports are not located at the polarization sensitivity zeros. Secondly, due to the off-axis optical elements, the beam profile at the pupil near the heated halo is not perfectly circular, and the asymmetric footprint rotates with scene mirror rotation. These considerations, coupled with the possibility that the axis of the scene mirror rotation and the optical axis of the instrument are most likely not perfectly aligned, it is likely that any remaining contribution from outside of the prescribed field of view due to vignetting of the beam by the blackbody or halo entrance apertures is dependent on scene mirror location.

The long-wave detector brightness temperature residual for an OARS temperature of 333 K in this configuration is shown in Figure 52 (dataset 130713B).

The DTGS detector consistently showed no change in calibration bias for any of the configuration changes, and the results for all configurations were within the predicted uncertainty.

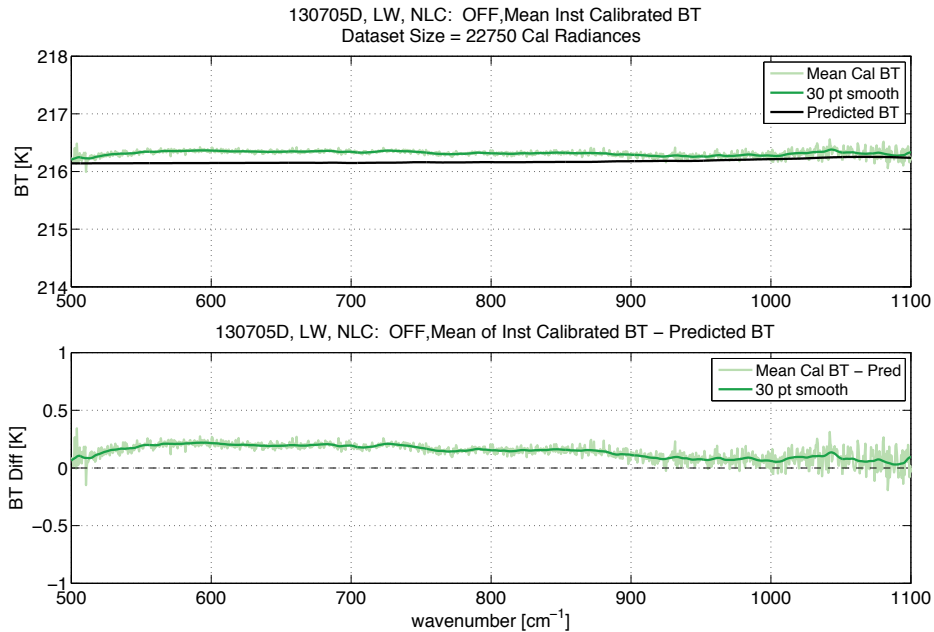


Figure 49: End-to-end calibration verification for a 217 K OARS target, with the Heated Halo assembly removed, at the 3:00 position with a 217 K CBB calibration reference source at the 6:00 position and a 305 K HBB calibration reference source at the 12:00 position. Results indicated a brightness temperature residual of roughly 0.2 K at 700 cm^{-1} for the long-wave MCT detector. Observed and predicted OARS brightness temperatures are shown in the top panel, and the difference is presented in the bottom panel. A 30-point moving average filter has been used to smooth the observed brightness temperature.

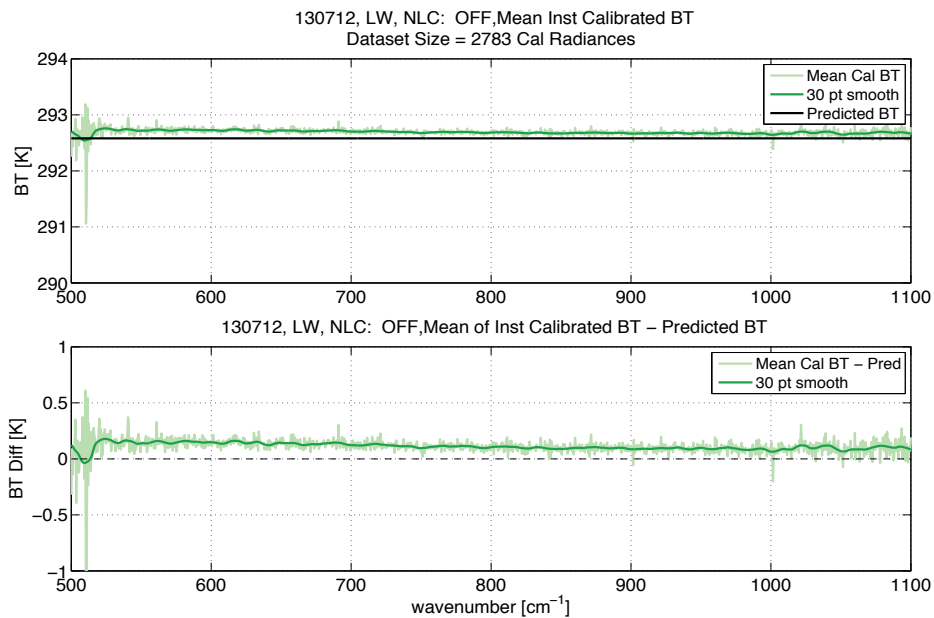


Figure 50: End-to-end calibration verification for a 217 K OARS target at the 3:00 position with a 217 K CBB calibration reference source at the 9:00 position (180 degrees separation from the OARS in scene mirror rotation angle) and a 305 K HBB calibration reference source at the 12:00 position. Results indicated a brightness temperature residual of roughly 0.2 K at 700 cm^{-1} for the long-wave MCT detector. Observed and predicted OARS brightness temperatures are shown in the top panel, and the difference is presented in the bottom panel. A 30-point moving average filter has been used to smooth the observed brightness temperature.

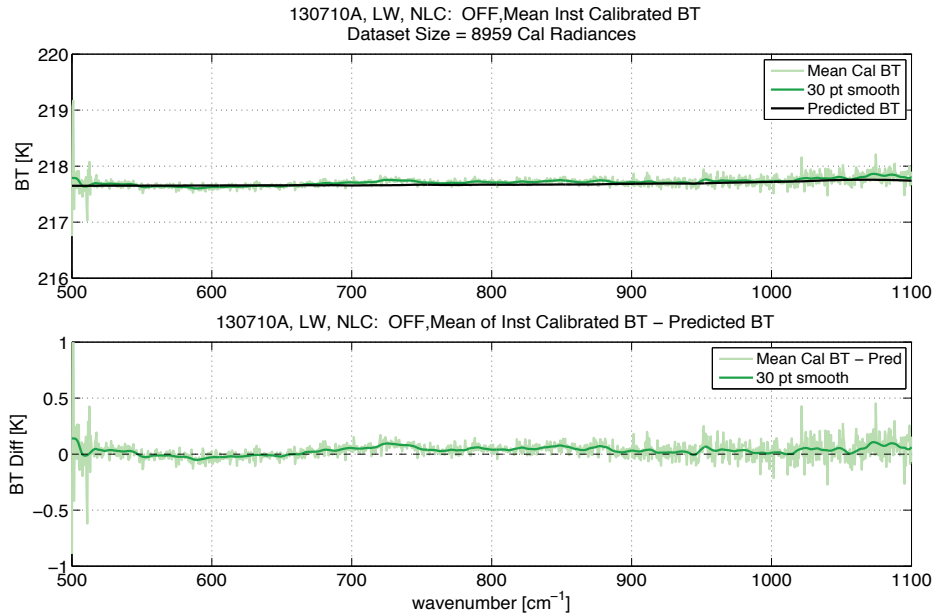


Figure 51: End-to-end calibration verification for a 217 K OARS target, with the Heated Halo assembly removed, at the 3:00 position with a 217 K CBB calibration reference source at the 9:00 position (180 degrees separation from the OARS in scene mirror rotation angle) and a 305 K HBB calibration reference source at the 12:00 position. Observed and predicted OARS brightness temperatures are shown in the top panel, and the difference is presented in the bottom panel. A 30-point moving average filter has been used to smooth the observed brightness temperature.

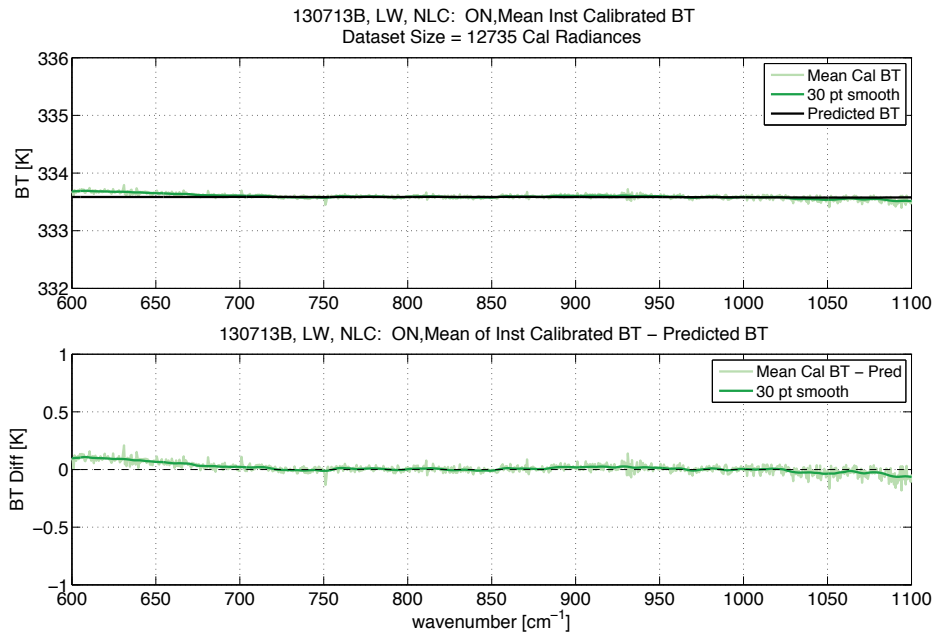


Figure 52: End-to-end calibration verification for a 333 K OARS target, with the Heated Halo assembly removed, at the 3:00 position with a 217 K CBB calibration reference source at the 9:00 position (180 degrees separation from the OARS in scene mirror rotation angle) and a 305 K HBB calibration reference source at the 12:00 position. Results show a small brightness temperature residual for wavenumbers below 700 cm⁻¹ for the long-wave MCT detector. Observed and predicted OARS brightness temperatures are shown in the top panel, and the difference is presented in the bottom panel. A 30-point moving average filter has been used to smooth the observed brightness temperature.

3.2.2 Post-vacuum stray light diagnostic testing

After completion of the vacuum data collection, analysis, and final review; follow-up tests were formulated. As noted in the prior section, based on the results of the vacuum testing it was hypothesized that the long-wave spectral band bias was the result of two error contributors, polarization and stray light. Placing the CBB and OARS at 180° to one another, and removing the heated halo reduced the calibration bias to within predicted uncertainty for the calibration verification tests conducted under vacuum. However, there was a remaining residual bias for the calibration verification results that increased with OARS temperature, and even if the remaining bias was within radiometric uncertainty, it was still quite evident for the 333 K OARS results.

After examination of the results, and a review of the instrument optical design and elements it was hypothesized that the main source of very low level, distributed stray light was potentially due to reflection from the black anodized flat surface at fore-optics aperture stop (AS). Tests showed no indication of a misalignment of the geometrical beam, and the area for reflection at the field stop knife-edge is very small. While the field stop is a transmitting element, the fore-optics aperture stop is at the M3 mirror, and the design of this element includes a black anodized and flat surface directly behind the M3 mirror. Black anodize has significant reflectance in the infrared, and it seemed possible that stray light was reflecting from this surface and reaching the LW detector. The aperture stop and field stop are labeled in the ARI optical ray-trace, presented in Figure 39 and Figure 40, and the solid model and a photo of the M3 mirror element are shown in Figure 53.

It was also proposed that the difference between DTGS and MCT sensitivity is related to the view of the aperture stop allowed by the different aft optics designs. Presumably, vignetting in the DTGS aft optics or at the DTGS detector itself, which is located at a pupil, were rejecting this stray light contribution.

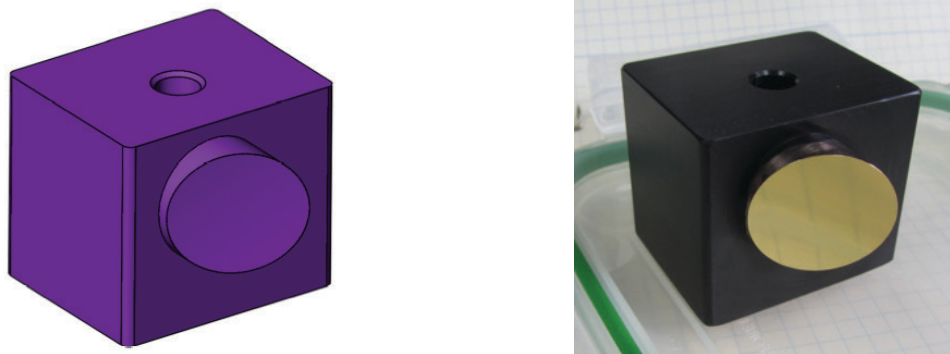


Figure 53: Solid model (left) and photo (right) of ARI aperture stop (mirror M3). Non-mirror surfaces are black anodized, which is significantly reflective in the infrared.

To investigate and resolve the stray light effects in the ARI prototype, a Z306 painted baffle was designed and fabricated for installation at the aperture stop, with a goal of improving rejection of stray light at the aperture stop element. Photos of the baffle prior to and after installation are provided in Figure 54. The baffle still presents a flat surface directly behind the mirror, but the emissivity of Z306 is much better than black anodized aluminum in the infrared.

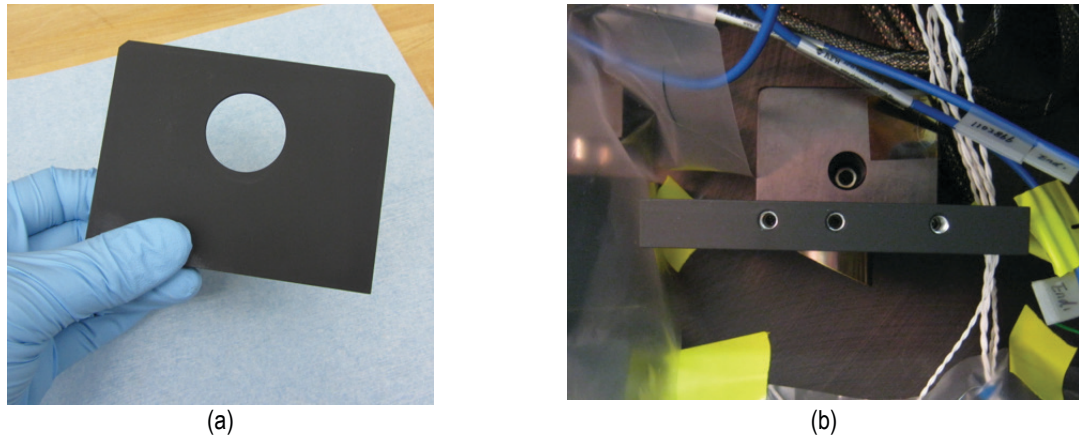


Figure 54: A stray-light baffle was added to the ARI aperture stop at mirror M3; (a) baffle after application of Z306, and (b) installed at mirror M3.

Additionally, entrance aperture ring assemblies with integral thin film heaters and thermistors were designed for installation at the CBB and OARS. These blackbody entrance aperture ring assemblies can be heated to a variable set point and facilitate testing for low-level stray light contributions associated with vignetting of the beam by the entrance aperture at the blackbodies. For a cold CBB or OARS, and hot entrance aperture ring assembly, the measurement is extremely sensitive to any direct view of the heated aperture ring outside of the prescribed beam footprint. The heated aperture ring assemblies are shown in Figure 55. Three sets of aperture ring sizes were machined (30 mm, 32 mm, and 34 mm diameter), and the 30 mm diameter rings were used for the testing described here.

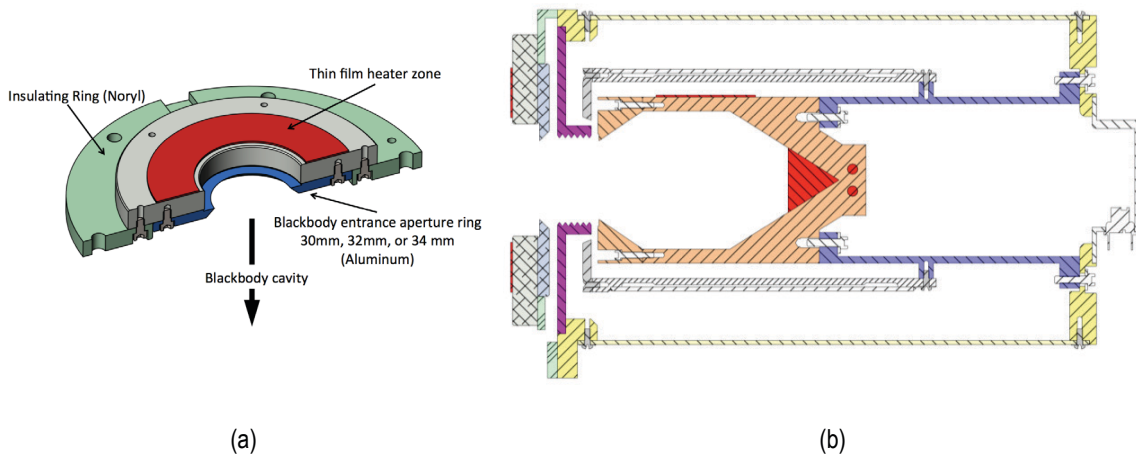


Figure 55: (a) Cutaway view of heated entrance aperture ring assembly with key components labelled, and (b) a cross-sectional view of the heated entrance aperture ring assembly installed on the OARS.

The 30 mm diameter entrance aperture ring is the same size as the entrance diameter for the ARI blackbody cavities. The fore-optics telescope was designed to provide a beam size compatible with a 30 mm blackbody aperture, with sufficient margin. Placing the pupil at the entrance to the blackbody would allow minimization of the cavity size, however, to optimize the geometric fill factor for the heated halo the pupil is located near the entrance aperture of the halo rather than at the blackbody. As a result, the footprint at the blackbody is slightly larger than at the pupil. The Zemax footprint diagram for the optical surface at the blackbody cavity opening is

shown in Figure 56. In the figure, the thin black circle defines the 30 mm diameter entrance aperture of the cavity and the coloured rings represent the footprints for the nine fields used in the Zemax prescription. For reference, the footprints of the fields at the field stop are shown in Figure 57.

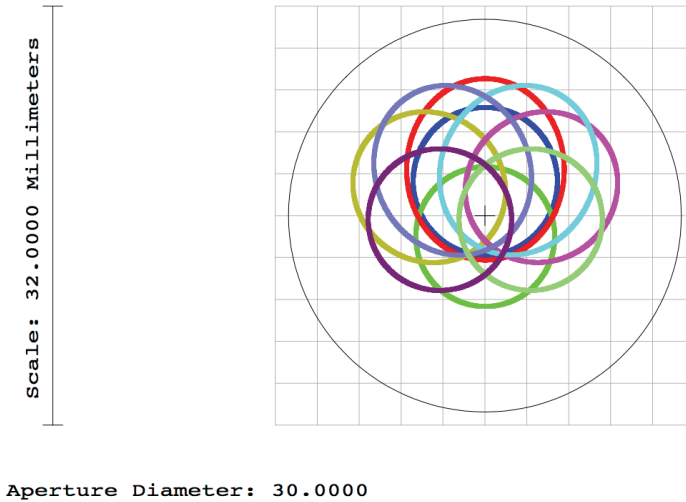


Figure 56: The Zemax footprint diagram for the optical surface located at the entrance to the blackbody. The sizing of the aperture and field stops, afocal ratio of the fore-optics telescope, and blackbody entrance diameter were specified to provide significant margin. The thin black line indicates the 30 mm entrance aperture diameter at the blackbody and the coloured rings represent the footprint for the nine fields used in the Zemax prescription. The pupil of the beam is located closer to the halo entrance aperture, rather than the blackbody entrance aperture.

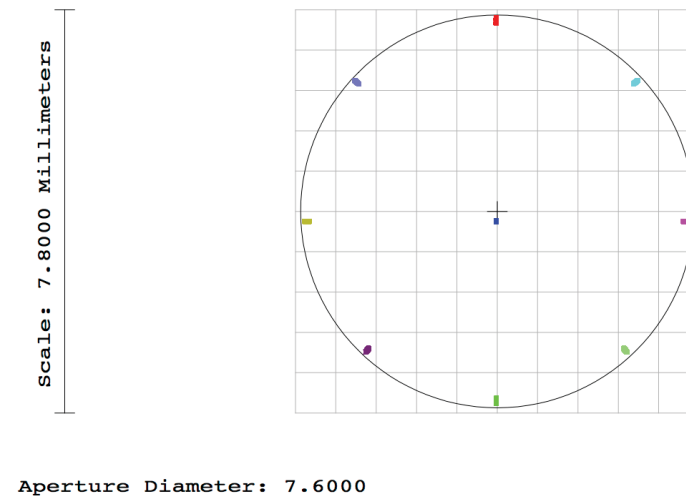


Figure 57: The positions of the nine field footprints at the field stop.

Before proceeding to the test and analysis details, it is useful to illustrate the beam shape at the front-end of the instrument. A plan and profile view of the optical ray trace between the scene mirror and blackbody entrance aperture surface are provided in Figure 58 and Figure 59, respectively. The footprint diagrams at the halo and the blackbody entrance planes are also indicated in the figures.

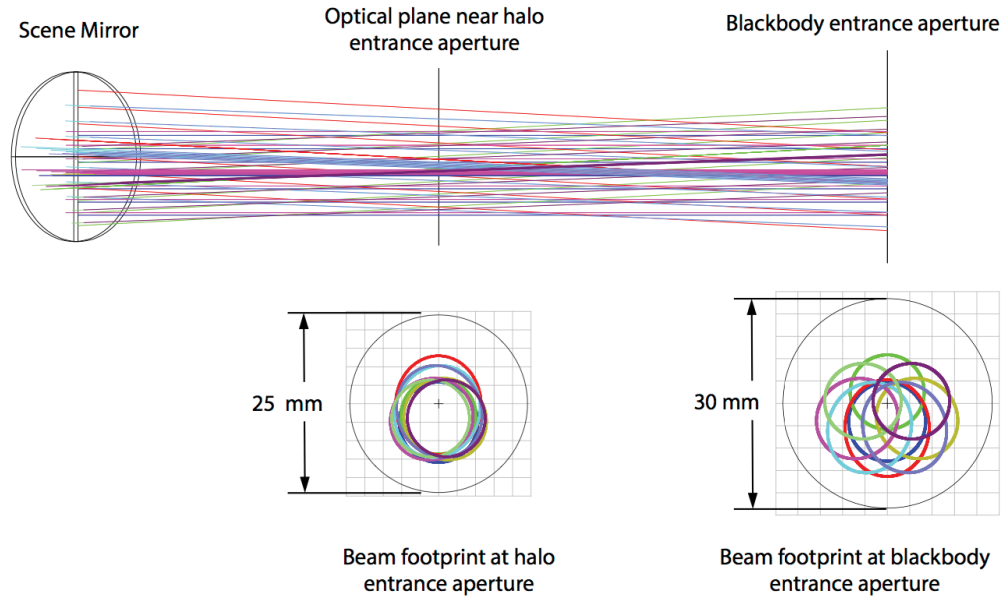


Figure 58: Plan view of the optical ray trace between the scene mirror and the blackbody entrance aperture. Beam footprints at the halo and blackbody optical planes are also provided. The coloured rings represent the footprint for the 9 fields used in the Zemax prescription. Zemax field positions at the field stop are shown in Figure 57.

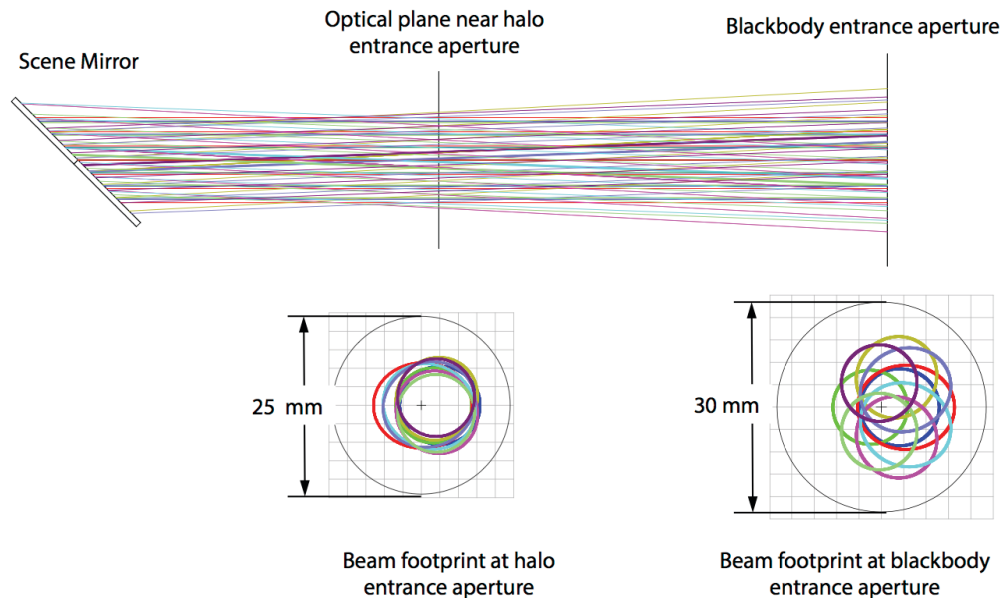


Figure 59: Profile view of the optical ray trace between the scene mirror and the blackbody entrance aperture. Beam footprints at the halo and blackbody optical planes are also provided. The coloured rings represent the footprint for the 9 fields used in the Zemax prescription. Zemax field positions at the field stop are shown in Figure 57.

The front-end configuration for the stray light testing is shown in Figure 60. Two blackbodies, the OARS and the CBB, are at 243 K, and located 180 degrees to one another at the 3:00 and 9:00 positions. A hot reference blackbody at 333 K is located at the 12:00 position, 90 degrees in scene mirror rotation angle to the other two blackbodies. The Heated Halos have been removed from both the OARS and CBB and replaced with the temperature-controlled aperture rings, which can be heated to a maximum temperature of 363 K. The

instrument, including the calibration and verification blackbodies, is enclosed in a purge tent during testing and a dew point of less than 233 K was maintained.

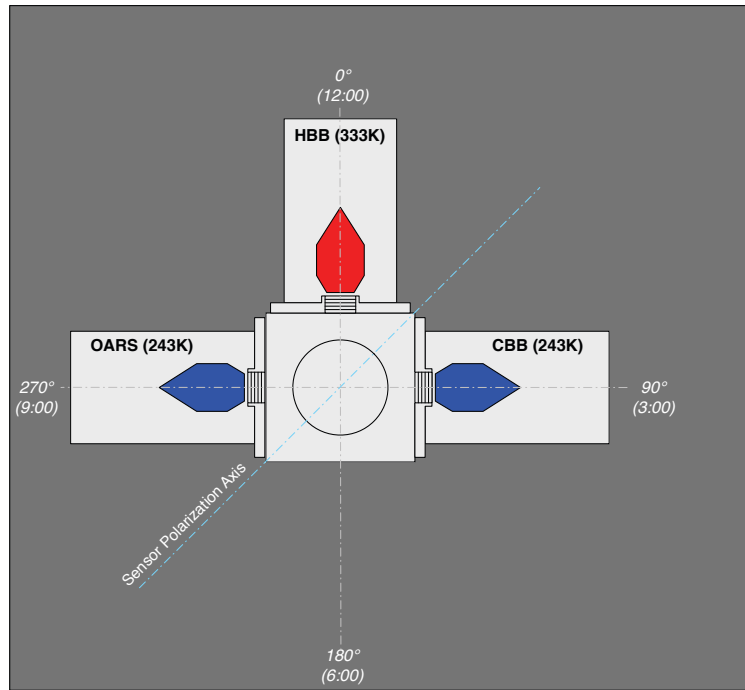


Figure 60: ARI front-end configuration and coordinate system definition used for stray light testing.



Figure 61: Stray light diagnostic tests. A recirculating chiller is used to cool the OARS and CBB to 243 K. The instrument, including the calibration and verification sources, is purged with dry air and a dew point of less than 233 K was maintained.

Prior to the installation of the aperture stop baffle, the following baseline end-to-end calibration verification datasets were collected:

- CBB and OARS aperture rings unheated (dataset 140127)
- OARS aperture ring heated to 333 K (dataset 140130)

As expected, the baseline datasets showed a clear bias for the long-wave detector (Figure 62, Figure 63), and no significant bias for the DTGS detector. With both the OARS and CBB heated aperture rings unpowered, the residual brightness temperature bias for the long-wave channel is approximately 0.1 K at 600 cm^{-1} (Figure 62). The residual brightness temperature bias for the long-wave channel with the OARS aperture ring heated to 333 K and the CBB aperture ring unheated is approximately 0.7 K at 600 cm^{-1} (Figure 63). These results directly demonstrate that there is a small radiance contribution from outside the blackbody for the long-wave field of view. However, for an artifact due to contributions from an additional highly emissive (Z306) source at 333 K in the OARS field of view, one would expect the error to increase in brightness temperature with wavenumber due to the relationship between radiance and brightness temperature. The observed bias has a clear spectral signature that does not match this expectation.

The baseline data collections were repeated after the installation of the aperture stop baffle. The improved aperture stop baffle had no significant impact on the long-wave bias (Figure 64, Figure 65).

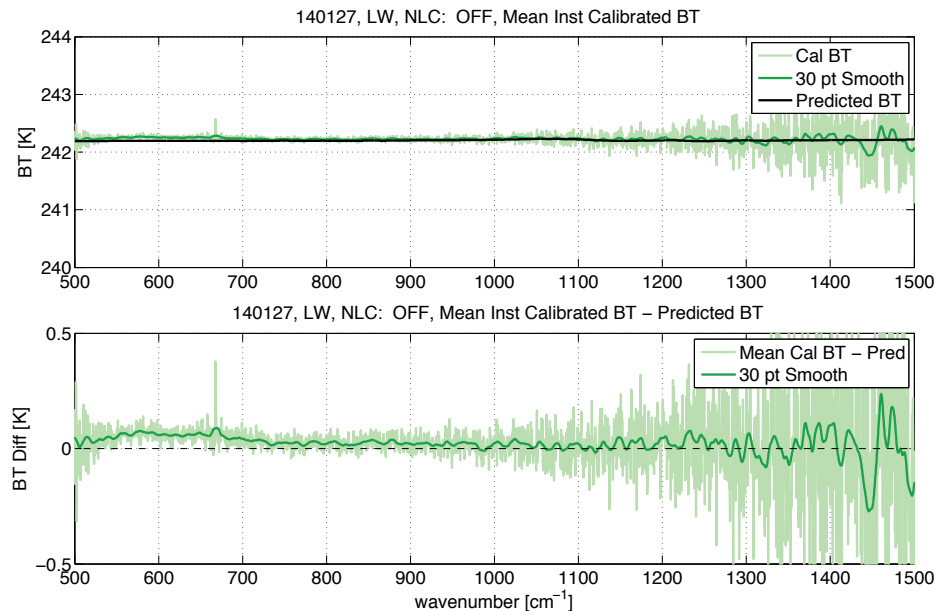


Figure 62: Long-wave detector brightness temperature results for the baseline end-to-end calibration verification dataset with CBB and OARS aperture rings unpowered. The OARS and the CBB cavity temperatures are approximately 243 K. The top panel shows the mean observed OARS brightness temperature, and the predicted OARS brightness temperature, with the difference provide in the bottom panel. A 30-point moving average filter has been used to smooth the observed brightness temperature.

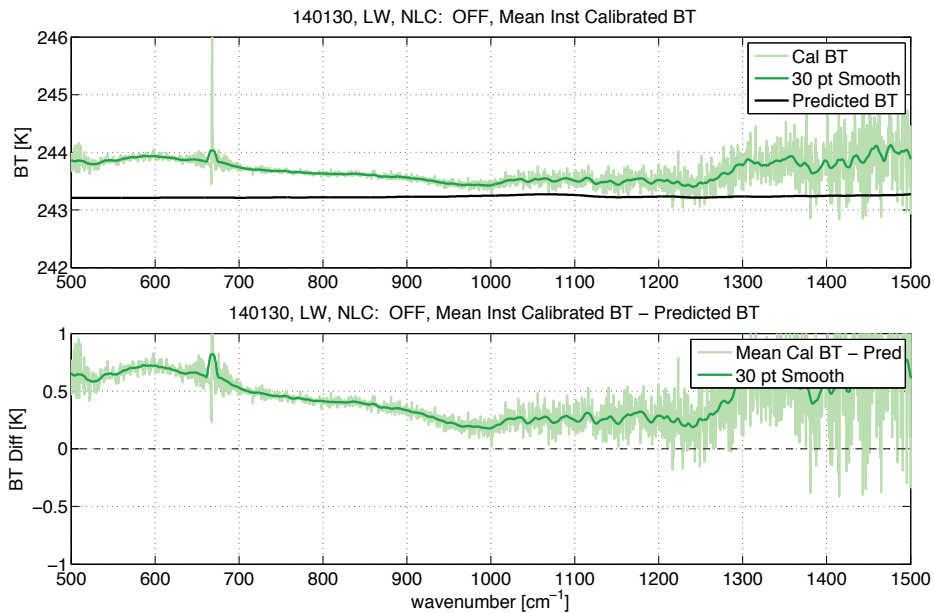


Figure 63: Long-wave detector brightness temperature results for the baseline end-to-end calibration verification dataset with CBB aperture ring unpowered, and the OARS aperture ring heated to 333 K. The OARS and the CBB cavity temperatures are approximately 243 K. The top panel shows the mean observed OARS brightness temperature, and the predicted OARS brightness temperature, with the difference provide in the bottom panel. A 30-point moving average filter has been used to smooth the observed brightness temperature.

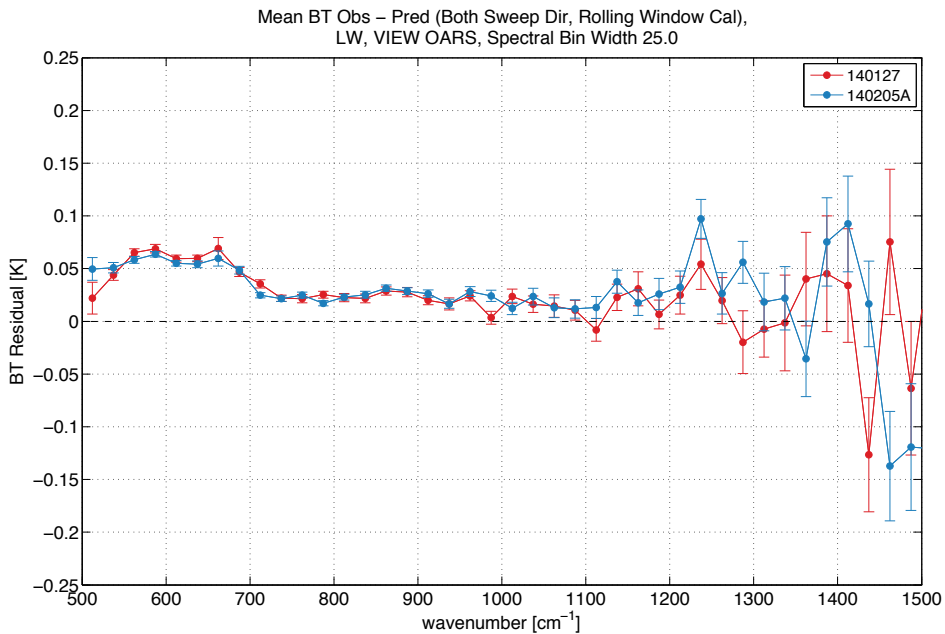


Figure 64: Long-wave detector brightness temperature residuals (observed – predicted) for end-to-end calibration verification datasets with the CBB and OARS aperture rings unpowered, baseline (red, dataset 140127), and after installation of the Z306 baffle at the aperture stop (blue, dataset 140205A). The OARS and the CBB cavity temperatures are approximately 243 K. The results have been spectrally averaged in 25 cm^{-1} wide bins for noise reduction. Error bars represent statistical error only.

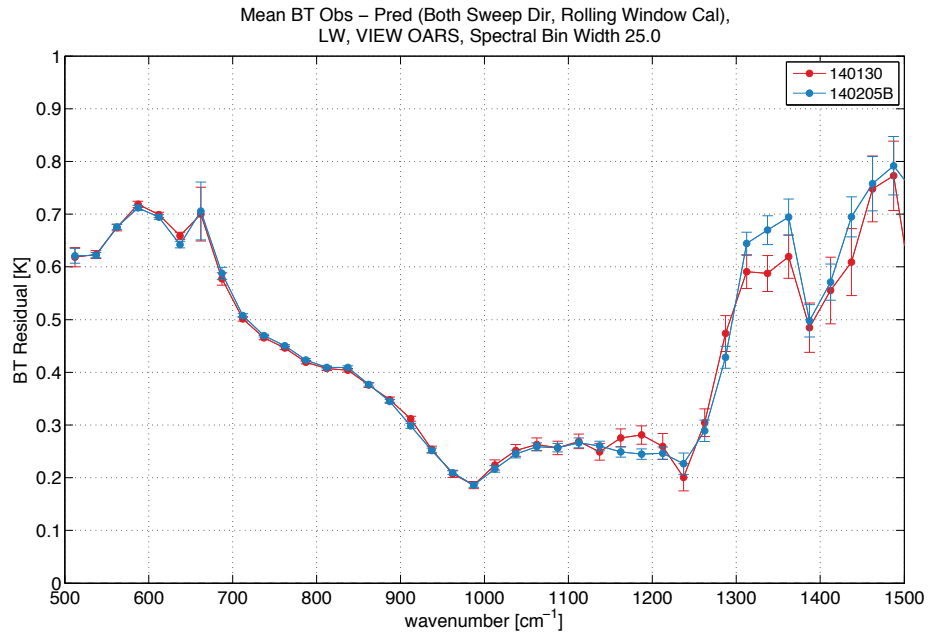


Figure 65: Long-wave detector brightness temperature residuals (observed – predicted) for end-to-end calibration verification datasets with the CBB aperture ring unpowered and the OARS aperture ring heated to 333 K, baseline (red, 140130), and after installation of the Z306 baffle at the aperture stop (blue, 140205B). The OARS and the CBB cavity temperatures are approximately 243 K. The results have been spectrally averaged in 25 cm⁻¹ wide bins for noise reduction. Error bars represent statistical error only.

To confirm that the heated ring assemblies were not causing additional vignetting issues, data was also collected with the AS baffle installed and the heated ring assemblies removed (dataset 140210). A comparison of the results for the configuration with the CBB and OARS aperture ring assemblies installed and unpowered, to those for the configuration with the aperture assemblies removed showed no difference in residual bias, confirming that the heated aperture ring assemblies were not causing additional vignetting (Figure 66).

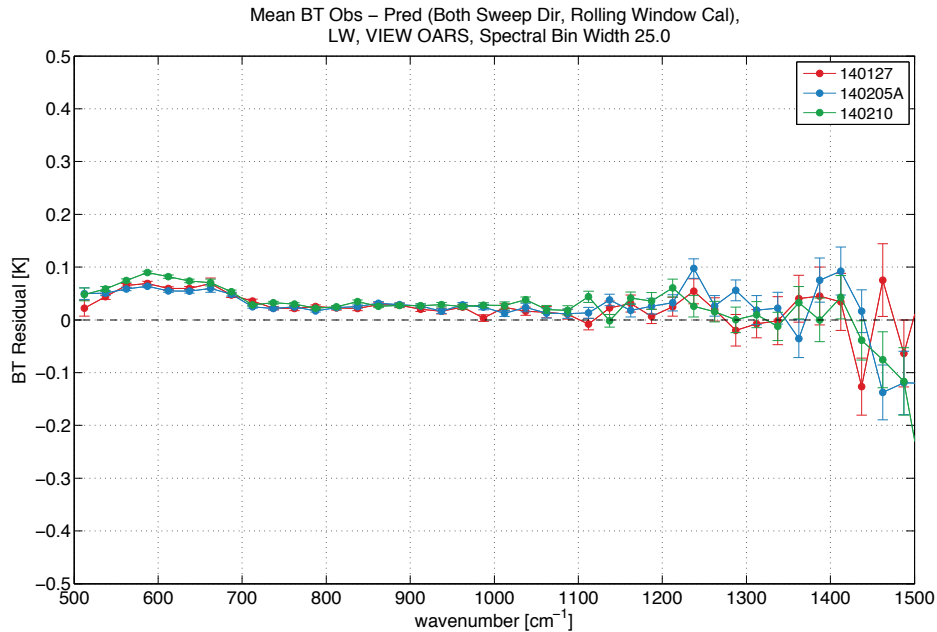


Figure 66: Long-wave detector brightness temperature residuals (observed – predicted) for end-to-end calibration verification datasets with the CBB and OARS aperture rings unpowered, baseline (red, dataset 140130), and after installation of the Z306 baffle at the aperture stop (blue, dataset 140205B). The result with the CBB and OARS entrance aperture rings removed is shown in green (dataset 14021). The OARS and the CBB cavity temperatures are approximately 243 K. The results have been spectrally averaged in 25 cm⁻¹ wide bins for noise reduction. Error bars represent statistical error only.

With no improvement in the long-wave bias with the installation of the aperture stop baffle, a series of alignment tests were conducted. The tests confirmed that the long-wave detector was sensitive to radiance from outside of the blackbody entrance apertures, and also indicated that the stray light contribution was scene mirror angle and blackbody position dependent. As noted earlier in the chapter, the field and aperture stop sizes, along with the afocal magnification of the fore-optics were specified to provide a beam size compatible with the blackbody entrance aperture size, with margin. The Zemax footprint diagram for the optical surface at the entrance to the blackbody clearly indicates significant margin (Figure 56).

The optical prescription is based on geometrical ray tracing and a top hat beam profile at the aperture stop. This consideration, along with the results of the testing, raised concerns that realistic imperfections in the optical elements, such as surface figure, alignment, and scattering required even more margin be added to the ray trace results, given the high radiometric accuracy requirements and impact of even very small stray light contributions.

Consequently, masks were designed to reduce the respective field and aperture stop sizes. During this process, an issue was identified with the field stop. The field stop is a transmitting element and the area for reflection at the field stop knife-edge is very small. However, the extent of the stopping surface of the field stop appeared to be potentially insufficient to effectively block stray light contributions. With consideration of extent of the field stop stopping surface relative to the size other optical elements in the fore-optics, it was concluded that it was very possible that light was being allowed to pass around the outside of the stop, as illustrated in Figure 67. Consequently, an extended baffle for the field stop was constructed. Like the aperture

stop baffle, the extended field stop baffle is painted with Z306. The field stop mask and extended stopping surface modification are shown in Figure 68, and the aperture stop mask is shown in Figure 69.

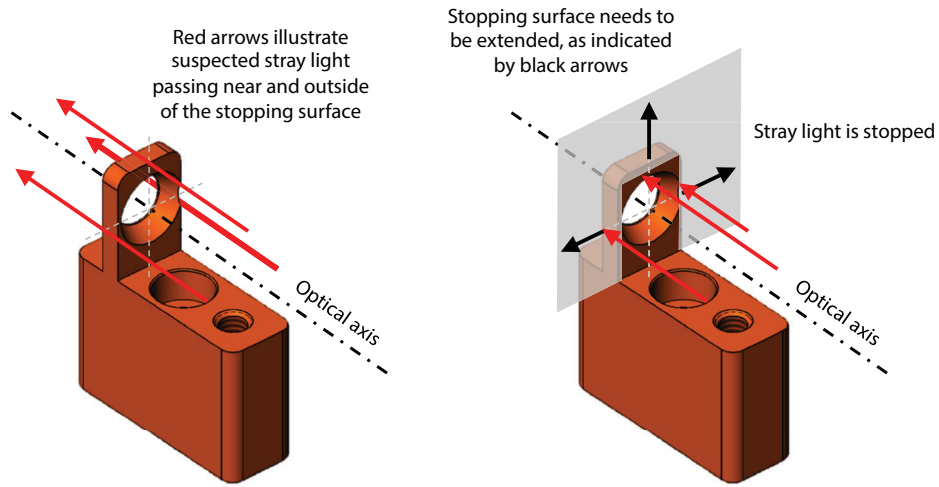
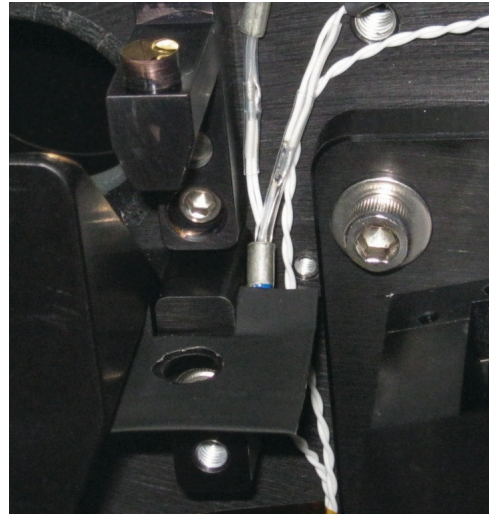


Figure 67: 3-d model of ARI field stop. In the diagram on the left, note the limited extent of the stopping surface, creating a potential susceptibility to stray light. The suggested modification is illustrated on the right.



(a)



(b)

Figure 68: (a) Field stop (FS) modification that both reduces diameter of field stop by 16%, and extends the stopping surface using Z306 painted aluminum tape. (b) Modified field stop with no reduction to field stop diameter, but with further extension of the stopping surface.

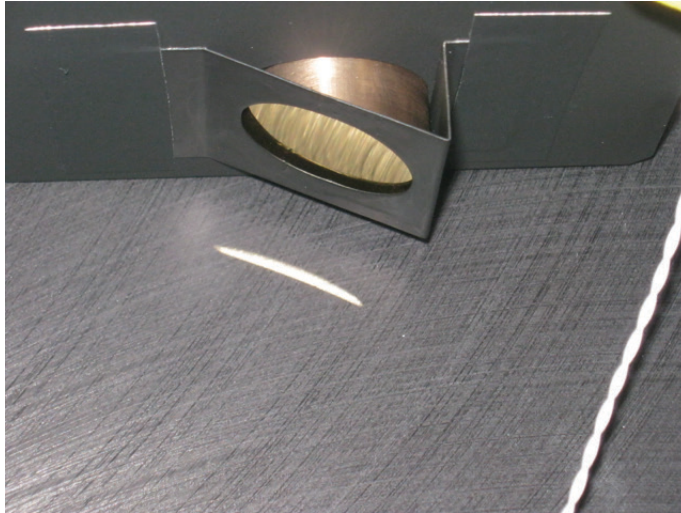


Figure 69: An aperture stop mask for testing the effect of reducing the aperture size was fabricated and installed in the ARI at the aperture stop at the M3 mirror. The aperture stop mask reduces the AS diameter by 25%.

Reduction of the aperture stop diameter had a very small effect on the long-wave stray light bias, with the largest improvement isolated to the 525 to 650 cm^{-1} region (Figure 70, dataset 140226). Conversely, reduction of the field stop size, without extension of the field stop surface resulted in a significant increase the residual error (Figure 70, dataset 140228A). This is because the reduction in the field stop diameter reduces the throughput associated with the prescribed beam, but without extending the field stop surface the same amount of stray light is still being transmitted past the field stop outside of the prescribed field of view. Thus the ratio of the out-of-field to in-field signal is larger for this configuration and a larger bias is observed.

Increasing the extent of the stop surface at the field stop resulted in a significant reduction in the long-wave bias. Results for a series of combinations of field stop and aperture stop sizes (nominal and reduced) are shown in Figure 71. There is little, if any, dependence on the field or aperture stop size with the improved field stop surface, and the spectral signature of the remaining residual error behaves like a small and highly emissive obstruction, monotonically increasing in brightness temperature with wavenumber. Recall that the results shown in Figure 65, Figure 70, and Figure 71, are for a configuration in which the OARS and CBB cavities are both controlled to 243 K, and only the entrance aperture ring heater at the OARS is heated (333 K). In this configuration, even a very small fractional view of the heated aperture ring will result in a significant calibration bias. This error can be modelled as a simple fractional obstruction. The model results are shown in Figure 72 and indicate a fractional obstruction of 0.11% at the CBB and 0.121% at the OARS. With both the CBB and OARS cold and at roughly the same temperature, the HBB reference has a comparatively small effect on the calibration accuracy. A fractional obstruction of 0.11% has been included for the HBB in the model.

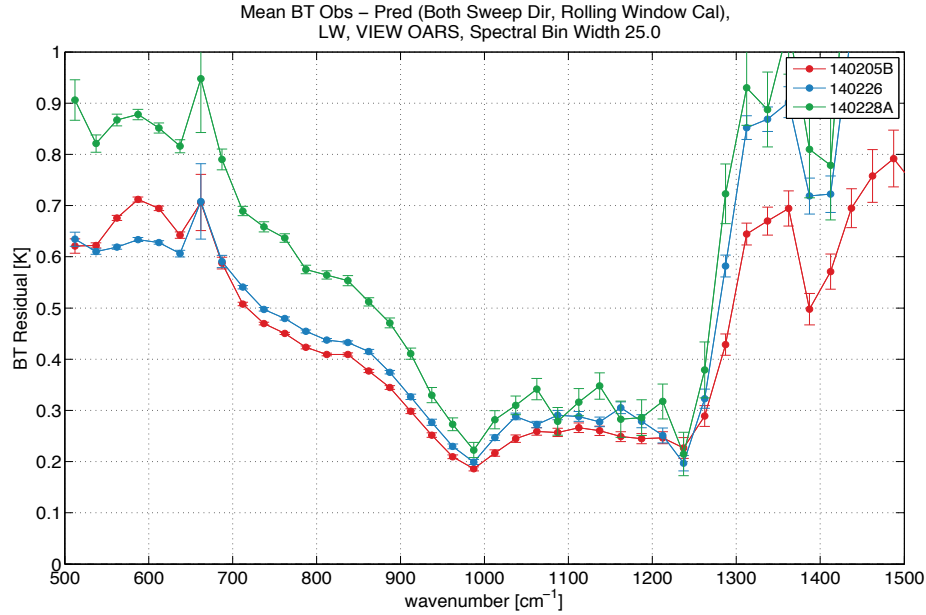


Figure 70: Impact of reduction of aperture and field stop sizes on long-wave residual brightness temperature error. The baseline result, with nominal aperture stop and field stop sizes, is shown in red (dataset 140205B). Reducing the aperture stop size (diameter reduced by 25%) provides a small improvement in the 500 – 650 cm^{-1} region (blue, dataset 140206). Reduction of the field stop size, without extension of the field stop surface resulted in a significant increase the residual error (green, dataset 140228A). The results have been spectrally averaged in 25 cm^{-1} wide bins for noise reduction. Error bars represent statistical error only.

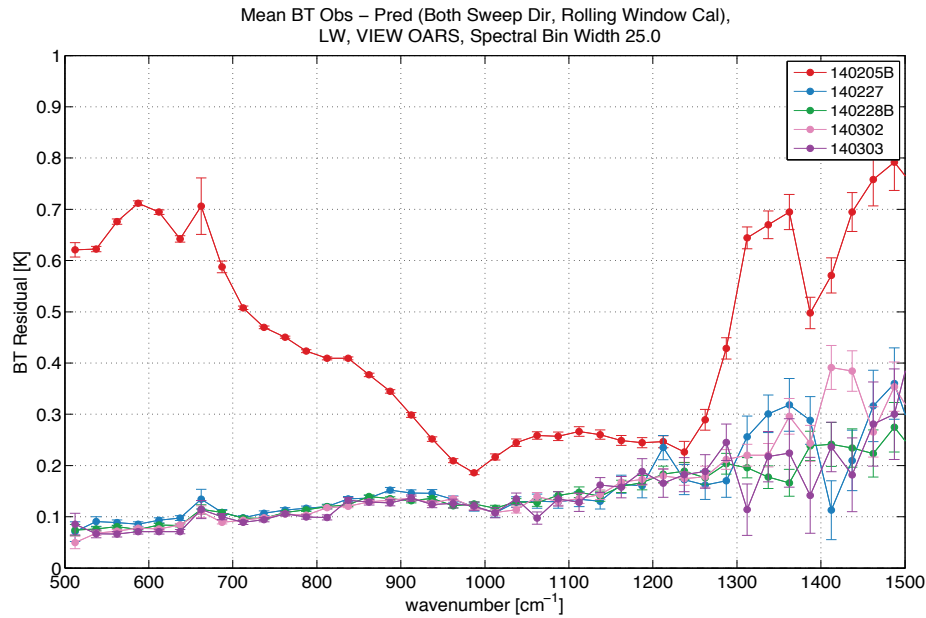


Figure 71: Increasing the extent of the stop surface at the field stop resulted in a significant reduction in the long-wave bias. The baseline result, with nominal aperture stop and field stop sizes, is shown in red (dataset 140205B). There is negligible dependence on the field or aperture stop size with the improved field stop surface installed; dataset 140227 (blue), reduced field stop diameter by 16%, reduced AS diameter by 25%; dataset 140228B (green), reduced AS diameter by 25%; dataset 140302 (pink), standard AS and FS sizes; dataset 140303 (purple), standard AS and FS sizes and extended baffling at field stop. The results have been spectrally averaged in 25 cm^{-1} wide bins for noise reduction. Error bars represent statistical error only.

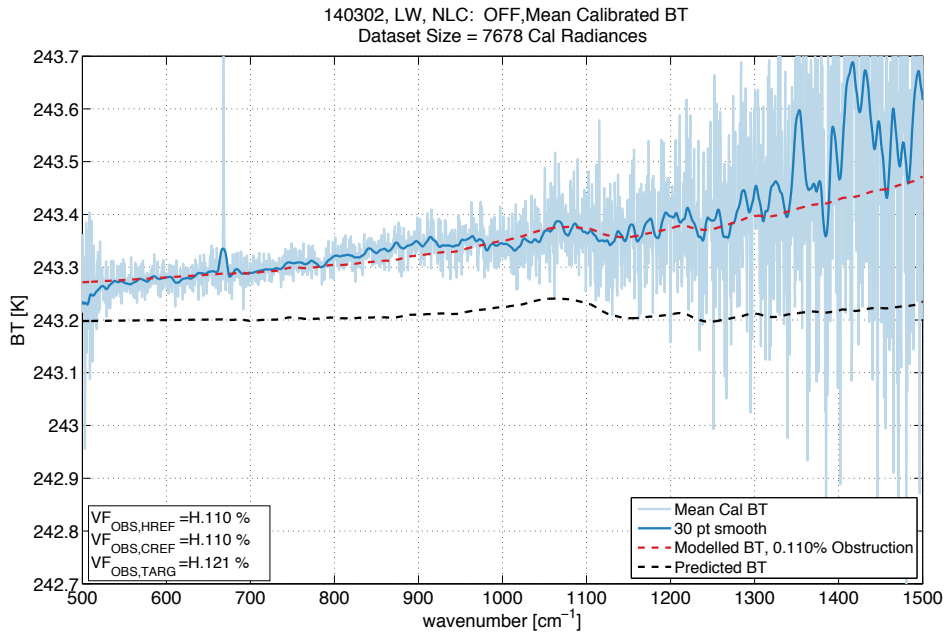


Figure 72: Long-wave detector brightness temperature result with OARS and CBB cavities at 243 K, OARS entrance aperture ring at 333 K, and CBB entrance aperture ring unheated (dataset 140302). The mean measured brightness temperature is shown in light blue, with the modelled measurement in red, and predicted OARS brightness temperature in black. The modelled measurement includes a 0.110% view (with respect to total beam area) outside of the blackbody for the CBB and HBB, and 0.121% for the OARS. A 30-point moving average filter has been used to smooth the observed brightness temperature. Note that the spectrally resolved brightness temperatures are not flat because the emissivity is not equal to one.

While having only the OARS (or only the CBB) entrance aperture ring heated provides a configuration that is very sensitive to stray light and particularly useful for diagnostics, operating with both entrance aperture rings at ambient represents the nominal operational configuration for the instrument. The long-wave brightness temperature residual for this configuration with improved aperture and field stops is shown in Figure 73 (dataset 140305B). Note that even though the improved baffling at the aperture stop was retained, tests showed only marginal improvement associated with the addition of the improved baffling at the aperture stop, and the majority of the improvement is due to improved rejection at the field stop. The baseline result (dataset 140127) with the original aperture and field stops is included for comparison. The model results for this configuration are shown in Figure 74. For completeness, the DTGS results are included in Figure 75.

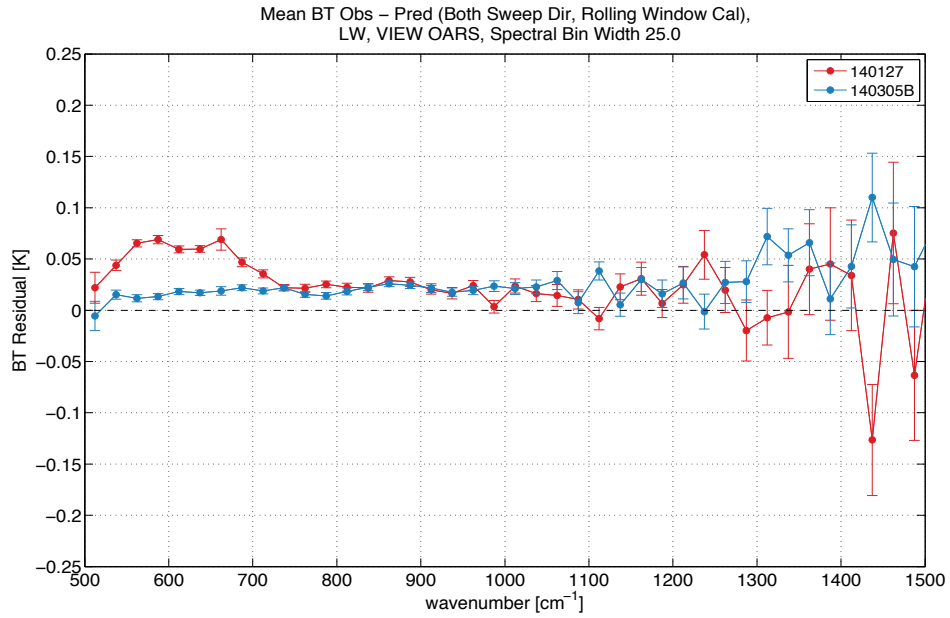


Figure 73: Long-wave brightness temperature residual with both entrance aperture rings at ambient. This configuration represents the nominal operational configuration for the instrument. The baseline result, with nominal aperture stop and field stop sizes, and no additional baffling at the aperture or field stop is shown in red (dataset 140127). With the improved aperture and field stops, only a small residual remains (blue, dataset 140305B). The remaining residual behaves like that due to a small obstruction, monotonically increasing in brightness temperature with wavenumber. The results have been spectrally averaged in 25 cm⁻¹ wide bins for noise reduction. Error bars represent statistical error only.

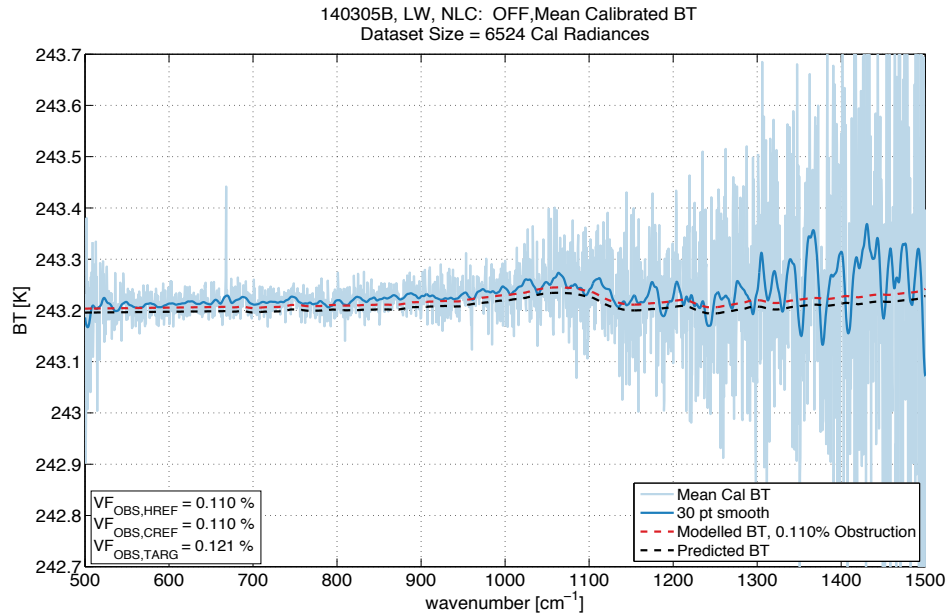


Figure 74: Long-wave detector brightness temperature result with OARS and CBB cavities at 243 K, OARS and CBB entrance aperture rings unheated (dataset 140305B). The mean measured brightness temperature is shown in light blue, with the modelled measurement in red, and predicted OARS brightness temperature in black. The modelled measurement includes a 0.110% view (with respect to total beam area) outside of the blackbody for the CBB and HBB, and 0.121% for the OARS. A 30-point moving average filter has been used to smooth the observed brightness temperature.

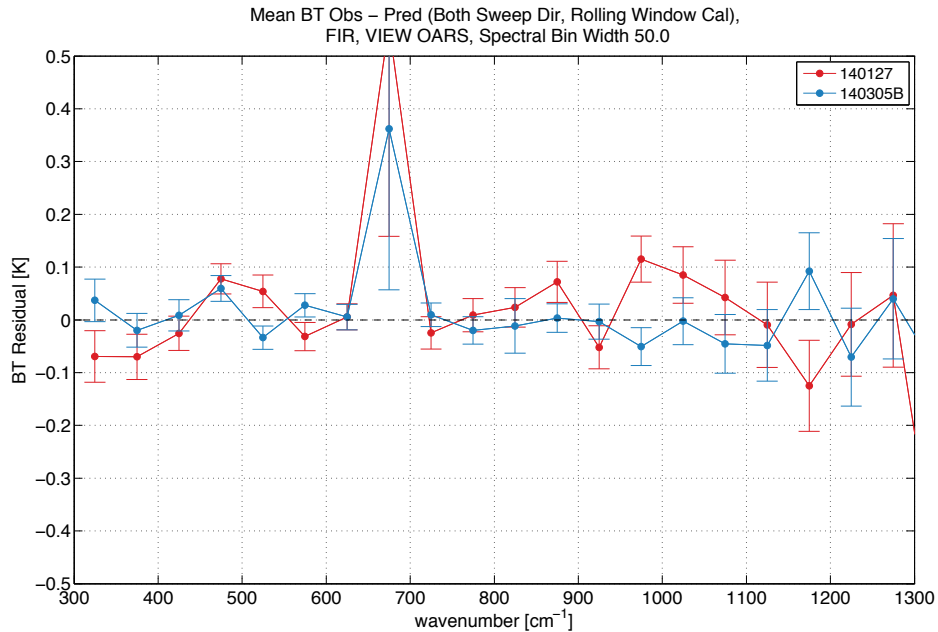


Figure 75: DTGS brightness temperature residual with both entrance aperture rings at ambient. This configuration represents the nominal operational configuration for the instrument. The baseline result, with nominal aperture stop and field stop sizes, and no additional baffling at the aperture or field stop is shown in red (dataset 140127). The result with improved aperture and field stops is shown in blue (dataset 140305B). Due to the higher noise in the DTGS measurement, the average size has been increased to 50 cm^{-1} , and the low SNR spectral regions at the edge of the bands have been omitted from the plot. The results have been spectrally averaged in 50 cm^{-1} wide bins for noise reduction. Error bars represent statistical error only.

3.3 Shear, field angle, and non-uniform scene

The shape of the spectral signature in the long-wave residual, prior to improving the rejection at the field stop, is noteworthy. As noted in the previous section, for a calibration error that is due to contributions from a small, but spectrally uniform obstruction, one would expect the error to smoothly increase in brightness temperature with wavenumber. The spectral emissivity of the obstruction will contribute to the shape of the residual, but an extreme spectral dependence in emissivity across the spectral band of interest would be required to produce the spectral signature of the observed residual error. This spectral dependence does not correspond to the materials at any of the candidate surfaces (Noryl, black anodized aluminum, bare aluminum, Z306).

To characterize the bias in further detail, it was useful to collect and examine data for a small range of scene mirror angles across the OARS. With the HBB at the 12:00 position (SSM angle of 0°), the CBB at the 3:00 position (SSM angle of 90°), and the OARS at the 9:00 position (SSM angle of 270°), and no additional baffling at the field stop, data was collected for the OARS at scene mirror angles of 267° to 271° at 1° increments. For small changes in scene mirror angle, changing the scene mirror angle for a fixed 9:00 OARS position is approximately equivalent to a vertical shift in the OARS position for a constant scene mirror angle (roughly 1.8 mm shift per 1° of scene mirror rotation). In this test, the OARS entrance aperture ring was maintained at 333 K and the CBB entrance aperture ring heaters were unpowered.

The results indicated a shift in ZPD position for the OARS measurement that was dependent on the scene mirror angle. The interferogram shift resembled a shift due to a sample position error with the size of the sample position error dependent on the scene select mirror angle.

Angular misalignment, commonly referred to as tilt, in a plane mirror interferometer produces an optical path difference that is a function of the spatial position in the interferometer pupil. Shear in a retroreflector-based interferometer adds an optical path difference that is a function of the angle of propagation in the interferometer. Thus, tilt is an aperture effect while shear is a field effect [25]. Figure 76(a) illustrates that no OPD results from the wavefront shear for rays propagating parallel to the optical axis. It can be shown via simple geometry that the optical path length is the same for the original and sheared beam. In this case, only a pure offset of the wave occurs.

However, this does not hold true for off-axis rays, as shown in Figure 76(b). A mechanical displacement ΔY_M of the retroreflector results in a wavefront shear of ΔY , which is no longer perpendicular to the optical axis. The displacement ΔY can be decomposed into two contributions: one along the optical axis and the other perpendicular to the optical axis. The component along the optical axis is the additional optical path difference for the ray due to shear and creates a sample position error that is dependent on angle of propagation through the interferometer.

The sizing of the fore-optics mirrors, and the original field stop design allowed for transmission of incident radiance at field angles greater than the prescribed maximum field angle. These contributions from outside of the prescribed field were seemingly rejected in the FIR aft-optics, but transmitted by the IR aft-optics. It is useful to consider a simple representation of instrument field of view at the entrance to the blackbody that is comprised of two contributions:

- The prescribed footprint which only views the cavity, with large margin between the radius of the footprint and the cavity entrance aperture;
- A stray light footprint that is significantly off-axis.

The simple model, with the optical axis centered in the blackbody aperture is shown in Figure 77. Small shifts of the blackbody cavity that are less than the margin between the radius of the prescribed footprint and the blackbody entrance aperture radius will not change the uniformity of the field of view associated with the prescribed footprint, and the effective view angle θ_1 for the prescribed footprint remains zero. However, the field of view for the stray light footprint may become significantly non-uniform for these small shifts. A change in scene uniformity can be considered as a change in the radiometric centroid of the field of view, which results in a shift of the effective angle θ_2 for the stray light footprint. This is illustrated in Figure 78 and Figure 79. A change in the effective off-axis angle for the stray light footprint, coupled with a static shear of the interferometer is a possible cause of the observed sample position error. Further tests and analysis need to be completed to verify this hypothesis.

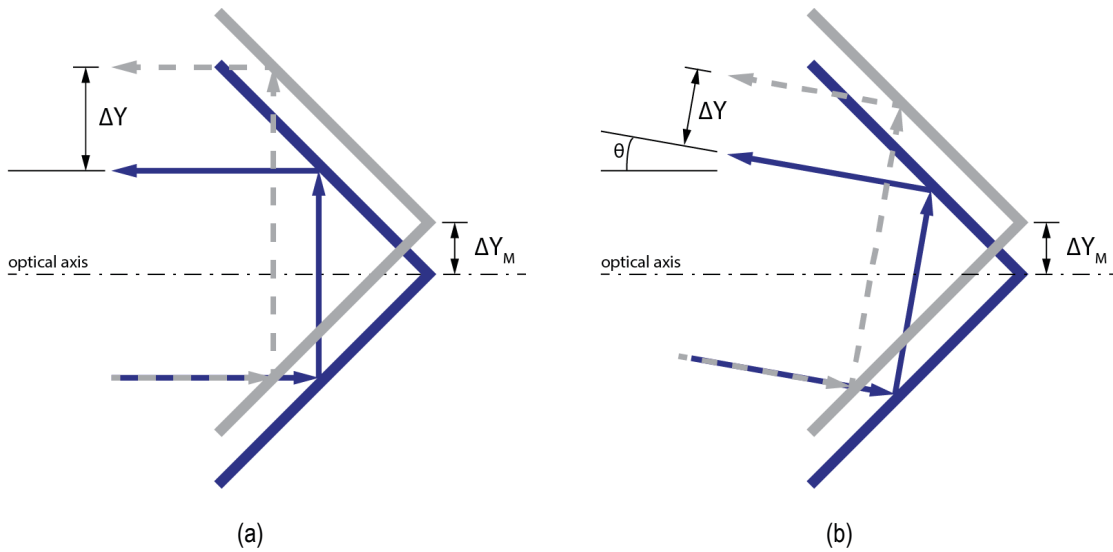


Figure 76: (a) Cube corner shear produces only a pure offset of the wavefront for rays propagating parallel to the optical axis. (b) Cube corner shear for off-axis rays results in a wavefront shear that is no longer perpendicular to the optical axis, and results in an additional optical path difference [25].

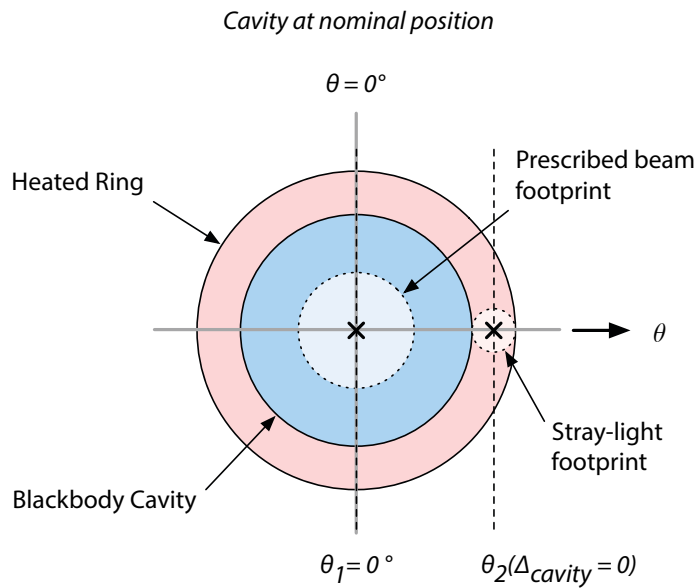


Figure 77: A simple representation of instrument field of view at the entrance to the blackbody that is comprised of the prescribed footprint and an off-axis footprint associated with stray light passing the field stop.

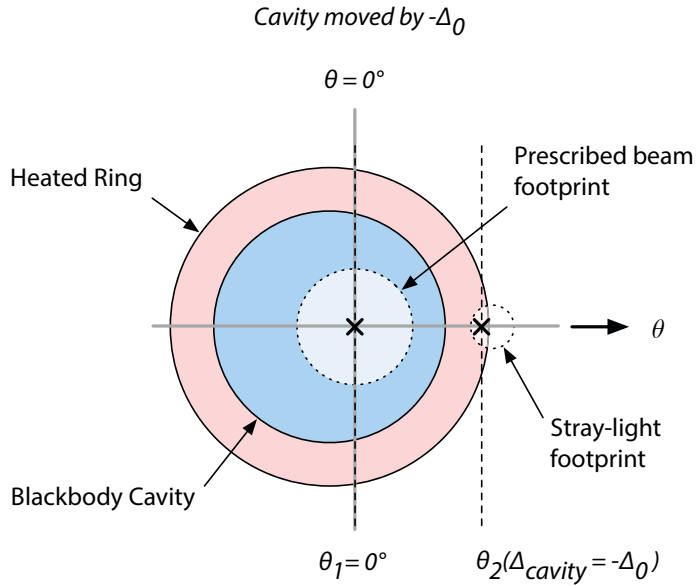


Figure 78: A small shift in the blackbody position ($-\Delta_0$) changes the uniformity and the effective angle for the stray light footprint.

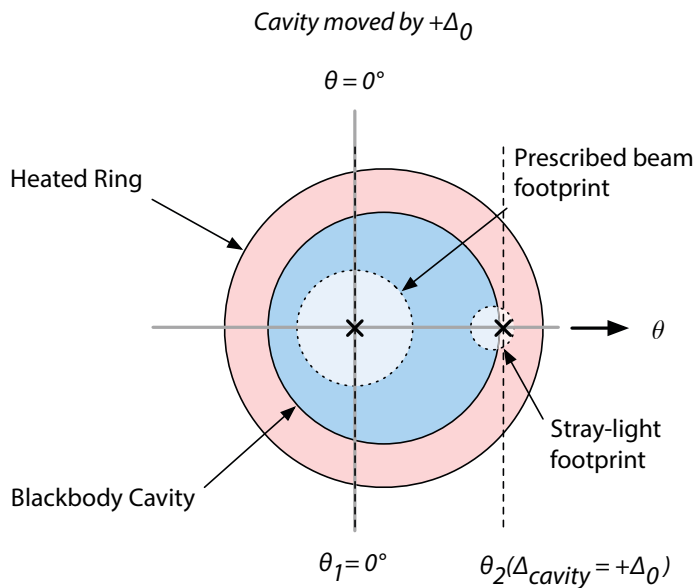


Figure 79: A small shift in the blackbody position ($+\Delta_0$) changes the uniformity and the effective angle for the stray light footprint.

3.4 Recommendations for future designs

During this testing, it became evident that even very small stray-light contributions are critical with respect to the high level of absolute accuracy required. Future designs should include an emphasis on aperture and field stop design and make use of high emissivity coatings in critical optical areas. The optical design of the ARI fore-optic telescope is fundamentally sound, and the long-wave calibration bias was the result of an oversight in the implementation of the field stop. While the physical aperture and field stops are located in the fore-

optics, it is also recognized that the aft optics have a role in stray light rejection, not simply capturing signal energy.

The addition of thermally controlled entrance aperture ring assemblies at the OARS and CBB were extremely valuable in the diagnosis and resolution of the long-wave bias due to radiance contributions from outside of the prescribed field and aperture stops. This feature should be included in future designs and could prove extremely useful for on-orbit diagnostics for a flight instrument.

4 Polarization induced calibration biases

It is useful to begin this chapter with a brief review of the mathematical representation of polarized light and the polarization ellipse. The reader is referred to Hecht [127], Collett [128], or Goldstein [129] for a more detailed explanation of the material summarized here.

Light can be represented mathematically in terms of the x- and y-axis projections of the transverse electrical field vector, for light propagating parallel to the z-axis. The propagation of the transverse field is shown in Figure 80.

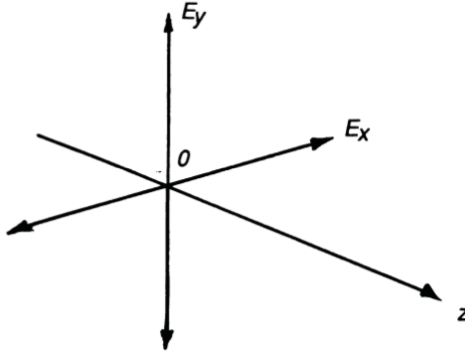


Figure 80: Propagation of the transverse optical field [129].

The transverse components are given by:

$$E_x(z, t) = E_{0x} \cos(\tau + \delta_x), \quad (4.1)$$

$$E_y(z, t) = E_{0y} \cos(\tau + \delta_y). \quad (4.2)$$

In equations (4.1) and (4.2), $\tau = \omega t - kz$ is the space-time propagator, where ω is the angular frequency and k is the wave vector; the subscripts x and y indicate the directions of the transverse axes, E_{0x} and E_{0y} are the maximum amplitudes of the projection of the electric field vector on the x and y axes; and δ_x and δ_y are the corresponding phases. The pattern traced out by the tip of the electric field vector in the x-y plane is described by:

$$\frac{E_x^2}{E_{0x}^2} + \frac{E_y^2}{E_{0y}^2} - 2 \frac{E_x E_y}{E_{0x} E_{0y}} \cos \delta = \sin \delta. \quad (4.3)$$

In Eq. (4.3), $\delta = \delta_y - \delta_x$ is the phase difference between the two components and the time-space propagator has been explicitly eliminated. Regardless, the electric field components E_x and E_y continue to be space and time dependent, and space and time define an instant on the curve described by Eq. (4.3).

Equation (4.3) is the equation of an ellipse with the major axis at an angle ψ to the x-axis, and is referred to as the polarization ellipse. The polarization ellipse can also be expressed in terms of the orientation angle ψ

($0 \leq \psi \leq \pi$) and the ellipticity angle χ ($-\pi/4 < \chi \leq \pi/4$). These angles can be defined in terms of the parameters of the polarization ellipse [128, 129]:

$$\tan(2\psi) = \frac{2E_{0x}E_{0y}}{E_{0x}^2 - E_{0y}^2} \cos \delta, \quad (4.4)$$

$$\sin(2\chi) = \frac{2E_{0x}E_{0y}}{E_{0x}^2 + E_{0y}^2} \sin \delta. \quad (4.5)$$

Equations (4.4) and (4.5) can be expressed as purely geometrical equations via the introduction of the auxiliary angle α , which represents the relation between E_{0x} and E_{0y} :

$$\tan(2\psi) = \tan(2\alpha) \cos \delta, \quad (4.6)$$

$$\sin(2\chi) = \sin(2\alpha) \sin \delta, \quad (4.7)$$

where:

$$\tan \alpha = \frac{E_{0x}}{E_{0y}}. \quad (4.8)$$

The limits on α and δ in equations (4.6) and (4.7) are $0 \leq \alpha \leq \pi/2$ and $0 \leq \delta < 2\pi$. The rotated polarization ellipse is shown in Figure 81.

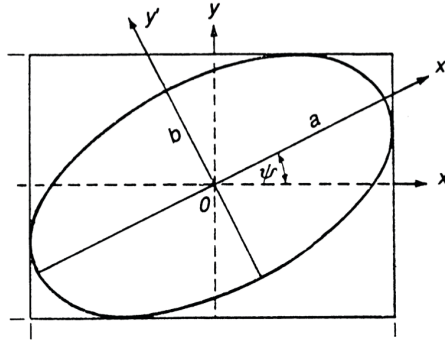


Figure 81: The rotated polarization ellipse [129].

When considering the calibration bias due to polarization, representing the scene select mirror and sensor as a series pair of partial polarizers helps provide insight into the problem. This is illustrated in Figure 82. The sensor polarization sensitivity includes contributions from all optical components within the sensor. The first polarizer represents the polarization due to the scene select mirror and the second polarizer represents the sensor contribution.

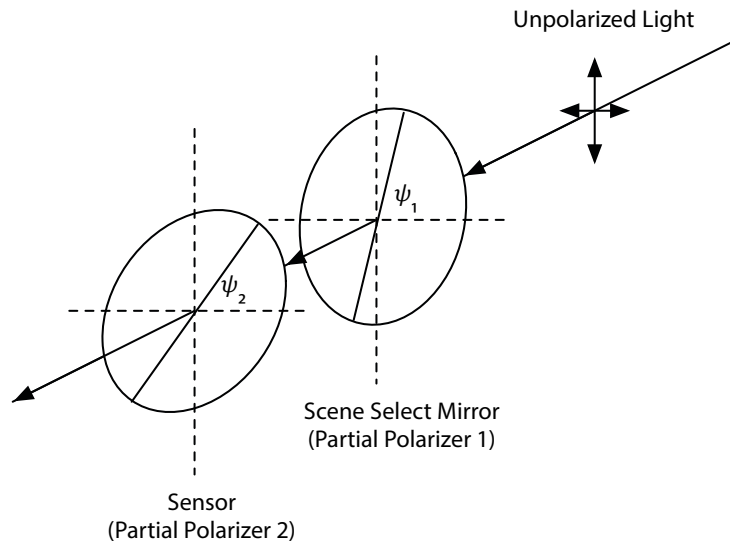


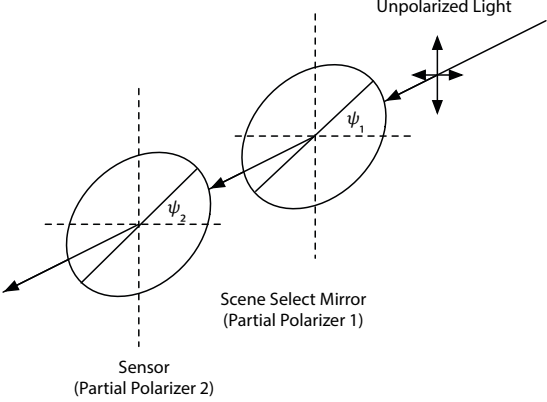
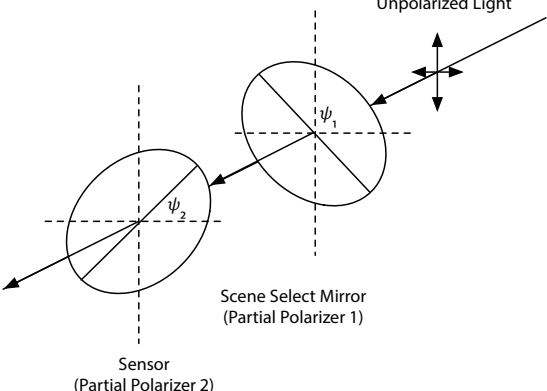
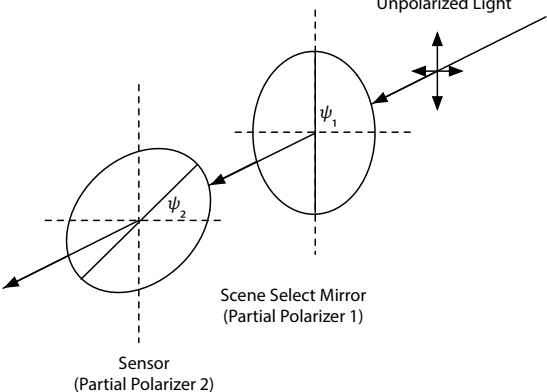
Figure 82: Representing the scene select mirror and sensor as a series pair of partial polarizers is useful when considering the calibration bias due to polarization. The first polarizer represents the scene select mirror, and the second polarizer represents the combined instrument polarization sensitivity due to the rest of the optical components within the sensor.

As presented in Chapter 1 (Section 1.3), a scene select mirror is used in the ARI to direct radiance from the calibration references, calibration verification sources, or the scene into the instrument. Mirrors inherently introduce polarization that depends both on the angle of incidence and the orientation of the mirror. The ARI employs a 45° scene mirror rotated about the local optical axis such that the incident angle at the scene mirror is independent of scene mirror rotation angle (Chapter 1, Figure 9). Thus, the amount of partial polarization introduced by the scene mirror is constant and independent of scene mirror rotation angle. However, the orientation of the partial polarization introduced by the scene select mirror does depend on the rotational position of the scene select mirror. The instrument also has a polarization sensitivity, which is primarily due to the beamsplitter, but also includes contributions from the other optical elements within the sensor. The polarization sensitivity and polarization plane of the instrument is constant and independent of the scene mirror rotation angle.

While the level of polarization is constant for the scene select mirror and sensor individually, the combined polarization due to the scene select mirror and the sensor is a function of the relative angle between the scene select mirror polarization axis at angle ψ_1 , which changes with rotation of the scene select mirror, and the instrument polarization axis, which is fixed and oriented at a constant angle, ψ_2 . Thus, the combined polarization depends on the scene mirror rotation angle, and the rotation of the reflection plane at the scene mirror will create a modulation of the measured signal. When the major axes of the polarization ellipses for the scene select mirror and sensor are aligned, transmission of unpolarized light is at a maximum (T_{\max}). When they are perpendicular the transmission is at a minimum (T_{\min}). For a 360° rotation of the scene select mirror, there will be two maxima and two minima. For the same 360° scene select mirror rotation, there will also be four scene select mirror angles for which the major axes of the polarization ellipses are at 45° to one another.

At these angles, the transmission will be the mean of the minimum and maximum response. A summary of these conditions is provided in Table 8.

Table 8: Relative orientation of scene select mirror and sensor polarizations, and resulting transmission for unpolarized light.

Illustration	Relative orientation of SSM and sensor polarization	Transmission of unpolarized light
 <p>Unpolarized Light</p> <p>Scene Select Mirror (Partial Polarizer 1)</p> <p>Sensor (Partial Polarizer 2)</p>	$ \psi_1 - \psi_2 = 0^\circ$ $ \psi_1 - \psi_2 = 180^\circ$	T_{\max}
 <p>Unpolarized Light</p> <p>Scene Select Mirror (Partial Polarizer 1)</p> <p>Sensor (Partial Polarizer 2)</p>	$ \psi_1 - \psi_2 = 90^\circ$ $ \psi_1 - \psi_2 = 270^\circ$	T_{\min}
 <p>Unpolarized Light</p> <p>Scene Select Mirror (Partial Polarizer 1)</p> <p>Sensor (Partial Polarizer 2)</p>	$ \psi_1 - \psi_2 = 45^\circ$ $ \psi_1 - \psi_2 = 135^\circ$ $ \psi_1 - \psi_2 = 225^\circ$ $ \psi_1 - \psi_2 = 315^\circ$	$\frac{1}{2}(T_{\max} + T_{\min})$

The potential for polarization errors contributing significantly to the uncertainty budget of infrared remote sounding sensors has been well recognized, particularly due to polarization dependent scene select mirrors and grating based instruments [130-134].

The Atmospheric Emitted Radiance Interferometer (AERI), Scanning High-resolution Interferometer Sounder (S-HIS), and the Cross-track Infrared Sounder (CrIS) all employ a gold 45° scene mirror configuration similar to that used with the Absolute Radiance Interferometer. The contribution of polarization-induced error to the calibration uncertainty is specified as less than 0.1% ($k = 3$) for the AERI [135]. Early test and analysis of the S-HIS and CrIS sensors had estimated the contribution of polarization induced error to the calibration uncertainty budget for each instrument to be less than 0.05%, which corresponds to an equivalent brightness temperature error of less than 0.04 K prior to any correction [136]. However, recent analyses indicate that the effect may be closer to 0.1 K [62, 137].

4.1 Theoretical model

In this section, we follow the approach described by Pagano et al [131] for the Atmospheric Infrared Sounder (AIRS). Similar to the ARI, the AIRS employs the use of a barrel-roll scene mirror that rotates about an axis that is 45° from the mirror normal, preserving the angle of incidence of the mirror and optical axis for all scene views. Key steps in the derivation of the expression for the calibration bias due to polarization are included here. A more complete derivation is included in Appendix A.

As noted earlier in the chapter, the orientation of the polarization axis of the scene select mirror changes with scene mirror rotation. When coupled with the polarization sensitivity of the sensor, this produces a radiometric modulation of the detected signal that is dependent on the rotation angle of the scene select mirror.

For this problem, we assume that the instrument has a polarization dependent transmission and the scan mirror has a polarization dependent reflectance. Equation (4.9) describes the total signal intensity generated for an arbitrary, unpolarized scene or calibration radiance observed at a scene selection mirror angle δ and a sensor polarization axis at an angle α . Note that the individual intensity terms in Eq. (4.9) follow from squaring the components of the scene selection mirror p-polarization and s-polarization amplitudes along both the maximum and minimum axis of the instrument transmission.

$$\begin{aligned}
V_{\delta} = & \frac{L_{\delta}}{2} r_p \left[t_{\max} \cos^2(\delta - \alpha) + t_{\min} \sin^2(\delta - \alpha) \right] \\
& + \frac{L_{\delta}}{2} r_s \left[t_{\max} \sin^2(\delta - \alpha) + t_{\min} \cos^2(\delta - \alpha) \right] \\
& + \frac{B_{SSM}}{2} \varepsilon_p \left[t_{\max} \cos^2(\delta - \alpha) + t_{\min} \sin^2(\delta - \alpha) \right] \\
& + \frac{B_{SSM}}{2} \varepsilon_s \left[t_{\max} \sin^2(\delta - \alpha) + t_{\min} \cos^2(\delta - \alpha) \right] \\
& + V_{inst}.
\end{aligned} \tag{4.9}$$

In Eq. (4.9), r_p and r_s are the reflectivity (not the reflection coefficients, which act on the field) of the scene mirror for the parallel and perpendicular polarization states, respectively; ε_p and ε_s are the corresponding emissivities and are equal to $1 - r_p$ and $1 - r_s$, since the transmittance for a metal mirror is zero; and t_{\max} and t_{\min} are respectively the intensity transmission on the major and minor axis of the instrument polarization ellipse, with the major axis oriented at angle α , and both α and δ are specified with respect to the nadir view (refer to Figure 83). The model depends on the relative orientation of the scene mirror and sensor

polarization axes, not the absolute angular position of either. Hence, the choice of the 0° position is arbitrary, and the angular position of the nadir view was chosen as the 0° reference for convenience. The total signal, V_δ , at scene mirror angle δ is composed of the scene radiance, L_δ , as attenuated by the scene mirror reflectance and the radiant emission from the scene mirror, where B_{SSM} is a radiance from a blackbody at the temperature of the scene selection mirror. Both contributions are polarized after reflection or emission from the scene select mirror, and are thus transmitted differently by the instrument, which has a polarization dependent transmission. For simplicity, we have assumed the detector responsivity is unity, since that term will divide out when the signals are substituted into the complex calibration equation.

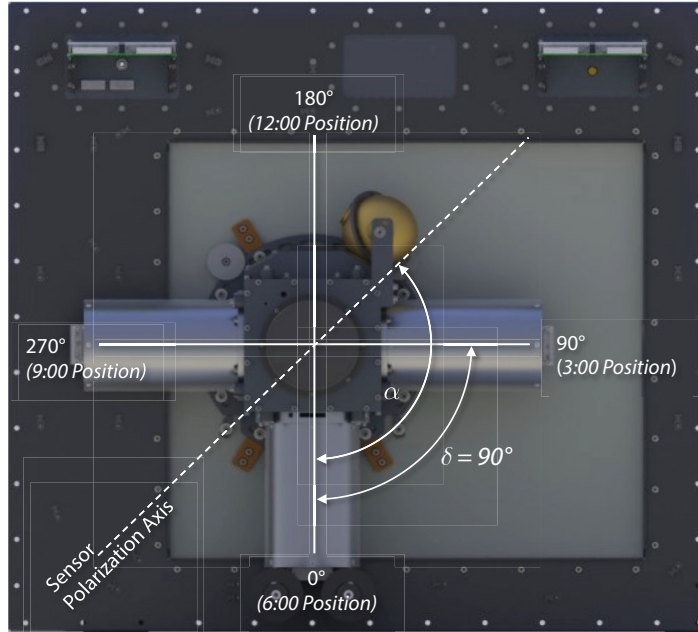


Figure 83: The coordinate system used for the sensor polarization angle (α) and the scene selection mirror angle (δ) is illustrated, with an example scene selection mirror angle corresponding to $\delta = 90^\circ$ indicated. A clock face position reference is also provided.

Using geometric identities, one can show:

$$\begin{aligned}
 a \cdot \cos^2(\theta) + b \cdot \sin^2(\theta) &= \frac{1}{2}(a+b)[\cos^2(\theta) + \sin^2(\theta)] \\
 &\quad + \frac{1}{2}(a-b)[\cos^2(\theta) - \sin^2(\theta)] \quad (4.10) \\
 &= \frac{1}{2}(a+b) + \frac{1}{2}(a-b)\cos(2\theta),
 \end{aligned}$$

and Eq. (4.9) can be re-written as,

$$V_{\delta} = \left[(L_{\delta} - B_{SSM}) \frac{1}{2} (r_p + r_s) + B_{SSM} \right] \frac{1}{2} (t_{\max} + t_{\min}) + (L_{\delta} - B_{SSM}) \frac{1}{2} (r_p - r_s) \frac{1}{2} (t_{\max} - t_{\min}) \cos 2(\delta - \alpha) + V_{inst} . \quad (4.11)$$

Finally, equation (4.11) can be further simplified:

$$V_{\delta} = (L_{\delta} - B_{SSM})rt + B_{SSM}t + (L_{\delta} - B_{SSM})p_r p_t rt \cos 2(\delta - \alpha) + V_{inst} , \quad (4.12)$$

where,

$$r = \frac{1}{2} (r_p + r_s) , \quad (4.13)$$

$$t = \frac{1}{2} (t_{\max} + t_{\min}) , \quad (4.14)$$

$$p_r = \frac{r_p - r_s}{r_p + r_s} , \quad (4.15)$$

$$p_t = \frac{t_{\max} - t_{\min}}{t_{\max} + t_{\min}} . \quad (4.16)$$

In equations (4.12) to (4.16), r is the scene select mirror reflectance, t is the sensor transmittance, p_r is the scene select mirror polarization, and p_t is the sensor polarization. An expression for the polarization-induced calibration error can be derived by substituting the expression for the total signal generated for an arbitrary, unpolarized scene or calibration radiance observed at a scene selection mirror angle (4.12) into the complex calibration equation.

For convenience, the complex calibration equation is reproduced here,

$$L_S(\sigma_k) = (L_H(\sigma_k) - L_C(\sigma_k)) \operatorname{Re} \left\{ \frac{\mathcal{S}_S(\sigma_k) - \mathcal{S}_C(\sigma_k)}{\mathcal{S}_H(\sigma_k) - \mathcal{S}_C(\sigma_k)} \right\} + L_C(\sigma_k) . \quad (4.17)$$

Therefore,

$$\begin{aligned} L_{\delta,S}(\sigma_k) &= L_S(\sigma_k) + E_p(\sigma_k) \\ L_S(\sigma_k) &= L_{\delta,S}(\sigma_k) - E_p(\sigma_k) , \end{aligned} \quad (4.18)$$

where $L_S(\sigma_k)$ is the correct calibrated radiance, $L_{\delta,S}(\sigma_k)$ is the calibrated radiance affected by the calibration bias due to polarization, and $E_p(\sigma_k)$ is the polarization induced error.

Substituting (4.12) into (4.17), and assuming non-complex spectral measurements for simplicity,

$$L_{\delta,S}(\sigma_k) = (L_H(\sigma_k) - L_C(\sigma_k)) \left[\frac{V_{\delta,S}(\sigma_k) - V_{\delta,C}(\sigma_k)}{V_{\delta,H}(\sigma_k) - V_{\delta,C}(\sigma_k)} \right] + L_C(\sigma_k). \quad (4.19)$$

While equation (4.19) does not properly represent the complex nature of FTS observations and the complex calibration methodology, that complication is not needed to characterize the polarization error.

The total signal V_δ generated for an arbitrary, unpolarized scene or calibration radiance observed at a scene selection mirror angle δ is provided in (4.12), and can be substituted into (4.19) for the scene ($V_{\delta,S}$), cold calibration reference ($V_{\delta,C}$), and hot calibration reference ($V_{\delta,H}$) measurements. For simplicity, we re-write equation (4.19) with these substitutions without the spectral dependence explicitly noted,

$$\begin{aligned} L_{\delta,S} &= (L_H - L_C) \left[\frac{V_{\delta,S} - V_{\delta,C}}{V_{\delta,H} - V_{\delta,C}} \right] + L_C \\ L_{\delta,S} &= (L_H - L_C) \left\{ \frac{(L_S - L_C) + p_r p_t \left[\begin{array}{l} L_S \cos 2(\delta_S - \alpha) - L_C \cos 2(\delta_C - \alpha) \\ - B_{SSM} [\cos 2(\delta_S - \alpha) - \cos 2(\delta_C - \alpha)] \end{array} \right]}{(L_H - L_C) + p_r p_t \left[\begin{array}{l} L_H \cos 2(\delta_H - \alpha) - L_C \cos 2(\delta_C - \alpha) \\ - B_{SSM} [\cos 2(\delta_H - \alpha) - \cos 2(\delta_H - \alpha)] \end{array} \right]} \right\} + L_C \\ L_{\delta,S} &= (L_S - L_C) \left\{ \frac{1 + \frac{p_r p_t}{L_S - L_C} \left[\begin{array}{l} L_S \cos 2(\delta_S - \alpha) - L_C \cos 2(\delta_C - \alpha) \\ - B_{SSM} [\cos 2(\delta_S - \alpha) - \cos 2(\delta_C - \alpha)] \end{array} \right]}{1 + \frac{p_r p_t}{L_H - L_C} \left[\begin{array}{l} L_H \cos 2(\delta_H - \alpha) - L_C \cos 2(\delta_C - \alpha) \\ - B_{SSM} [\cos 2(\delta_H - \alpha) - \cos 2(\delta_H - \alpha)] \end{array} \right]} \right\} + L_C. \end{aligned} \quad (4.20)$$

Note that for the ARI, the goal of the optical design is to eliminate the polarization induced calibration error, E_p . This is accomplished by separating the calibration references, verification source, and nadir viewport by 90° in scene select mirror rotation with each located 45° from the instrument polarization plane. Thus, $\delta_C - \alpha$, $\delta_H - \alpha$, $\delta_{OARS} - \alpha$, and $\delta_{SCENE} - \alpha$ are equal to 45° , and the $\cos 2(\delta - \alpha)$ terms are zero, and Eq. (4.20) reduces to the correct calibrated radiance that is absent of polarization induced calibration error:

$$\begin{aligned} L_{\delta,S} &= (L_S - L_C) \left\{ \frac{1 + \frac{p_r p_t}{L_S - L_C} \left[\begin{array}{l} L_S \cos 2(45^\circ) - L_C \cos 2(45^\circ) \\ - B_{SSM} [\cos 2(45^\circ) - \cos 2(45^\circ)] \end{array} \right]}{1 + \frac{p_r p_t}{L_H - L_C} \left[\begin{array}{l} L_H \cos 2(45^\circ) - L_C \cos 2(45^\circ) \\ - B_{SSM} [\cos 2(45^\circ) - \cos 2(45^\circ)] \end{array} \right]} \right\} + L_C \\ L_{\delta,S} &= (L_S - L_C) + L_C \\ L_{\delta,S} &= L_S. \end{aligned} \quad (4.21)$$

The scene select mirror reflectance and polarization, and instrument polarization parameters used in the model are shown in Figure 84. The spare ARI scene select mirror is scheduled for reflectance measurement (p- and s-plane at 45° incidence angle) at NIST, but the measurements have been delayed. In lieu of the ARI scene select mirror measurements, existing data for the reflectance from gold on diamond point turned aluminum was used. The long-wave limit of the measurement data was 500 cm⁻¹. Accordingly, the 500 cm⁻¹ values were assumed for the 200 – 500 cm⁻¹ region in the model. The instrument polarization was obtained from the 2-source with linear polarizer measurements, which are described in Section 4.3.2. With consideration for the responsivity of the DTGS and LW MCT detectors, the DTGS measurement was used for the spectral region from 300 – 650 cm⁻¹, the LW MCT measurement for the region above 950 cm⁻¹, and an average of the DTGS and LW MCT measurements for the 650 – 950 cm⁻¹ region. The DTGS measurement at 300 cm⁻¹ was used assumed for the spectral region below 300 cm⁻¹, as the degree of polarization measurement is affected by low signal to noise in this range.

Table 9: Polarization model parameters.

Temperatures		Value	Notes
Cold Cal Ref (CBB)	T_{CBB}	243 K	Temperature used for lab tests
Hot Cal Ref (HBB)	T_{HBB}	333 K	Temperature used for lab tests
Verification Target (OARS)	T_{OARS}	240 - 340 K	243 K and 333 K used for lab tests
Reflected Radiance, Cold Cal Ref	$T_{R,CBB}$	295 K	Temperature used for lab tests
Reflected Radiance, Hot Cal Ref	$T_{R,HBB}$	295 K	Temperature used for lab tests
Reflected Radiance, Verification Target	$T_{R,OARS}$	295 K	Temperature used for lab tests
Emissivities			
Cold Cal Ref (Space Target)	e_{CBB}	0.999	
Hot Cal Ref (Internal Cal Target)	e_{HBB}	0.999	
Verification Target (OARS)	e_{OARS}	0.999	
Polarization			
Scene mirror reflectivity (parallel)	r_p	See Figure 84	From generic measurement
Scene mirror reflectivity (perpendicular)	r_s	See Figure 84	From generic measurement
Instrument polarization ellipse, major axis	t_{max}	See Figure 84	From linear polarizer test
Instrument polarization ellipse, minor axis	t_{min}	See Figure 84	From linear polarizer test
Instrument polarization ellipse, angle	α	45°	The model depends on $\delta - \alpha$, not the absolute angular position of either δ or α . Hence, the choice of the 0° position is arbitrary, and the angular position of the nadir view was chosen as the 0° reference for convenience.
Cold Cal Ref (CBB) Position (Nominal)	δ_{CBB}	180°	
Hot Cal Ref (HBB) Position (Nominal)	δ_{HBB}	0°	
Cold Ver. Target (OARS) Position (Nominal)	δ_{OARS}	270°	
Hot Ver. Target (ABB) Position (Nominal)	δ_{ABB}	90°	

The model results for an OARS temperature of 243 K (the tested configuration) are presented in Figure 85 and Figure 86. Figure 85 shows the spectrally resolved brightness temperature error as a function of ARI front-end rotation angle, while Figure 86 provides the brightness temperature residual versus front-end angle for a series of wavenumber values. A sinusoidal modulation, with period Δ , of the brightness temperature is clearly evident in these figures. It is also clear that the scene, calibration, and calibration views must be optimally placed with

respect to the polarization axis of the instrument in order to achieve the accuracy requirement of the climate benchmark measurement.

The instrument calibration and verification module is designed such that the position of the scene, calibration, and calibration views are separated by 90° in scene select mirror rotation, and the entire assembly can be rotated to fine-tune the viewport placement with respect to the instrument's polarization sensitivity zero-crossing points. The location of the zero-crossing points can be estimated during the design phase via a polarization model for the instrument that follows Stokes formalism. The validity of this result depends on accurate parameterization for the polarization properties of all optical components. Details are provided in the following section (4.2). More importantly, empirical testing to verify the location of the polarization sensitivity zero-crossing points must be conducted, and the instrument calibration and verification module should be adjusted for optimal viewport placement with respect to the instrument's polarization sensitivity zero-crossing points based on these results. The laboratory characterization and verification of modelled polarization sensitivity of the instrument is described in Section 4.3.

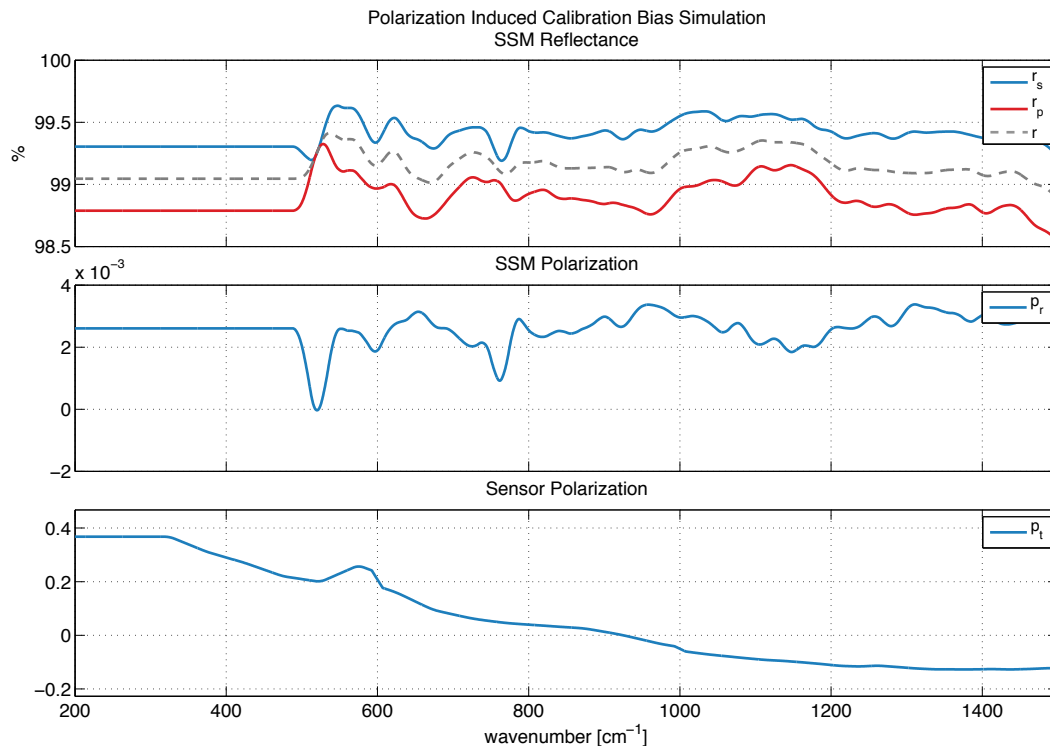


Figure 84: Scene select mirror reflectance and polarization (top and middle panel, respectively), and instrument polarization (bottom panel) parameters used in the model. Measurements of the ARI scene select mirror reflectance were not available, so existing data for reflectance from gold on diamond point turned aluminum mirror was used. The long-wave limit of the measurement data was 500 cm^{-1} . Consequently, the 500 cm^{-1} values were assumed for the $200 - 500 \text{ cm}^{-1}$ region in the model.

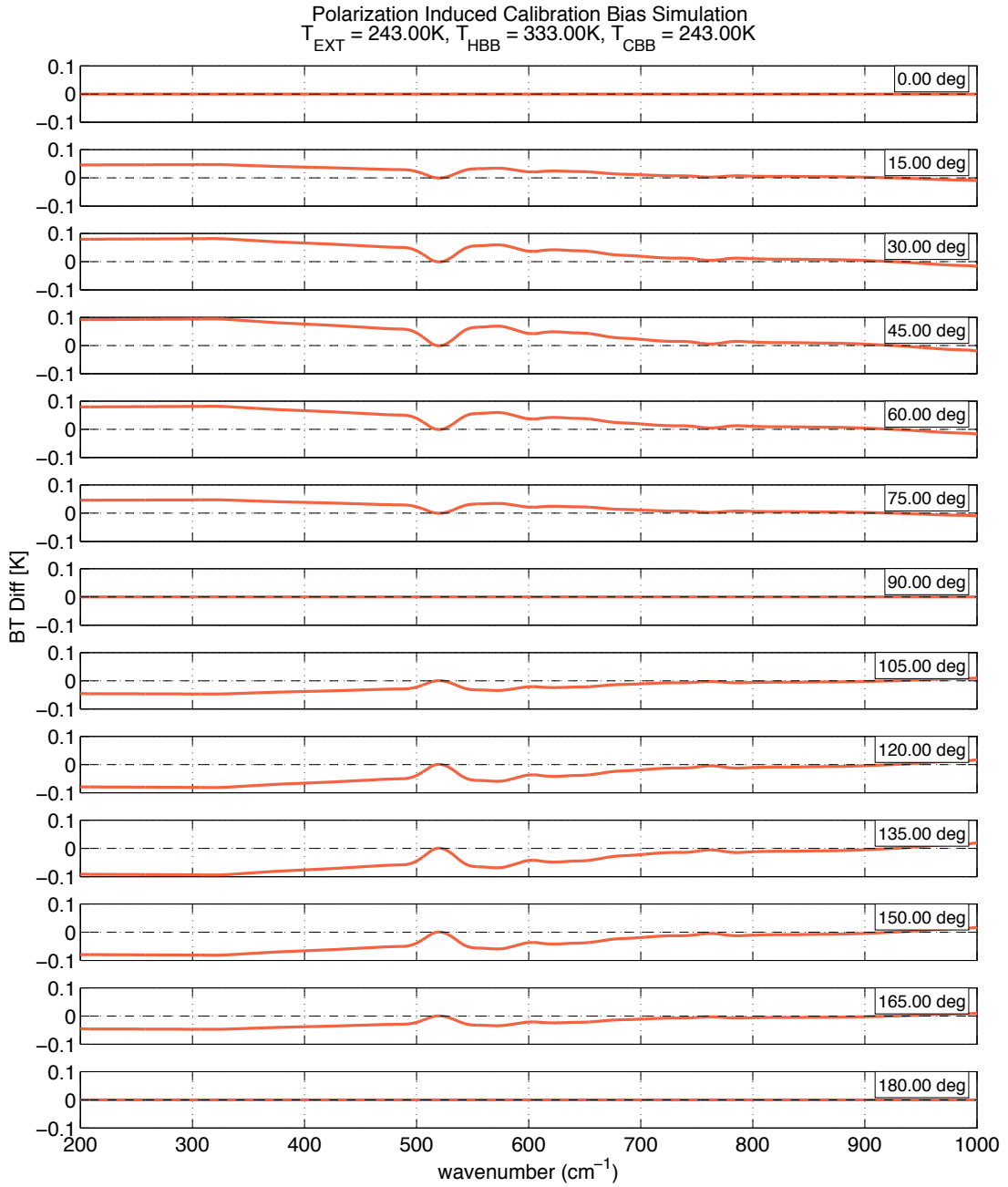


Figure 85: Modelled spectrally resolved brightness temperature error due to polarization as a function of ARI front-end rotation angle.

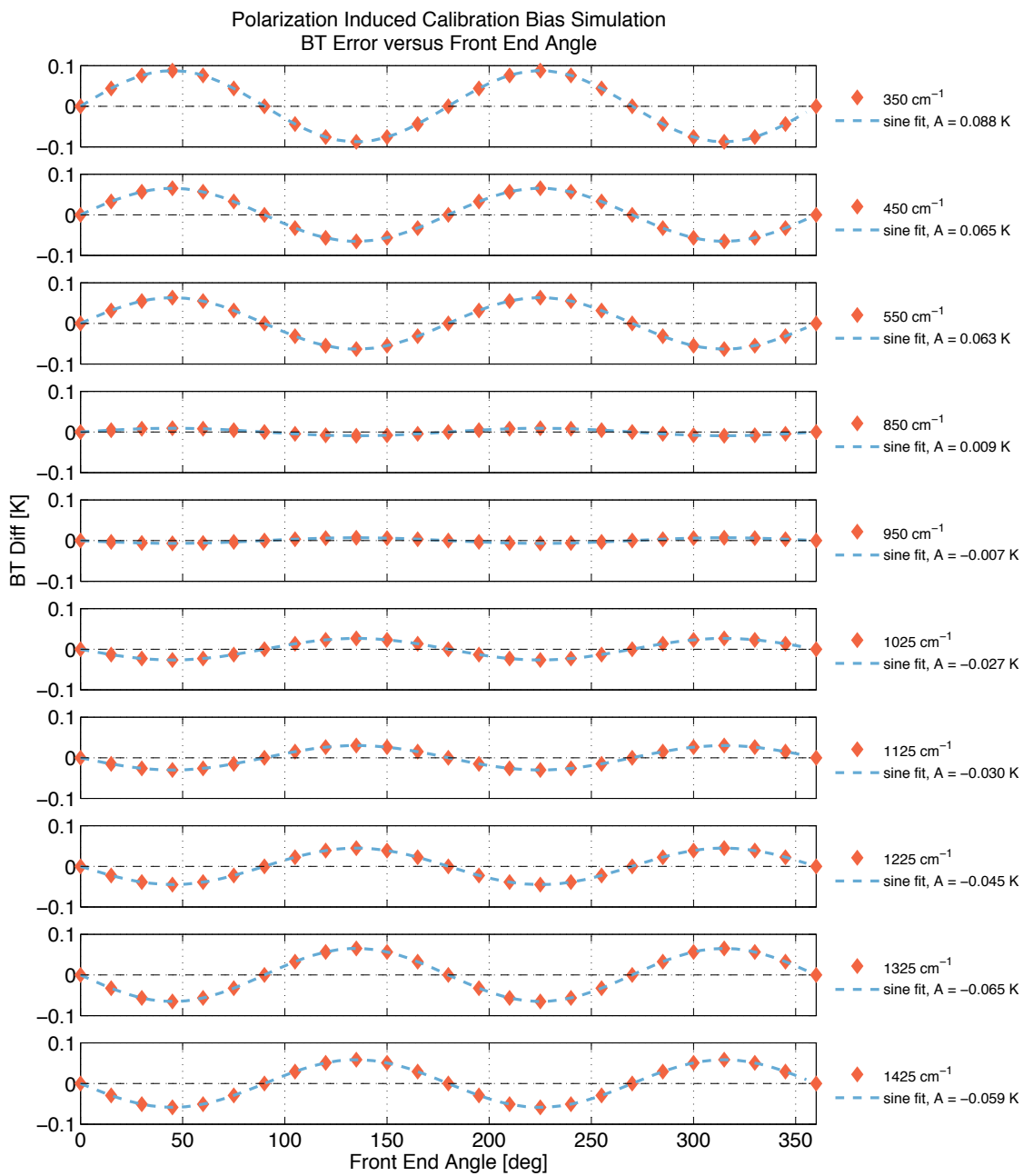


Figure 86: Modelled brightness temperature error due to polarization as a function of front-end rotation angle with respect to the nominal orientation for a series of wavenumber values. The amplitude of the variation is indicated to the right of each plot. It is clear that the scene, calibration, and calibration views must be optimally placed with respect to the polarization axis of the instrument in order to achieve the accuracy requirement of the climate benchmark measurement.

4.2 Refined polarization model following Stokes formalism

As concluded in the previous section, the modulation of the measured signal associated with the rotation of the plane of reflection at the scene select mirror and the polarization sensitivity of the instrument can be represented by a sinusoid of period λ . The positions of the polarization sensitivity zero crossings were predicted via a polarization model for the instrument by Gero [138] during the instrument design phase. The primary objective of the design phase analysis was to predict the polarization plane orientation for the instrument, and establish the nominal locations for the instrument viewports.

The model utilizes Mueller calculus, a matrix method for manipulating Stokes vectors, which are used to represent the polarization state of electromagnetic radiation. Any fully polarized, partially polarized, or unpolarized state of light can be represented by a Stokes vector (\vec{S}), while a Mueller matrix (\vec{M}), represents the effect of a particular optical element [128].

The coordinate system for the design phase polarization model is shown in Figure 87 and Gero's results (LW MCT, output port 1) at $10 \mu\text{m}$ are presented in Figure 88. The Stokes parameters are plotted as a function of scene selection mirror angle. The quantity of primary interest is the phase of the intensity (S_0). As shown in Figure 88, the predicted phase of the pattern was 2° , and the four zero-crossings of the sinusoidal polarization intensity occur at 2° , 92° , 182° , and 272° . These results confirmed the expectation that the angle of incidence at the beam splitter (45°) would be the dominant contributor to the instrument polarization angle.

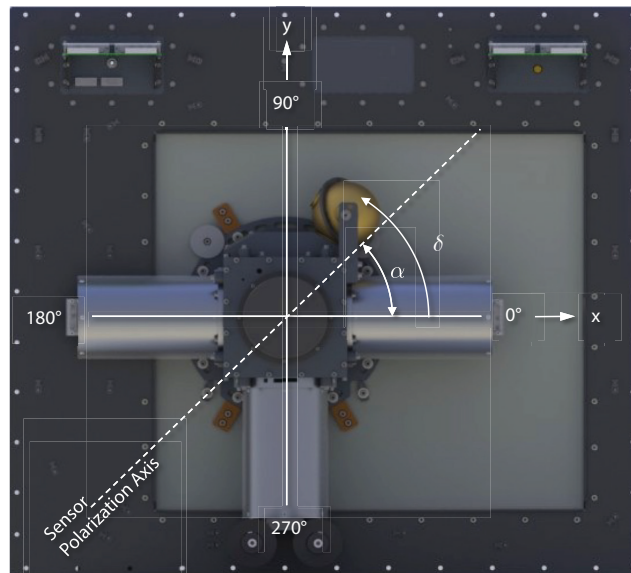


Figure 87: The coordinate system used for Stokes formalization polarization model is illustrated. The sensor polarization sensitivity axis is at angle α . A right-handed notation is used, with positive counter clockwise rotation with the zero degree reference on the x-axis.

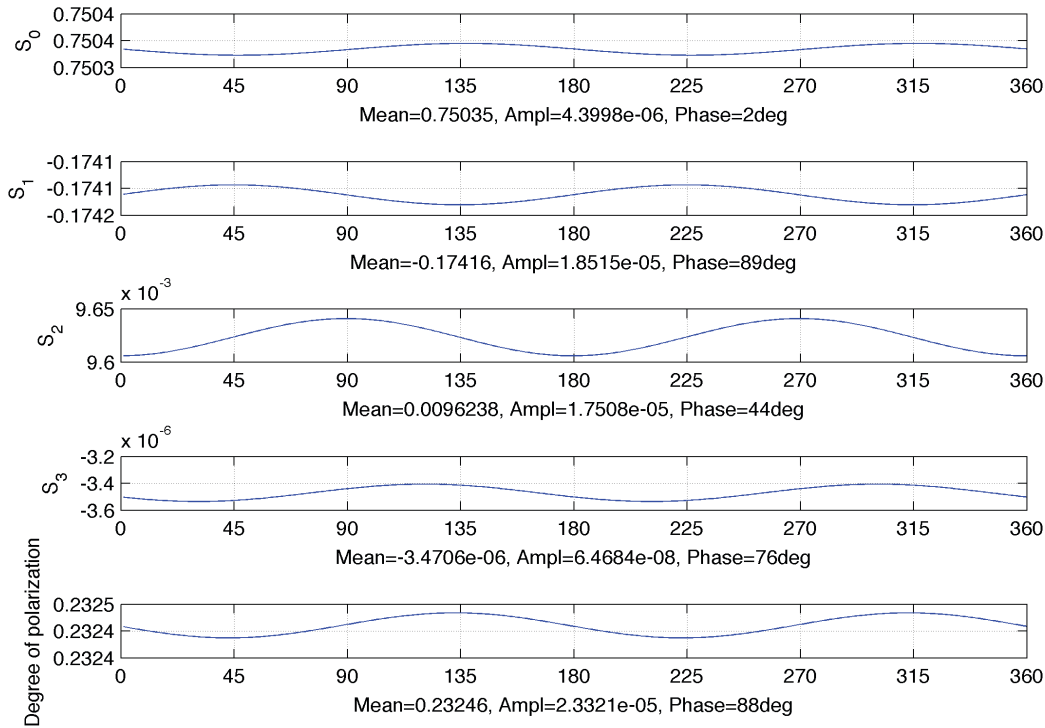


Figure 88: The positions of the polarization sensitivity zero crossings were predicted via a polarization model for the instrument during the design phase [138]. The results for output port 1 are shown, with the Stokes parameters plotted as a function of scene selection mirror angle (δ). The key quantity is the phase, indicated under each plot. The phase of the intensity ($I = S_0$) is 2 degrees, and the four zero-crossings of the sinusoidal polarization intensity occur at 2° , 92° , 182° , and 272° .

Preliminary design values for the instrument optical geometry were used for the design phase Mueller calculus model. It is desirable to verify consistency between the Mueller calculus model, complete with the final design optical parameters, and the experimental characterization and verification of the polarization sensitivity presented in the following section. Accordingly, a re-analysis of the Mueller calculus model, incorporating final design parameters, was performed during polarization testing and analysis.

The re-analysis is based closely on the design phase model completed by Gero et al [138], and uses the same formalism and assumptions. Specifically:

- The Mueller matrices representing reflection from a metal surface and from a cube-corner are based on the derivation by Kalibjian [139], while the Mueller matrices for reflection and transmission at a planar dielectric surface and a dielectric slab are from Goldstein [129];
- A non-diverging beam has been assumed, and the Mueller matrix for on-axis uniform irradiation of a cube-corner, described by Kalibjian, is used. It has been shown that small tilts of the entire cube-corner ($< 5^\circ$) with respect to the incident ray, do not impact diattenuation for hollow metal coated cube-corner reflectors [140]. The ARI divergence half-angle is well within this limit (25.8 milliradians). Accordingly, the assumption of a non-diverging beam at the cube-corner is expected to have no first order impact on the model results.
- The Mueller matrix for a plane mirror with the incident angle defined by the chief ray is used to approximate reflection from the off-axis parabolic and ellipsoidal mirrors. It is expected that this

approximation (to first order) adequately represents the integrated reflection of the divergent beam at each off-axis asphere.

- Polarization measurements were not available for the beam splitter or the gold mirrors. Consequently, documented values for the complex index of refraction for gold and Caesium Iodide were used as an approximation and the beam splitter coating was not accounted for. It is expected that the beam splitter coatings will have a large impact on the spectrally dependent magnitude of the instrument polarization. The calculation of the angle of the instrument polarization ellipse depends on both the polarization angle and magnitude of the contributing elements. As a result, these approximations have the potential to significantly impact the accuracy of the calculation.

The differences between the design-phase and revised model should also be noted:

- The orientation of the cube-corners differs between the two models. The relative angle between the incident plane at the cube corner and the incident plane at the beamsplitter was 60° in the initial model, and was based on the preliminary Zemax prescription. The revised model uses a relative angle between the incident plane at the cube corner and the incident plane at the beamsplitter of 47° , which is consistent with the final design.
- Small refinements were made to the incident angles at the fore-optics elements for consistency with the final optical design.
- The FIR aft-optics and detector were added to the model at output port 2.
- The IR aft-optics were updated to represent the use of the spare S-HIS detector and dewar, and small changes to the reflective IR aft-optics elements.

Consistency between the model used in the re-analysis and Gero's original results (provided in Figure 88) was confirmed when using the same preliminary design values for both models.

The results of the revised model at $10\ \mu\text{m}$, with parameters representative of the final design are presented in Figure 89 (output port 1) and Figure 90 (output port 2). The model predicts the phase of the intensity ($I = S_0$) to be 86° (for both output port 1 and output port 2), and the four zero-crossings of the sinusoidal polarization intensity occur at -4° , 86° , 176° , and 266° .

The predicted phase of the polarization-modulated intensity and the experimental results presented in the following section (§4.3) agree within a few degrees ($<4^\circ$). However, the modelled amplitude of the polarization-modulated intensity is negligible, which is inconsistent with the experimental results presented in Section 4.3 and the radiometric model presented in Section 4.1. Finally, varying the cube-corner orientation in the Mueller calculus model produces a significant and unexpected dependence of the results on cube-corner orientation. Given these results, it is highly likely that the approximation of the beam splitter as a Caesium Iodide slab is not valid, and the contribution of the beam splitter to the instrument polarization is significantly underestimated as a result. It is also clear that while the model verifies that the viewports need to be located at 90° intervals in scene select mirror angle; it is difficult to confidently and accurately predict the exact location of the polarization sensitivity zero crossings. Thus it is critical that the instrument design accommodates rotation of the calibration and verification module with respect to the instrument to allow for optimization of the viewport placement with respect to the sensor polarization sensitivity axis based on experimental measurements.

Ideally, for the flight instrument, polarization analysis will be included in the ray-trace analysis, and polarization measurements for all optical elements, especially the beam splitter will be available. For the scope of this project, the assumptions and approximations made in the model described in this section were necessary.

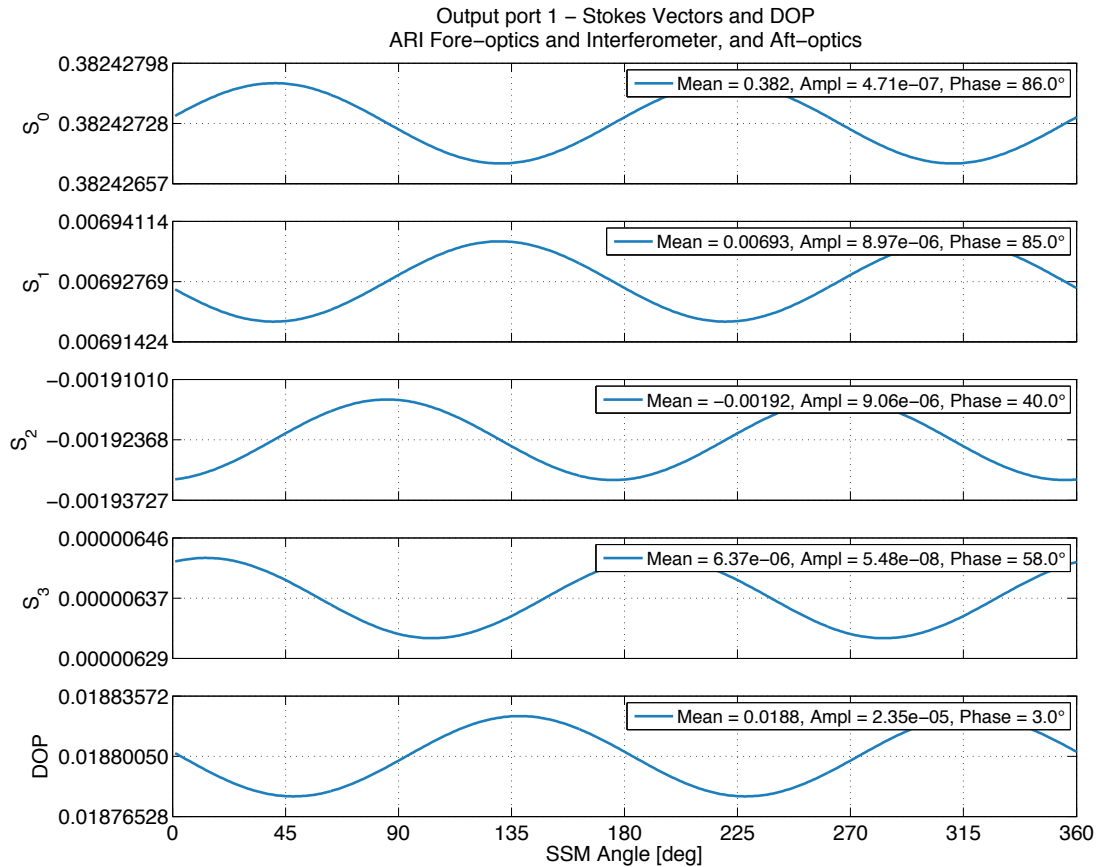


Figure 89: The positions of the polarization sensitivity zero crossings were predicted via the Mueller calculus based polarization model for the instrument. The results for the LW MCT channel (fore-optics, interferometer, IR aft optics at output port 1) are shown, with the Stokes parameters plotted as a function of scene selection mirror angle. The key quantity of interest is the intensity (S_0). The model predicts the phase of the intensity to be 86° and the four zero-crossings of the sinusoidal polarization intensity occur at -4° , 86° , 176° , and 266° .

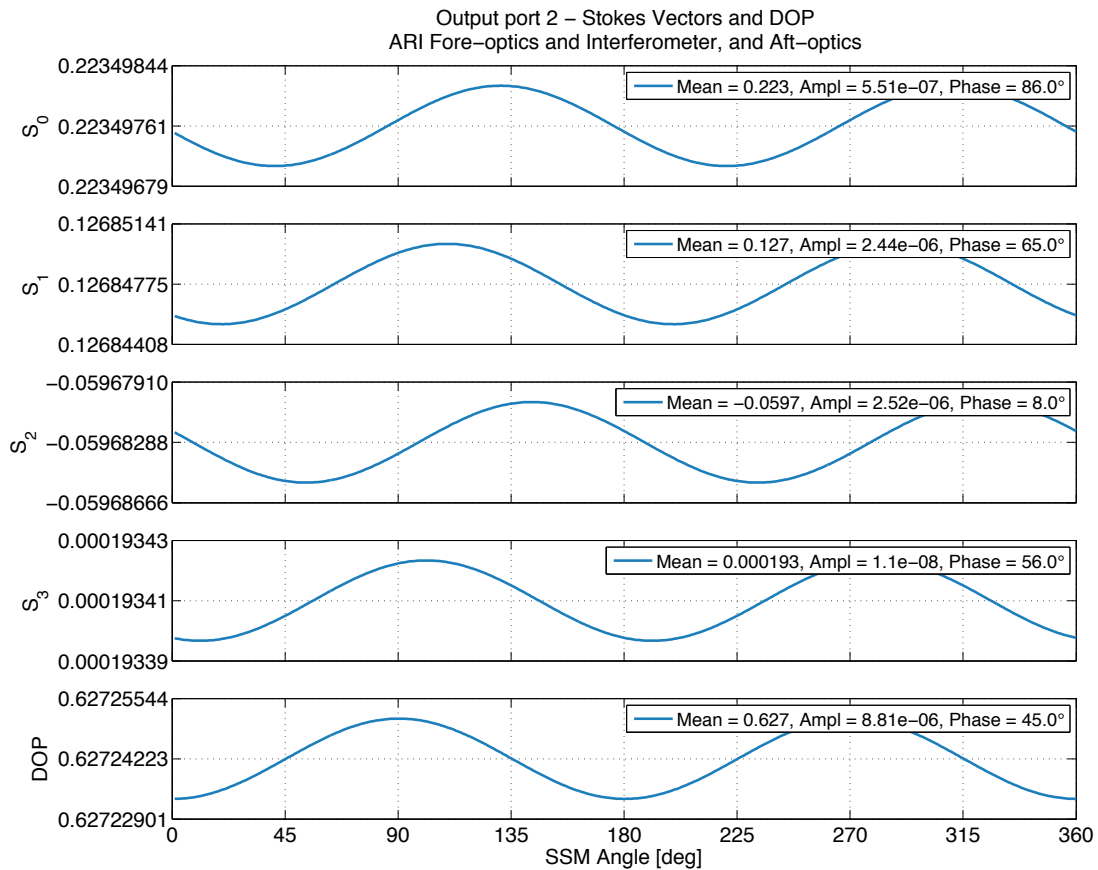


Figure 90: The positions of the polarization sensitivity zero crossings were predicted via the Mueller calculus based polarization model for the instrument. The results for the DTGS channel (fore-optics, interferometer, FIR aft optics at output port 2) are shown, with the Stokes parameters plotted as a function of scene selection mirror angle. The key quantity of interest is the intensity (S_0). The model predicts the phase of the intensity to be 86° and the four zero-crossings of the sinusoidal polarization intensity occur at -4° , 86° , 176° , and 266° .

4.3 Polarization sensitivity characterization and verification

As noted earlier in the chapter, the instrument calibration and verification module has been designed such that the position of the scene, calibration, and calibration views are separated by 90° in scene select mirror rotation, and the entire assembly can be rotated to fine-tune the viewport placement with respect to the instrument's polarization sensitivity zero-crossing points (which are located at 45° from the sensor polarization axis). The calibration and verification assembly also provides a polarization characterization viewport located midway between two of the 90° spaced viewports (Figure 91). With optimal positioning of the calibration and verification module for elimination of polarization induced calibration biases, the calibration bias due to polarization should be largest at the polarization characterization viewport. Periodic views of the polarization characterization viewport can be used to verify that the stability of the polarization sensitivity without rotation of the angular position of the calibration and verification assembly.

Two methods were used for characterizing the ARI polarization sensitivity and the contribution of polarization-induced error to the ARI calibration uncertainty:

- A four-source polarization test in which the calibration verification module was rotated with respect to the instrument over a range of 130° in 15° intervals.
- A two-source polarization test with linear polarizer located between the calibration verification module and the instrument. Data was collected at a 180° range of linear polarizer rotation angles in 15° increments.

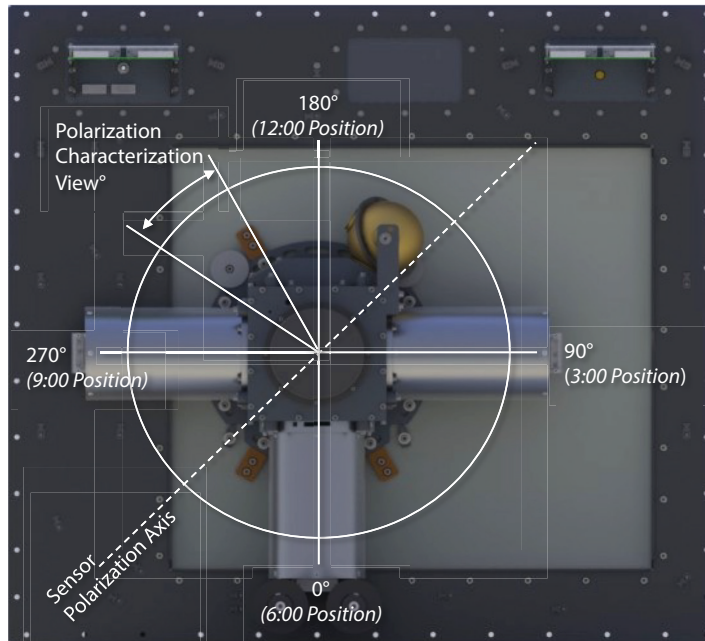


Figure 91: With optimal positioning of the calibration and verification module for elimination of polarization induced calibration biases, the calibration bias due to polarization should be largest at the polarization characterization view and zero at the calibration, calibration verification, and scene viewports.

4.3.1 Four-source polarization test

The primary purpose of the four-source polarization test is to determine the impact of the polarization-induced error on the calibrated radiance. This test allows for direct measurement of the contribution of the polarization-induced error to the calibration accuracy, and the dependence on the scene mirror angle is determined. Given the radiometric model results presented in Section 4.1, the maximum polarization dependent biases in the 4-source polarization test are expected to be 0.1 K or less. This is on the same order as the LW biases due to stray light discussed in Chapter 3. Thus, the polarization dependence will not be obvious on the measurement without proper identification and correction of the stray light problem. Accordingly, the test was completed after the stray light testing was complete and the error due to stray light was resolved.

The front-end configuration for the test is shown in Figure 92. Two blackbodies are at 333 K, and located 90° to one another at the 12:00 and 3:00 positions. The other two blackbodies (OARS and CBB) are at controlled to 243 K and positioned 90° to one another at the 6:00 and 9:00 positions. The heated halos have been removed from both the OARS and CBB and replaced with the heated aperture ring assemblies (see Chapter 3

for details). The heated aperture ring assemblies are not required for this test, and are left unpowered for all testing. Counter-clockwise rotation (when facing towards the instrument) is considered positive. Data was collected at a range of front-end rotation angles of -15° to 105° , with respect to the nominal orientation of the calibration verification assembly depicted in Figure 92. The electrical harness and the OARS and CBB coolant lines limit the maximum angle of front-end rotation.

The duration of the data collection for each front-end rotation angle is approximately 20 hours such that the DTGS detector noise can be sufficiently reduced. The four-source polarization test allows direct measurement of the amplitude and dependence on scene mirror angle of the polarization-induced calibration bias. However, the residuals are small and subject to signal to noise considerations for the DTGS detector, even with 20-hour data collects. The temperature set points of the hot blackbodies are selected such that the effective temperatures of both blackbodies are at approximately the same temperature (best effort, within 25 mK). Likewise, the cold blackbodies are operated at approximately the same effective temperature as one another. Cavity gradients in the purged environment depend on cavity orientation, and the blackbody set points were adjusted as required.

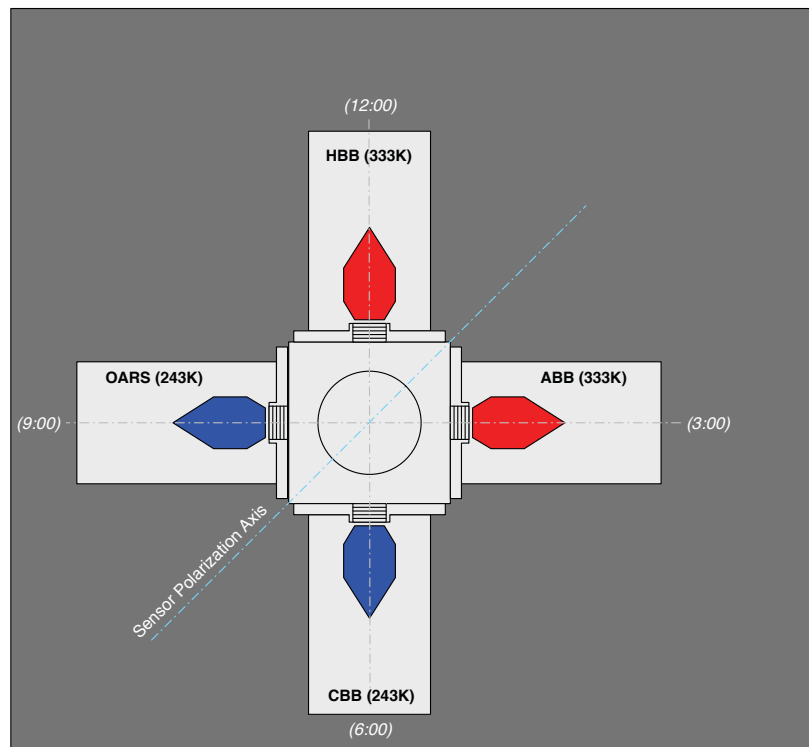


Figure 92: ARI front-end configuration for the four-source polarization tests.

The possible target and calibration reference combinations for the front-end configuration used for the four-source polarization test are provided in Table 10.

Table 10: Possible target and calibration reference combinations for the four-source polarization test. The results presented herein are for an OARS target with HBB and CBB calibration references.

Target	Cold Calibration Reference	Hot Calibration Reference
OARS	CBB	HBB
OARS	CBB	ABB
CBB	OARS	HBB
CBB	OARS	ABB
HBB	CBB	ABB
HBB	OARS	ABB
ABB	CBB	HBB
ABB	OARS	HBB

The bias in the measured spectra due to polarization is equal for scene mirror positions separated by 180°. To provide the maximum sensitivity of the calibration bias due to polarization a configuration with both calibration references located at 90° in scene mirror rotation angle to the target source is desirable. Furthermore, when the calibration bias is expressed in brightness temperature, the bias signals will be largest for a cold target. For the results presented herein, the OARS was used as the target source, the HBB as the hot calibration reference, and the CBB for the cold calibration reference. Other target and reference combinations were also analyzed, and the results were consistent with the results for the configuration presented here.

The measured calibrated radiance for the OARS target is calculated using the complex calibration equation (Eq. (1.1)), converted to an equivalent brightness temperature (BT_{obs}), and compared to with the predicted equivalent brightness temperature (BT_{pred}) for the OARS target. The predicted radiance for the OARS target is calculated using Eq. (1.2). For reference, equations (1.1) and (1.2) are reproduced here:

$$L_S(\sigma_k) = (L_H(\sigma_k) - L_C(\sigma_k)) \operatorname{Re} \left\{ \frac{S_S(\sigma_k) - S_C(\sigma_k)}{S_H(\sigma_k) - S_C(\sigma_k)} \right\} + L_C(\sigma_k), \quad (1.1)$$

$$L(\sigma_k) = e(\sigma_k) B(\sigma_k, T) + (1 - e(\sigma_k)) B(\sigma_k, T_R). \quad (1.2)$$

The radiances are converted to equivalent brightness temperatures via inversion of Planck's Law:

$$BT(\sigma_k) = \frac{hc(1 \times 10^2)\sigma_k}{k \cdot \ln \left(1 + \frac{2hc^2(1 \times 10^8)\sigma_k^3}{L(\sigma_k)/(1 \times 10^3)} \right)}. \quad (4.22)$$

In Eq. (4.22), BT is the equivalent brightness temperature associated with the radiance L (expressed in units of $\text{mW}/(\text{m}^2 \cdot \text{sr} \cdot \text{cm}^{-1})$), h is Planck's constant (units of J·s), c is the speed of light in a vacuum (units of m/s), and k is the Boltzmann constant (units of J/K).

The experimental results of the four-body polarization test for an OARS target (243 K, 9:00 position), HBB hot calibration reference (333 K, 12:00 position), and CBB cold calibration reference (243 K, 6:00 position), are shown in Figure 93 and Figure 95 for the LW MCT detector, and in Figure 94 and Figure 96 for the DTGS

detector. The results are expressed as effective brightness temperature residuals (observed – predicted). The predicted brightness temperature does not account for polarization induced calibration biases, while the observed brightness temperature residual is sensitive to the calibration bias associated with the instrument polarization sensitivity.

As noted in the previous sections, the modulation of the measured signal associated with the rotation of the plane of reflection and the polarization sensitivity of the instrument, for any spectral region ν_k , is described by a sinusoid of period λ , with no offset ($b_k = 0$),

$$\begin{aligned} [BT_{obs} - BT_{pred}]_{\nu_k} &\propto A_k \sin(2\theta + \phi) + b_k \\ &\propto A_k \sin(2\theta + \phi). \end{aligned} \quad (4.23)$$

Eq. (4.23) is the standard expression for the sine function, where A is the maximum amplitude of the sinusoidal variation, θ is the front-end rotation angle, and $\phi/2$ is the phase shift. It has been assumed that the scene select mirror and sensor can be considered as partial linear polarizers, and as a result the phase shift is expected to be independent of wavenumber. In this sign notation, a negative phase shift corresponds to a rightward shift of the zero-crossings of the sinusoid.

To further improve signal to noise, the 0.5 cm^{-1} resolution data is averaged to a lower spectral resolution. The spectral bin size was chosen based on noise criteria for each respective detector weighted against the goal of providing a sufficiently spectrally resolved result. It is desirable to be able to resolve the spectral dependency of the polarization induced calibration bias. The required spectral resolution depends on the spectral signatures of the coatings and surfaces in the system. For tests conducted during the demonstration effort, it was decided that it was desirable to keep the spectral resolution 100 cm^{-1} or better. The spectral bin positions were selected to avoid the strong CO_2 atmospheric lines (Q branches), and limited to within the spectral response region that provided acceptable signal to noise. H_2O features have been mitigated via the use of a high flow rate dry air purge. A spectral bin width of 50 cm^{-1} , with spectral bin centers at 575, 825, 925, 1025, 1125, 1225, 1325, and 1425 cm^{-1} was selected for the LW MCT, while a bin width of 100 cm^{-1} and spectral bin centers at 350, 450, 550, 850, 950, 1050, 1150 cm^{-1} was selected for the DTGS detector. The spectrally resolved, and spectrally averaged residuals are shown in Figure 93 (LW MCT) and Figure 94 (DTGS). Error bars for the spectrally averaged residuals represent the statistical variation for the spectral average, and are specified as the 3- σ standard deviation of the data in the average divided by the square root of the number of data points in the average. The spectrally averaged data is presented as a function of front-end rotation angle, for each spectral average in Figure 95 and Figure 96.

Referring to Figure 95, for the LW MCT it is clear that the brightness temperature residuals are quite small and are comparable in magnitude to the noise for the 800 – 850 cm^{-1} and 900 – 950 cm^{-1} averages. The residuals for the 1400 – 1450 cm^{-1} region are large in comparison, but still on the same order as the noise for this spectral range. Similarly, for the DTGS, it is evident in Figure 96 that the brightness temperature residuals for the 800 – 900 cm^{-1} and 900 – 1000 cm^{-1} averages are near zero. The DTGS residuals for the 1000 – 1100 cm^{-1} and 1100 – 1200 cm^{-1} averages are also less than the noise levels for these regions. When fitting the data, it is important to weight the fit both for the magnitude of the residual and the noise. Details of the fitting process are provided in the following paragraphs.

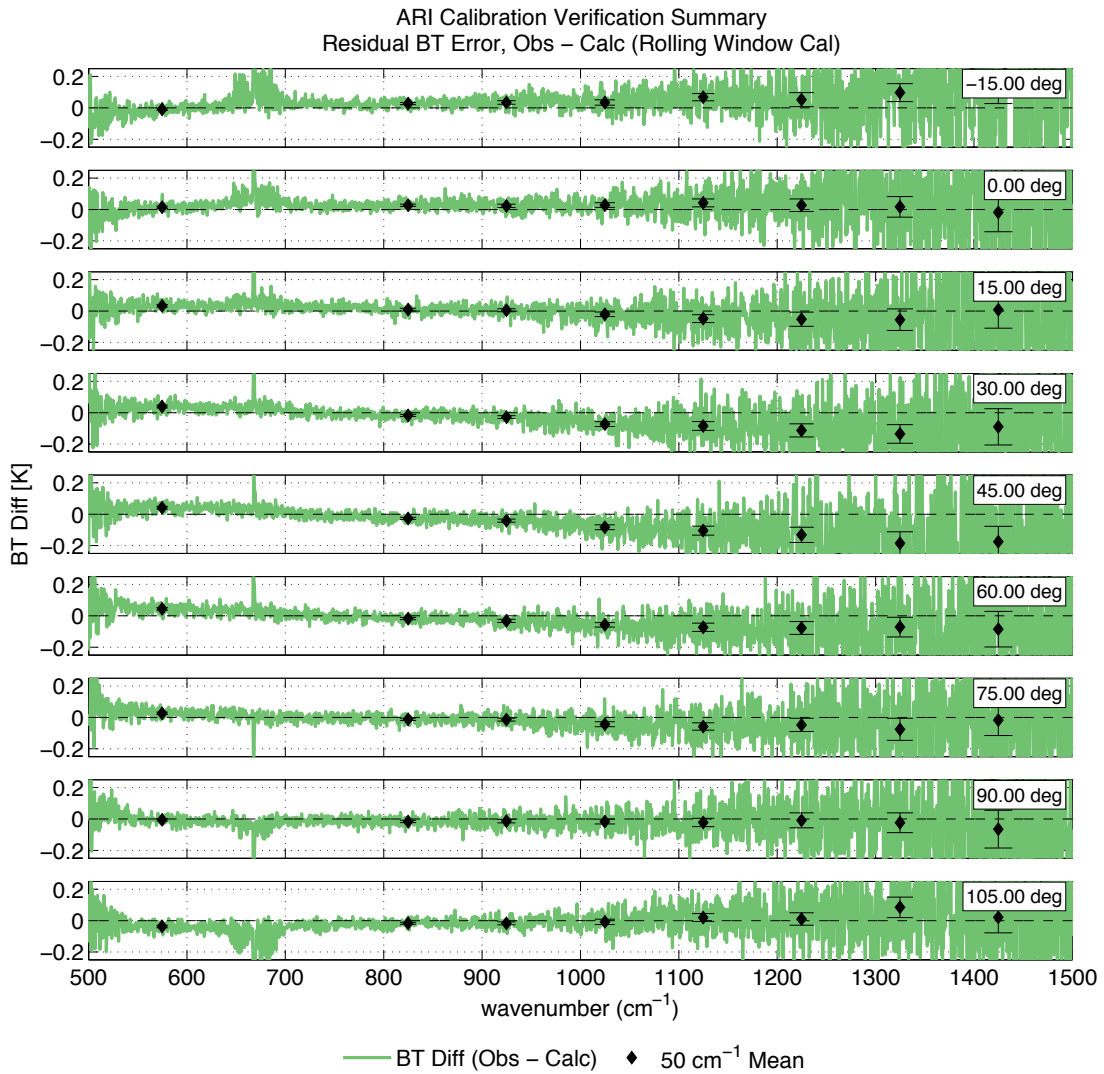


Figure 93: Measured spectrally resolved brightness temperature error (LW MCT, green) as a function of ARI front-end rotation angle. Spectral averages (50 cm^{-1} width) are shown as black markers with error bars. Error bars represent the statistical variation in the average ($3\sigma/N$).

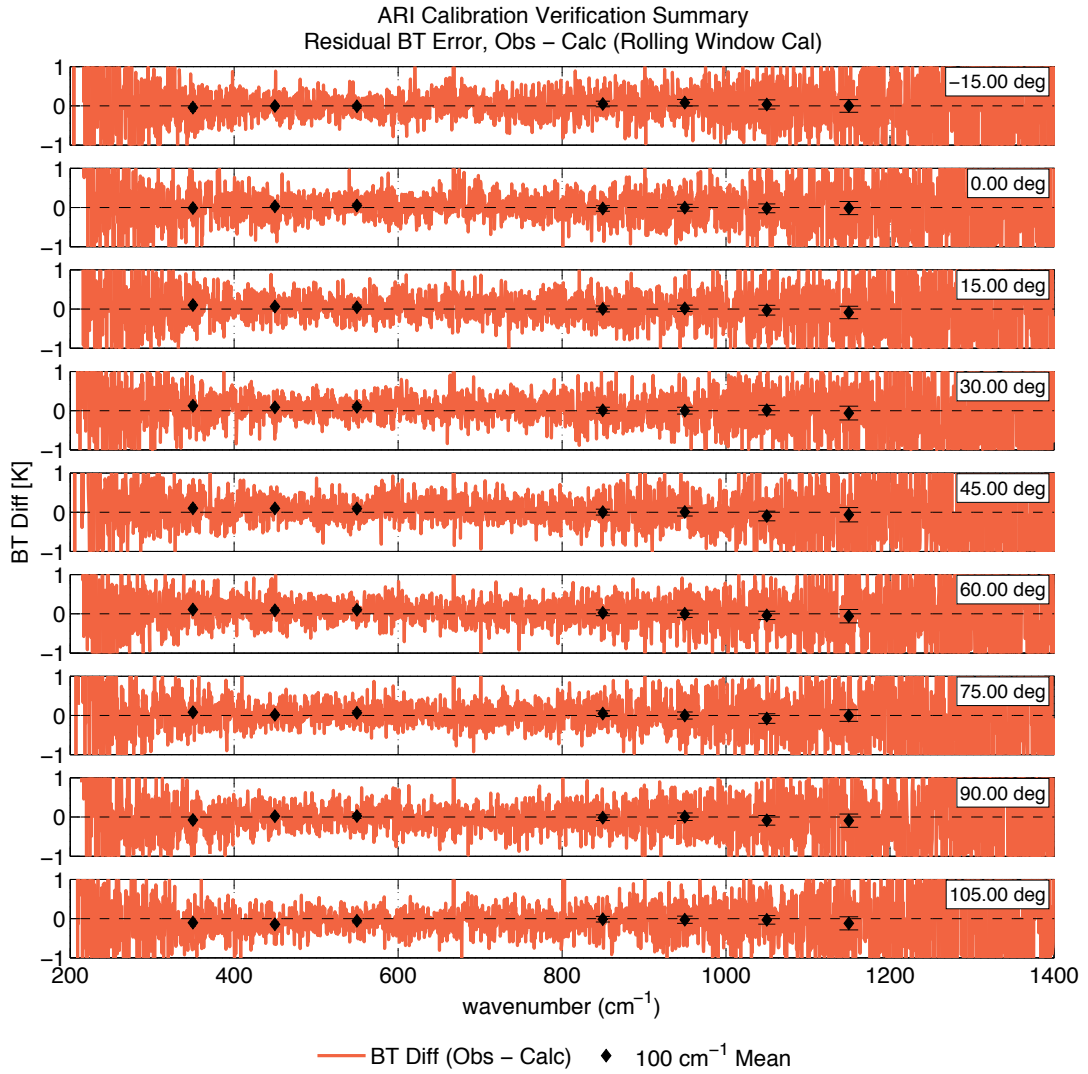


Figure 94: Measured spectrally resolved brightness temperature error (DTGS, red) as a function of ARI front-end rotation angle. Spectral averages (100 cm⁻¹ width) are shown as black markers with error bars. Error bars represent the statistical variation in the average (3σ/N).

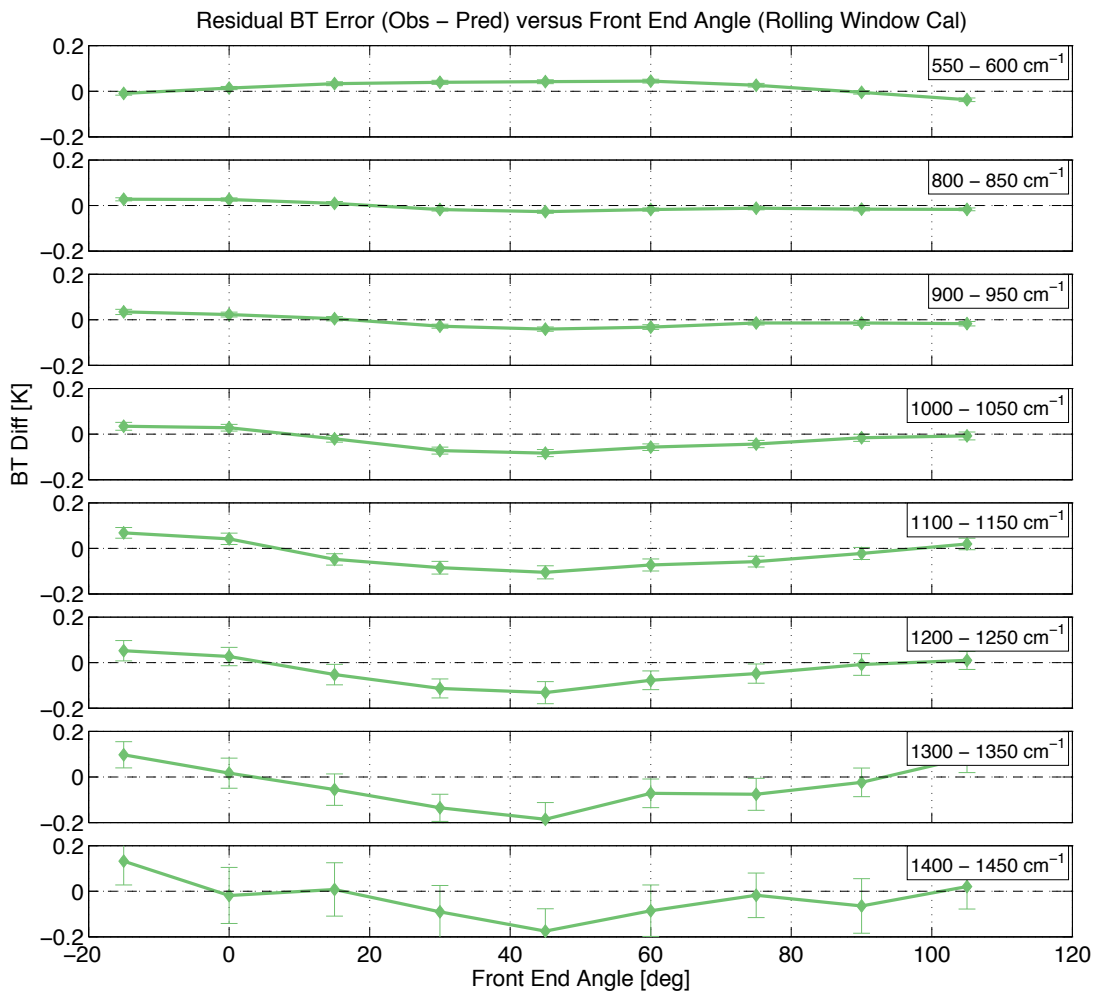


Figure 95: Spectrally averaged, measured brightness temperature error (LW MCT, green) as a function of ARI front-end rotation angle. Spectral averages (50 cm^{-1} width) are shown with error bars. Error bars represent the statistical variation in the spectral average ($3\sigma/N$).

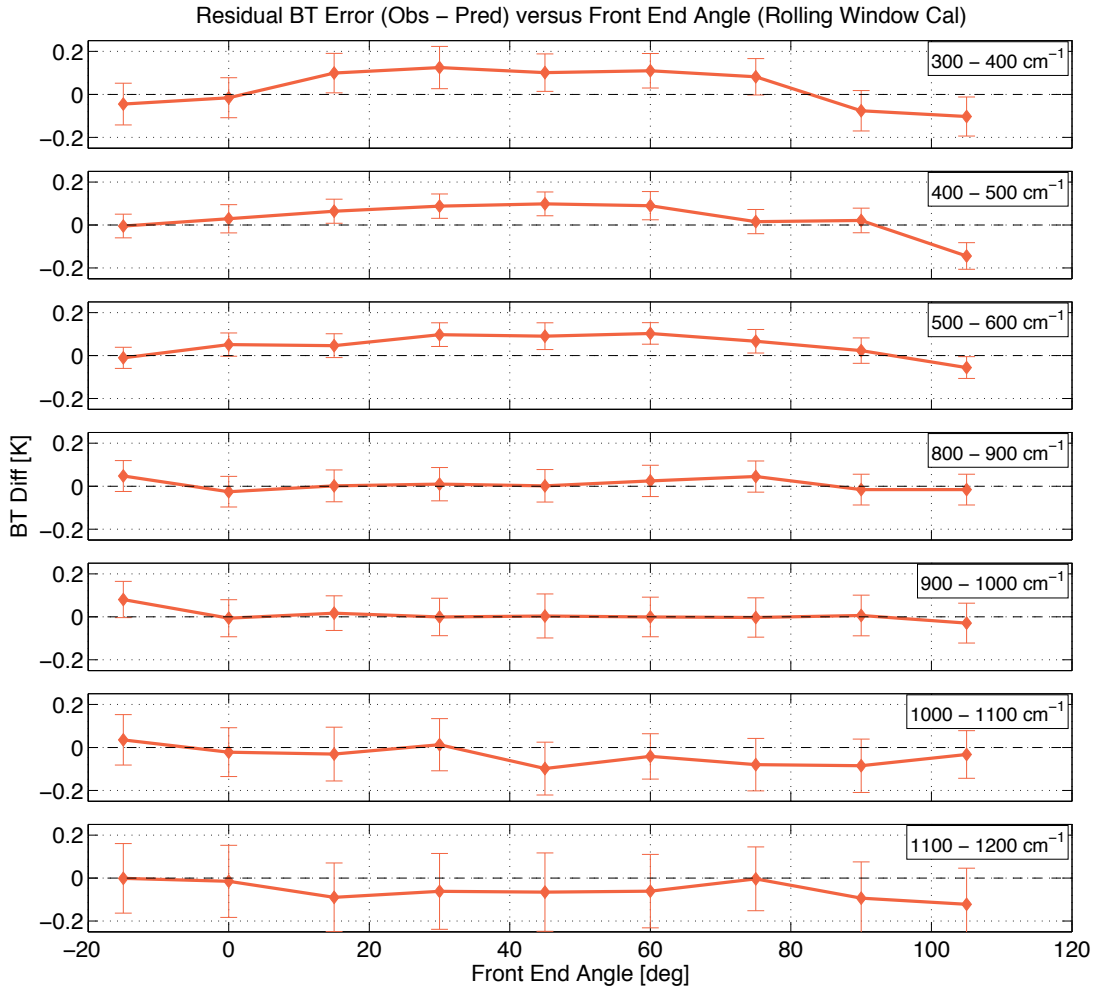


Figure 96: Spectrally averaged, measured brightness temperature error (DTGS, red) as a function of ARI front-end rotation angle. Spectral averages (100 cm^{-1} width) are shown with error bars. Error bars represent the statistical variation in the spectral average ($3\sigma/N$).

The fitting of the brightness temperature residuals for the spectrally averaged data as a function of front-end rotation angle by the sinusoid described in Eq. (4.23) was completed in a two-step process. Based on the work by Pagano [131], and the material properties of uncoated gold and Caesium Iodide, it was assumed that the scene select mirror and sensor would nominally behave as partial linear polarizers. Accordingly, the phase shift is primarily dependent on the geometry of the optical system and will have insignificant wavelength dependence. The two-step approach described below, forces the fit to this behavior. The Matlab nonlinear least squares curve fitting function (`lsqnonlin`), was used for both steps.

In the first step of the fitting process, the phase shift $\phi/2$ is determined. A first order estimate of the amplitude A_k for each linear equation was used in this step. The estimate of A_k is based on the maximum absolute value of the brightness temperature residual for the spectral bin average centered at ν_k . The objective function for the nonlinear least squares fit is the root mean square of the fit error for all spectral bins, proportionally weighted by residual size and inversely weighted by residual noise:

$$f(\phi) = \sqrt{\frac{1}{n} \sum_k \frac{a_{1k}}{a_{2k}} \left[A_k \sin(2\theta + \phi) - (BT_{obs} - BT_{pred})_{v_k} \right]^2}, \quad (4.24)$$

$$a_{1k} = \left\langle \left(BT_{obs} - BT_{pred} \right)_{v_k} \right\rangle_{\theta}, \quad (4.25)$$

$$a_{2k} = \left\langle \left(\frac{3\sigma_{BT_{obs}-BT_{pred}}}{N} \right)_{v_k} \right\rangle_{\theta}. \quad (4.26)$$

In Eq. (4.25) and (4.26), $\langle \rangle_{\theta}$ denotes the mean over all front-end angles θ , $3\sigma_{BT_{obs}-BT_{pred}}$ is the 3- σ standard deviation for a given spectral bin, and N is the number of data points in the spectral bin.

The amplitude of each sinusoid is solved for in the second step of the data fitting process. The phase shift ϕ_{opt} from the first step of the fitting process is used as an input to the second step. A similar objective function is used for the second nonlinear least squares fit, but in this case the function is optimized for each A_k sequentially, and ϕ_{opt} is provided as an input:

$$f(A_k) = A_k \sin(2\theta + \phi_{opt}) - (BT_{obs} - BT_{pred})_{v_k}. \quad (4.27)$$

The results of the fitting process are shown in Figure 97 (LW MCT), and Figure 98 (DTGS). The results indicate a phase shift angle of 0° for the LW MCT, and 4.2° for the DTGS. By design, the ideal phase shift of 0° should result in no polarization induced calibration bias for the ARI nominal viewport locations. The results also indicate maximum polarization induced calibration biases of approximately 0.1 K at $300 - 400 \text{ cm}^{-1}$ for the DTGS and 0.2 K at $1400 - 1450 \text{ cm}^{-1}$ for the LW MCT, at a front-end rotation of 45° . The simulated results presented in Section 4.1 predicted an error of roughly 0.09 K at 350 cm^{-1} , and 0.06 K at 1425 cm^{-1} . The large difference in the predicted and measured polarization induced bias at 1425 cm^{-1} may indicate that the gold mirror data used in the simulation is not representative of the ARI scene mirror polarization properties at all wavelengths. The analysis should be revisited when measurement data for the ARI scene mirror is available.

As noted previously, the LW MCT brightness temperature residuals are quite small and are comparable to the noise for the $800 - 850 \text{ cm}^{-1}$ and $900 - 950 \text{ cm}^{-1}$ averages. While the residuals for the $1400 - 1450 \text{ cm}^{-1}$ region are large in comparison, they are still on the same order as the noise for this spectral range. Similarly, for the DTGS it is evident that the brightness temperature residuals for the $800 - 900 \text{ cm}^{-1}$, $900 - 1000 \text{ cm}^{-1}$, $1000 - 1100 \text{ cm}^{-1}$ and $1100 - 1200 \text{ cm}^{-1}$ averages are near zero and smaller than the noise levels for these regions. While the fit is weighted for signal to noise, the low signal to noise associated with this measurement for the DTGS will have an impact on the accuracy of the results. The two-source polarization test with linear polarizer, described in the following section, provides better signal to noise levels and increased sensitivity in determination of the effective polarization plane and sensitivity of the instrument. The phase shift difference between the two detector channels (0° for the LW MCT, and 4.2° for the DTGS) is concerning, and indicative of aft-optic or detector dependent polarization effects. Referring to Figure 97 and Figure 98, shifting the

viewport position by 2° from the zero-crossing results in a calibration bias as large as 0.02 K (DTGS, 300 – 400 cm^{-1} spectral bin).

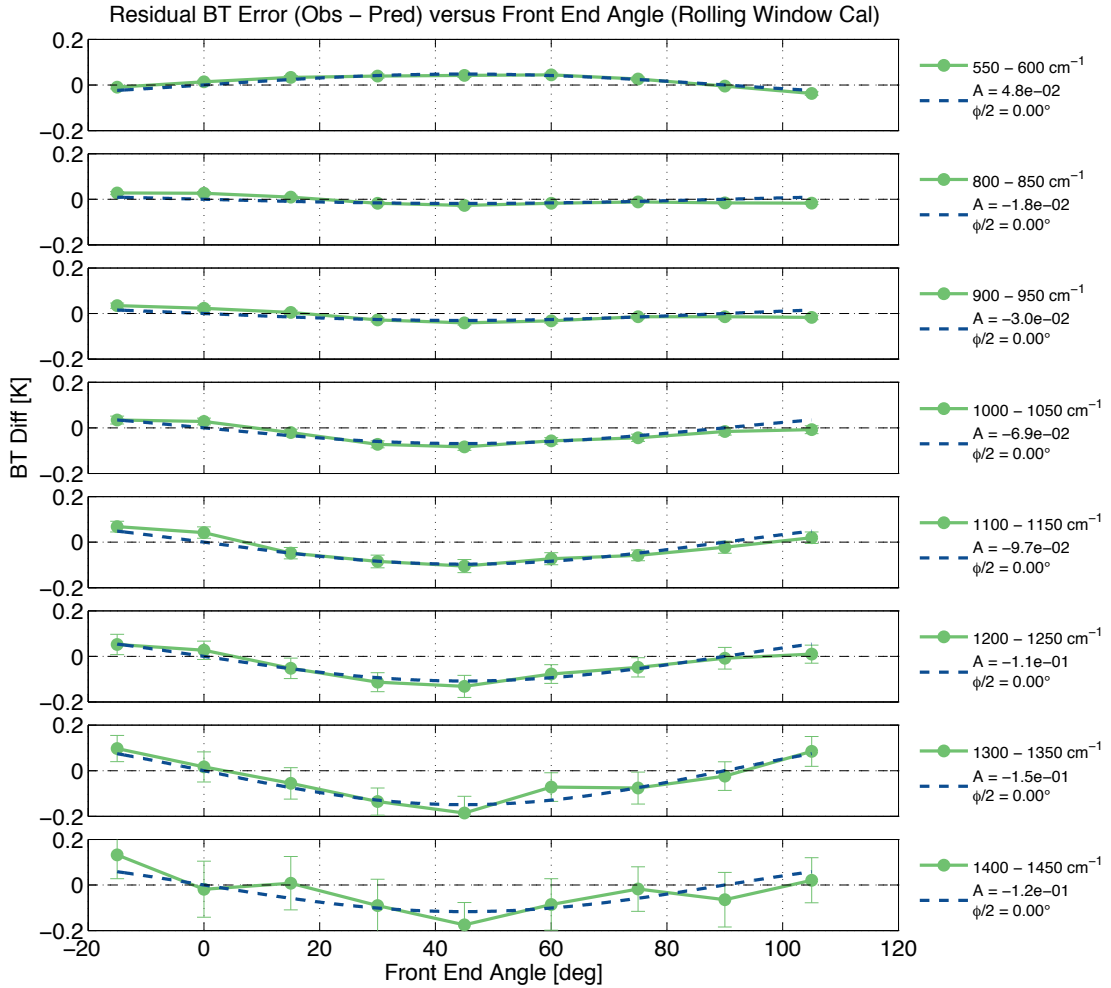


Figure 97: Spectrally averaged, measured brightness temperature error (LW MCT, green) as a function of ARI front-end rotation angle. Spectral averages (50 cm^{-1} width) are shown with error bars. Error bars represent the statistical variation in the spectral average ($3\sigma/N$). The dark blue dashed line indicates the resulting curve fit.

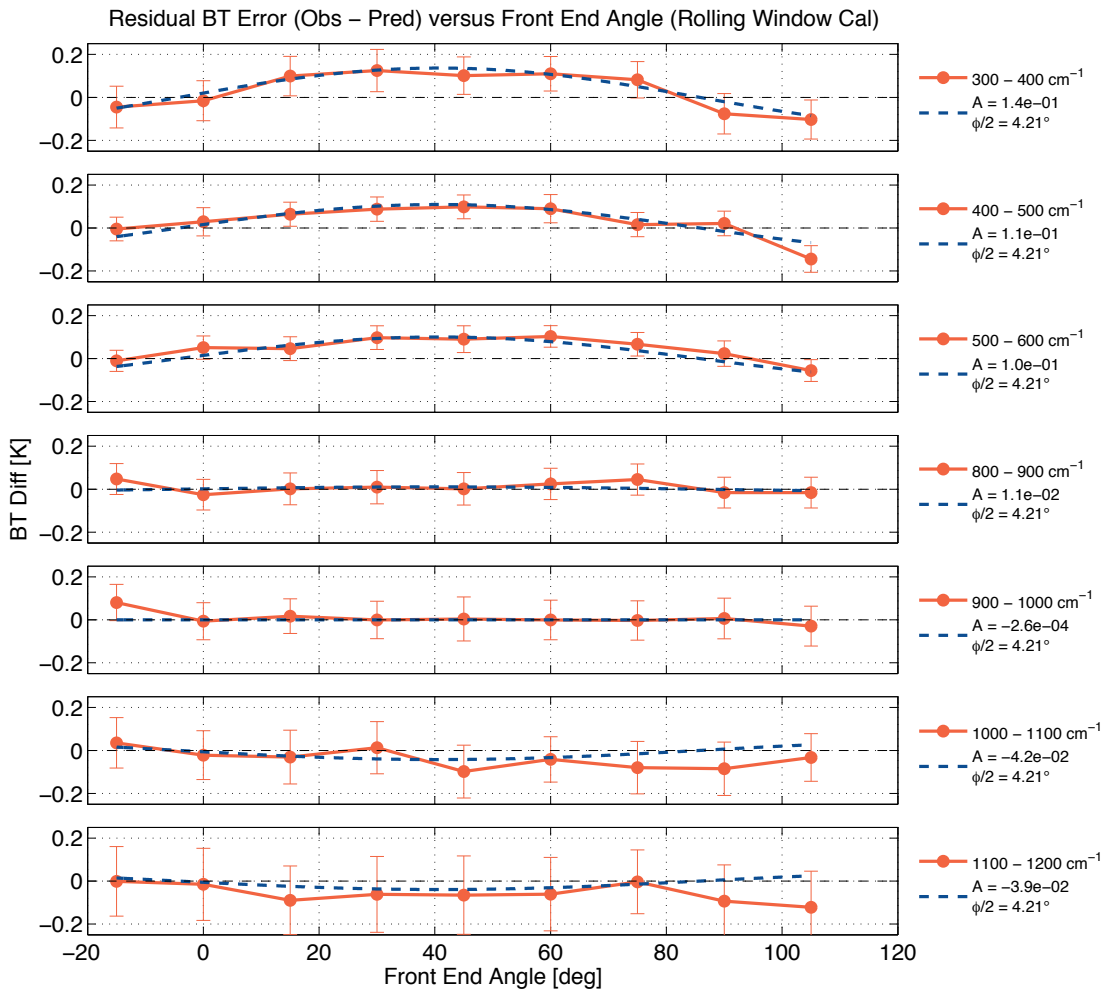


Figure 98: Spectrally averaged, measured brightness temperature error (DTGS, red) as a function of ARI front-end rotation angle. Spectral averages (100 cm^{-1} width) are shown with error bars. Error bars represent the statistical variation in the spectral average ($3\sigma/N$). The dark blue dashed line indicates the resulting curve fit.

4.3.2 Two source polarization test with linear polarizer

The two-source polarization test with linear polarizer allows determination of the effective polarization plane and sensitivity of the full optical chain of the instrument for the LW MCT and DTGS outputs. While this test does not provide direct measurement of the polarization-induced calibration error, the polarization dependent signal levels in the 2-source polarization test are much larger than the four-source polarization test. This allows for shorter data collection durations, and more accurate determination of the effective polarization plane of the instrument.

The front-end configuration used for this test is shown in Figure 99 (top view), and Figure 100 (front view). Two blackbodies are mounted on the front end at 180° to one another at the 3:00 and 9:00 positions. Having the blackbodies 180° to one another mitigates the effect of the scene mirror rotation on the polarization measurement. One blackbody is the hot reference (indicated in red in the configuration diagrams) and is heated to 60C while the other blackbody is the 'ambient' reference (indicated in blue in the configuration

diagrams) and controlled to a fixed temperature slightly warmer than ambient room temperature. The first cylindrical baffle for the scene mirror has been modified to mount a 50mm rotating polarizer mount (see Figure 101 and Figure 102).

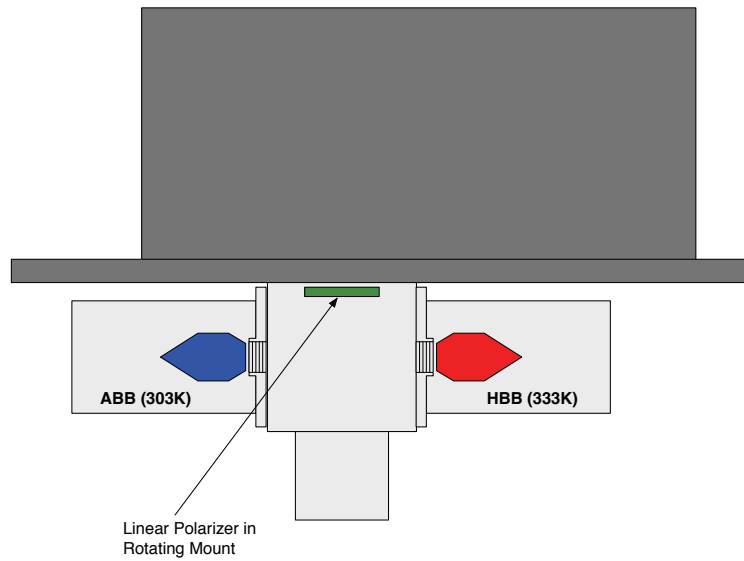


Figure 99: Front-end configuration for the 2-source polarization test with linear polarizer (top view). The linear polarizer position is indicated in green.

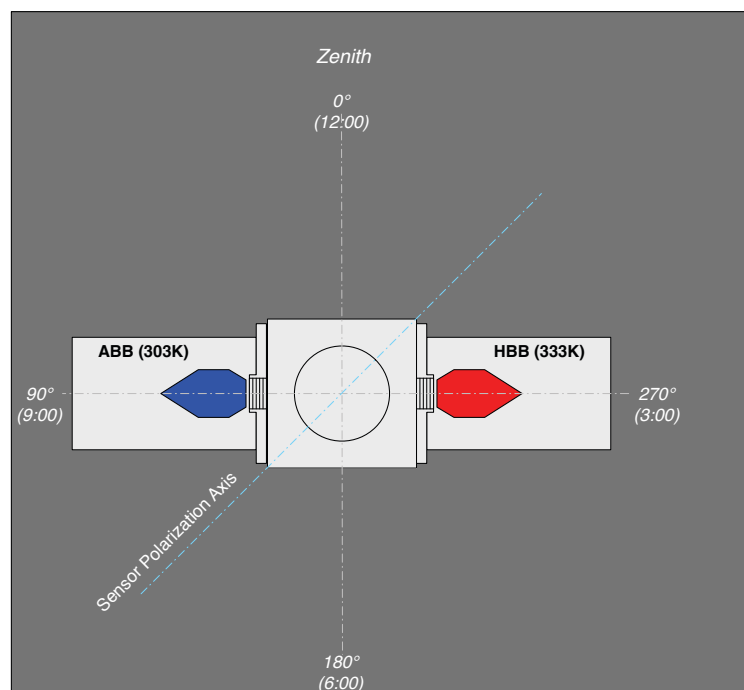


Figure 100: Front-end configuration for 2-source polarization test with linear polarizer (front view).

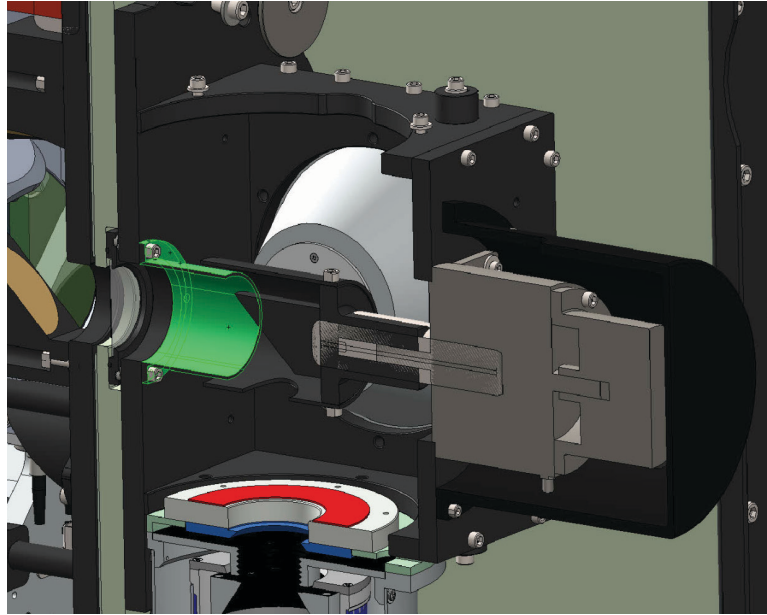


Figure 101: The scene mirror cylindrical baffle is replaced with a modified baffle, highlighted in green, that accommodates the mounting of a 50 mm rotating polarizer mount. The heated halo is not installed for the tests (but is included in this solid model assembly).

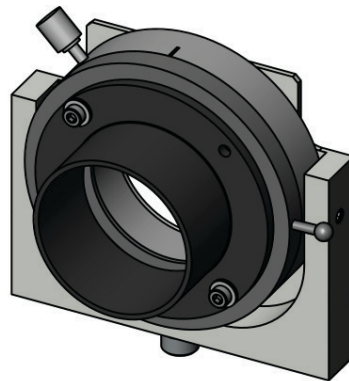


Figure 102: Modified scene mirror baffle and linear polarizer assembly.

Data was collected at a range of linear polarizer rotation angles of 0° to 180° degrees in 15° increments (with the 0° reference at the zenith position as illustrated in Figure 100), and the magnitude responsivities were compared. While the magnitude responsivity is not used in the complex calibration method, it is a useful approximation of the end-to-end instrument transmission, including detector response. This data can be used to directly determine the instrument's polarization plane orientation, with high measurement sensitivity. It also provides a measure of the spectrally resolved amplitude of the instrument polarization.

The magnitude responsivity R is defined as:

$$R = \frac{\left| \langle S_H(\sigma_k) \rangle - \langle S_C(\sigma_k) \rangle \right|}{\left| \langle L_H(\sigma_k) \rangle - \langle L_C(\sigma_k) \rangle \right|}, \quad (4.28)$$

where \mathcal{S}_H and \mathcal{S}_C are the complex spectra for the corresponding hot and cold blackbody calibration references, and $\langle \rangle$ denotes the mean over the data collection period. L_H and L_C are the mean predicted radiances for the hot and cold blackbody calibration references, respectively:

$$\langle L(\sigma_k) \rangle = e(\sigma_k) \langle B(\sigma_k, T) \rangle + (1 - e(\sigma_k)) \langle B(\sigma_k, T_R) \rangle. \quad (4.29)$$

The spectrally resolved magnitude responsivities, for linear polarization orientations from 0° to 180° degrees in 15° increments, are shown in Figure 103 (LW MCT) and Figure 104 (DTGS). To provide optimum signal to noise at the responsivity band edges, means over the full duration of the dataset (approximately 2 hours per data collection) were used as indicated in Eq. (4.28) and (4.29).

To further improve signal to noise, the 0.5 cm⁻¹ resolution data is averaged to a lower spectral resolution. The spectral bin size is selected to optimize measurement signal to noise while maintaining sufficient spectral resolution to resolve low frequency features. Since the signal to noise is better in this test than it is for the four-body polarization measurement, smaller spectral bins can be used (25 cm⁻¹ versus 50 cm⁻¹ for the LW MCT, and 50 cm⁻¹ versus 100 cm⁻¹ for the DTGS). The magnitude responsivity after spectral binning is shown in Figure 105 and Figure 106 for the LW MCT and DTGS channels, respectively.

When analyzing the dependence of the instrument response on linear polarizer orientation, the spectral bin positions were again selected to avoid the strong CO₂ atmospheric lines (Q branches), and limited to within the spectral response region that provided acceptable signal to noise. Again, H₂O features have been mitigated via the use of a dry air purge. Spectral bin centers at 612.5, 812.5, 912.5, 1012.5, 1112.5, 1212.5, 1312.5, and 1412.5 cm⁻¹ were selected for the LW MCT, while spectral bin centers at 325, 425, 525, 825, 925, 1025, and 1125 cm⁻¹ were selected for the DTGS detector. The spectrally averaged data is presented as a function of linear polarizer angle for each spectral bin in Figure 107 (LW MCT) and Figure 108 (DTGS). Error bars for the spectrally averaged residuals indicate the statistical variation for the spectral average, and are specified as the 3- σ standard deviation of the data in the average divided by the square root of the number of data points in the average. In Figure 107 and Figure 108, the phase shift of the dependence of the instrument responsivity on polarizer angle for the spectral bins in the 800 – 950 cm⁻¹ spectral range are out of family from the rest of the results. Referring to Figure 103 and Figure 104, we see that the magnitude response for both detector channels in this spectral region shows little dependence on linear polarizer angle. When the magnitude responsivities are plotted as a relative difference with respect to the magnitude response for the linear polarizer at 45° (LW MCT in Figure 109 and DTGS in Figure 110), it is also evident that the sign of the relative differences changes in this region for all linear polarizer angles. The sign change is an unexpected result, and discussed further at the end of the section. From these figures, we can conclude that the instrument polarization is at a minimum in this spectral region. A holographic wire grid polarizer (KRS-5 substrate) was used for this test, with a manufacturer specified typical crossed polarizer transmission (the transmission for a series polarizer pair with perpendicular transmission axes) of approximately 0.4% from 6 – 20 μ m and typical extinction ratio of 300:1 at 15 μ m. Despite a reasonably high extinction ratio, it is realistic to expect that the use of a non-ideal linear polarizer may have appreciable effects on the accuracy of this measurement in the region in which the instrument degree of polarization is near zero.

For spectral regions ν_k in which the degree of polarization of the instrument is significant, the modulation of the instrument magnitude response R as a function of the linear polarizer angle γ , is described by a sinusoid of period π with offset b_k ,

$$R_{\nu_k} = A_k \sin(2\gamma + \phi) + b_k . \quad (4.30)$$

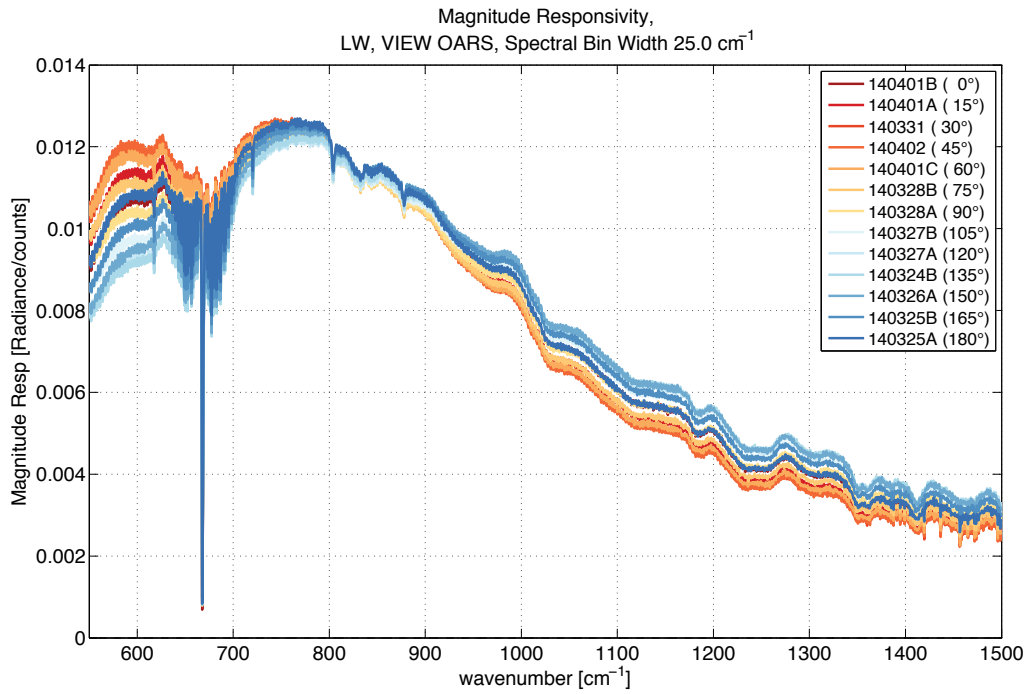


Figure 103: LW MCT channel spectrally resolved magnitude instrument responsivity, for linear polarization orientations from 0° to 180° degrees in 15° increments.

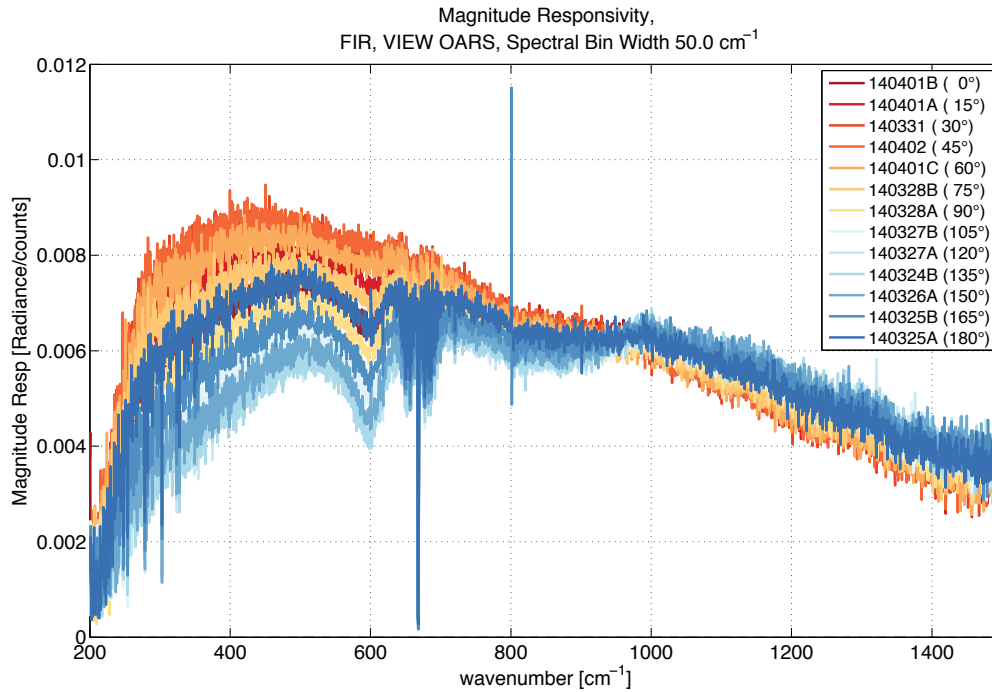


Figure 104: DTGS channel spectrally resolved magnitude instrument responsivity, for linear polarization orientations from 0° to 180° degrees in 15° increments.

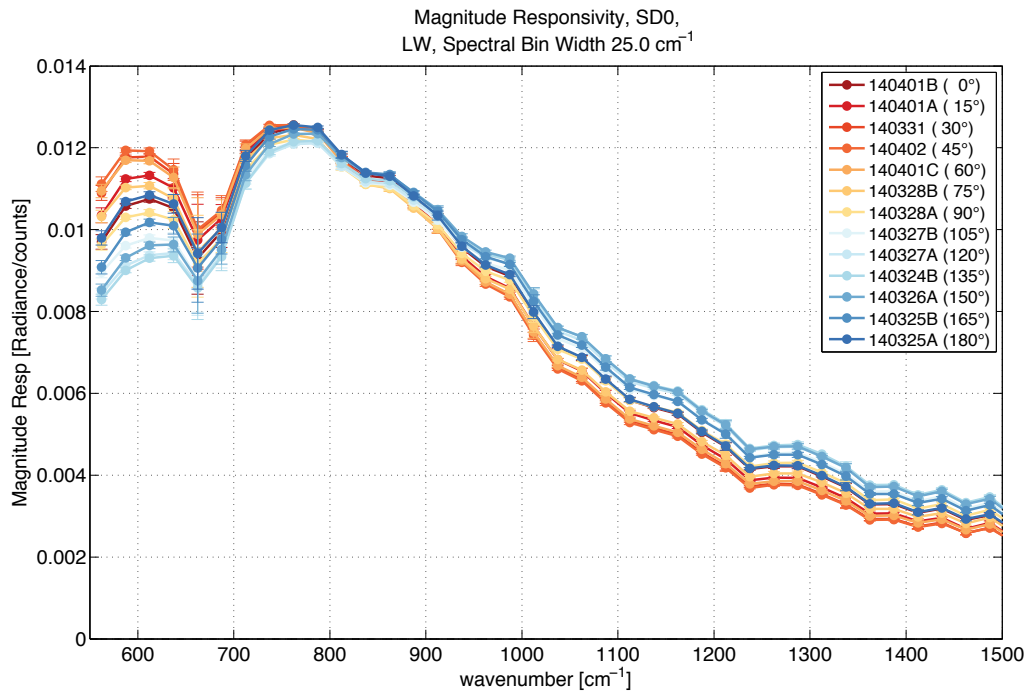


Figure 105: LW MCT channel magnitude instrument responsivity with spectral averaging. To further improve signal to noise, the 0.5 cm⁻¹ resolution data is averaged to a lower spectral resolution. The spectral bin size is selected to optimize signal to noise while maintaining sufficient spectral resolution to resolve low frequency features.

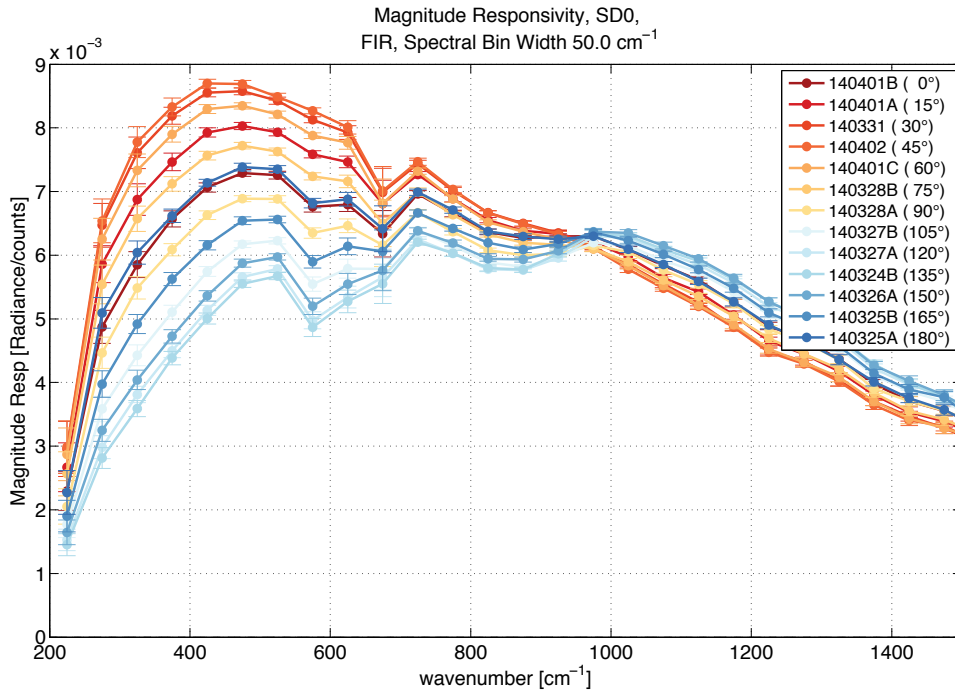


Figure 106: DTGS channel magnitude instrument responsivity with spectral averaging. To further improve signal to noise, the 0.5 cm^{-1} resolution data is averaged to a lower spectral resolution. The spectral bin size is selected to optimize signal to noise while maintaining sufficient spectral resolution to resolve low frequency features.

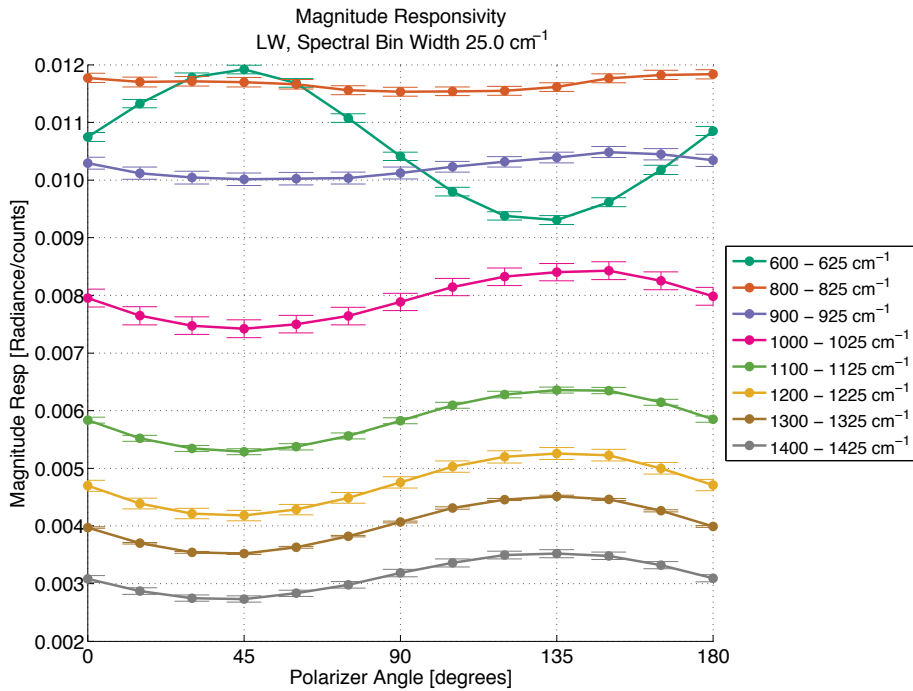


Figure 107: LW MCT channel spectrally averaged magnitude responsivity versus linear polarizer angle.

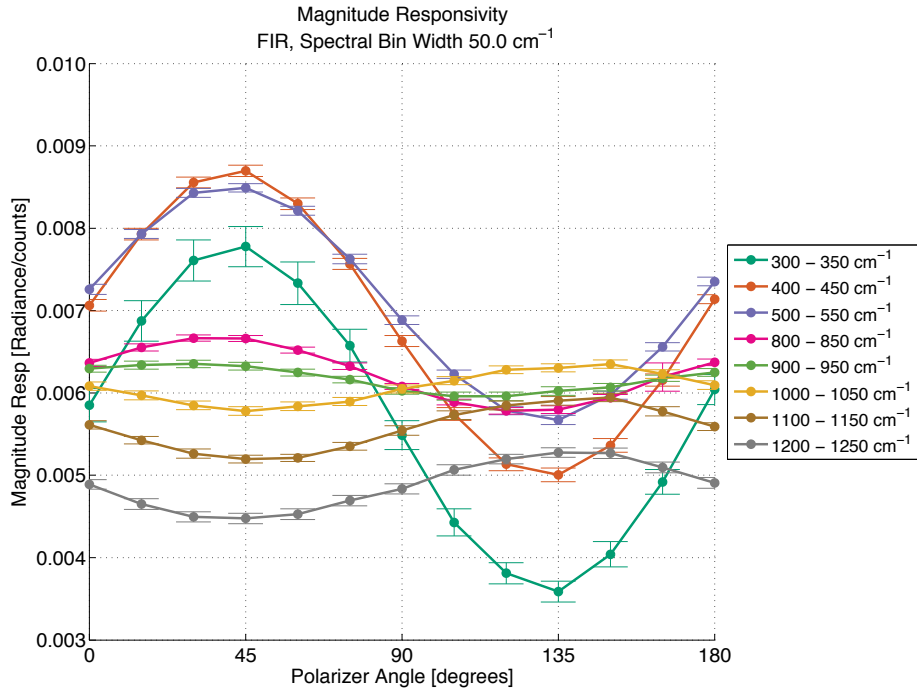


Figure 108: DTGS channel spectrally averaged magnitude responsivity versus linear polarizer angle.

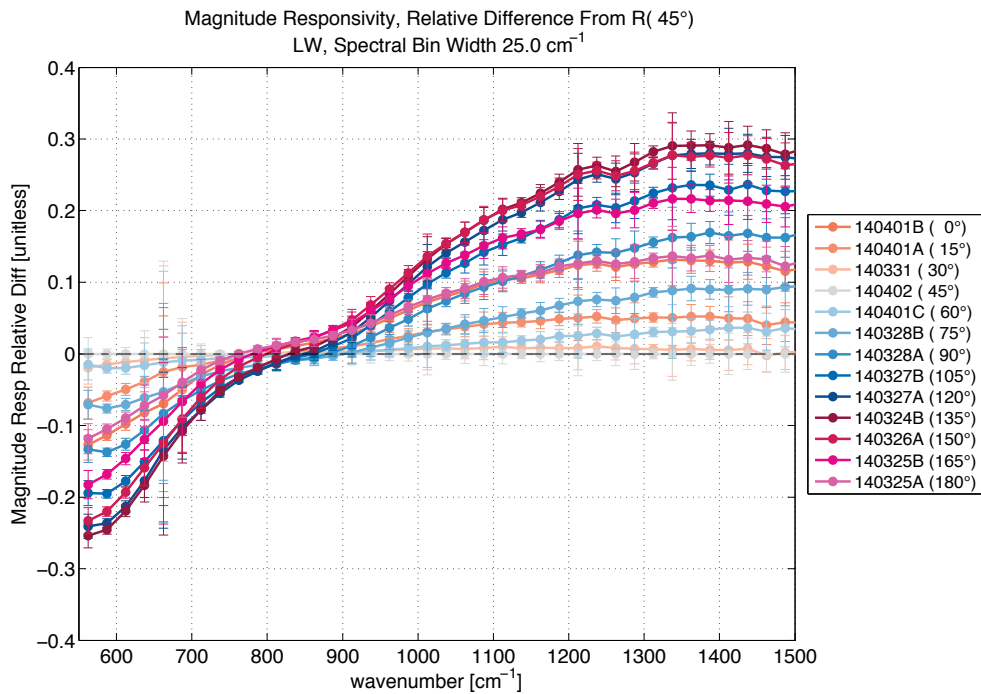


Figure 109: LW MCT magnitude responsivities plotted as a relative difference with respect to the magnitude response for the linear polarizer at 45°. Note that the sign of the relative difference changes in the 750 – 950 cm^{-1} region for all linear polarizer angles.

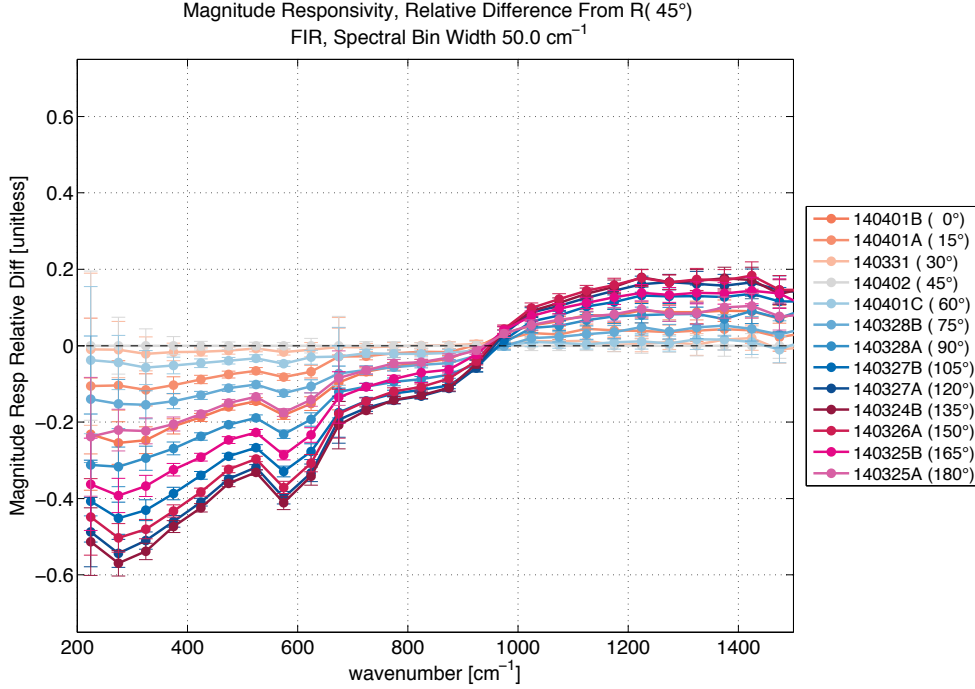


Figure 110: DTGS magnitude responsivities plotted as a relative difference with respect to the magnitude response for the linear polarizer at 45°. Note that the sign of the relative difference changes in the 850 – 950 cm⁻¹ region for all linear polarizer angles.

A two-step fitting process similar to that described in Section 4.3.1, was utilized to fit Eq. (4.30) to the data, and nonlinear least squares curve fitting methodology was used for both steps.

Once again, the phase shift is determined in the first step of the fitting process, and the amplitudes and offsets are determined in the second step. Consistent with the four-body test, it is assumed that the sensor will act as a partial linear polarizer, with no birefringence. As a result, the phase shift is expected to be independent of wavenumber and the common to all spectral bin averages. Unlike the prior section, our data has a nonzero offset, and spans a full period of the sine function. Accordingly, for the phase shift fit the offset is estimated as the average value of the responsivity for the spectral bin, and the amplitude is estimated as the maximum deviation from this offset.

The objective function for the nonlinear least squares fit is the root mean square of the fit error for all spectral bins, proportionally weighted by responsivity magnitude and inversely weighted by noise:

$$f(\phi) = \sqrt{\frac{1}{n} \sum_k \frac{b_{1_k}}{b_{2_k}} [A_k \sin(2\gamma + \phi) - R_{v_k}]^2}, \quad (4.31)$$

$$b_{1_k} = \langle R_{v_k} \rangle_\gamma, \quad (4.32)$$

$$b_{2_k} = \left\langle \left(\frac{3\sigma_R}{N} \right)_{v_k} \right\rangle_\gamma. \quad (4.33)$$

The amplitude and offset of each sinusoid is solved for in the second step of the data fitting process, with the phase shift from the first stop of the fitting process provided as an input. The objective function is optimized for each spectral average separately,

$$f(A_k, b_k) = A_k \sin(2\gamma + \phi_{opt}) + b_k - R_{v_k}. \quad (4.34)$$

The results of the curve fit are shown in Figure 111 for the LW MCT and Figure 112 for the DTGS.

The curve fit results for both detector bands are quite good, with the exception of the 800 – 950 cm^{-1} region. Note that the sign of the amplitude changes in this region. The results indicate an instrument polarization plane angle of 41.8° (phase shift of 3.2° from the assumed 45°), as measured by the LW MCT channel and 41.2° (3.8° phase shift) for the DTGS channel.

The results for the 800 – 950 cm^{-1} spectral region show a phase shift that is out family when compared to the other spectral averages. Earlier in this section, we had noted that the magnitude response for both detector channels in this spectral region shows little dependence on linear polarizer angle and concluded that the instrument polarization is low in this region. This makes it particularly sensitive to other possible bias contributors, such as the finite extinction ratio associated with a real linear polarizer. It is also noteworthy that the sign of the amplitude also changes in this region.

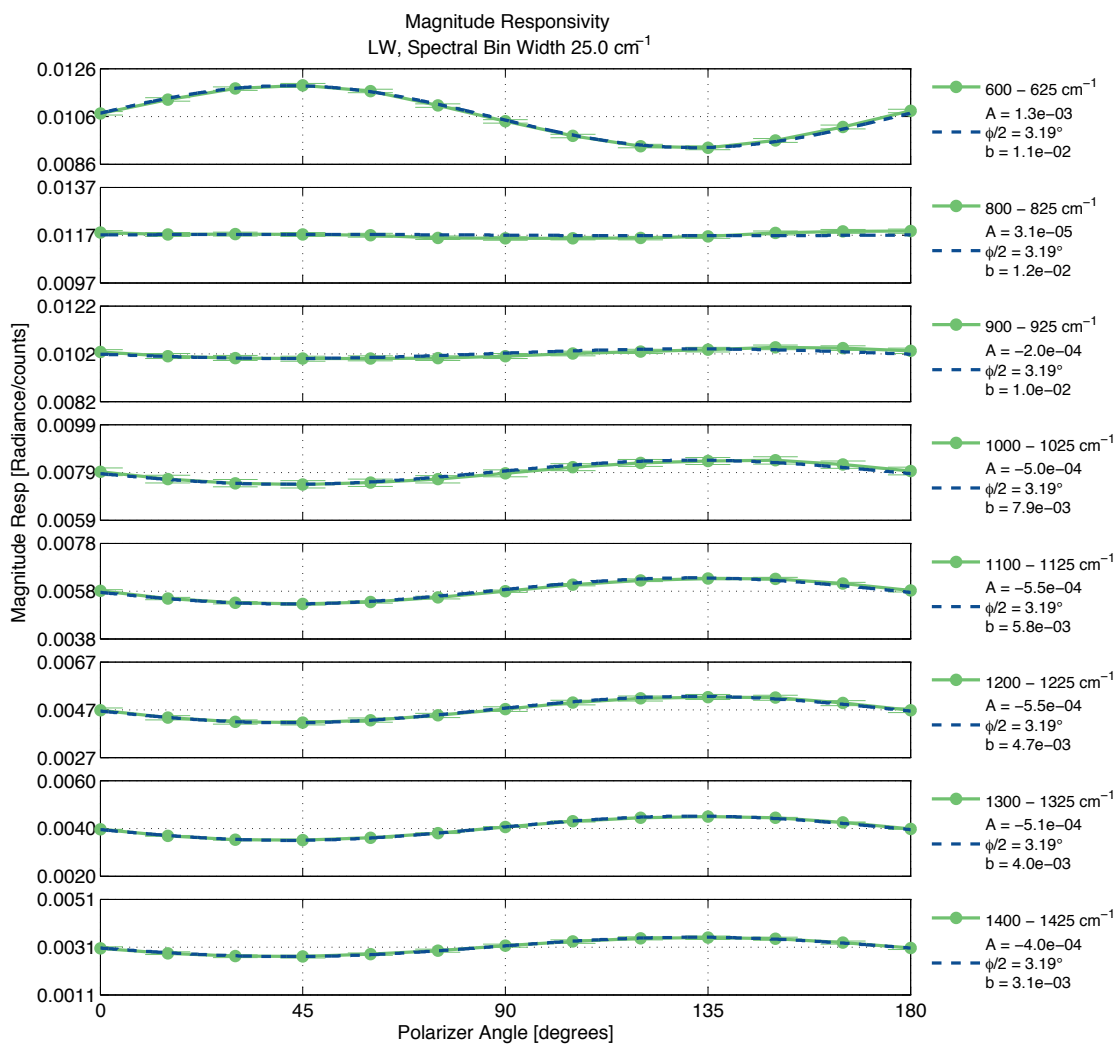


Figure 111: LW MCT channel spectrally averaged magnitude responsivity plotted as a function of linear polarizer angle for a series of spectral bins. The blue dashed line indicates the sinusoidal fit, and the fit parameters are provided on the right.

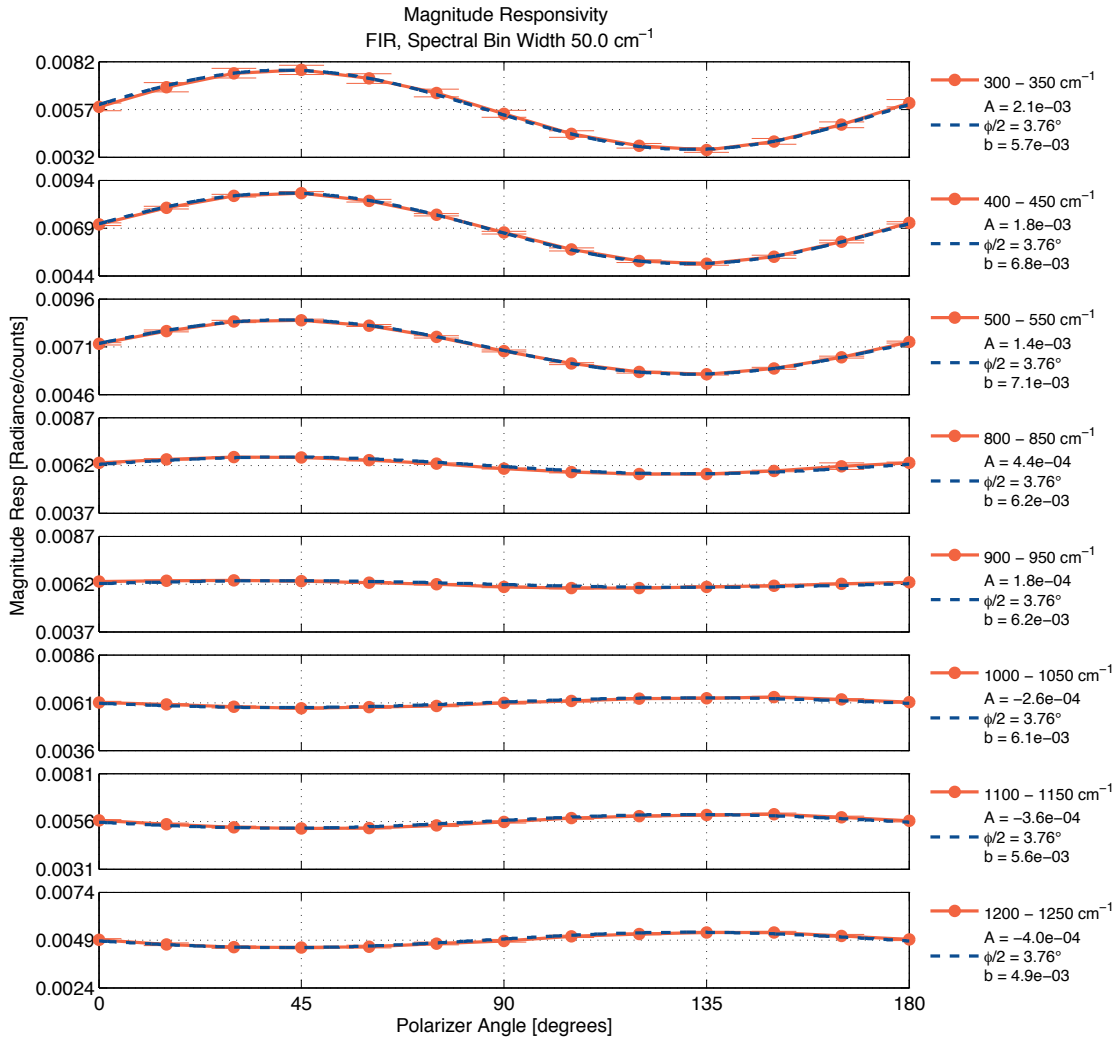


Figure 112: DTGS channel spectrally averaged magnitude responsivity plotted as a function of linear polarizer angle for a series of spectral bins. The blue dashed line indicates the sinusoidal fit, and the fit parameters are provided on the right.

Recall that the instrument transmission polarization sensitivity was defined as,

$$p_t = \frac{t_{\max} - t_{\min}}{t_{\max} + t_{\min}}, \quad (4.35)$$

and t_{\max} and t_{\min} are the major and minor axis of the instrument transmission polarization ellipse, with the major axis oriented at angle α . p_t is also commonly referred to as the diattenuation, and the major and minor axis of the polarization ellipse are, by definition, oriented at 90° to one another. The dependence of the magnitude responsivity measurements on linear polarizer angle can be used to estimate the instrument diattenuation directly. Noting that the magnitude responsivity is representative of the instrument transmission,

Eq. (4.35) can be generalized for magnitude responsivity measurement pairs R_γ and R_{γ_2} , measured at polarizer angles separated by 90° ,

$$p_i'(\gamma, \sigma) = \frac{R_\gamma - R_{\gamma_2}}{R_\gamma + R_{\gamma_2}}, \quad (4.36)$$

$$\gamma_2 = \gamma + 90^\circ. \quad (4.37)$$

For the responsivity pair with the magnitude responsivity measurement R_γ corresponding to the configuration with the linear polarizer aligned with the major axis of the instrument transmission polarization ellipse ($\gamma = \alpha$), and the second magnitude responsivity measurement R_{γ_2} made with the linear polarizer aligned with the minor axis of the instrument transmission polarization ellipse ($\gamma_2 = \alpha + 90^\circ$), Eq. (4.36) provides an estimate of the instrument diattenuation p_i .

The measurement results for the magnitude responsivity pairs described by Eq. (4.36) and (4.37) are provided in Figure 113 (LW MCT) and Figure 114 (DTGS). The results illustrate that the maximum difference in the measured magnitude responsivity pairs occur at $\gamma = 45^\circ$, the measurement pair for which the linear polarizer is most closely aligned with, and at 90° to, the instrument polarization angle. For this condition, the result provides an estimate of the diattenuation due to the instrument.

There are noticeable differences in the result for the LW MCT and DTGS detectors. It is not clear whether these differences are due to real differences in the polarization sensitivity of the aft-optics for each output, or indicative of the limitations due to uncertainty associated with this method. The DTGS measurement appears to be subject to low signal to noise considerations below 300 cm^{-1} and above 1100 cm^{-1} . The same consideration limits the useful extent of the LW MCT measurement for this data is $600 - 1500 \text{ cm}^{-1}$.

To conclude this section, $p_i'(\gamma, \sigma)$ is plotted versus the polarization orientation angle γ (which corresponds to the R_γ measurement) and fit with a sinusoid. The maximum value of p_i' occurs when the linear polarizer orientation for the R_γ measurement is aligned with the major axis of the instrument transmission polarization ellipse ($\gamma = \alpha$). The LW MCT results are shown in Figure 115 and DTGS results are provided in Figure 116. The fit results indicate a phase shift from the assumed 45° instrument polarization angle of 2.2° ($\alpha = 42.8^\circ$ for the LW MCT and 3.4° ($\alpha = 41.6^\circ$) for the DTGS).

Recall, the fit to the individual responsivity measurements described earlier in the section, resulted in $\alpha = 41.8^\circ$ for the LW MCT, and $\alpha = 41.2^\circ$ for the DTGS. The usage of the magnitude responsivity pairs described by equation (4.36) should result in a determination of the instrument polarization axis orientation that is less sensitive to bias contributors that are independent of linear polarizer angle. This method also provides a direct estimate of the instrument polarization diattenuation. The preceding analysis, which was based on the individual magnitude responsivities, is more susceptible to measurement biases that are independent of polarizer orientation.

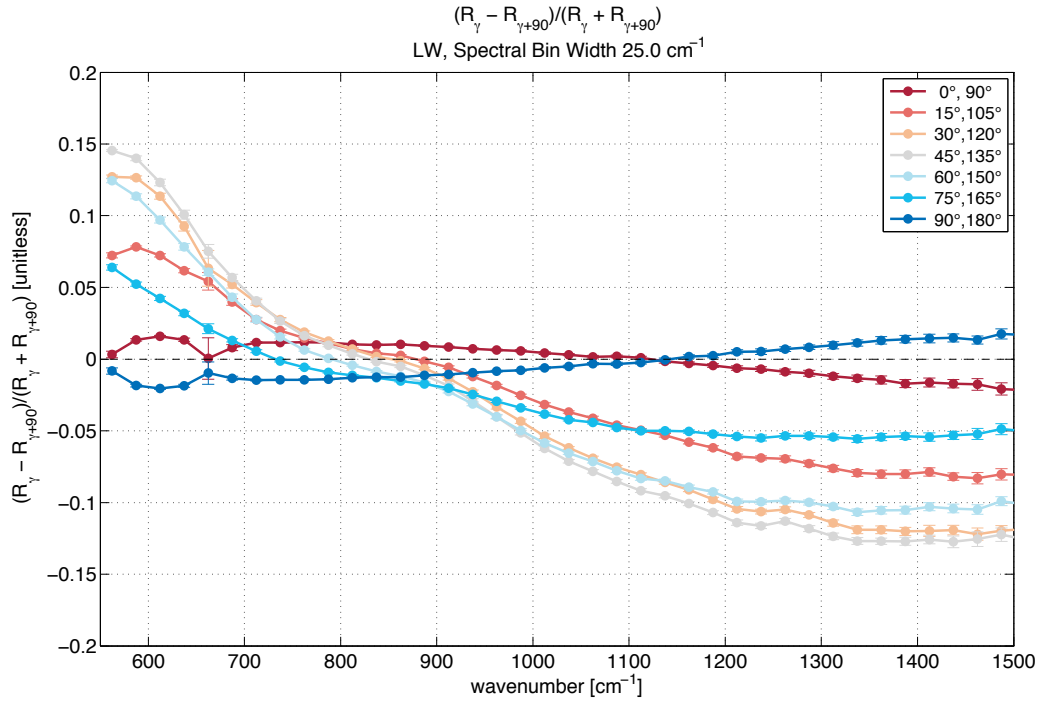


Figure 113: LW MCT 90° responsivity pair plot, as defined by Eq. (4.36). The legend specifies the polarizer angles used for the magnitude responsivity pair (γ , $\gamma_2 = \gamma + 90^\circ$).

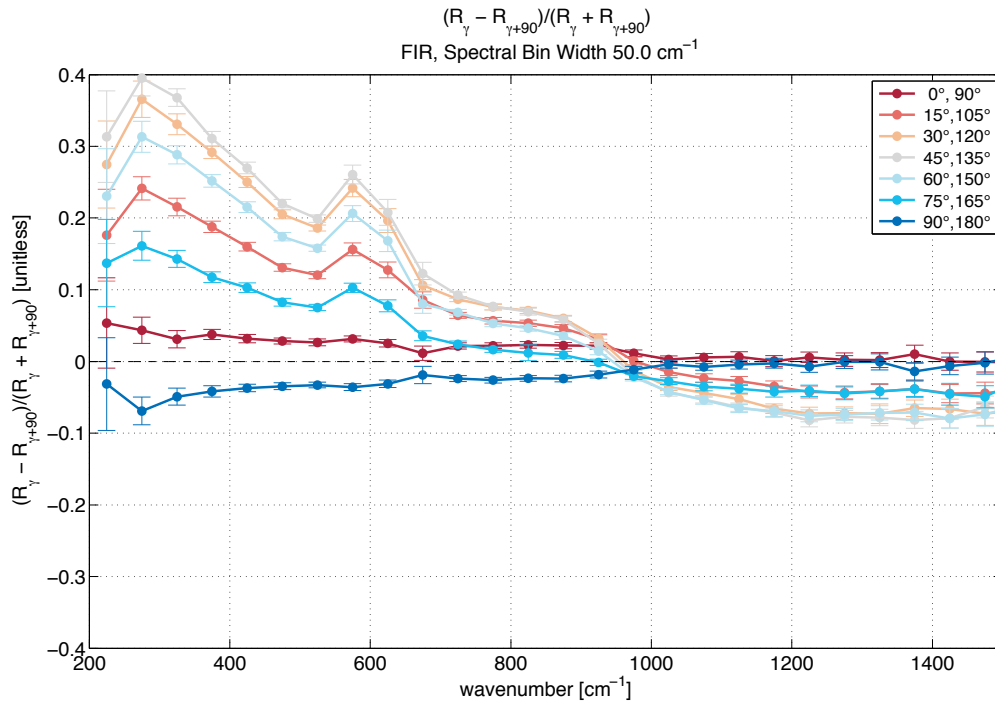


Figure 114: DTGS 90° responsivity pair plot, as defined by Eq. (4.36). The legend specifies the polarizer angles used for the magnitude responsivity pair (γ , $\gamma_2 = \gamma + 90^\circ$).

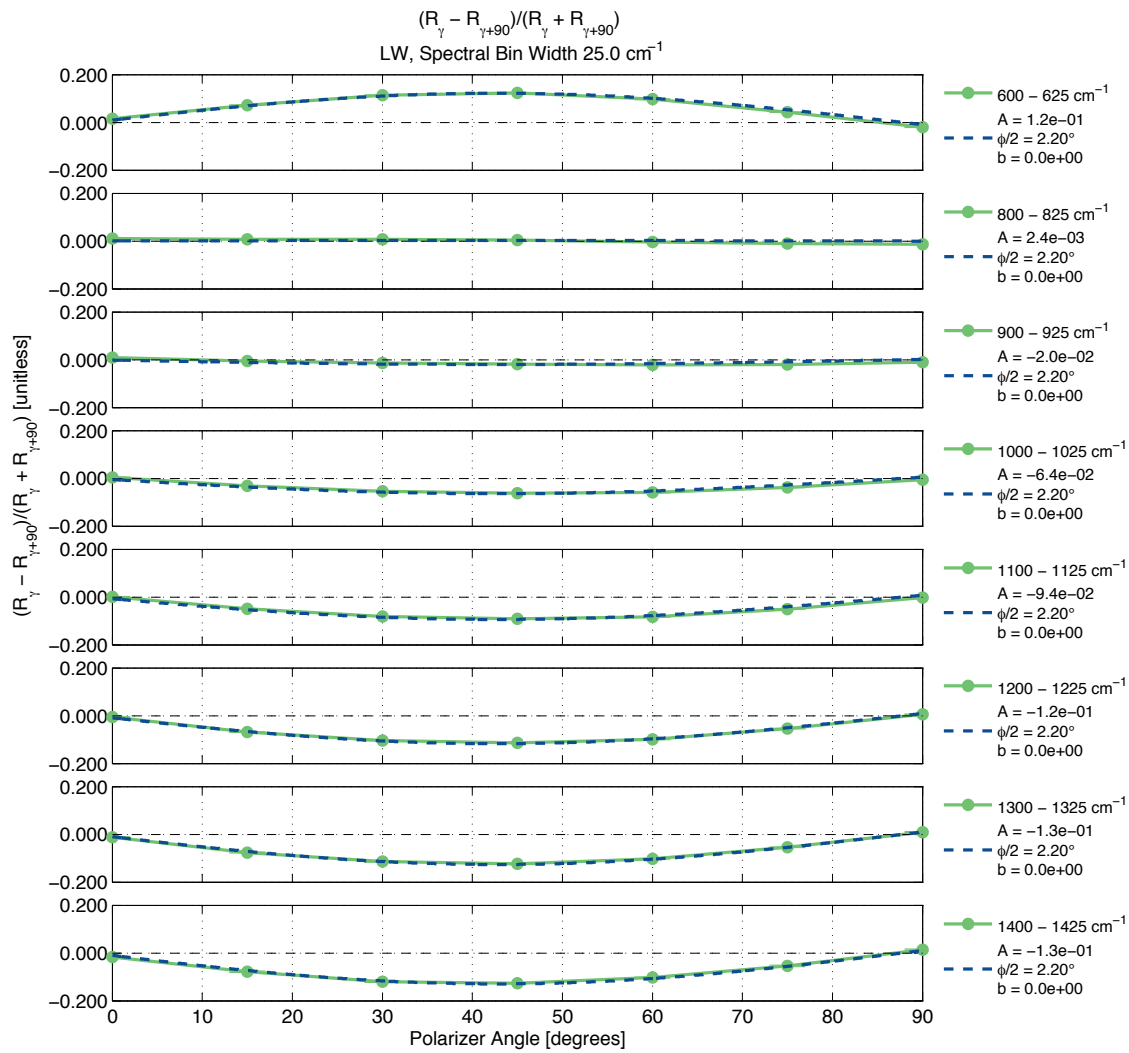


Figure 115: LW MCT 90° responsivity pair, as defined by Eq. (4.36), plotted as a function of γ . Spectral range and fit parameters are specified to the right of each panel.

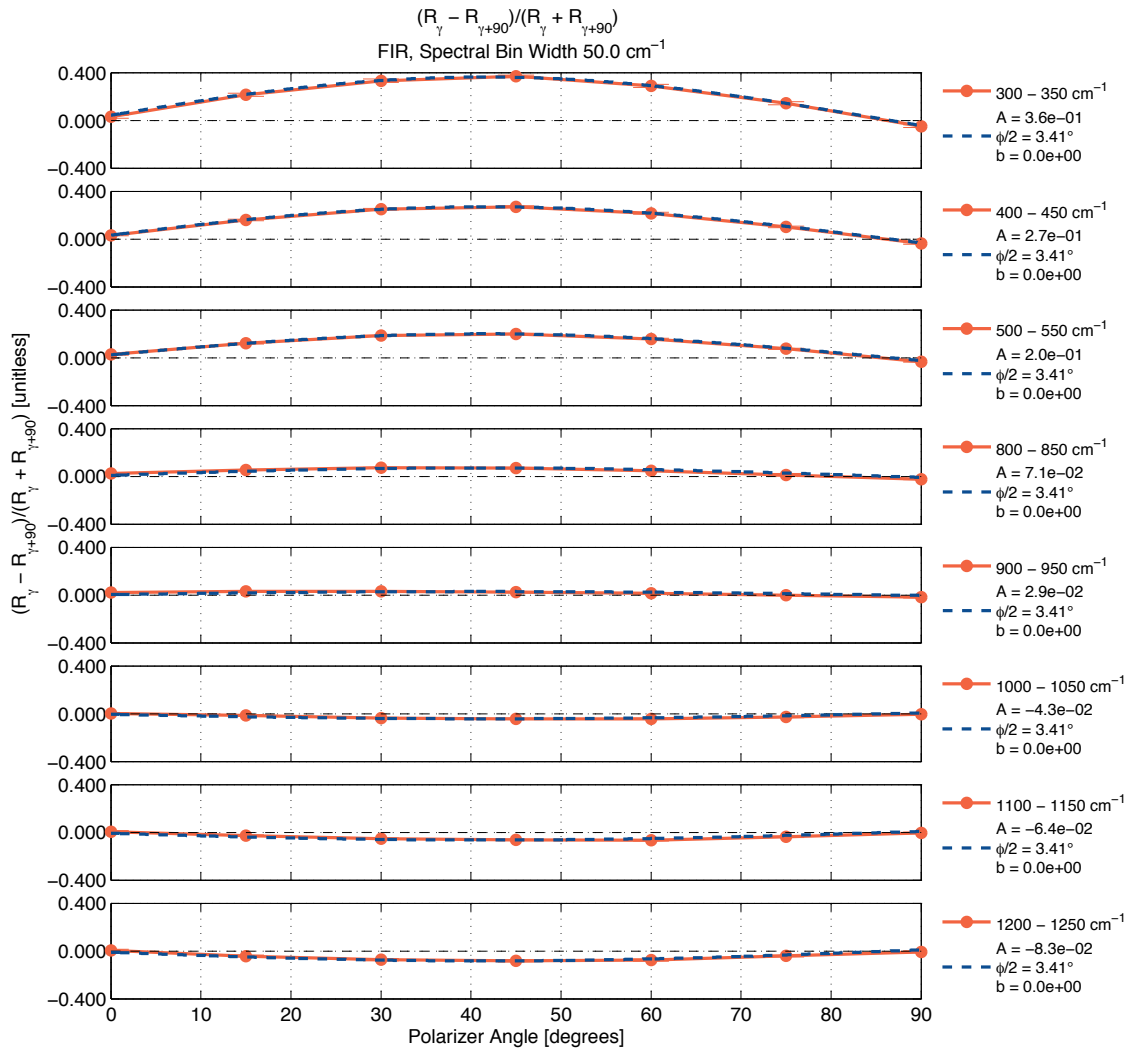


Figure 116: DTGS 90° responsivity pair, as defined by Eq. (4.36), plotted as a function of γ . Spectral range and fit parameters are specified to the right of each panel.

4.3.3 Polarization characterization and verification summary

A summary of the polarization characterization measurement results for the two-source and four-source polarization tests is presented in Table 11. The results are reasonably consistent, considering the limitations due to the uncertainties in the measurements.

As described earlier in the section, the four-source polarization measurements have worse signal to noise than that of the two-source polarization with linear polarizer measurements. As a result the four-source data has the highest uncertainty with respect to determination of the location of the polarization sensitivity zeroes. However, it has the advantage of providing a direct characterization of the radiometric calibration bias associated with the instrument polarization sensitivity and non-optimal orientation of the calibration and verification assembly. The usage of the magnitude responsivity pairs described by equation (4.36) facilitates

determination of the instrument polarization axis orientation and mitigates sensitivity to bias contributors that are independent of linear polarizer angle, and provides a direct estimate of the instrument polarization diattenuation. It is reasonable to expect that this combination of data collection and analysis methods provide the most accurate determination of the polarization sensitivity zero crossings. Finally, the two-source polarization test analysis that is based on the individual magnitude responsivities, is susceptible to measurement biases that are independent of polarizer orientation, but this method still provides better signal to noise than the four-source measurements.

Table 11: A summary of the polarization characterization measurement results for the two-source and four-source polarization tests is presented here. Brackets are used to indicate results that were not explicitly measured, but have been extrapolated assuming a 90° spacing of the zero-crossing polarization sensitivity points.

Detector	Polarization Sensitivity Zero Locations		
	Four-source Polarization Test	2-Source Polarization Test Magnitude Responsivities	2-Source Polarization Test Mag. Responsivity Pairs
LW MCT	0°, 90°, (180°, 270°)	-3.2°, 86.8°, 176.8°, (266.8°)	-2.2°, 87.8°, (177.8°, 267.8°)
DTGS	-4.2°, 85.8°, (175.8°, 265.8°)	-3.8°, 86.2°, 176.2°, (266.2°)	-3.4°, 86.6°, (176.6°, 266.6°)

It has been noted that the results for the 800 – 950 cm⁻¹ spectral region for both detectors show a phase shift that is out family when compared to the other spectral averages. The magnitude response for both detector channels in this spectral region shows little dependence on linear polarizer angle and it is reasonable to conclude that the instrument polarization sensitivity is lowest in this region. This makes it particularly sensitive to other possible bias contributors, such as the finite extinction ratio associated with a real linear polarizer. A holographic wire grid polarizer (KRS-5 substrate) was used for the two-source test. The manufacturer specifications indicated a typical crossed polarizer transmission of approximately 0.4% from 6 – 20 μm and typical extinction ratio of 300:1 at 15 μm. Despite a reasonably high extinction ratio, it is realistic to expect that the use of a non-ideal linear polarizer may have appreciable effects on the accuracy of this measurement in the region in which the instrument degree of polarization is near zero. Repeating the test using a polarizer with a higher extinction ratio, or alternatively two polarizers in series with their polarization axes aligned, may provide further insight into the impact of a finite extinction ratio on the measurement.

The change of sign of the polarization sensitivity in 800 – 950 cm⁻¹ region was also unexpected. It is possible that the use of a single linear polarizer is not sufficient, as it does not allow independent characterization of linear and circular polarization sensitivities, or the measurement of both diattenuation and retardation for the sensor. Finally, it is important to recall that the output of the interferometer is a differential measurement of the incident radiances at both input ports. In both the 4-source and 2-source measurement, the polarization of the incident radiance is only being modified at the first input port; by the orientation of the incident plane at the scene select mirror for the 4-source measurement, and by the linear polarizer in the 2-source measurement. The analysis does not explicitly consider the impact of the constant and unpolarized radiance at the second input port, and it is conceivable that there is a spectral dependence for this unaccounted for effect. When the analysis involves the difference between two measurements, the contribution from the second input port will be removed if the second port and instrument temperatures are consistent between datasets.

Referring to Table 11, the difference between the optimum angular position of the calibration and verification module for the two detector channels is noteworthy. It ranges from a difference of 0.6° for the two-source with

linear polarizer test that utilized a magnitude responsivity analysis, to 4.2° for the four-source polarization test. This is potentially due to aft-optic or detector dependent polarization effects. If the angular orientation of the calibration and verification module was positioned midway between the optimum positions for the two detector channels, the viewports would be displaced from the polarization induced calibration bias zero-crossings by 2.1° for both outputs (assuming a difference of 4.2°). Referring again to Figure 97 and Figure 98, an angular shift of 2° from the zero-crossing results in a calibration bias as large as 0.02 K (DTGS, 300 – 400 cm^{-1} spectral bin).

4.4 Recommendations for future designs

The instrument calibration and verification module on the ARI prototype was designed such that the position of the views can be rotated to fine-tune the view placement with respect to the instrument's polarization sensitivity zero-crossing points, and provide an end-to-end verification of the polarization induced error. This capability should be planned, if not for the flight unit, at least for an optically representative engineering model. It is clear that the exact location of the instrument's polarization sensitivity zero-crossing points is difficult to predict via model, and the capability to fine-tune the placement of the view placement with respect to the instrument's polarization sensitivity zero-crossing points based on measurement data is necessary. Measurements of the instrument polarization sensitivity should be conducted early in the instrument testing, and the placement of the views adjusted accordingly.

It is also important to retain a polarization characterization viewport of deep space located midway between two of the 90° spaced viewports. This will accommodate periodic on-orbit checks of polarization-induced bias at the scene select mirror angle corresponding to the polarization characterization viewport. Having two cold space views at approximately 45° spacing will provide a very sensitive measurement of any changes in polarization at the scene mirror positions of these two deep space views.

Pre-launch characterization should include S.I. traceable measurements of the s- and p-polarization reflectance for witness samples that are representative of all reflective components, as well as s- and p-polarization transmission of the beam splitter and any other transmissive components, or witness samples representative of those components (including optical coatings). These measurements are necessary for the development of an accurate polarization model.

While the instrument is designed to eliminate calibration biases due to polarization, knowledge and characterization of the polarization parameters at the component and system level will allow traceable verification of polarization immunity. As noted, testing and analysis indicated a difference between the optimum angular position of the calibration and verification module for the two detector channels for the ARI prototype. This is likely due to aft-optic or detector dependent polarization effects. To minimize the differences between the two channels, the same aft-optic design should be used for both output ports, including the window at the respective detectors.

5 Low signal to noise ratio and calibration

As outlined in Chapter 1, the complex calibration method uses spectra of hot and cold calibration reference sources to calculate calibrated spectral radiances. Error in the calibrated radiance is thus due to uncertainties in the raw scene and calibration spectra, in addition to other sources of uncertainty such as the temperatures and emissivities of the calibration sources, as indicated in Eq. (1.16) [141]. It can be shown that a low responsivity threshold exists, below which a bias in the calibration occurs for high noise measurements [142, 143]. The sensor responsivity depends primarily on detector sensitivity, the throughput and transmission of the optical system, and atmospheric absorption by trace gases within the sensor.

The calibration bias due to low signal responsivity and high noise, as presented by Rowe et al [142, 143], can be understood more clearly by first examining the complex calibration equation, presented in Chapter 1, and reproduced here:

$$L_S(\sigma_k) = (L_H(\sigma_k) - L_C(\sigma_k)) \operatorname{Re} \left\{ \frac{\mathcal{S}_S(\sigma_k) - \mathcal{S}_C(\sigma_k)}{\mathcal{S}_H(\sigma_k) - \mathcal{S}_C(\sigma_k)} \right\} + L_C(\sigma_k). \quad (5.1)$$

Recall, in Eq. (5.1), $L_S(\sigma_k)$ is the calibrated radiance; $\mathcal{S}_S(\sigma_k)$, $\mathcal{S}_C(\sigma_k)$ and $\mathcal{S}_H(\sigma_k)$ are the complex measured spectra for the scene, cold reference, and hot reference views respectively; and $L_C(\sigma_k)$ and $L_H(\sigma_k)$ are the calculated radiances for the respective cold and hot reference views. The calculated radiance from a non-ideal blackbody cavity is the sum of the emitted and reflected radiance from the cavity

$$L(\sigma_k) = e(\sigma_k) B(\sigma_k, T) + (1 - e(\sigma_k)) B(\sigma_k, T_R), \quad (5.2)$$

where $e(\sigma_k)$ is the effective emissivity of the blackbody, $B(\sigma_k, T)$ is the Planck radiance for an ideal blackbody of temperature T , and $B(\sigma_k, T_R)$ is the Planck radiance of the background, of mean temperature T_R , that is reflected from the cavity.

The potential bias due to low signal to noise ratio measurements is associated with the zero signal limit of the complex spectral measurement ratio \mathbb{X} in the calibration equation:

$$\begin{aligned} \mathbb{X} &= \frac{\mathcal{S}_S(\sigma_k) - \mathcal{S}_C(\sigma_k)}{\mathcal{S}_H(\sigma_k) - \mathcal{S}_C(\sigma_k)} \\ &= \frac{\mathcal{S}_S(\sigma_k)}{\mathcal{S}_H(\sigma_k) - \mathcal{S}_C(\sigma_k)} - \frac{\mathcal{S}_C(\sigma_k)}{\mathcal{S}_H(\sigma_k) - \mathcal{S}_C(\sigma_k)}. \end{aligned} \quad (5.3)$$

Considering measurements with only Type A uncertainty it is clear that the limit of the mean of the first term in (5.3) approaches zero as the signal to noise ratio (SNR) approaches zero:

$$\lim_{SNR \rightarrow 0} \left\langle \frac{\mathcal{S}_S(\sigma_k)}{\mathcal{S}_H(\sigma_k) - \mathcal{S}_C(\sigma_k)} \right\rangle = 0. \quad (5.4)$$

The limit of the mean of the second term in (5.3) approaches a nonzero constant as the signal to noise ratio approaches zero:

$$\lim_{SNR \rightarrow 0} \left\langle \frac{S_C(\sigma_k)}{S_H(\sigma_k) - S_C(\sigma_k)} \right\rangle = C. \quad (5.5)$$

S_C appears both in the numerator and denominator in equation (5.5) and can be assumed to be completely correlated for each measurement of S_C . When the noise in S_H and S_C are equal, the limit in equation (5.5) approaches -0.5.

Combining equations (5.4) and (5.5), it is clear that the limit of the mean complex spectral measurement ratio \mathbb{X} also approaches the negative value of the nonzero constant in equation (5.5):

$$\begin{aligned} \lim_{SNR \rightarrow 0} \langle \mathbb{X} \rangle &= \lim_{SNR \rightarrow 0} \left\langle \frac{S_S(\sigma_k) - S_C(\sigma_k)}{S_H(\sigma_k) - S_C(\sigma_k)} \right\rangle \\ &= \lim_{SNR \rightarrow 0} \left\langle \frac{S_S(\sigma_k)}{S_H(\sigma_k) - S_C(\sigma_k)} - \frac{S_C(\sigma_k)}{S_H(\sigma_k) - S_C(\sigma_k)} \right\rangle \\ &= -C. \end{aligned} \quad (5.6)$$

When the noise levels in all measured signals are the same amplitude, the limit in equation (5.6) approaches +0.5.

Changes in the noise levels of S_C or S_H such that they are no longer equal results in a zero signal limit of equation (5.6) that is not equal to 0.5. Increasing the signal to noise ratio in S_C moves the zero signal to noise limit of the mean of \mathbb{X} closer towards zero, and increasing the signal to noise ratio in S_H moves the zero signal to noise limit of the mean of \mathbb{X} towards unity, with limits of zero and unity respectively.

Simulated results illustrating this effect are provided in Figure 118, Figure 119, and Figure 120. The results for 900 cm^{-1} are shown. In the simulation, ideal blackbody radiances have been used for the hot and cold calibration references as well as the scene radiance, with temperatures of 333 K, 243 K, and 320 K, respectively (refer to Figure 117). A dataset size consisting of 1×10^7 measurements for each radiance source was used, with Gaussian white noise added to each measurement. A range of signal to noise values were tested, and the 3- σ value for the noise distribution was defined using the specified signal to noise ratio and the signal amplitude for the hot calibration reference. Thus the noise level is the same for the cold, hot, and scene radiance for a given SNR.

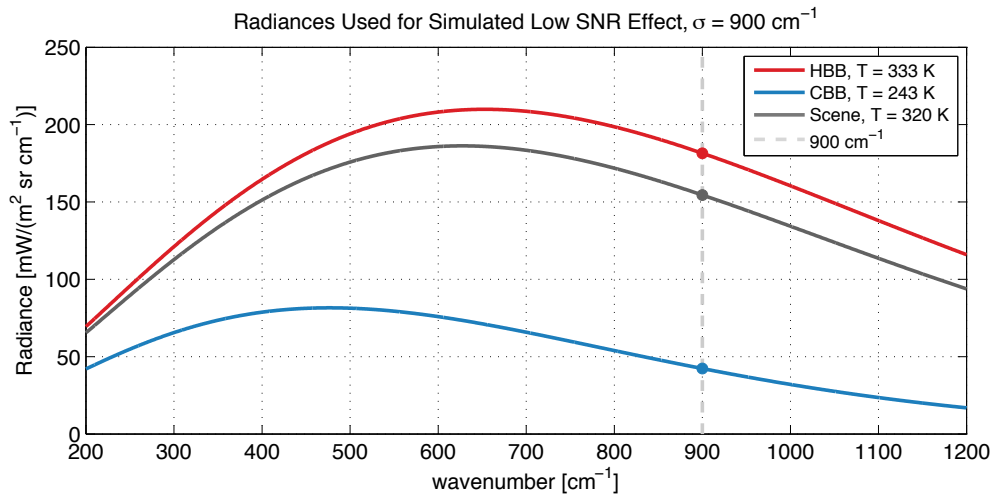


Figure 117: Ideal blackbody radiances were used for the simulation of the low signal to noise effect. Results are presented for 900 cm⁻¹.

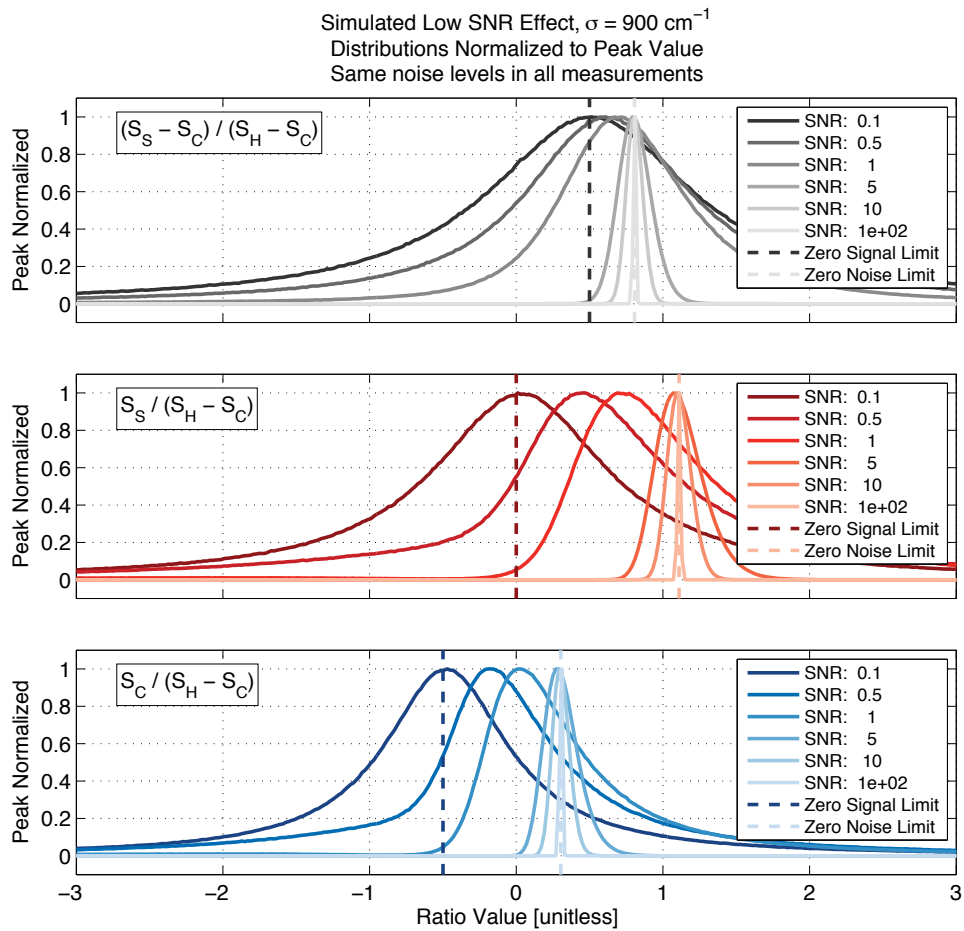


Figure 118: Simulated low SNR effect. The distributions (normalized to peak value) are provided for a range of signal to noise values. The results for the measurement ratio in the calibration equation are shown in the top panel (grey). The individual scene and cold reference measurement ratios are shown in the middle (red) and bottom (blue) panels, respectively. The zero noise and zero signal limits are also indicated.

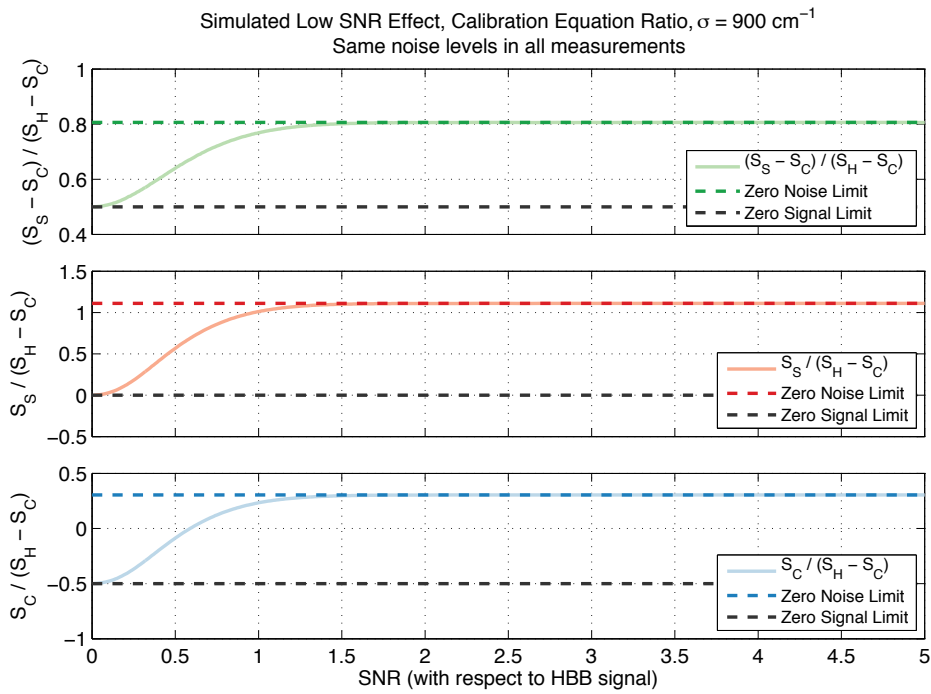


Figure 119: Simulated low SNR effect. The dependence of the mean value on the SNR for the calibration equation measurement ratio is shown in the top panel (green). The individual scene and cold reference measurement ratios are shown in the middle (red) and bottom (blue) panels, respectively. The zero noise and zero signal limits are also indicated.

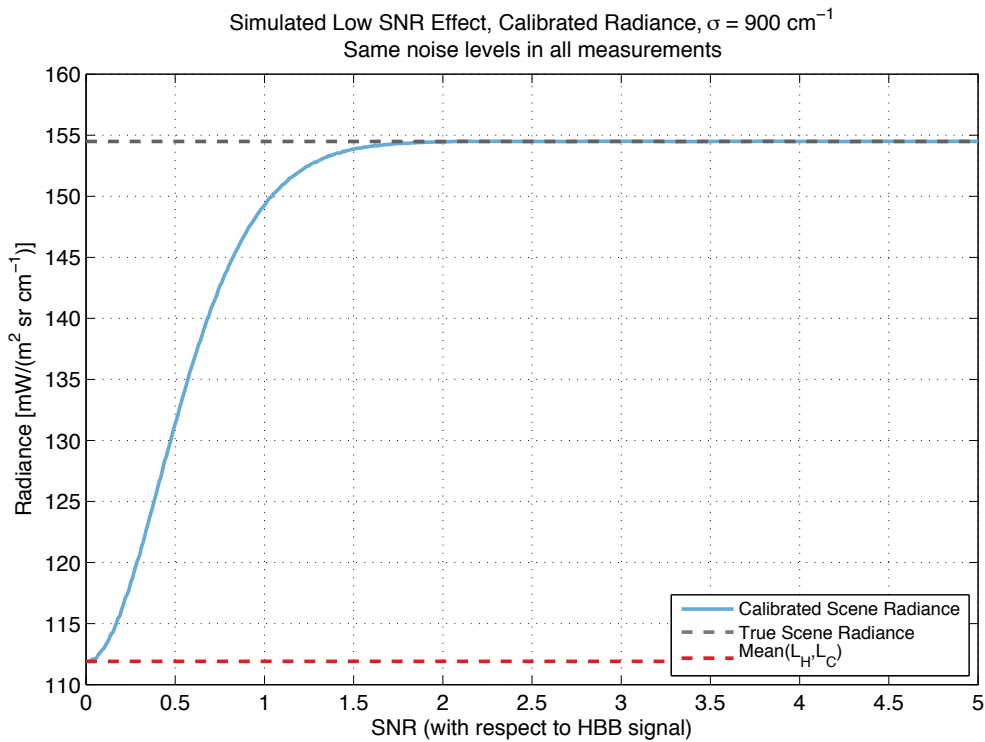


Figure 120: Simulated low SNR effect. The mean value of the radiance is plotted versus SNR.

As presented in Chapter 1, in the nominal measurement sequence for the ARI, groups of scene views are separated by several samples of the blackbody references and calibration is performed frequently (on the order of once per minute).

Typically, the calibration equation is applied using a moving window interpolation method (referred to here as the ‘rolling window’ calibration). The calibration reference temperatures (cavity and reflected), and spectra are interpolated to the time of the measurement using the data inside a window centred on the time of the scene measurement. This process eliminates small, well behaved variations occurring between calibration and unknown views and reduces noise in the calibration spectra [144]. The calibration equation can be re-written to explicitly note the interpolation:

$$L_S(\sigma_k) = (L_H(\sigma_k) - L_C(\sigma_k)) \operatorname{Re} \left\{ \frac{S_S(\sigma_k) - S_C(\sigma_k) \Big|_{N_C}^{\operatorname{interp}}}{S_H(\sigma_k) \Big|_{N_H}^{\operatorname{interp}} - S_C(\sigma_k) \Big|_{N_C}^{\operatorname{interp}}} \right\} + L_C(\sigma_k), \quad (5.7)$$

$$L(\sigma_k) = e(\sigma_k) B(\sigma_k, T \Big|_N^{\operatorname{interp}}) + (1 - e(\sigma_k)) B(\sigma_k, T_R \Big|_N^{\operatorname{interp}}). \quad (5.8)$$

Where $\Big|_N^{\operatorname{interp}}$ indicates interpolation of the value (temperature or spectra) to the time of the spectra to be calibrated with interpolation window size N . The window size defines the number of ‘nearest neighbour’ values used for each interpolation in the calibration.

The effect of low signal to noise on the calibration is observed in the DTGS data for the ARI, and an example is provided in Figure 121 for a 252.8 K target, calibrated using a cold reference blackbody at 215.6 K, and a hot reference blackbody at 301.7 K. The calibration results using full dataset averages, as well as the moving window interpolation method are shown. The moving window interpolation method (‘rolling window’ calibration) is described by equations (5.7) and (5.8). The rolling window calibration result is clearly impacted by the low SNR effect near the band edges of the detector response, and the resulting calibrated brightness temperature approaches the brightness temperature associated with 50% of the combined hot and cold reference blackbody radiance in that spectral region. Using measurement averages over the full dataset effectively improves the signal to noise in the measurements and provides robustness to the effect, but is sensitive to biases associated with temperature variations over the data collection period.

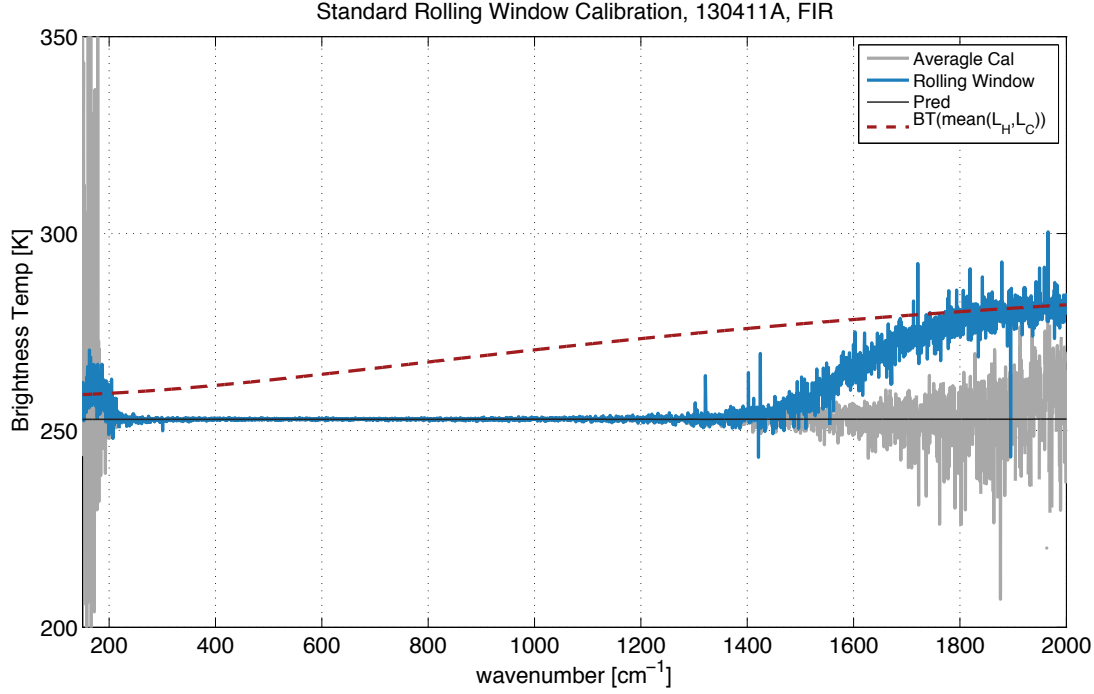


Figure 121: Predicted and measured brightness temperature for the ARI DTGS detector channel for a 252.8 K OARS target, calibrated using a cold reference blackbody at 215.6 K, and a hot reference blackbody at 301.7 K. The calibration results the full dataset average (grey) and a standard rolling window method (blue) are provided. The predicted brightness temperature is indicated in black, and the dashed red line represents the brightness temperature associated with 50% of the combined hot and cold reference blackbody radiance. The rolling window calibration result is impacted by the low SNR effect near the edges of the detector response, and the resulting calibrated brightness temperature approaches the brightness temperature associated with 50% of the combined hot and cold reference blackbody radiance in that spectral region.

For signals with low signal to noise ratio, the rolling window calibration process can be optimized accordingly:

$$L_S(\sigma_k) = \text{Re} \left\{ \frac{S_S(\sigma_k) - S_C(\sigma_k) \Big|_{N_C}^{\text{interp}}}{\mathbb{R} \Big|_{N_R}^{\text{interp}}} \right\} + L_C(\sigma_k), \quad (5.9)$$

where,

$$\mathbb{R} \Big|_{N_R}^{\text{interp}} = \left[\frac{S_H(\sigma_k) - S_C(\sigma_k)}{L_H(\sigma_k) - L_C(\sigma_k)} \right]_{N_R}^{\text{interp}}. \quad (5.10)$$

In equations (5.9) and (5.10), the interpolation window for \mathbb{R} is much larger than the interpolation window for the cold reference blackbody spectra,

$$N_R \gg N_C. \quad (5.11)$$

Thus, the noise in the responsivity term can be significantly decreased while still accurately accounting for changes in instrument temperature that directly contribute to the instrument background. Note that the

interpolation in Eq. (5.10) is applied to the quotient, and not to the individual terms in the numerator and denominator prior to differencing and division.

With respect to the period of the nominal calibration cycle scheme, in which groups of scene views are separated by several samples of the blackbody references, the thermal design of the ARI provides large thermal time constants of the optical bench and elements, second port reference, and instrument enclosure. The detectors are also maintained at sufficiently stable temperatures. With consideration for the sample timing and calibration cycle period used for the prototype demonstration, relative to the instrument thermal time constants, it was determined that linear interpolation was sufficiently accurate and would produce negligible interpolation errors.

The impact on calibration accuracy and biases due to low signal to noise can be investigated by comparing the results from the low signal to noise rolling window calibration, the standard rolling window calibration, and the average calibration that utilizes means over the full dataset. The results for the ARI DTGS detector, for the 252.8 K OARS dataset (252.8 K OARS, 215.6 K cold reference blackbody, 301.7 K hot reference blackbody) are shown in Figure 122 through Figure 125. Figure 122 shows the predicted and ARI DTGS measured brightness temperature from 150 – 2000 cm^{-1} . The calibration results for the full dataset average, a standard rolling window method, and the low SNR optimized rolling window calibration with responsivity interpolation window sizes of 100 and 250 samples are shown. The impact of low signal to noise on the standard rolling window implementation of the complex calibration is obvious at both ends of the spectral coverage, limiting the useful spectral coverage significantly. To facilitate a more clear visualization of the results and further reduce noise of the results presented in Figure 122, spectral averaging is applied to the results (Figure 123). The impact of the responsivity interpolation window size above 1600 cm^{-1} is easier to discern in Figure 123. Clearly, the larger interpolation window provides increased robustness to the low signal to noise, but it is important to note that the interpolation window size is limited by considerations of the time constants for temperature variations that are critical to the calibration responsivity and offset terms. In general, responsivity is primarily a function of detector temperature, and radiative loading is a secondary effect. Typically, detector temperature is well controlled and responsivity is highly stable with only very small, slow variations.

Finally, a closer view of the results in the 180 – 400 cm^{-1} and 1000 – 2000 cm^{-1} spectral regions is provided in Figure 124 and Figure 125, respectively. While the impact of the low signal to noise optimized calibration method is most evident in 1000 – 2000 cm^{-1} spectral region, it is clear that there is improvement over the standard rolling window calibration at the long-wave limit as well.

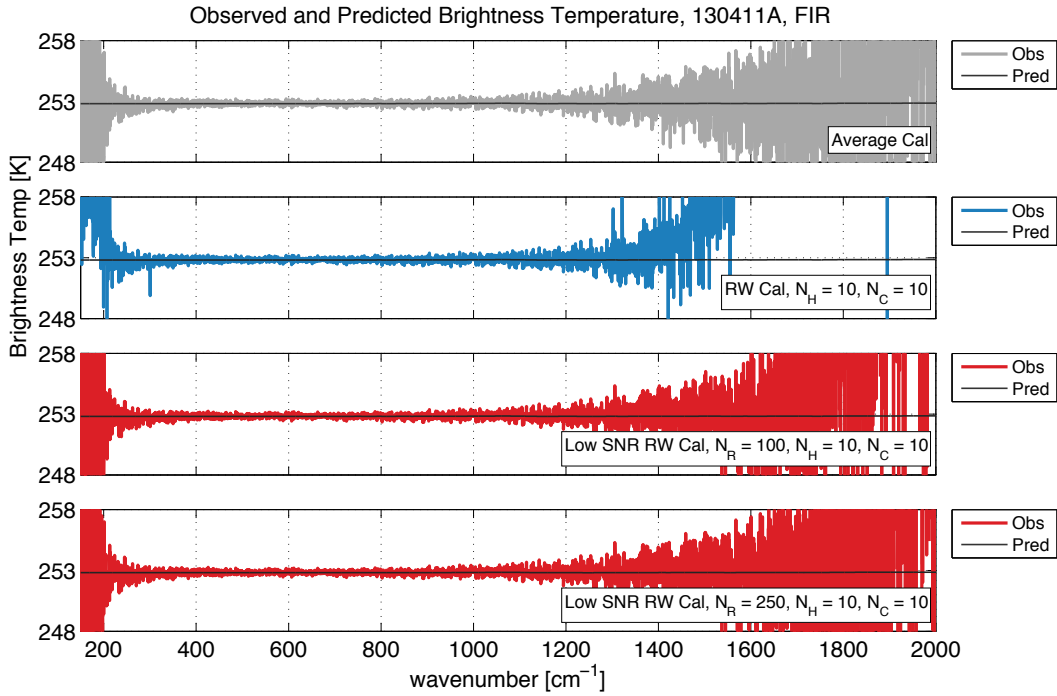


Figure 122: Predicted and ARI DTGS measured brightness temperature for a 252.8 K OARS target, calibrated using a cold reference blackbody at 215.6 K, and a hot reference blackbody at 301.7 K. The calibration results for the full dataset average (grey) are shown in the top panel, a standard rolling window method (blue) in the second panel, and the low SNR optimized rolling window calibration (red) in the bottom two panels. The results in the third panel correspond to a responsivity interpolation window size of 100 samples, and 250 samples for the bottom panel.

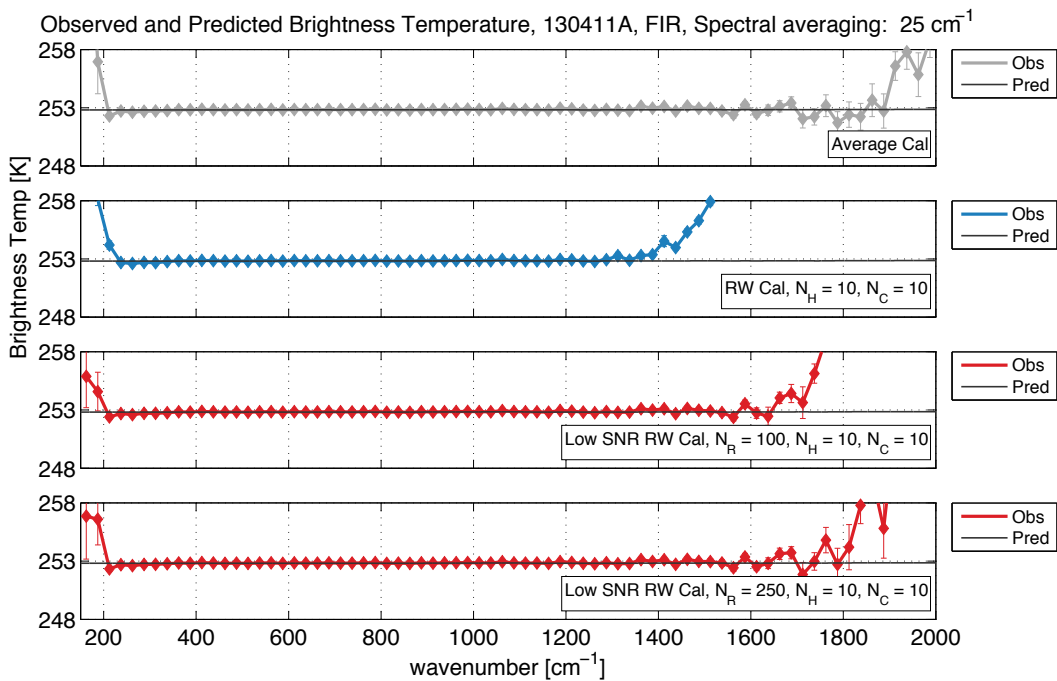


Figure 123: To further reduce noise, and provide a better visualization of the results provided in Figure 122, spectral averaging of the results has been applied (bin width of 25 cm⁻¹).

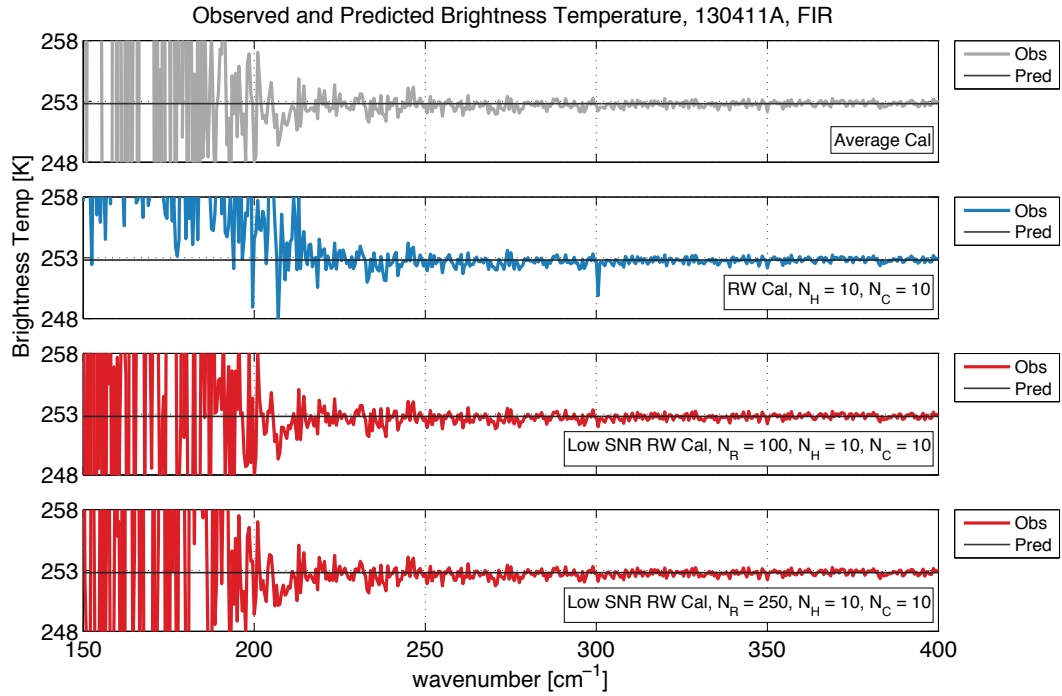


Figure 124: A closer view of the results presented in Figure 122 in the long wavelength region of the measurement. The long-wave spectral cut-off is dominated by the transmission properties of the Caesium iodide beam splitter.

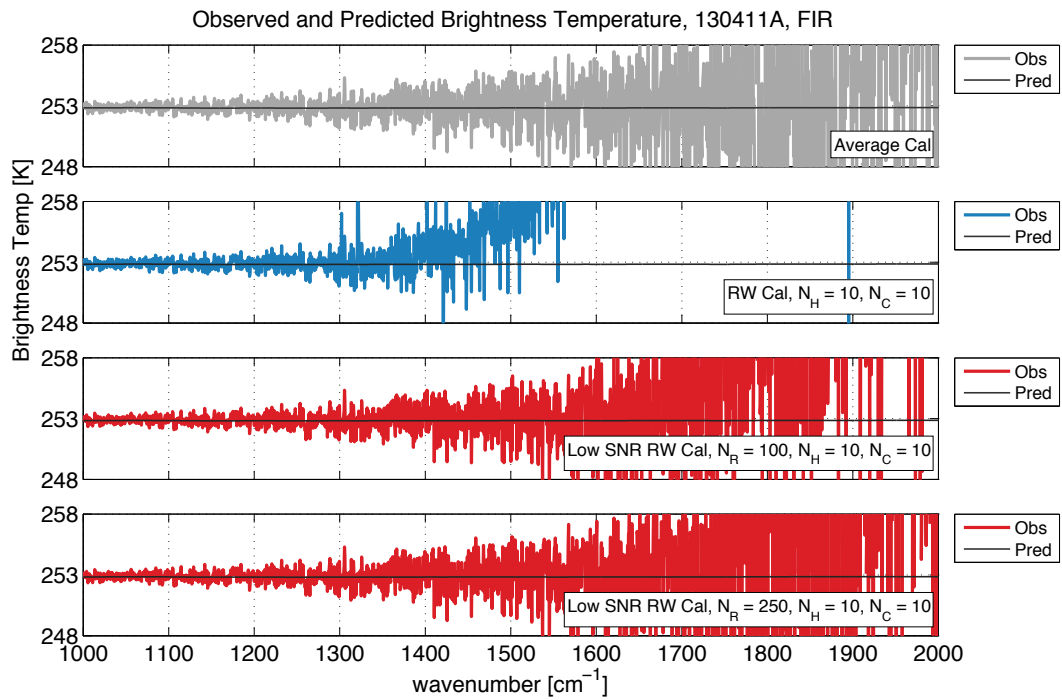


Figure 125: A closer view of the results presented in Figure 122 in the short wavelength limit of the DTGS measurement. The impact of the low signal to noise optimized calibration method is most evident in this spectral region.

6 Conclusion: demonstration of 0.1 K calibration accuracy

In this final chapter, the experimental results demonstrating the achievement of the required 0.1 K accuracy are presented. Additionally, the results are compared to related research efforts, and further work is identified.

The ARI calibration verification for the DTGS and LW MCT channels presented here was completed in the vacuum calibration configuration and environment using the OARS at temperature set points of approximately 216 K, 233 K, 253 K, 273 K, 293 K, 313 K, and 333 K. The cold calibration reference was operated at a temperature of approximately 217 K, and the hot calibration reference at 300 K. The average temperatures of the OARS, blackbody reference, and instrument for the calibration verification datasets are provided in Table 12 and Table 13. The calibration verification was also successfully completed in the laboratory environment [39, 41, 45, 47], but is not presented here.

6.1 Radiometric uncertainty

As noted in Chapter 1, the calibration reference configurations are significantly different for the on-orbit, laboratory, and vacuum configurations. This results in significant differences in the radiometric uncertainty estimate for each. For convenience, the radiometric calibration and calibration verification uncertainty figures for the on-orbit, laboratory, and vacuum environments and calibration reference configurations from Chapter 1 (Figure 10, Figure 12, Figure 14, respectively) are reproduced here (Figure 126, Figure 127, Figure 128, respectively). The radiometric contributors are discussed in detail in Chapter 1, and summarized in Table 4 – Table 6.

The radiometric uncertainty associated with nonlinearity correction for the LW MCT detector is not included in the radiometric uncertainty estimates. Based on the radiometric uncertainty analysis and the required calibration accuracy for the on-orbit configuration, the residual nonlinearity, expressed as a percentage error of the calibrated radiance, should be limited to less than 0.03% for the flight instrument to achieve the required 0.1 K radiometric accuracy on-orbit. As noted in Chapter 2, the radiometric uncertainty associated with the nonlinearity correction required for the LW MCT used for the demonstration effort approaches 0.1 K, and would not be acceptable for a flight unit.

As detailed in Chapter 1, the radiometric uncertainty for the laboratory and vacuum configurations and environment is higher than that for on-orbit. The primary sources of the increased uncertainty in these environments include the increased uncertainty associated with a blackbody compared to that of a space view, increased uncertainty associated with emissivity of OARS verification blackbody used for the demonstration effort, and reduced separation between the calibration reference temperatures.

The combined ARI calibration and calibration verification radiometric uncertainty predicted for the on-orbit configuration and thermal environment is within the 0.1 K ($k = 3$) accuracy requirement. For a consistent radiometric uncertainty analysis with accurate parameterization for each configuration and environment, it is valid to conclude that meeting the combined calibration and calibration verification uncertainty in one configuration demonstrates the ability to meet the predicted uncertainty associated with the other configurations as well. Thus, meeting the radiometric uncertainty in the vacuum or laboratory configurations demonstrates the capability to meet the 0.1 ($k = 3$) on-orbit requirement.

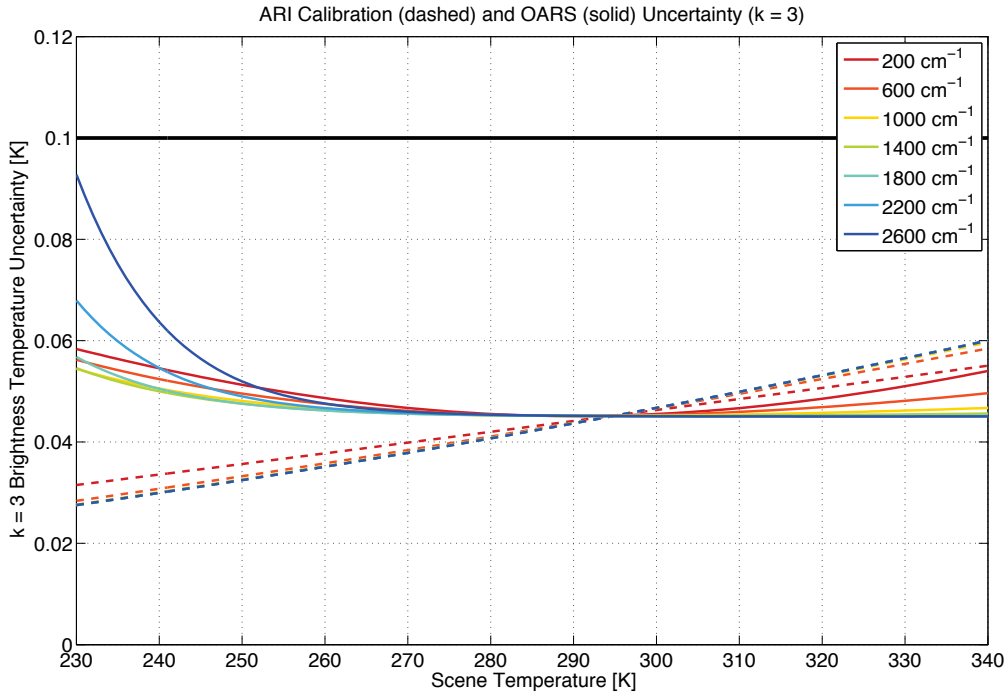


Figure 126: Predicted on-orbit radiometric calibration uncertainty (dashed) and calibration verification source uncertainty (solid) ($k = 3$).

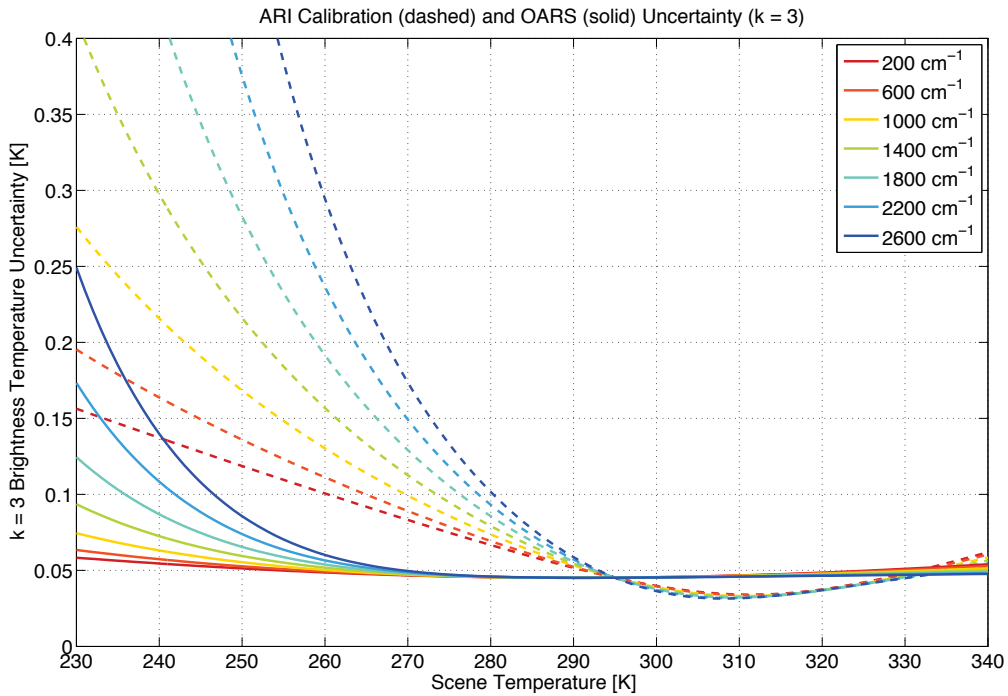


Figure 127: Predicted laboratory radiometric calibration uncertainty (dashed) and calibration verification source uncertainty (solid) ($k = 3$).

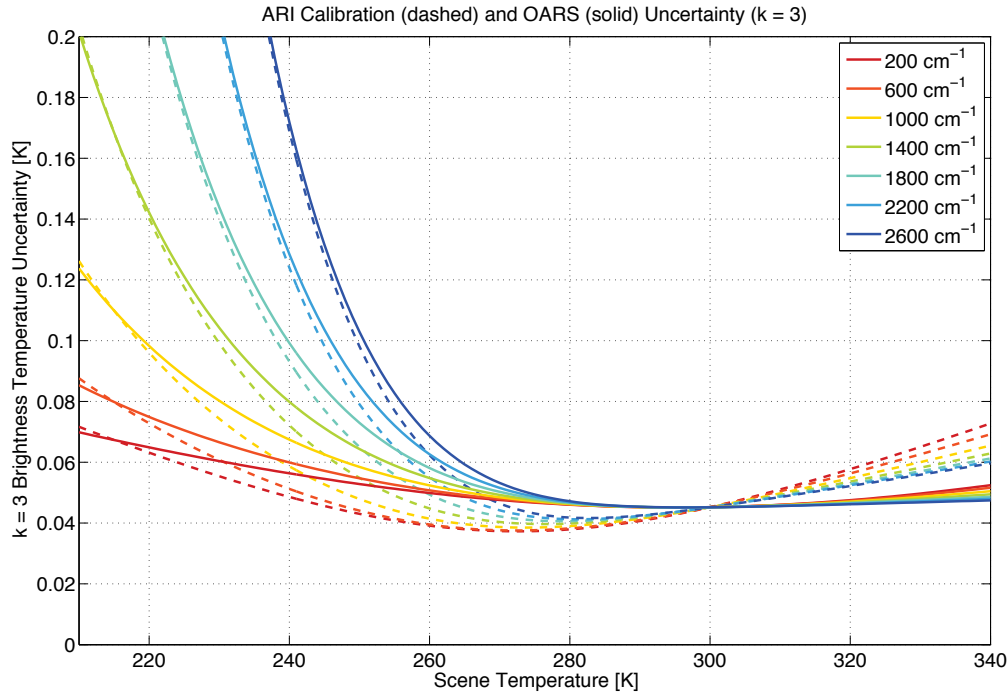


Figure 128: Predicted vacuum radiometric calibration uncertainty (dashed) and calibration verification source uncertainty (solid) ($k = 3$).

6.2 Calibration verification results

Calibration verification was completed in the vacuum calibration configuration and environment using the OARS at temperature set points of approximately 216 K, 233 K, 253 K, 273 K, 293 K, 313 K, and 333 K. The cold calibration reference was operated at a temperature of approximately 217 K, and the hot calibration reference at 300 K. The average temperatures of the OARS, blackbody reference, and instrument for the calibration verification datasets are provided in Table 12 and Table 13. Calibration of the data was completed using a rolling window implementation of the complex calibration method [82], optimized for low signal to noise measurements as described in Chapter 5.

The measured and predicted radiances for all OARS set points are shown for the ARI DTGS and ARI LW MCT channels in Figure 129 and Figure 130, respectively. Nonlinearity correction has been applied to the ARI LW MCT channel. While it is difficult to resolve any details on these plots due to the scale, they provide a useful visualization of the wide range of OARS radiances used during the calibration verification process.

Results of the calibration verification using the OARS, expressed as observed and predicted OARS brightness temperatures for the DTGS detector are shown in Figure 131. The difference between the observed and predicted brightness temperatures is shown Figure 132. Spectral averaging has been applied to the residuals in Figure 132, with a spectral bin width of 50 cm^{-1} and error bars represent statistical error in each average. The difference between observed and predicted brightness temperature is very close to zero and random noise in the regions with sufficient signal to noise. Despite the use of the low signal to noise formulation of the rolling window calibration equation, the impact of low signal to noise on the calibration accuracy is evident in Figure 132 in the spectral regions near the band edges. With the exclusion of the results for which low signal

to noise is an issue, the results for the DTGS detector are within the prescribed radiometric uncertainty for the data collected during the ARI demonstration under vacuum.

For the vacuum demonstration, the DTGS noise is roughly a factor of 4 larger than the on-orbit noise specification due to shorter dwell times alone. A commercially available DTGS detector was used for the prototype, and improved DTGS detector sensitivity is also a realistic expectation for future versions of the instrument. Furthermore, as noted earlier, due to resource constraints a beam splitter coating based on an existing production recipe was used for the ARI prototype. It is also expected that the beam splitter coating will be optimized for improved far infrared modulation efficiency in a flight unit. Finally, the measurement duration for the vacuum duration was approximately 24 hours for each OARS temperature. The number of observations averaged for the climate radiance products will be significantly larger, with a corresponding reduction in noise via the larger averages. With these considerations, the signal to noise for the DTGS channel is not expected to be an issue for the flight unit and the on-orbit climate benchmark measurement.

The results for the LW MCT detector with nonlinearity correction are presented in Figure 133 and Figure 134. The observed and predicted OARS brightness temperatures for the LW MCT detector are shown in Figure 133 and the brightness temperature residuals are provided in Figure 134. Spectral averaging has been applied to the residuals, with a spectral bin width of 5 cm^{-1} and the error bars represent the statistical error in each average. Nonlinearity correction has been applied for the LW MCT (refer to Chapter 2 for details). The results are within the predicted combined radiometric calibration and calibration verification uncertainty. A small bias, associated with the stray light issue that was resolved after vacuum testing (refer to Chapter 3), is evident for the 313.16 K and 333.61 K OARS data collection results.

Results of the calibration verification at 800 cm^{-1} ($700 - 900 \text{ cm}^{-1}$ average), expressed as differences in observed and predicted brightness temperatures for the LW MCT detector with and without nonlinearity correction are shown in Figure 135 and Figure 136, respectively. The results at 1000 cm^{-1} ($900 - 1100 \text{ cm}^{-1}$ average) for the LW MCT detector with and without nonlinearity correction are provided in the same format in Figure 137 and Figure 138. These figures clearly illustrate the nature of the calibration bias associated with nonlinear response. The bias due to nonlinearity approaches zero when the effective brightness temperature of the scene approaches the brightness temperature of either calibration reference, and the bias increases as the temperature difference between the scene and the nearest reference temperature increases. The effect is compounded by extrapolation for scene temperatures outside of the range defined by the reference blackbody temperatures.

The result for the DTGS detector at 450 cm^{-1} ($400 - 500 \text{ cm}^{-1}$ average) and 800 cm^{-1} ($700 - 900 \text{ cm}^{-1}$ average) are shown in a similar format in Figure 139 and Figure 140. The trends of the results show no indication of nonlinear response for the DTGS detector,

Table 12: ARI DTGS data collections used for instrument calibration verification results presented herein. Average OARS, blackbody reference, and instrument temperatures are provided.

Dataset	OARS Temperature [K]	Hot Blackbody Reference Temperature [K]	Cold Blackbody Reference Temperature [K]	Instrument Temperature [K]
130412C	333.9	301.7	215.6	295.2
130420A	313.2	301.7	215.6	297.0
130419A	293.0	301.7	215.6	297.5
130418A	272.9	301.7	215.6	297.9
130411A	252.8	301.7	215.6	295.0
130421B	232.6	301.7	215.6	295.8
130425A	216.1	301.7	215.6	291.5

Table 13: ARI LW MCT data collections used for instrument calibration verification results presented herein. Average OARS, blackbody reference, and instrument temperatures are provided.

Dataset	OARS Temperature [K]	Hot Blackbody Reference Temperature [K]	Cold Blackbody Reference Temperature [K]	Instrument Temperature [K]
130713B	333.6	300.2	217.6	297.3
130713A	313.2	300.2	216.9	296.6
130712B	292.6	300.2	214.0	295.5
130711A	272.9	300.2	217.6	297.2
130710C	252.8	300.2	217.6	296.2
130710B	232.7	300.2	217.6	295.5
130710A	217.6	300.2	217.6	292.5

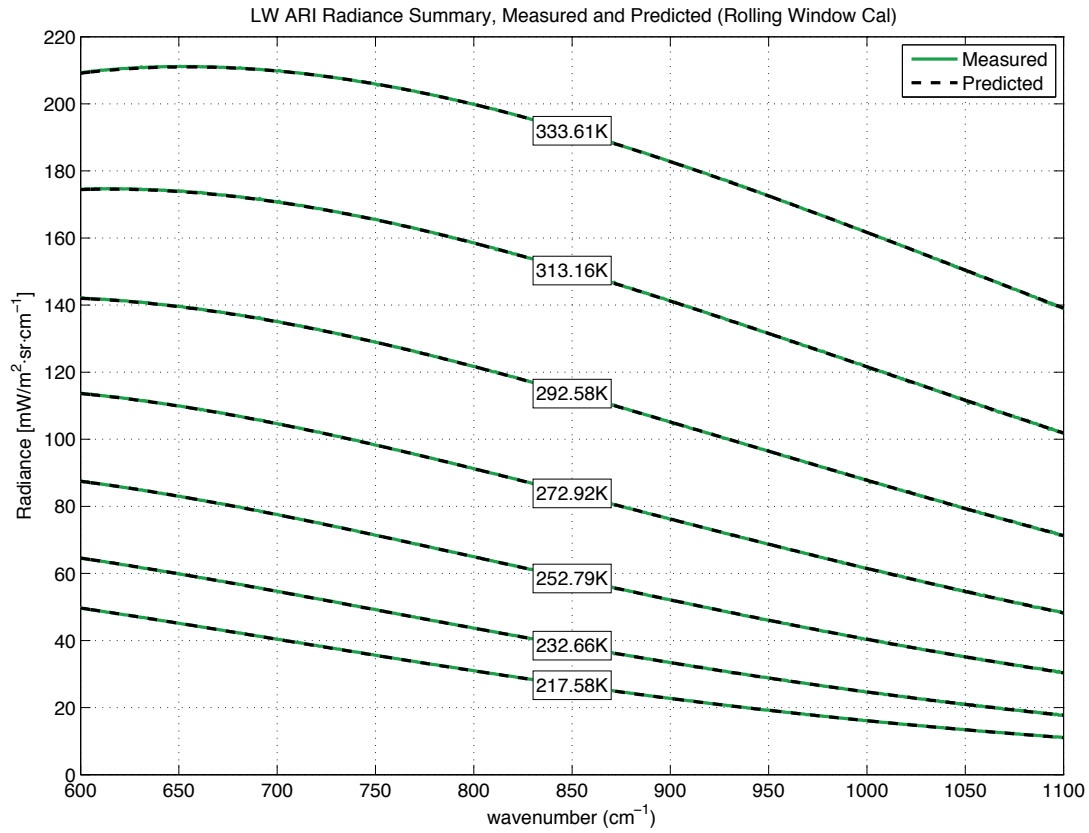


Figure 129: Radiance summary for the ARI LW MCT channel calibration verification conducted under vacuum. The OARS was operated over a range of temperatures from approximately 218 K to 334 K.

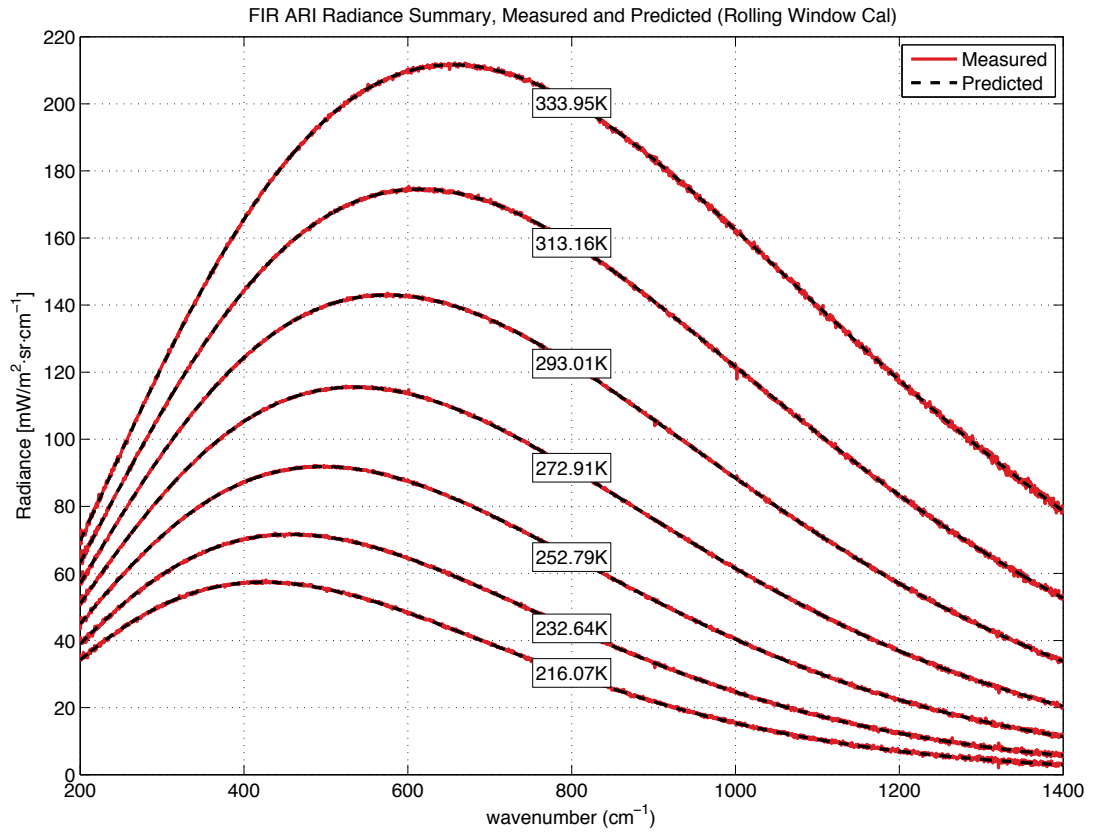


Figure 130: Radiance summary for the ARI DTGS channel calibration verification conducted under vacuum. The OARS was operated over a range of temperatures from approximately 216 K to 334 K.

FIR ARI Calibration Verification Summary,
Measured and Predicted Residual BT (Rolling Window Cal)

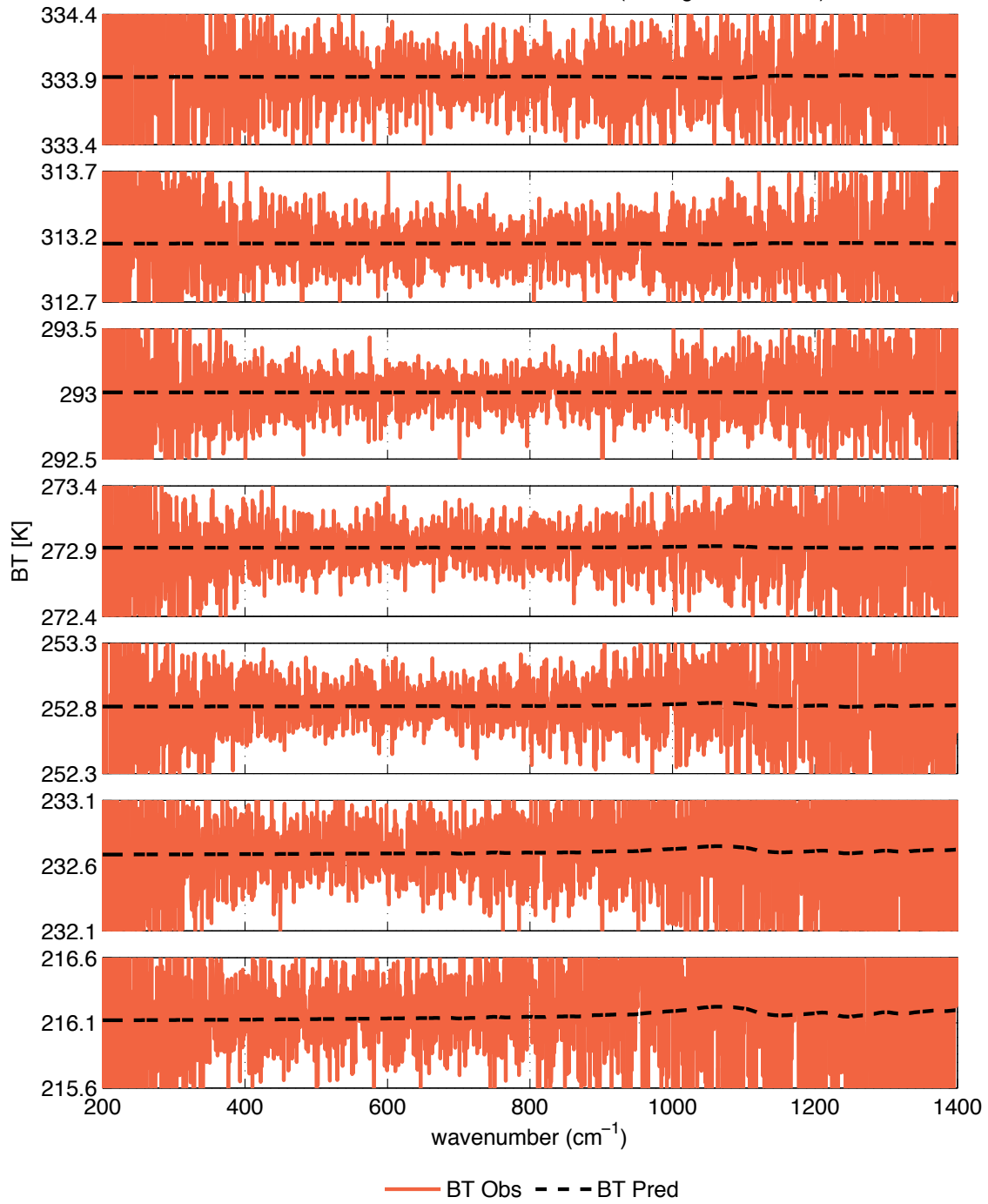


Figure 131: ARI calibration verification results for tests conducted under vacuum. Observed brightness temperature for the DTGS detector is shown in red and the black dashed line indicates predicted brightness OARS brightness temperature. The noise is roughly a factor of 4 larger than the on-orbit noise specification due to shorter dwell times.

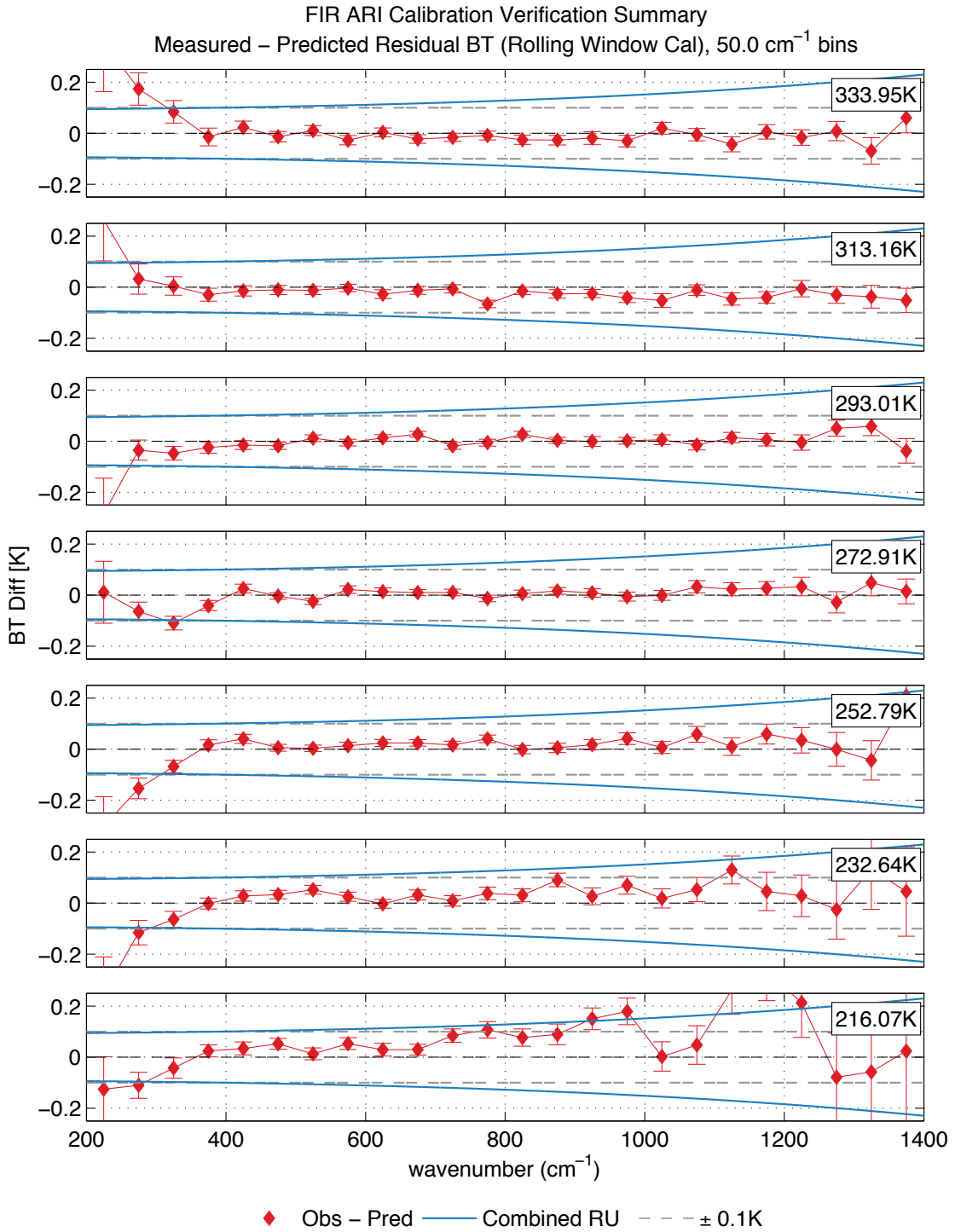


Figure 132: DTGS detector brightness temperature residuals (observed – predicted) for end-to-end calibration verification datasets conducted under vacuum. The results have been spectrally averaged in 50 cm⁻¹ wide bins for noise reduction. Error bars represent statistical error only. Total (calibration and calibration verification) radiometric uncertainty is shown in blue, and the grey dashed lines indicate ± 0.1 K. The effect of low SNR is evident at the edges of the spectral band (refer to Chapter 5 for details).

LW ARI Calibration Verification Summary,
Measured and Predicted Residual BT (Rolling Window Cal)

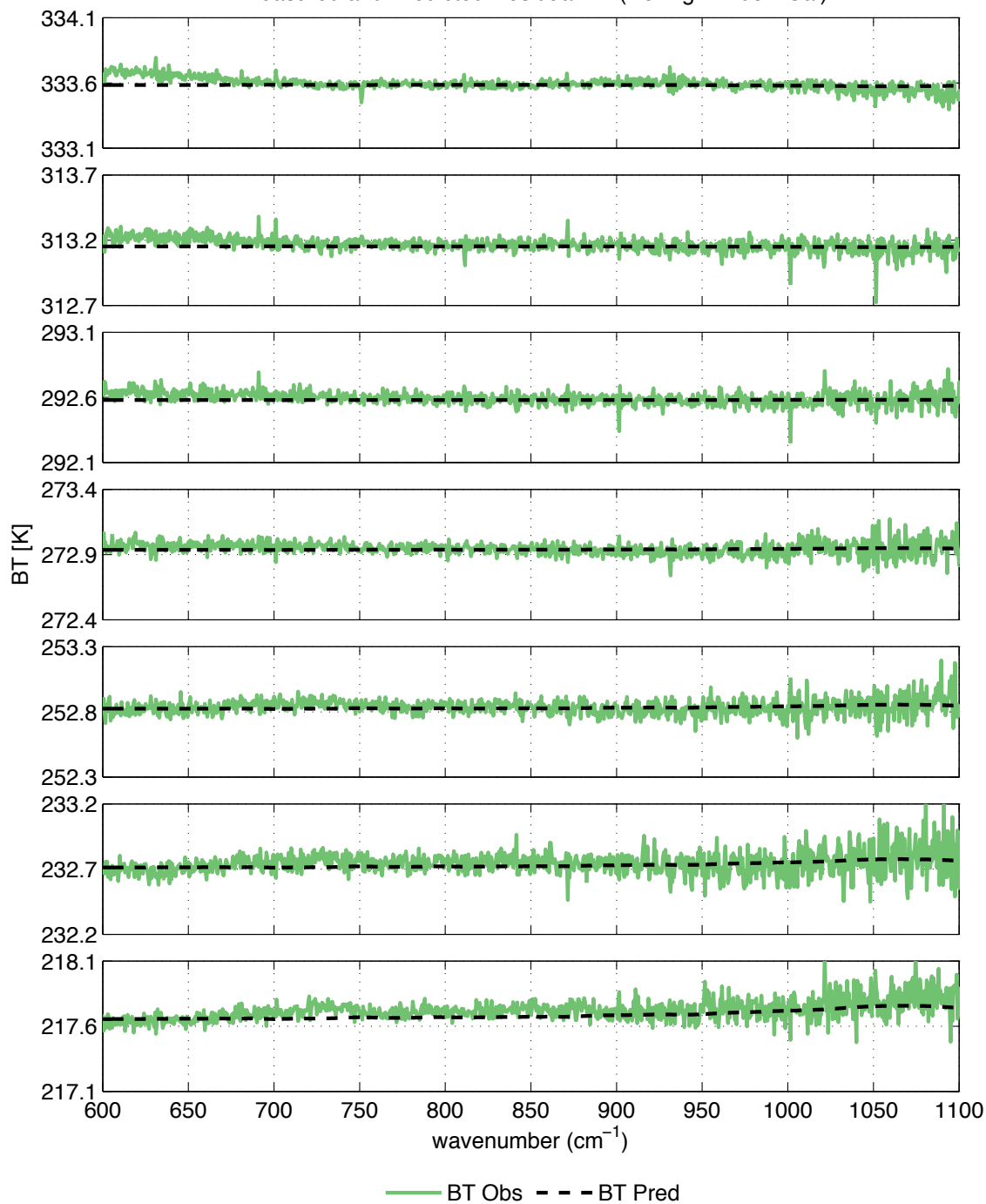


Figure 133: ARI calibration verification results for tests conducted under vacuum. Observed brightness temperature for the long-wave MCT detector is shown in green and the black dashed line indicates predicted brightness OARS brightness temperature.

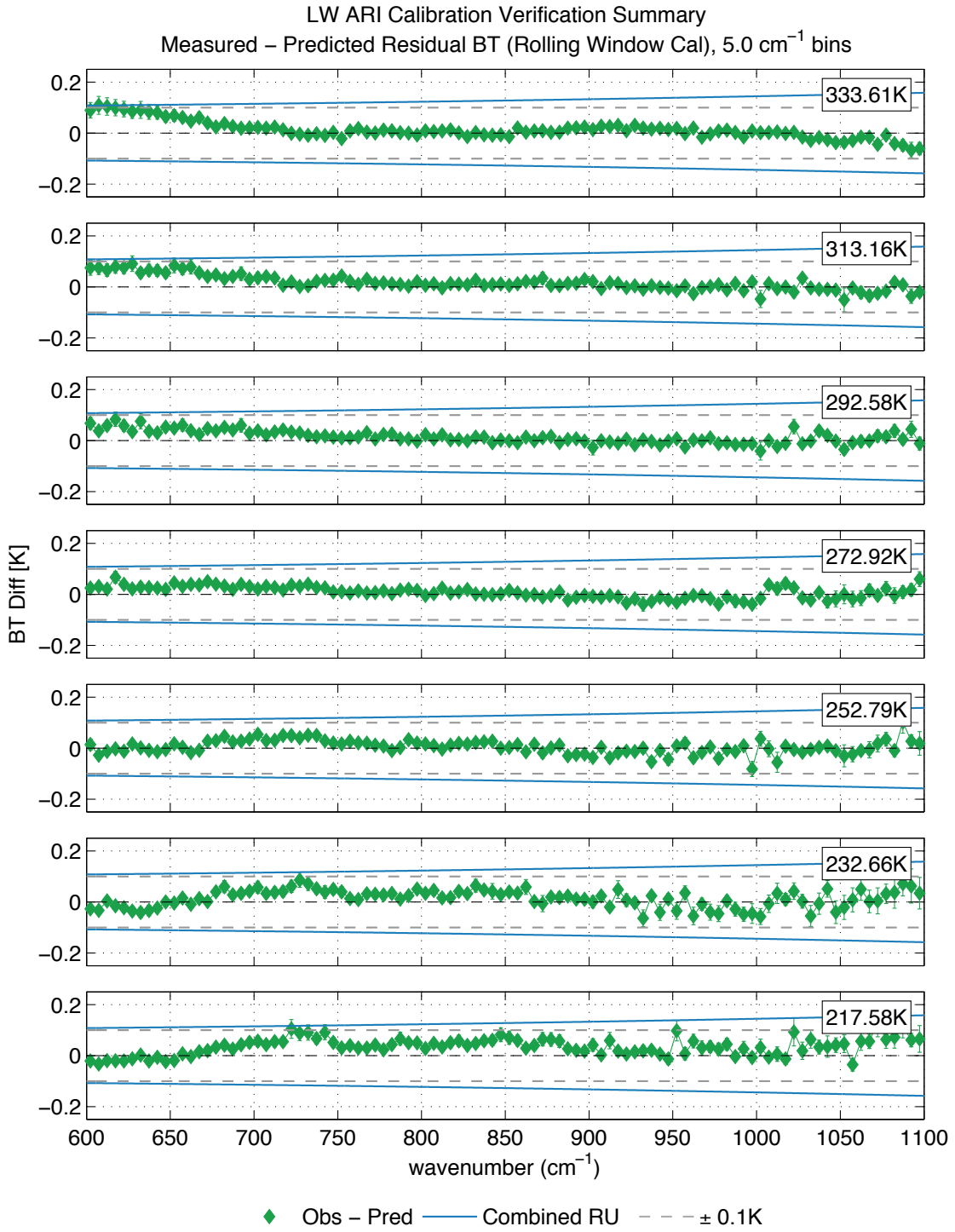


Figure 134: Long-wave MCT detector brightness temperature residuals (observed – predicted) for end-to-end calibration verification datasets conducted under vacuum. The results have been spectrally averaged in 25 cm⁻¹ wide bins for noise reduction. Error bars represent statistical error only. Total (calibration and calibration verification) radiometric uncertainty is shown in blue, and the grey dashed lines indicate ± 0.1 K. The artifact associated with the original field stop is evident. The solution to this issue was implemented post-vacuum testing (see Chapter 4).

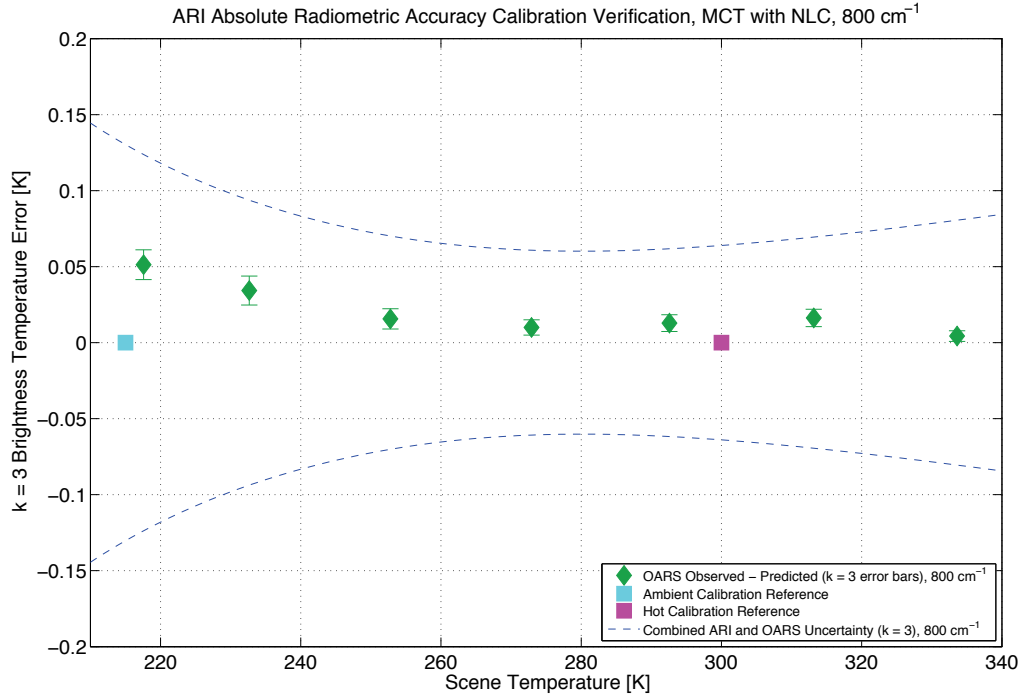


Figure 135: ARI vacuum calibration verification results for the long-wave detector with nonlinearity correction, 800 cm⁻¹. Meeting these uncertainty bounds in the vacuum environment demonstrates the capability to meet the 0.1 K (k = 3) uncertainty requirement on-orbit.

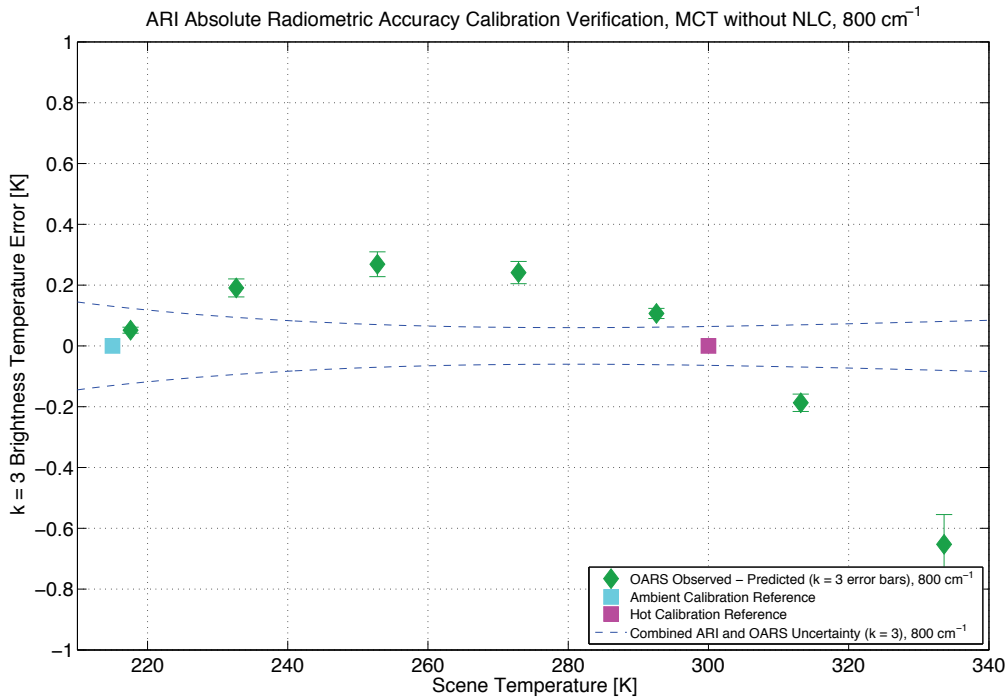


Figure 136: ARI vacuum calibration verification results for the long-wave detector without nonlinearity correction, 800 cm⁻¹.

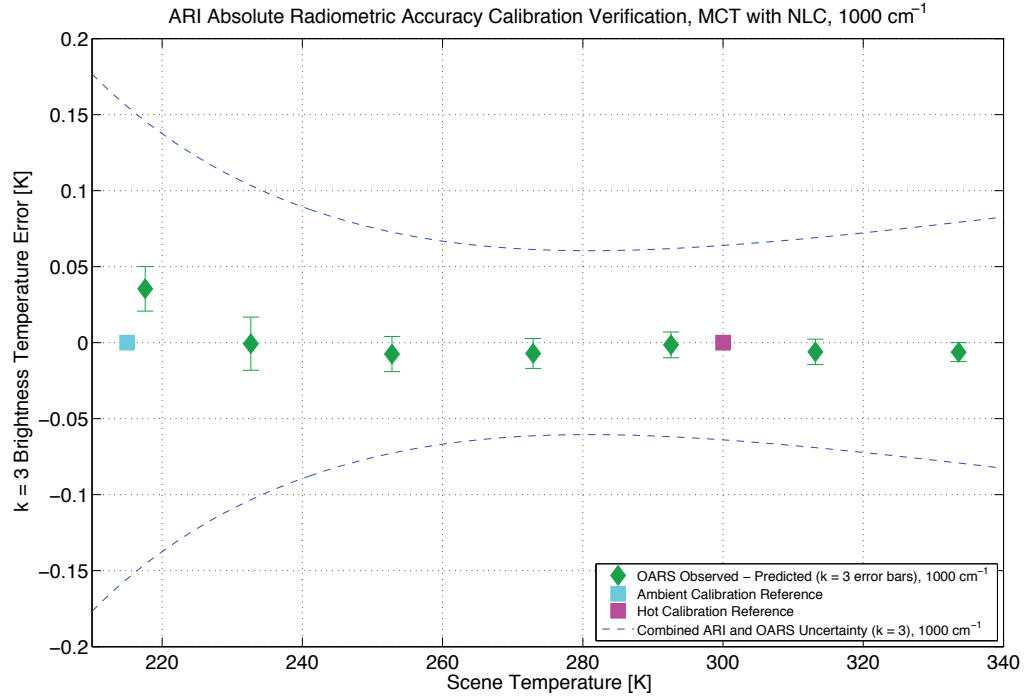


Figure 137: ARI vacuum calibration verification results for the long-wave detector with nonlinearity correction, 1000 cm⁻¹. Meeting these uncertainty bounds in the vacuum environment demonstrates the capability to meet the 0.1 K (k = 3) uncertainty requirement on-orbit.

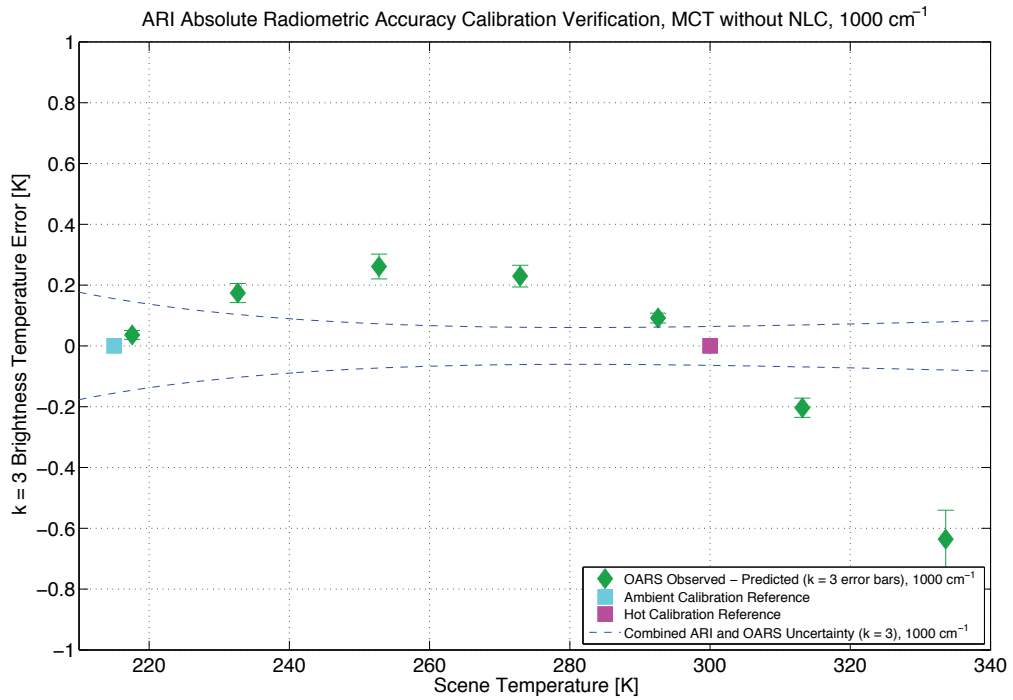


Figure 138: ARI vacuum calibration verification results for the long-wave detector without nonlinearity correction, 1000 cm⁻¹.

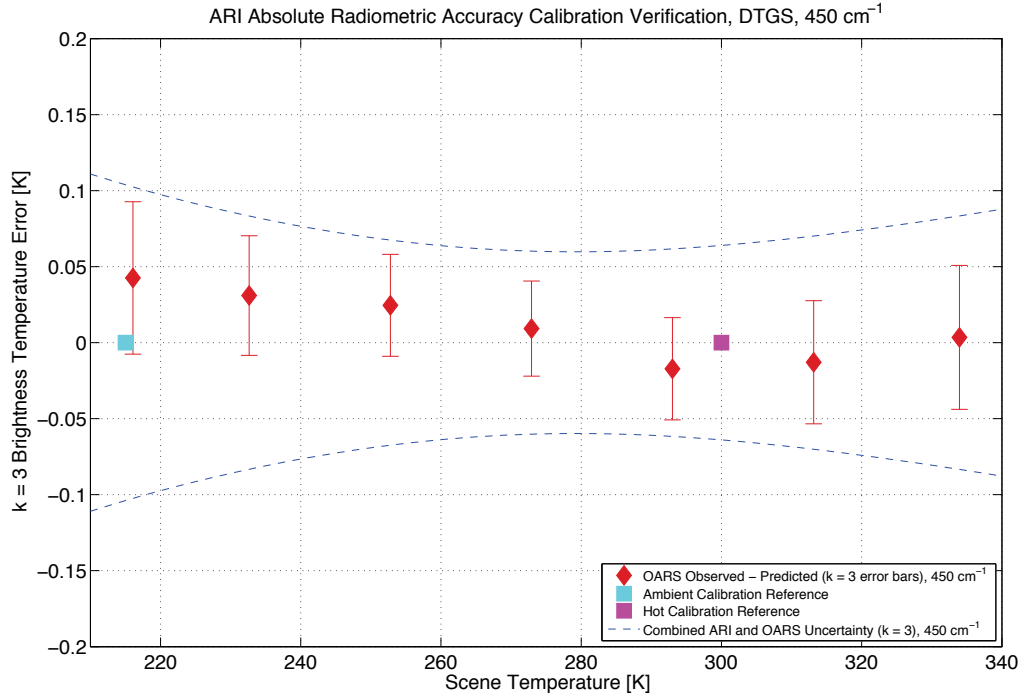


Figure 139: ARI vacuum calibration verification results for the far infrared (DTGS) detector, 450 cm⁻¹. Meeting these uncertainty bounds in the vacuum environment demonstrates the capability to meet the 0.1 K (k = 3) uncertainty requirement on-orbit.

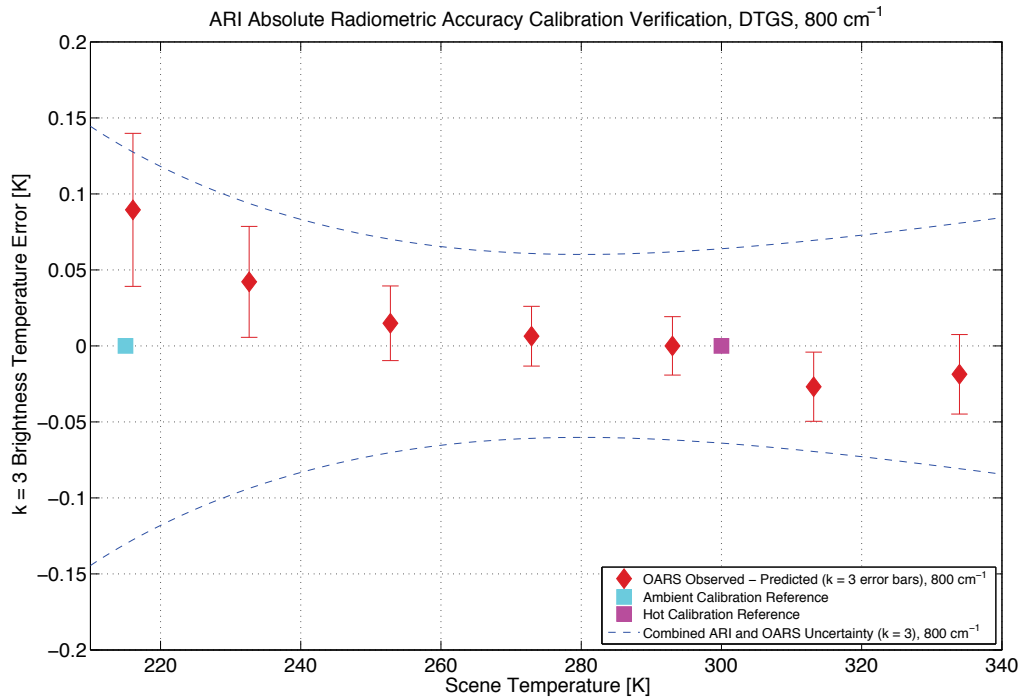


Figure 140: ARI vacuum calibration verification results for the far infrared (DTGS) detector, 800 cm⁻¹. Meeting these uncertainty bounds in the vacuum environment demonstrates the capability to meet the 0.1 K (k = 3) uncertainty requirement on-orbit.

6.3 Conclusion

The ability to achieve the 0.1 K (99% confidence, $k = 3$) on-orbit measurement accuracy required for climate benchmark measurements in the infrared has been successfully demonstrated. The only exceptions are associated with limitations imposed by the signal to noise for the DTGS detector at the spectral band edges for the prototype unit. As noted earlier in the chapter, this is not anticipated to be an issue for the flight unit given the reasonable expectation of improved DTGS signal to noise associated with slower interferometer scan speeds than that used for the prototype unit, and the use of a custom beamsplitter coating optimized for improved far infrared modulation efficiency in the flight unit. Furthermore, the measurement duration for the vacuum data collections was limited by practical considerations to approximately 24 hours for each OARS temperature. The number of observations averaged for the climate radiance products will be significantly larger, with a corresponding reduction in noise via the larger averages. The limit on noise reduction via averaging needs to be quantified using an Allen variance analysis.

It has been noted that the radiometric uncertainty associated with the laboratory and vacuum environments is larger than that associated with the on-orbit calibration configuration and environment. However, a consistent radiometric uncertainty analysis with accurate parameterization for each configuration and environment has been used, and it is valid to conclude that meeting the combined calibration and calibration verification uncertainty in one configuration demonstrates the ability to meet the predicted uncertainty associated for the other configurations as well. Thus, the demonstration of accuracy within the radiometric uncertainty in the vacuum configuration, as documented herein, demonstrates the capability to meet the 0.1 K ($k = 3$) on-orbit requirement.

Moreover, despite the higher radiometric uncertainty associated with the vacuum testing compared to that for on-orbit, the calibration biases demonstrated during vacuum testing are still within the 0.1 K on-orbit requirement, with the exclusion of the results for which low signal to noise remained an issue for the DTGS detector.

The primary challenges encountered and successfully resolved during this demonstration effort included signal chain linearity (Chapter 2), stray light (Chapter 3), calibration biases due to sensor polarization sensitivity (Chapter 4), and the low signal to noise ratio for the FIR measurements (Chapter 5).

An estimate for the limit of acceptable nonlinear response was quantified based on the on-orbit accuracy requirement and the radiometric uncertainty analysis. The long-wave MCT detector used for the demonstration effort exhibited significant nonlinear response that was above the identified limit. Accordingly, a nonlinearity correction was developed, optimized, and successfully applied to the LW MCT measurements. The resulting calibrated radiances agreed well with those for the highly linear DTGS detector, and were within the predicted radiometric uncertainty. The need for a nonlinearity correction adds an additional source of radiometric uncertainty, and it is desirable to emphasize linearity rather than sensitivity during detector selection for a flight unit due to the high radiometric accuracy requirements of the infrared climate benchmark measurement.

As noted in Chapter 3, a radiometric bias for the long-wave detector was discovered during the end-to-end ARI radiometric calibration verification testing conducted under vacuum. It was determined that the bias was due to stray light arising from non-optimal rejection at the field stop. The field stop was modified to improve stray light rejection and testing confirmed elimination of the long wave bias observed during vacuum testing. The

addition of a variable temperature annulus at the entrance of both the OARS and cold blackbody proved to be an extremely valuable tool for the stray light testing. It is highly recommended that the variable temperature blackbody aperture rings be included for all blackbody sources in the flight design.

Given the high absolute accuracy requirements for the climate benchmark measurement, calibration biases due to polarization were identified as a concern at the beginning of the project. In the ARI, the polarization induced calibration bias depends on the scene select mirror rotation angle. Models confirmed that the dependence is sinusoidal in nature with four equally spaced zero-crossings for 360° of rotation of the scene select mirror. The instrument was designed with the calibration, calibration verification, and scene viewports at 90° spacing in scene selection mirror rotation angle. Additionally, the ARI instrument design provides the ability to rotate the calibration and verification module with respect to the sensor such that the position of the viewports can be rotated to finely tune the viewport placement with respect to the zeroes of the polarization induced calibration bias. This design feature also provides the capability to determine the orientation of the sensor's polarization sensitivity via measurement. Two tests were conducted to determine the polarization sensitivity of the instrument and the position of the polarization induced calibration bias zero-crossings. The results indicated small differences in the location of the zero-crossings between the two detector channels. This is likely due to aft-optic or detector dependent polarization effects. Consequently, it is desirable to use a common aft-optic design for both output ports for the flight unit.

The final challenge presented in the thesis, was the effect of low signal to noise on the calibration accuracy. The effect was examined and characterized via simulation and a modification to the complex calibration equation that improves robustness to this effect was developed and tested. Results at the edges of the pass band for the DTGS detector showed significant improvement with the use of the modified complex calibration equation.

The work described herein currently represents the only successful demonstration of the ability to meet the on-orbit measurement accuracy required for climate benchmark measurements in the infrared and far infrared. Furthermore, the demonstration has been accomplished with a design that is representative of a flight instrument, and makes use of components with strong spaceflight heritage (direct analogs with high TRL), with a short path to a full flight prototype. The closest related research effort has been conducted at NASA Langley with their development of the CLARREO Calibration Demonstration System (CDS). The CDS is a breadboard instrument that utilizes a 4-port FTS operating in a single sweep direction mode, and has been tested under vacuum at NASA Langley using a variable temperature blackbody. For the tested equivalent scene temperature range of 200 K – 300 K and spectral range from 250 – 1350 cm^{-1} , a brightness temperature bias generally less than 0.2 K has been reported [145, 146]. While the Cross-track Infrared Sounder does not provide far infrared coverage or traceability to absolute standards on-orbit, analysis by Tobin [61, 62] has shown that the CrIS on-orbit radiometric uncertainty is better than 0.2 K in the shortwave and midwave bands, and 0.3 K in the longwave band (at 99% confidence). This represents the current state of the art in radiometric uncertainty for on-orbit infrared sounders.

The CLARREO program is currently in "Extended Pre-Phase A" status through 2016 due to congressionally mandated budget cuts, effectively putting the mission on hold. During this period, funding is limited and primarily used for continued support of the CLARREO Science Definition Team (SDT). Opportunities for a pathfinder demonstration on the International Space Station (ISS) are being explored, but it is not clear that

NASA will choose to leverage the developments and advancements accomplished during the successful demonstration effort described here.

7 References

1. National Research Council Committee on Earth Science, *Earth science and applications from space: National imperatives for the next decade and beyond*. 2007: National Academies Press.
2. Ohring, G., ed. *Achieving Satellite Instrument Calibration for Climate Change (ASIC3)*. NOAA, NASA, NIST, NPOESS Workshop Report. 2007, National Oceanic and Atmospheric Administration (US).
3. Ohring, G., et al., eds. *Satellite Instrument Calibration For Measuring Global Climate Change (Report Of A Workshop At The University Of Maryland Inn And Conference Center, College Park, MD, November 12-14, 2002)*. Vol. NISTIR 7047. 2004, National Institute of Standards and Technology (US). 114.
4. Ohring, G., et al., *Achieving satellite instrument calibration for climate change*. Eos, Transactions American Geophysical Union, 2007. **88**(11): p. 136-136.
5. Ohring, G., et al., *Satellite instrument calibration for measuring global climate change: Report of a workshop*. Bulletin of the American Meteorological Society, 2005. **86**(9): p. 1303-1313.
6. Battrick, B., *Global Earth Observation System of Systems (GEOSS): 10-year Implementation Plan Reference Document*. 2005: ESA Publications Division, ESTEC.
7. Goldberg, M., et al., *The Global Space-Based Inter-Calibration System*. Bulletin of the American Meteorological Society, 2011. **92**(4).
8. Goldberg, M.D. *Global space-based inter-calibration system (GSICS)*. in *Optical Engineering+ Applications*. 2007. International Society for Optics and Photonics.
9. Bureau International des Poids et Mesures (BIPM). *Traceability*. 2004; Available from: <http://www.bipm.org/en/convention/wmd/2004/traceability.html>.
10. Huang, Y., et al., *Separation of longwave climate feedbacks from spectral observations*. Journal of Geophysical Research: Atmospheres (1984–2012), 2010. **115**(D7).
11. Huang, Y., S.S. Leroy, and J.G. Anderson, *Determining Longwave Forcing and Feedback Using Infrared Spectra and GNSS Radio Occultation*. Journal of Climate, 2010. **23**(22).
12. Leroy, S., et al., *Testing climate models using thermal infrared spectra*. Journal of Climate, 2008. **21**(9).
13. Leroy, S.S. and J.G. Anderson, *Optimal Detection of Regional Trends Using Global Data*. Journal of Climate, 2010. **23**(16).
14. Tobin, D., *An SNO analysis of IASI and AIRS spectral radiance*. GSICS Quarterly, 2008. **2**(3): p. 2-4.
15. Tobin, D.C., et al. *Inter-calibration of Operational IR Sounders using CLARREO*. in *CLARREO Workshop*. 2008. Washington DC.
16. Anderson, J.G., et al., *Absolute, spectrally-resolved, thermal radiance: a benchmark for climate monitoring from space*. Journal of Quantitative Spectroscopy and Radiative Transfer, 2004. **85**(3): p. 367-383.
17. Kirk-Davidoff, D.B., R.M. Goody, and J.G. Anderson, *Analysis of sampling errors for climate monitoring satellites*. Journal of climate, 2005. **18**(6): p. 810-822.
18. Connes, J.R., *Recherches sur la spectroscopie par transformations de Fourier*. 1961: Éd. de la" Revue d'optique théorique et instrumentale.
19. White, R., *Chromatography/Fourier transform infrared spectroscopy and its applications*. Vol. 10. 1989: CRC Press.
20. Goody, R. and R. Haskins, *Calibration of radiances from space*. Journal of climate, 1998. **11**(4): p. 754-758.
21. Revercomb, H.E., et al. *FTS calibration: Demonstrated absolute accuracy for IR remote sensing and future for monitoring climate*. in *Fourier Transform Spectroscopy*. 2005. Optical Society of America.
22. Tobin, D.C., et al., *Radiometric and spectral validation of Atmospheric Infrared Sounder observations with the aircraft-based Scanning High-Resolution Interferometer Sounder*. Journal of Geophysical Research, 2006. **111**(D9): p. D09S02.

23. Michelson, A.A., *XXVIII. Visibility of interference-fringes in the focus of a telescope*. Philosophical Magazine Series 5, 1891. **31**(190): p. 256-259.
24. Michelson, A.A., *Light waves and their uses*. Vol. 3. 1903: The University of Chicago Press.
25. Genest, J. and P. Tremblay, *Understanding Fourier-transform spectrometers*. 2008, Quebec: University of Laval.
26. Davis, S.P., M.C. Abrams, and J.W. Brault, *Fourier transform spectrometry*. 2001: Academic Pr.
27. Johnston, S.F., *Fourier transform infrared: a constantly evolving technology*. 1991: Ellis Horwood.
28. Persky, M.J., *A review of spaceborne infrared Fourier transform spectrometers for remote sensing*. Review of scientific instruments, 1995. **66**(10): p. 4763-4797.
29. Fellgett, P., *The multiplex advantage*. 1951, Ph. D. dissertation (University of Cambridge, Cambridge, UK, 1951).
30. Fellgett, P.B., *The Theory of Infrared Sensitivities and Its Application to Investigations of Stellar Radiation in the Near Infra-red*. 1951.
31. Jacquinet, P., *The luminosity of spectrometers with prisms, gratings, or Fabry-Perot etalons*. JOSA, 1954. **44**(10): p. 761-765.
32. Mertz, L., *Rapid scanning fourier transform spectroscopy*. J. Phys. Coll. C2, Suppl. 3, 1967. **4**: p. 28-88.
33. Cooley, J.W., P.A. Lewis, and P.D. Welch, *Historical notes on the fast Fourier transform*. Proceedings of the IEEE, 1967. **55**(10): p. 1675-1677.
34. Cooley, J.W. and J.W. Tukey, *An algorithm for the machine calculation of complex Fourier series*. Math. comput, 1965. **19**(90): p. 297-301.
35. Gero, P.J., et al. *The Zeus climate reference mission*. in *16th International Workshop on Atmospheric Science from Space using Fourier Transform Spectrometry (ASSFTS16)*. 2012. Madison, WI USA.
36. Revercomb, H., et al. *Accuracy Advances in Measuring Earth Emission Spectra for Weather and Climate*. in *AGU Fall Meeting Abstracts*. 2011.
37. Taylor, J.K., et al. *The University of Wisconsin Space Science and Engineering Center Absolute Radiance Interferometer (ARI)*. in *Fourier Transform Spectroscopy*. 2011. Optical Society of America.
38. Taylor, J.K., et al. *The University of Wisconsin Space Science and Engineering Center Absolute Radiance Interferometer (ARI): Predicted and Demonstrated Radiometric Performance*. in *International TOVS Study Conference XiX (ITSC-19)* 2014. Jeju, South Korea.
39. Taylor, J.K., et al. *The University of Wisconsin Space Science and Engineering Center Absolute Radiance Interferometer (ARI): instrument overview and radiometric performance*. in *Proceedings of SPIE (8527)*. 2012. International Society for Optics and Photonics.
40. Taylor, J.K., et al., *The University of Wisconsin Space Science and Engineering Center Absolute Radiance Interferometer (ARI)*, in *Workshop on Infrared Remote Sensing Applications (WIRSA)*. 2010: Quebec.
41. Taylor, J.K., et al. *The University of Wisconsin Space Science and Engineering Center Absolute Radiance Interferometer (ARI): Instrument Overview and Radiometric Performance*. in *16th International Workshop on Atmospheric Science from Space using Fourier Transform Spectrometry (ASSFTS16)*. 2012. Madison, WI USA.
42. Taylor, J.K., et al., *The University of Wisconsin Space Science and Engineering Center Absolute Radiance Interferometer (ARI)*, in *11th International Conference on New Developments and Applications in Optical Radiometry (NEWRAD 2011)*. 2011: Maui, HI, USA.
43. Taylor, J.K., et al. *The University of Wisconsin Space Science and Engineering Center Absolute Radiance Interferometer (ARI)*. in *AGU Fall Meeting Abstracts*. 2010.
44. Taylor, J.K., et al. *The University of Wisconsin Space Science and Engineering Center Absolute Radiance Interferometer (ARI): Radiometric Performance*. in *AGU Fall Meeting Abstracts*. 2011.
45. Taylor, J.K., et al. *The University of Wisconsin Space Science and Engineering Center Absolute Radiance Interferometer (ARI): Predicted and Demonstrated Radiometric Performance*. in *AGU Fall Meeting Abstracts*. 2012.

46. Taylor, J.K., et al. *The University of Wisconsin Space Science and Engineering Center Absolute Radiance Interferometer (ARI)*. in *Proceedings of SPIE (7857)*. 2010. International Society for Optics and Photonics.
47. Taylor, J.K., et al. *The University of Wisconsin Space Science and Engineering Center Absolute Radiance Interferometer (ARI): Instrument Overview and Radiometric Performance*. in *Fourier Transform Spectroscopy*. 2013. Optical Society of America.
48. Taylor, J.K., et al., *The University of Wisconsin Space Science and Engineering Center Absolute Radiance Interferometer (ARI): Instrument Overview and Radiometric Performance*, in *Workshop on Infrared Remote Sensing Applications (WIRSA)*. 2012: Quebec.
49. Taylor, J.K., et al. *A New Class of Advanced Accuracy Satellite Instrumentation (AASI) for the CLARREO Mission: Interferometer Test-bed Tradestudies and Selection*. in *AGU Fall Meeting Abstracts*. 2009.
50. Knuteson, R.O., et al., *Atmospheric emitted radiance interferometer. Part II: Instrument performance*. *Journal of Atmospheric and Oceanic Technology*, 2004. **21**(12): p. 1777-1789.
51. Best, F.A., et al. *Traceability of absolute radiometric calibration for the Atmospheric Emitted Radiance Interferometer (AERI)*. in *Proceedings of the Year 2003 Conference on Characterization and Radiometric Calibration for Remote Sensing*. 2003.
52. Best, F.A., et al. *Determination of the Atmospheric Emitted Radiance Interferometer (AERI) Blackbody Emissivity and Radiance Using Multiple Techniques*. in *Conference on Characterization and Radiometric Calibration for Remote Sensing (CALCON)*. 2009. Logan UT.
53. Best, F.A. and H.E. Revercomb. *Calibration of the Scanning High-resolution Interferometer Sounder (S-HIS) Infrared Spectrometer: Blackbody Reference Standards (Part 2)*. in *Conference on Characterization and Radiometric Calibration for Remote Sensing (CALCON)*. 2005. Logan, UT, USA.
54. Revercomb, H.E. and F.A. Best. *Calibration of the Scanning High-resolution Interferometer Sounder (S-HIS) Infrared Spectrometer: Overview (Part 1)*. in *Conference on Characterization and Radiometric Calibration for Remote Sensing (CALCON)*. 2005. Logan, UT, USA.
55. Taylor, J.K., et al. *Suomi NPP/JPSS Cross-track Infrared Sounder (CrIS): Calibration validation with the aircraft based Scanning High-resolution Interferometer Sounder (S-HIS)*. in *Annual Symposium on Future Operational Environmental Satellite Systems, 10th*. 2014. Atlanta, GA.
56. Best, F.A., et al., *NIST TXR Validation of Scanning HIS Radiances and a UW-SSEC Blackbody*, in *First IASI International Conference*. 2007: Anglet, France.
57. Best, F.A., et al., *High Accuracy Infrared Radiances for Weather and Climate, Part 1: NIST TXR Validation of Scanning HIS radiances and a UW-SSEC Blackbody*, in *Joint 2007 EUMETSAT Meteorological Satellite & 15th AMS Satellite Meteorology and Oceanography Conference*. 2007: Amsterdam, The Netherlands.
58. Taylor, J.K., et al. *SI Traceable Infrared Radiance Measurements and Sources: NIST TXR Validation of S-HIS radiances and a UW-SSEC Blackbody*. in *AGU Fall Meeting Abstracts*. 2008.
59. Taylor, J.K., et al. *NIST TXR Validation of S-HIS radiances and a UW-SSEC Blackbody*. in *AGU Fall Meeting Abstracts*. 2007.
60. Taylor, J.K., et al., *NIST TXR Validation of Scanning HIS Radiances and a UW-SSEC Blackbody*, in *CALCON 2007*. 2007: Utah State University, Logan UT USA.
61. Tobin, D.C., et al., *Suomi-NPP CrIS radiometric calibration uncertainty*. *Journal of Geophysical Research: Atmospheres*, 2013. **118**(18): p. 10,589-10,600.
62. Tobin, D.C., et al. *CrIS Radiometric Calibration: Uncertainty Estimates and Evaluations*. in *SUOMI NPP SDR Science and Validated Product Maturity Review 2013*. College Park, MD: NOAA.
63. Taylor, J.K., *Achieving 0.1 K Absolute Calibration Accuracy For High Spectral Resolution Infrared And Far Infrared Climate Benchmark Measurements*, in *Department of Electrical Engineering and Computer Engineering*. 2011, University of Laval.
64. Goody, R., J. Anderson, and G. North, *Testing climate models: An approach*. *Bulletin of the American Meteorological Society*, 1998. **79**(11): p. 2541-2549.

65. Best, F.A., et al. *On-orbit Absolute Temperature Calibration for CLARREO*. in *Conference on Characterization and Radiometric Calibration for Remote Sensing (CALCON)*. 2007. Logan, UT, USA.
66. Revercomb, H., et al. *The CLARREO Climate Benchmark Mission: Key New Paradigms and Requirements*. in *AGU Fall Meeting Abstracts*. 2008.
67. Taylor, J.K., et al., *The CLARREO Benchmark Climate Mission: A new emphasis on high accuracy for high spectral resolution IR observations*, in *Workshop on Infrared Remote Sensing Applications (WIRSA)*. 2008: Quebec.
68. Best, F.A., et al. *On-Orbit Absolute Radiance Standard for the Next Generation of IR Remote Sensing Instruments*. in *Proceedings of SPIE (8527)*. 2012. International Society for Optics and Photonics.
69. Best, F.A., et al. *On-orbit absolute temperature calibration using multiple phase change materials: overview of recent technology advancements*. in *Proceedings of SPIE (7857)*. 2010. International Society for Optics and Photonics.
70. Dykema, J., M. Witinski, and J. Anderson. *Testing Space-based Infrared Sensors for Systematic Errors*. in *Fourier Transform Spectroscopy*. 2011. Optical Society of America.
71. Gero, P.J., J.A. Dykema, and J.G. Anderson, *A quantum cascade laser-based reflectometer for on-orbit blackbody cavity monitoring*. *Journal of Atmospheric and Oceanic Technology*, 2009. **26**(8): p. 1596-1604.
72. Gero, P.J., et al., *On-orbit absolute blackbody emissivity determination using the heated halo method*. *Metrologia*, 2012. **49**(2): p. S1.
73. Gero, P.J., et al. *The heated halo for space-based blackbody emissivity measurement*. in *Proceedings of SPIE (8527)*. 2012.
74. Gero, P.J., et al. *On-orbit Absolute Blackbody Emissivity Determination Using the Heated Halo Method*. in *Proceedings of SPIE (7857)*. 2010.
75. Best, F.A., et al., *GIFTS On-board Blackbody Calibration Subsystem*, in *NASA GIFTS EDU and Other FTS Instruments*. 2006.
76. Best, F.A., et al. *Performance verification of the Geosynchronous Imaging Fourier Transform Spectrometer (GIFTS) on-board blackbody calibration system*. in *Proceedings of SPIE (6405)*. 2006. Goa, India: SPIE-International Society for Optical Engineering.
77. Hawkins, G.J., *Spectral characterisation of infrared optical materials and filters*. 1998, University of Reading.
78. Buijs, H. and R. Desbiens, *Beamsplitters for various occasions*, in *Workshop on Infrared Remote Sensing Applications (WIRSA)*. 2008: Quebec.
79. Moreau, L., "Figures for Tech Note", J.K. Taylor and M.A. Soucy, Editors. 2009.
80. Grandmont, F.J., *GICS-OMA-2010-01-08*. 2010.
81. BIPM, et al., *The International Vocabulary of Metrology—basic and general concepts and associated terms (VIM)*. JCGM, 2008. **200**.
82. Revercomb, H.E., et al., *Radiometric calibration of IR Fourier transform spectrometers: solution to a problem with the High-Resolution Interferometer Sounder*. *Applied Optics*, 1988. **27**(15): p. 3210-3218.
83. BIPM, et al., *Guide to the Expression of Uncertainty in Measurement*. International Organization for Standardization, Geneva. ISBN. 1995. 92-67.
84. Taylor, B.N. and C.E. Kuyatt, *Guidelines for Evaluating and Expressing the Uncertainty of NIST Measurement Results*. 1994.
85. Pettersen, C. *On-Orbit Absolute Radiance Standard for Future IR Remote Sensing Instruments- Overview of Recent Technology Advancements*. in *Imaging and Applied Optics*. 2011. Optical Society of America.
86. Best, F.A., et al. *Accurately calibrated airborne and ground-based Fourier Transform Spectrometers II: HIS and AERI calibration techniques, traceability, and testing*. in *Council for Optical Radiation Measurements (CORM) 1997 Annual Meeting*. 1997. Gaithersburg, MD.

87. Revercomb, H.E., et al. *Atmospheric emitted radiance interferometer (AERI) for ARM*. in *Fourth Symposium on Global Change Studies*. 1993.
88. Turner, D.D., et al., *An evaluation of the nonlinearity correction applied to Atmospheric Emitted Radiance Interferometer (AERI) data collected by the Atmospheric Radiation Measurement Program*. 2004, Department of Energy Atmospheric Radiation Measurement (ARM) Program.
89. Revercomb, H.E., et al. *Scanning High-resolution Interferometer Sounder (S-HIS) aircraft instrument and validation of the Atmospheric InfraRed Sounder (AIRS)*. in *Fourier Transform Spectroscopy*. 2003. Optical Society of America.
90. Revercomb, H.E., et al. *Highly accurate FTIR observations from the scanning HIS aircraft instrument*. in *Proceedings of SPIE (5655)*. 2005.
91. Taylor, J., et al. *Performance of an infrared sounder on several airborne platforms: the scanning high resolution interferometer sounder (S-HIS)*. in *Proceedings of SPIE (5882)*. 2005.
92. Taylor, J.K., et al. *GIFTS EDU Radiometric Calibration Performance Assessment*. in *NASA GIFTS EDU and Other FTS Instruments*. 2006. Hampton, VA, USA.
93. Taylor, J.K., et al., *Analysis of CrIS Flight Model 1 Radiometric Linearity and Radiometric Uncertainty*, in *ASSFTS 14*. 2009.
94. Taylor, J.K., et al. *Analysis of the CrIS Flight Model 1 Radiometric Linearity*. in *Fourier Transform Spectroscopy*. 2009. Optical Society of America.
95. Tobin, D.C., et al. *UW Analysis of CrIS FM1 TVAC Data*. in *2009 SOAT Meeting*. 2009. Silver Spring, MD, USA.
96. Tobin, D.C. and H.E. Revercomb, *Non-uniform scene ILS effects and correction: Initial analysis for CrIS*. 2012.
97. Abrams, M.C., G.C. Toon, and R.A. Schindler, *Practical example of the correction of Fourier-transform spectra for detector nonlinearity*. *Applied optics*, 1994. **33**(27): p. 6307-6314.
98. Alam, M.S. and J. Predina, *Identification and estimation of nonlinearity in constant-voltage-biased infrared sensor detected signals*. *Optical Engineering*, 2000. **39**: p. 3264.
99. Chase, D.B., *Nonlinear detector response in FT-IR*. *Applied spectroscopy*, 1984. **38**(4): p. 491-494.
100. Zhang, Z.M., C.J. Zhu, and L.M. Hanssen, *Absolute detector calibration applied to nonlinearity error correction in FT-IR measurements*. *Applied spectroscopy*, 1997. **51**(4): p. 576-579.
101. Reine, M.B., et al. *Photovoltaic HgCdTe detectors for advanced GOES instruments*. in *SPIE's 1996 International Symposium on Optical Science, Engineering, and Instrumentation*. 1996. International Society for Optics and Photonics.
102. Theocharous, E., *Absolute linearity measurements on a PV HgCdTe detector in the infrared*. *Metrologia*, 2012. **49**(2): p. S99.
103. Theocharous, E., J. Ishii, and N.P. Fox, *Absolute linearity measurements on HgCdTe detectors in the infrared region*. *Applied optics*, 2004. **43**(21): p. 4182-4188.
104. Knuteson, R.O., et al. *Suomi NPP/JPSS Cross-Track Infrared Sounder (CrIS): Non-Linearity Assessment And On-Orbit Monitoring*. in *93rd AMS Annual Meeting*. 2013. Austin, TX, USA.
105. Lachance, R.L., *Non-linearity correction of FTIR instruments*. 2000, ABB Bomem Inc. p. 1-36.
106. Guelachvili, G., *Distortion free interferograms in Fourier transform spectroscopy with nonlinear detectors*. *Applied optics*, 1986. **25**(24): p. 4644-4648.
107. Carengelo, R.M., D.G. Hamblen, and C.R. Brouillette, *Method and system for photoconductive detector signal correction*. 1992: United States of America.
108. Curbelo, R., *Techniques for correcting non-linearity in a photodetector using predefined calibration information*. 1993: United States of America.
109. Jeseck, P., et al., *Detector nonlinearity correction scheme for the LPMA balloonborne Fourier transform spectrometer*. *Applied optics*, 1998. **37**(27): p. 6544-6549.
110. Tobin, D.C. *NAST-I Detector Nonlinearity Characterization*. in *AIRS Science Team Meeting*. 1999. Santa Barbara, CA, USA.
111. Wilson, S., N. Atkinson, and J. Smith, *The development of an airborne infrared interferometer for meteorological sounding studies*. *Journal of Atmospheric & Oceanic Technology*, 1999. **16**(12).

112. Reine, M.B., *Nonlinear Response of 8-12 μm (HgCd)Te Photoconductor to Large Signal Photon Flux Levels*, P.G. Morse, Editor. 1979, Honeywell.
113. Revercomb, H.E. *Techniques for Avoiding Phase and Non-linearity Errors in Radiometric Calibration: A Review of Experience with the Airborne HIS and Ground-based AERI*. in *Proceedings of the 5th International Workshop on Atmospheric Science from Space using FTS*. 1994.
114. Revercomb, H.E., et al. *Recent results from two new aircraft-based Fourier transform interferometers: The Scanning High-resolution Interferometer Sounder and the NPOESS Atmospheric Sounder Testbed Interferometer*. in *8th International Workshop on Atmospheric Science from Space using Fourier Transform Spectrometry (ASSFTS8)*. 1998. Toulouse, France.
115. Farmer, C.B., *High resolution infrared spectroscopy of the Sun and the Earth's atmosphere from space*. *Microchimica Acta*, 1987. **93**(1-6): p. 189-214.
116. Gunson, M.R., et al., *The Atmospheric Trace Molecule Spectroscopy (ATMOS) experiment: Deployment on the ATLAS space shuttle missions*. *Geophysical Research Letters*, 1996. **23**(17): p. 2333-2336.
117. Revercomb, H.E., *Non-linearity correction issues 17-Jan-2012*, D.C. Tobin, et al., Editors. 2012.
118. Revercomb, H.E., *ATBD Non-Linearity Update-pages 42-44 13June13*, Y. Han, et al., Editors. 2013. p. 2.
119. White, G., J. Predina, and L. Suwinski, *NL Correction TIM*. 2008, ITT.
120. Tobin, D.C., et al., *CrIS Calibration Algorithm and Science Testbed (CCAST)*. 2012.
121. Revercomb, H.E., et al., *CrIS T/V Non-linearity, UW Analysis*. 2008, University of Wisconsin-Madison Space Science and Engineering Center.
122. Revercomb, H.E., *Zeus-Calibration_&_validation_uncertainty-12June09CLARREO-18July11.xls*. 2011.
123. Carter, R.O., N.E. Lindsay, and D. Beduhn, *A solution to baseline uncertainty due to MCT detector nonlinearity in FT-IR*. *Applied Spectroscopy*, 1990. **44**(7): p. 1147-1151.
124. Eppeldauer, G. and L. Novak. *Linear HgCdTe radiometer*. in *Proceedings of SPIE (1110)*. 1989.
125. Grandmont, F.J., *B/S swap and noise*, J.K. Taylor, et al., Editors. 2011.
126. Schwarz, M.A., *CLARREO IIP Optical Design Draft Report*. 2011, Midwest Optical Engineering.
127. Hecht, E. and A. Zajac, *Optics Addison-Wesley*. Reading, Mass, 1974: p. 301-305.
128. Collett, E., *Field guide to polarization*. Vol. 15. 2005: SPIE Press Bellingham.
129. Goldstein, D., *Polarized light*. Polarized light, by D. Goldstein. 2nd, rev. and exp. ed. New York, NY: Marcel Dekker, 2003, 2003. **1**.
130. Knight, E.J., C. Mellow, and C. Salo, *Interaction between polarization and response vs. scan angle in the calibration of imaging radiometers*. *Proceedings of SPIE (3754)*, 1999. **3754**: p. 308.
131. Pagano, T., et al., *Scan Angle Dependent Radiometric Modulation due to Polarization for the Atmospheric Infrared Sounder (AIRS)*. *Optical Science and Technology*, 2000.
132. Shaw, J.A., *The effect of instrument polarization sensitivity on sea surface remote sensing with infrared spectroradiometers*. *Journal of Atmospheric and Oceanic Technology*, 2002. **19**(5): p. 820-827.
133. Sun, J.Q. and X. Xiong, *MODIS polarization-sensitivity analysis*. *Geoscience and Remote Sensing, IEEE Transactions on*, 2007. **45**(9): p. 2875-2885.
134. Young, J.B., E. Knight, and C. Mellow, *MODIS polarization performance and anomalous four-cycle polarization phenomenon*. *Proceedings of SPIE*, 1998. **3439**: p. 247.
135. Knuteson, R.O., et al., *Atmospheric emitted radiance interferometer. Part I: Instrument design*. *Journal of Atmospheric and Oceanic Technology*, 2004. **21**(12): p. 1763-1776.
136. Revercomb, H.E., et al. *Calibration Status for the Infrared: HIRS, AIRS, IASI, CrIS, HES*. in *Achieving Satellite Instrument Calibration for Climate Change (ASIC3)*. 2006. Lansdowne, VA.
137. Revercomb, H. and D. Tobin, *Assessment of Potential Error from CrIS Scene Mirror Induced Polarization*. 2013. p. 1-22.
138. Gero, P.J., *ARI Polarization Sensitivity Model (email)*, J.K. Taylor, Editor. 2011.

139. Kalibjian, R., *Stokes polarization vector and Mueller matrix for a corner-cube reflector*. Optics communications, 2004. **240**(1): p. 39-68.
140. He, W., et al., *Polarization properties of a corner-cube retroreflector with three-dimensional polarization ray-tracing calculus*. Applied optics, 2013. **52**(19): p. 4527-4535.
141. Sromovsky, L.A., *Radiometric errors in complex Fourier transform spectrometry*. Applied optics, 2003. **42**(10): p. 1779-1787.
142. Rowe, P.M., et al., *A responsivity-based criterion for accurate calibration of FTIR emission spectra: identification of in-band low-responsivity wavenumbers*. Optics Express, 2011. **19**(7): p. 5930-41.
143. Rowe, P.M., S.P. Neshyba, and V.P. Walden, *Responsivity-based criterion for accurate calibration of FTIR emission spectra: theoretical development and bandwidth estimation*. Optics Express, 2011. **19**(6): p. 5451-5463.
144. Revercomb, H.E., et al., *UW Approach to Calibration Including Interpolation*, in *CLARREO IR IPT Meeting*. 2011: NASA Langley Flight Research Center.
145. Johnson, D.G. *Radiometric Performance of the Calibration Demonstration System Infrared Fourier Transform Spectrometer*. in *Fourier Transform Spectroscopy*. 2013. Optical Society of America.
146. Johnson, D.G. *Radiometric Performance of the Calibration Demonstration System Infrared Fourier Transform Spectrometer*. in *CLARREO Science Team Meeting*. 2014. NASA Langley.

A. Polarization induced calibration bias model

Appendix A provides the full derivation of the polarization induced calibration bias model presented in Section 4.1.

Assume that the instrument has a polarization dependent transmission and the scan mirror has a polarization dependent reflectance. Equation (6.1) describes the total signal intensity generated for an arbitrary, unpolarized scene or calibration radiance observed at a scene selection mirror angle δ and a sensor polarization axis at an angle α . Note that the individual intensity terms in Eq. (6.1) follow from squaring the components of the scene selection mirror p-polarization and s-polarization amplitudes along both the maximum and minimum axis of the instrument transmission.

$$\begin{aligned}
 V_\delta = & \frac{L_\delta}{2} r_p [t_{\max} \cos^2(\delta - \alpha) + t_{\min} \sin^2(\delta - \alpha)] \\
 & + \frac{L_\delta}{2} r_s [t_{\max} \sin^2(\delta - \alpha) + t_{\min} \cos^2(\delta - \alpha)] \\
 & + \frac{B_{SSM}}{2} \varepsilon_p [t_{\max} \cos^2(\delta - \alpha) + t_{\min} \sin^2(\delta - \alpha)] \\
 & + \frac{B_{SSM}}{2} \varepsilon_s [t_{\max} \sin^2(\delta - \alpha) + t_{\min} \cos^2(\delta - \alpha)] \\
 & + V_{inst}.
 \end{aligned} \tag{6.1}$$

In Eq. (6.1), r_p and r_s are the of the scene mirror for the parallel and perpendicular polarization states, respectively; ε_p and ε_s are the corresponding emissivities and are equal to $1 - r_p$ and $1 - r_s$, since the transmittance for a metal mirror is zero; and t_{\max} and t_{\min} are the major and minor axis of the instrument polarization ellipse, with the major axis oriented at angle α , and both α and δ are specified with respect to the nadir view (refer to Figure 83). The model depends on the relative orientation of the scene mirror and sensor polarization axes, not the absolute angular position of either. The total signal, V_δ , at scene mirror angle δ is composed of the scene radiance, L_δ , as attenuated by the scene mirror reflectance and the radiant emission from the scene mirror, where B_{SSM} is a radiance from a blackbody at the temperature of the scene selection mirror. Both contributions are polarized after reflection or emission from the scene select mirror, and are thus transmitted differently by the instrument, which has a polarization dependent transmission. For simplicity, we have assumed the detector responsivity is unity, since that term will divide out when the signals are substituted into the complex calibration equation.

Using geometric identities, one can show:

$$\begin{aligned}
 a \cdot \cos^2(\theta) + b \cdot \sin^2(\theta) &= \frac{1}{2}(a + b)[\cos^2(\theta) + \sin^2(\theta)] \\
 &+ \frac{1}{2}(a - b)[\cos^2(\theta) - \sin^2(\theta)] \\
 &= \frac{1}{2}(a + b) + \frac{1}{2}(a - b)\cos(2\theta),
 \end{aligned} \tag{6.2}$$

Therefore:

$$t_{\max} \cos^2(\delta - \alpha) + t_{\min} \sin^2(\delta - \alpha) = \frac{1}{2}(t_{\max} + t_{\min}) + \frac{1}{2}(t_{\max} - t_{\min}) \cos 2(\delta - \alpha), \quad (6.3)$$

$$t_{\max} \sin^2(\delta - \alpha) + t_{\min} \cos^2(\delta - \alpha) = \frac{1}{2}(t_{\min} + t_{\max}) + \frac{1}{2}(t_{\min} - t_{\max}) \cos 2(\delta - \alpha). \quad (6.4)$$

Equation (6.1) can be rewritten:

$$\begin{aligned} V_{\delta} = & \frac{L_{\delta}}{2} r_p \left[\frac{1}{2}(t_{\max} + t_{\min}) + \frac{1}{2}(t_{\max} - t_{\min}) \cos 2(\delta - \alpha) \right] \\ & + \frac{L_{\delta}}{2} r_s \left[\frac{1}{2}(t_{\min} + t_{\max}) + \frac{1}{2}(t_{\min} - t_{\max}) \cos 2(\delta - \alpha) \right] \\ & + \frac{B_{SSM}}{2} \varepsilon_p \left[\frac{1}{2}(t_{\max} + t_{\min}) + \frac{1}{2}(t_{\max} - t_{\min}) \cos 2(\delta - \alpha) \right] \\ & + \frac{B_{SSM}}{2} \varepsilon_s \left[\frac{1}{2}(t_{\min} + t_{\max}) + \frac{1}{2}(t_{\min} - t_{\max}) \cos 2(\delta - \alpha) \right] \\ & + V_{inst}. \end{aligned} \quad (6.5)$$

The sensor transmittance t is defined as:

$$t = \frac{1}{2}(t_{\max} + t_{\min}). \quad (6.6)$$

Therefore, equation (6.5) becomes:

$$\begin{aligned} V_{\delta} = & \frac{L_{\delta}}{2} r_p t + \frac{L_{\delta}}{2} r_p \frac{1}{2}(t_{\max} - t_{\min}) \cos 2(\delta - \alpha) \\ & + \frac{L_{\delta}}{2} r_s t + \frac{L_{\delta}}{2} r_s \frac{1}{2}(t_{\min} - t_{\max}) \cos 2(\delta - \alpha) \\ & + \frac{B_{SSM}}{2} \varepsilon_p t + \frac{B_{SSM}}{2} \varepsilon_p \frac{1}{2}(t_{\max} - t_{\min}) \cos 2(\delta - \alpha) \\ & + \frac{B_{SSM}}{2} \varepsilon_s t + \frac{B_{SSM}}{2} \varepsilon_s \frac{1}{2}(t_{\min} - t_{\max}) \cos 2(\delta - \alpha) \\ & + V_{inst}, \end{aligned} \quad (6.7)$$

$$\begin{aligned}
V_\delta &= \frac{L_\delta}{2} r_p t + \frac{L_\delta}{2} r_p \frac{1}{2} (t_{\max} - t_{\min}) \cos 2(\delta - \alpha) \\
&+ \frac{L_\delta}{2} r_s t - \frac{L_\delta}{2} r_s \frac{1}{2} (t_{\max} - t_{\min}) \cos 2(\delta - \alpha) \\
&+ \frac{B_{SSM}}{2} \varepsilon_p t + \frac{B_{SSM}}{2} \varepsilon_p \frac{1}{2} (t_{\max} - t_{\min}) \cos 2(\delta - \alpha) \\
&+ \frac{B_{SSM}}{2} \varepsilon_s t - \frac{B_{SSM}}{2} \varepsilon_s \frac{1}{2} (t_{\max} - t_{\min}) \cos 2(\delta - \alpha) \\
&+ V_{inst} .
\end{aligned} \tag{6.8}$$

The scene mirror reflectance r is defined as:

$$r = \frac{1}{2}(r_p + r_s), \tag{6.9}$$

thus,

$$\begin{aligned}
V_\delta &= L_\delta \frac{1}{2}(r_p + r_s)t + B_{SSM} \frac{1}{2}(\varepsilon_p + \varepsilon_s)t \\
&+ \frac{L_\delta}{2}(r_p - r_s) \frac{1}{2}(t_{\max} - t_{\min}) \cos 2(\delta - \alpha) \\
&+ \frac{B_{SSM}}{2}(\varepsilon_p - \varepsilon_s) \frac{1}{2}(t_{\max} - t_{\min}) \cos 2(\delta - \alpha) + V_{inst}
\end{aligned}$$

$$\begin{aligned}
V_\delta &= L_\delta r t + B_{SSM} \frac{1}{2}(1 - r)t \\
&+ \frac{L_\delta}{2}(r_p - r_s) \frac{1}{2}(t_{\max} - t_{\min}) \cos 2(\delta - \alpha) \\
&+ \frac{B_{SSM}}{2}(\varepsilon_p - \varepsilon_s) \frac{1}{2}(t_{\max} - t_{\min}) \cos 2(\delta - \alpha) + V_{inst}
\end{aligned}$$

$$\begin{aligned}
V_\delta &= (L_\delta - B_{SSM}) r t + B_{SSM} t \\
&+ \frac{L_\delta}{2} \left(\frac{r_p - r_s}{2} \right) (t_{\max} - t_{\min}) \cos 2(\delta - \alpha) \\
&- \frac{B_{SSM}}{2} \left(\frac{r_p - r_s}{2} \right) (t_{\max} - t_{\min}) \cos 2(\delta - \alpha) + V_{inst} .
\end{aligned} \tag{6.10}$$

The following substitution has been used in the final step of equation (6.10),

$$\begin{aligned}
\varepsilon_p - \varepsilon_s &= 1 - r_p - (1 - r_s) \\
\varepsilon_p - \varepsilon_s &= 1 - r_p - 1 + r_s \\
\varepsilon_p - \varepsilon_s &= -(r_p - r_s) .
\end{aligned}$$

Equation (6.10) is further reduced:

$$V_{\delta} = (L_{\delta} - B_{SSM})rt + B_{SSM}t + (L_{\delta} - B_{SSM})\frac{1}{2}\left(\frac{r_p - r_s}{2}\right)(t_{\max} - t_{\min})\cos 2(\delta - \alpha) + V_{inst} . \quad (6.11)$$

The degree of polarization for the scene select mirror (p_r) is defined as:

$$p_r = \frac{r_p - r_s}{r_p + r_s} . \quad (6.12)$$

Similarly, the degree of polarization (diattenuation) of the instrument (p_t) is given by:

$$p_t = \frac{t_{\max} - t_{\min}}{t_{\max} + t_{\min}} . \quad (6.13)$$

Therefore:

$$\begin{aligned} p_r &= \frac{r_p - r_s}{r_p + r_s} \\ (r_p + r_s)p_r &= r_p - r_s \\ \frac{(r_p + r_s)}{2}p_r &= \frac{r_p - r_s}{2} \\ rp_r &= \frac{r_p - r_s}{2} . \end{aligned} \quad (6.14)$$

In the same fashion, it can also be shown that:

$$tp_t = \frac{t_{\max} - t_{\min}}{2} . \quad (6.15)$$

Substituting equations (6.14) and (6.15) equation (6.11):

$$V_{\delta} = (L_{\delta} - B_{SSM})rt + B_{SSM}t + (L_{\delta} - B_{SSM})p_r p_t rt \cos 2(\delta - \alpha) + V_{inst} . \quad (6.16)$$

An expression for the polarization-induced calibration error can be derived by substituting the expression for the total signal generated for an arbitrary, unpolarized scene or calibration radiance observed at a scene selection mirror angle into the complex calibration equation. The complex calibration equation is provided in equation (6.17) for reference,

$$L_S(\sigma_k) = (L_H(\sigma_k) - L_C(\sigma_k))\text{Re}\left\{\frac{S_S(\sigma_k) - S_C(\sigma_k)}{S_H(\sigma_k) - S_C(\sigma_k)}\right\} + L_C(\sigma_k) . \quad (6.17)$$

Therefore,

$$\begin{aligned} L_{\delta,S}(\sigma_k) &= L_S(\sigma_k) + E_p(\sigma_k) \\ L_S(\sigma_k) &= L_{\delta,S}(\sigma_k) - E_p(\sigma_k), \end{aligned} \quad (6.18)$$

where $L_S(\sigma_k)$ is the correct calibrated radiance, $L_{\delta,S}(\sigma_k)$ is the calibrated radiance affected by the calibration bias polarization and $E_p(\sigma_k)$ is the polarization induced error.

The calibrated radiance affected by the calibration bias polarization ($L_{S,\delta}(\sigma_k)$) is:

$$L_{\delta,S}(\sigma_k) = (L_H(\sigma_k) - L_C(\sigma_k)) \left[\frac{V_{\delta,S}(\sigma_k) - V_{\delta,C}(\sigma_k)}{V_{\delta,H}(\sigma_k) - V_{\delta,C}(\sigma_k)} \right] + L_C(\sigma_k). \quad (6.19)$$

The total signal V_δ generated for an arbitrary, unpolarized scene or calibration radiance observed at a scene selection mirror angle δ is provided in equation (6.16), and can be substituted into (6.19) for the scene ($V_{\delta,S}$), cold calibration reference ($V_{\delta,C}$), and hot calibration reference ($V_{\delta,H}$) measurements.

For simplicity, the spectral dependence is not explicitly noted for the remainder of the derivation.

The difference in the numerator of the measured term is simplified:

$$\begin{aligned} V_{\delta,S} - V_{\delta,C} &= (L_S - B_{SSM})rt + B_{SSM}t + (L_S - B_{SSM})p_r p_t rt \cos 2(\delta_S - \alpha) + V_{inst} \\ &\quad - [(L_C - B_{SSM})rt + B_{SSM}t + (L_C - B_{SSM})p_r p_t rt \cos 2(\delta_C - \alpha) + V_{inst}] \\ &= (L_S - L_C)rt + p_r p_t rt [(L_S - B_{SSM})\cos 2(\delta_S - \alpha) - (L_C - B_{SSM})\cos 2(\delta_C - \alpha)]. \end{aligned} \quad (6.20)$$

A similar result is obtained for the difference in the denominator of the measured term:

$$\begin{aligned} V_{\delta,H} - V_{\delta,C} &= (L_H - B_{SSM})rt + B_{SSM}t + (L_H - B_{SSM})p_r p_t rt \cos 2(\delta_H - \alpha) + V_{inst} \\ &\quad - [(L_C - B_{SSM})rt + B_{SSM}t + (L_C - B_{SSM})p_r p_t rt \cos 2(\delta_C - \alpha) + V_{inst}] \\ &= (L_H - L_C)rt + p_r p_t rt [(L_H - B_{SSM})\cos 2(\delta_H - \alpha) - (L_C - B_{SSM})\cos 2(\delta_C - \alpha)]. \end{aligned} \quad (6.21)$$

Combining the numerator and denominator for the measured term:

$$\begin{aligned} \frac{V_{\delta,S} - V_{\delta,C}}{V_{\delta,H} - V_{\delta,C}} &= \frac{(L_S - L_C)rt + p_r p_t rt [(L_S - B_{SSM})\cos 2(\delta_S - \alpha) - (L_C - B_{SSM})\cos 2(\delta_C - \alpha)]}{(L_H - L_C)rt + p_r p_t rt [(L_H - B_{SSM})\cos 2(\delta_H - \alpha) - (L_C - B_{SSM})\cos 2(\delta_C - \alpha)]} \\ &= \frac{(L_S - L_C) + p_r p_t [(L_S - B_{SSM})\cos 2(\delta_S - \alpha) - (L_C - B_{SSM})\cos 2(\delta_C - \alpha)]}{(L_H - L_C) + p_r p_t [(L_H - B_{SSM})\cos 2(\delta_H - \alpha) - (L_C - B_{SSM})\cos 2(\delta_C - \alpha)]} \\ \frac{V_{\delta,S} - V_{\delta,C}}{V_{\delta,H} - V_{\delta,C}} &= \frac{L_S - L_C}{L_H - L_C} \left[\frac{1 + \frac{p_r p_t}{L_S - L_C} [(L_S - B_{SSM})\cos 2(\delta_S - \alpha) - (L_C - B_{SSM})\cos 2(\delta_C - \alpha)]}{1 + \frac{p_r p_t}{L_H - L_C} [(L_H - B_{SSM})\cos 2(\delta_H - \alpha) - (L_C - B_{SSM})\cos 2(\delta_C - \alpha)]} \right] \end{aligned} \quad (6.22)$$

Substituting (6.22) into the expression for calibrated radiance affected by the calibration bias polarization provided in Eq. (6.19):

$$\begin{aligned}
L_{\delta,S} &= (L_H - L_C) \left[\frac{V_{\delta,S} - V_{\delta,C}}{V_{\delta,H} - V_{\delta,C}} \right] + L_C \\
&= (L_H - L_C) \left[\frac{V_{\delta,S} - V_{\delta,C}}{V_{\delta,H} - V_{\delta,C}} \right] + L_C \\
&= (L_H - L_C) \frac{L_S - L_C}{L_H - L_C} \left[\frac{1 + \frac{p_r p_t}{L_S - L_C} \left[\begin{array}{c} (L_S - B_{SSM}) \cos 2(\delta_S - \alpha) \\ -(L_C - B_{SSM}) \cos 2(\delta_C - \alpha) \end{array} \right]}{1 + \frac{p_r p_t}{L_H - L_C} \left[\begin{array}{c} (L_H - B_{SSM}) \cos 2(\delta_H - \alpha) \\ -(L_C - B_{SSM}) \cos 2(\delta_C - \alpha) \end{array} \right]} \right] + L_C \\
&= (L_S - L_C) \left[\frac{1 + \frac{p_r p_t}{L_S - L_C} \left[\begin{array}{c} (L_S - B_{SSM}) \cos 2(\delta_S - \alpha) \\ -(L_C - B_{SSM}) \cos 2(\delta_C - \alpha) \end{array} \right]}{1 + \frac{p_r p_t}{L_H - L_C} \left[\begin{array}{c} (L_H - B_{SSM}) \cos 2(\delta_H - \alpha) \\ -(L_C - B_{SSM}) \cos 2(\delta_C - \alpha) \end{array} \right]} \right] + L_C \\
L_{\delta,S} &= (L_S - L_C) \left\{ \frac{1 + \frac{p_r p_t}{L_S - L_C} \left[\begin{array}{c} L_S \cos 2(\delta_S - \alpha) - L_C \cos 2(\delta_C - \alpha) \\ - B_{SSM} [\cos 2(\delta_S - \alpha) - \cos 2(\delta_C - \alpha)] \end{array} \right]}{1 + \frac{p_r p_t}{L_H - L_C} \left[\begin{array}{c} L_H \cos 2(\delta_H - \alpha) - L_C \cos 2(\delta_C - \alpha) \\ - B_{SSM} [\cos 2(\delta_H - \alpha) - \cos 2(\delta_C - \alpha)] \end{array} \right]} \right\} + L_C . \tag{6.23}
\end{aligned}$$